NASA

DEVELOPMENT OF A ROTATING GRAVITY GRADIOMETER FOR EARTH ORBIT APPLICATIONS (AAFE)

FINAL REPORT

JANUARY 1973

PREPARED UNDER CONTRACT NAS 1-10945

BY
HUGHES RESEARCH LABORATORIES
3011 MALIBU CANYON ROAD
MALIBU, CALIFORNIA 90265

FOR
ADVANCED APPLICATIONS FLIGHT EXPERIMENTS PROGRAM OFFICE
NATIONAL AERONAUTICS AND SPACE ADMINISTRATION
LANGLEY RESEARCH CENTER
HAMPTON, VIRGINIA 23365

DEVELOPMENT OF A ROTATING GRAVITY GRADIOMETER FOR EARTH ORBIT APPLICATIONS (AAFE)

Robert L. Forward, Principal Investigator
Curtis C. Bell
Philip M. LaHue
Eugene F. Mallove
David W. Rouse

FINAL REPORT

Contract No. NAS 1-10945

Advanced Applications Flight Experiments Program Office
National Aeronautics and Space Administration
Langley Research Center
Hampton, Virginia

Period Covered: 22 June 1971 through 21 September 1972

TABLE OF CONTENTS

LIST OF ILLUSTRATIONS

ABSTRACT

A large gravity gradiometer flown in a low earth orbit would significantly improve man's knowledge of the earth's gravitational field. Such knowledge would be of value to the geodesy, geophysics and geology fields, and would have application to orbital mechanics, navigation, guidance, earth dynamics, and mineral prospecting. This report describes some preliminary mission studies and the design, fabrication, and test of a breadboard model of an earth orbital, rotating gravity gradiometer with a design goal of 10^{-11} sec^{-2} (0.01 EU) in a 35-sec integration time.

The proposed mission uses a Scout vehicle to launch one (or two orthogonally oriented) spin-stabilized satellites into a 330-km circular polar orbit some 20 days before an equinox. During the short orbital lifetime, the experiment would obtain two complete maps of the gravity gradient field with a resolution approaching 270 km (degree 75). Individual point anomalies, although smaller than 270 km, would be measured to 0.01 EU. The higher order harmonics would be sampled independently over 100 times during the mission to give an amplitude accuracy after data reduction below 0.001 EU.

The breadboard model of the gradiometer demonstrated a combined thermal and electronic noise threshold of 0.015 EU per data channel. Hughes Research Laboratories (HRL) identified the design changes needed to reduce the noise to less than 0.01 EU. Variations of the sensor output signal with temperature were experimentally determined and a suitable method of temperature compensation was developed and tested. Other possible error sources, such as sensor interaction with satellite dynamics and magnetic fields, were studied analytically and shown to be small.

SECTION I

INTRODUCTION

This final report contains the results of a 15-month, $110,000 contract for the design, fabrication, and test of a rotating gravity gradiometer for earth orbit applications. The work was carried out under the auspices of the NASA Advanced Applications Flight Experiments Program Office, Langley Research Center, Hampton, Virginia. The objective of the AAFE program is to carry forward instrument development independent of flight opportunities.

On this contract HRL developed a preliminary design of an experiment for measurement of the gravity gradients of the earth's field from orbit, and determined a set of mission, spacecraft, and sensor parameters that would achieve the desired scientific goals. HRL then executed a detailed design of a sensor structure, fabricated a breadboard model of the sensor structure and the important parts of the data processing electronics, and conducted tests of the sensor performance.

Because of the relatively low level of effort, the testing program was limited to simulated signals. However, past testing with real gravity gradient signals (see Appendix B and Attachment A) had shown the validity of these simulations. The stated design goal of the contract was a sensor with a threshold sensitivity of 0.1 EU (1 EU $= 10^{-9}$ gals/cm $= 10^{-9}$ sec^{-2} $\approx 10^{-12}$ g/cm) with a 35-sec integration time. As a result of preliminary design studies, HRL determined that a design goal of 0.01 EU would produce a sensor that obtains useful scientific return from the experiment. A sensor was fabricated, having parameters that would result in a noise level of 0.015 EU, and modifications that would result in a sensor with a noise level approaching 0.007 EU were identified.

Prior testing on feasibility models of the rotating gravity gradiometer (1969 through 1970) have indicated that near thermal noise limited threshold signal levels could be attained with the sensor operating in a sufficiently quiet (simulated free-fall) environment. Because of the low resonant frequency and large size of the earth orbital model, the cost of attaining such an environment was considered beyond the scope of the contract. Such a test could be run, and provided the recommended improvements made in Section V of this report were completed, such a test should result in demonstrating a threshold noise level near the sensor thermal noise limit (<0.02 EU). The estimated excess noise over the combined thermal and electronic noise of the sensor (<0.01 EU) would be the result of the residual sensor interaction with the laboratory vibrational environment. The foregoing estimate assumes a test involving a carefully isolated, magnetically shielded, and thermally controlled sensor, not rotating, with nearby rotating masses providing a dynamically varying gravitational gradient field.

Because of the high vibration levels, concomitant with rotating this large size gradiometer in an earth-bound environment, an attempt to conduct a threshold sensitivity test in which the gradiometer rotates in a static gradient field is considered unfavorable. Such tests could quite readily be conducted, however, in a free-fall environment such as Skylab.

SECTION II

DESIGN STUDIES

The contract began with a series of design studies to determine the relevant parameters of the gravity field to be measured, the various possible missions that could be considered, and the effects of these missions on the satellite and sensor design parameters. The design of the gravity gradiometer is strongly dependent upon the particular mission and using vehicle, a condition that is especially true for this particular application to earth geodesy. The size and operational parameters of the sensor are determined by the orbital altitude and inclination, mission lifetime, and measurement requirements of geodesy. The sensor, in turn, has an effect on the spacecraft, especially the requirements for spin speed, temperature, and attitude control.

The presently envisioned experiment is the result of these design studies. It uses a Scout vehicle with a 42-in. diameter payload shroud to launch one (or two orthogonally oriented) spin-stabilized satellites into a 330-km circular polar orbit some 15 to 20 days before the vernal or autumnal equinox. The satellite would carry a 76-cm diameter gravity gradiometer with a sensitivity of 0.01 EU at 35-sec integration time. The orbital lifetime would be short, but during that time the experiment would obtain at least two complete maps of the gravity gradient field with a resolution approaching 270 km (540-km wavelength or degree 75). Individual point anomalies, although smaller than 270 km in extent, would be measured to 0.01 EU while the higher order harmonic components would be sampled independently up to 170 times during each orbit, thereby giving an amplitude accuracy after data reduction down to 0.0008 EU for the higher order harmonics.

HRL conducted brief design studies early in 1971, that resulted in the proposed general experiment design, and were verified in detail by a separate Phase A study[1] carried out by Jet Propulsion

Laboratory (JPL) during late 1971 and early 1972. The reader is referred to this more recent and more comprehensive report for detailed discussion of the mission parameters and two different satellite designs, including power, weight, subsystem, and data reduction estimates.

A. GRAVITY FIELD PARAMETERS

To determine the gravity gradient sensitivity requirements for the sensor, HRL performed certain calculations of the gravity gradient field strengths to be expected in earth orbit. At the time of its design studies, little published data existed. Prior to the contract, HRL had undertook various studies to estimate the gravity gradient fields at altitude. For its estimates HRL used the Kaula "rule of thumb"[2] that the strength of the various harmonic orders goes as

$$\frac{1}{2n+1} \sum_m \left(\bar{C}_{nm}^{\,2} + \bar{S}_{nm}^{\,2} \right) \approx \frac{10^{-10}}{n^4} \quad n > 2 \ .$$

A summation of this HRL effort was presented at the Washington AGU meeting in April 1971, and the reprint is included as Attachment A. HRL re-examined this work in its design effort (see Appendix B) and found it adequate for an initial examination of the problem. A calculation was made of the gravity gradients to be expected for typical single anomalies (Fig. 1) and for various harmonic orders (Fig. 2), and the conclusion was drawn that in order to make a significant contribution to geodesy and geophysics, the gradiometer sensitivity should be better than the 0.1 EU which was the stated design goal in the contract statement of work. As a result of these studies, HRL adopted 0.01 EU as the design goal for the sensor.

These preliminary studies early in 1971 were followed by a number of studies by others that generally confirmed HRL's preliminary studies. A paper by Sandson and Strange of Computer Sciences

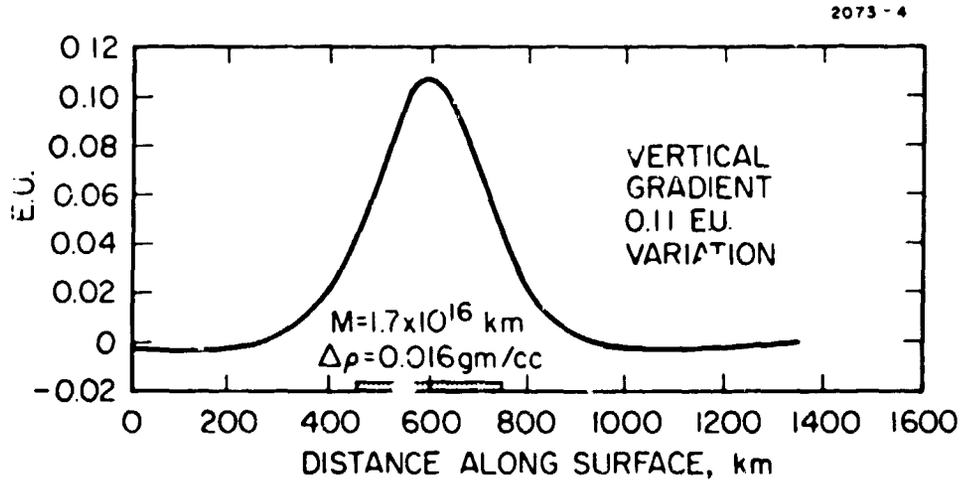

Fig. 1. Vertical Gravity Gradient of Single 300-km Diameter Disk at 250-km Altitude.

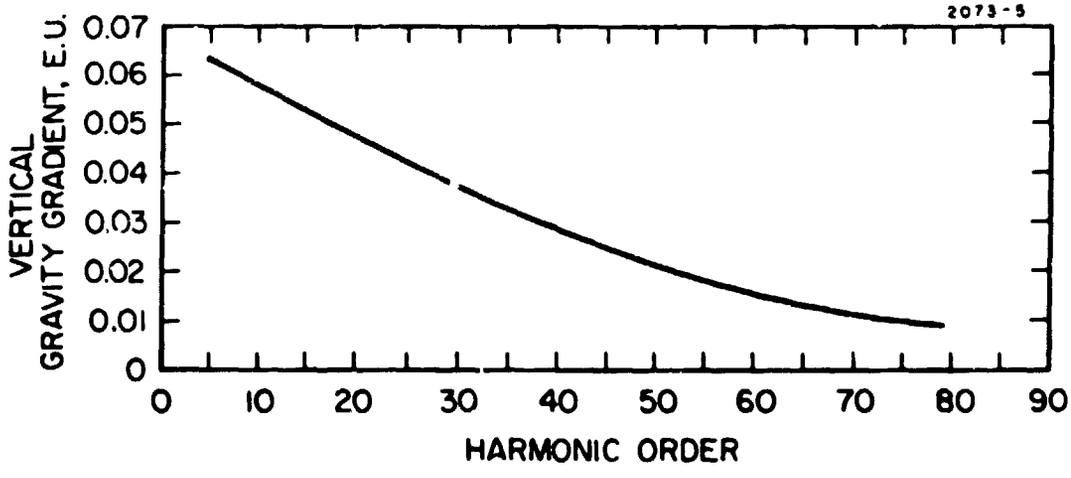

Fig. 2. Vertical Gravity Gradient of Various Harmonic Orders at 250-km Altitude.

Corporation[3] calculated the gradient at altitude from $1^{o} \times 1^{o}$ surface gravity data, and a 12th degree and order satellite gravity field at 300 km altitude. The results (Fig. 3) indicated that accuracies better than 0.1 EU were required to provide useful improvements to present geophysical knowledge.

A paper by Chovitz, Lucas, and Morrison of NOAA[4] calculated the gravity gradients along hypothetical 300-km altitude orbits selected in regions of dense 1^{o} coverage. These results verified the validity of the Kaula "rule of thumb" to 30%. Typical results of their computer simulation were a magnitude of 0.008 EU caused by the harmonics of the 61st degree only, and of 0.02 EU caused by the combined harmonics of the 61st through the 70th degree.

A paper by Glaser of JPL[5], using extrapolations of Kaula's rule of thumb, obtained similar results (Fig. 4) and also compared the relative accuracy of doppler, altimeter, and gradiometer techniques of obtaining gravity field data from orbital satellites (Fig. 5). As expected, each technique has its region of applicability and the three techniques should be considered as complementary rather than as competitive techniques.

B. MISSION PARAMETERS

To map the higher order harmonics of the earth's gravity field, it would be desirable to have the measurements take place at as low an orbit as possible. Because of the mathematical characteristics of the potential field, the resolution of any gravity measurement at altitude is roughly equivalent to the altitude. A low orbit, however, has a very short lifetime because of atmospheric drag, and a short lifetime makes it difficult to obtain the complete coverage of the earth that is also desired.

Therefore, a low orbit with orbital parameters is needed such that the orbital tracks interleave so complete coverage is obtained in a period shorter than the orbital lifetime, and where the track spacing

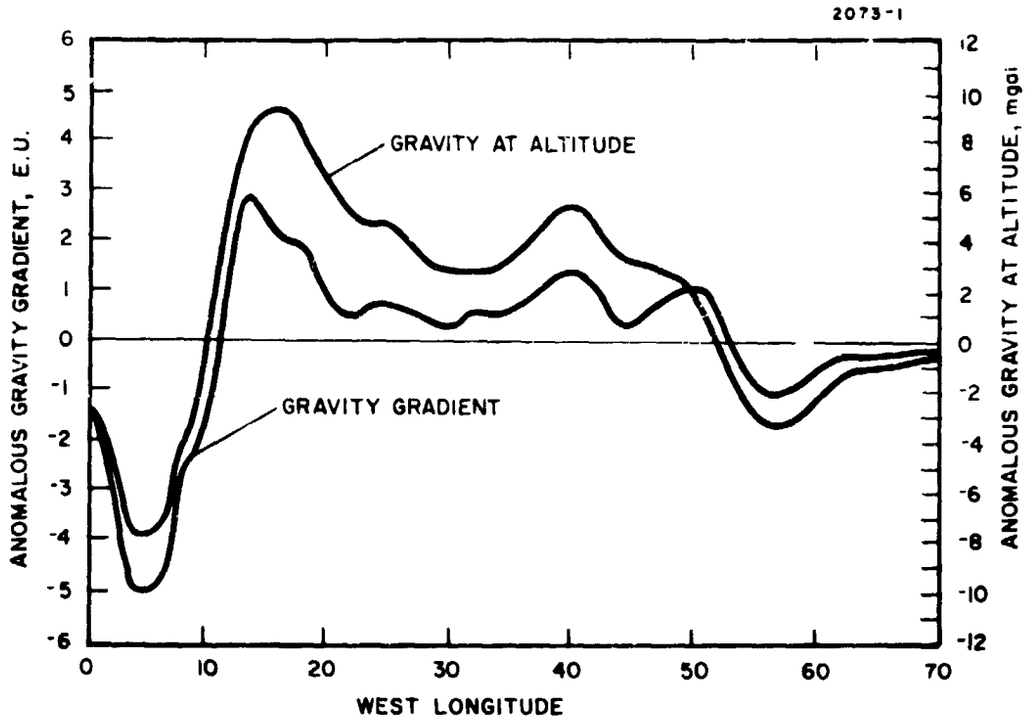

Fig. 3. Unmodelled Anomalous Gravity and Gravity Gradient at Satellite Altitude (300 cm) (from Ref. 3).

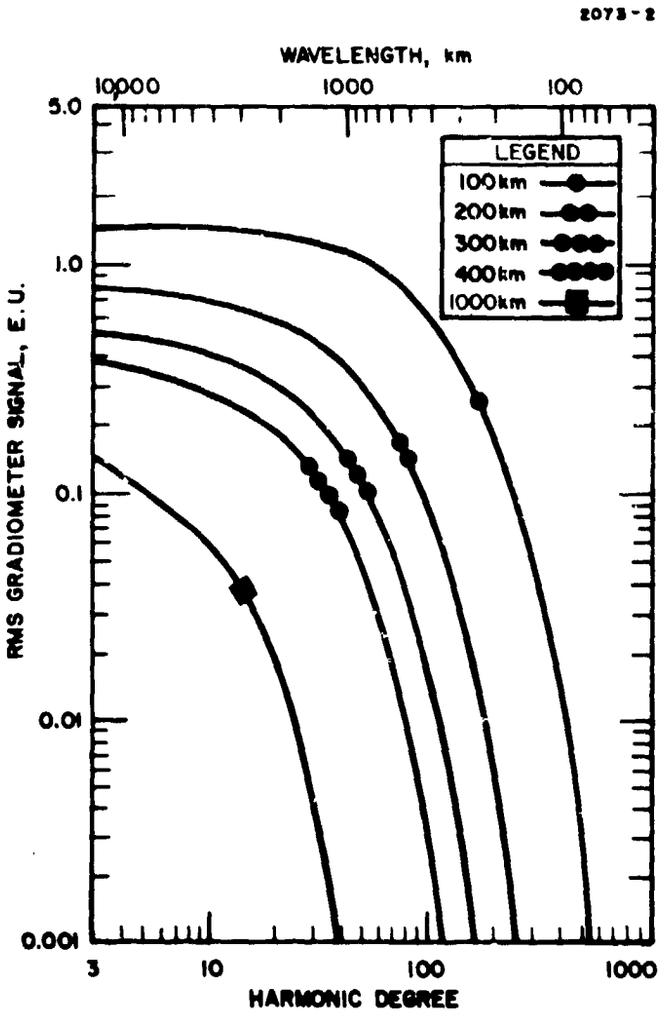

Fig. 4. Gravity Signal Remaining by Harmonic Degress and Altitude (from Ref. 5).

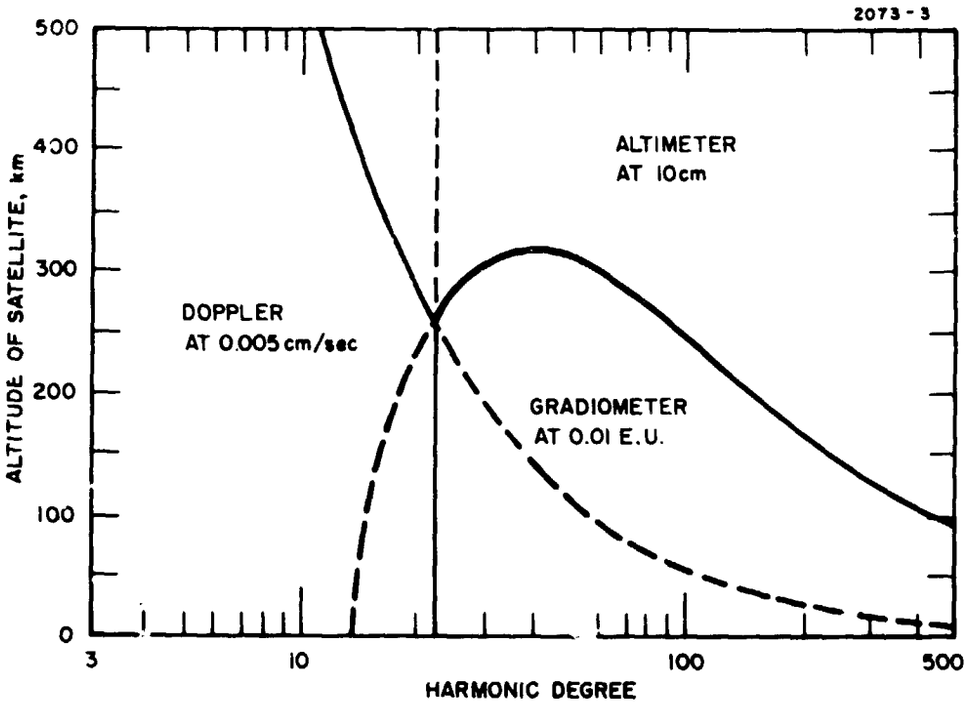

Fig. 5. Regions of Best Sensitivity for Altimeter, Doppler, and Gradiometer by Harmonic Degree and Altitude (from Ref. 5).

is matched to the swath width (equal to the altitude). A set of orbital parameters is existent that fits these requirements fairly well. At an orbital altitude of 270 km, an "integer orbit"[6,7] exists. The orbital track repeats upon itself after exactly 16 orbits. This orbit can be polar, with 16 orbits per sidereal day, or a sun synchronous orbit (at a slightly different altitude and inclination) with 16 orbits per solar day. If the altitude is slightly higher or lower, then the orbital track drifts so that the 16th orbit is displaced to either one side or the other of the first track. These offset orbits finally begin to repeat after a number of days when the drift has caused the satellite track to overlap the second ground track. Two of these orbits are of interest. They repeat after about 5 days, and their track spacing is approximately equal to the altitude. One is a polar orbit at about 320 km that repeats after 79 orbits, and the other is a polar orbit with altitude of 220 km that repeats after 81 orbits. The track spacing between the half arcs for both orbits is approximately 250 km, so that there is a good match between the track spacing and the swath width.

In reality, the orbital altitudes decay as a result of drag, so that these simple orbital path models are not followed exactly. HRL presently envisions launching into a 330-km polar orbit and allowing the altitude to decay through these two altitudes where overlapping coverage is obtained. Hughes has chosen a polar orbit rather than a sun synchronous orbit in order to obtain full coverage of the earth and provide for calibration points twice per orbit at the two poles. The orbital lifetime estimated for the mission is approximately 30 to 50 days. The time spent near 320 km would be long enough to obtain good coverage of the earth at that resolution (640-km wavelength or degree 62). As the altitude decreases, resolution will improve. There should be a substantial amount of coverage at around 220-km altitude with excellent resolution (440-km wavelength or degree 90), but some coverage will be lost because of the rapidly decreasing altitude and the fact that the track spacing at the equator of 250 km is slightly larger than the sensor resolution.

1. Non-Eclipse Orbits (See Appendix E)

It would be desirable to launch the gradiometer satellites into a polar orbit of the earth that does not cause the satellites to be eclipsed by the earth throughout the mission. The advantages of the non-eclipse orbit are the weight reduction and reliability increase available by elimination of batteries for electrical power during the eclipse portion of the flight. Also, the thermal control system required for the sensor would only have to contend with one state of thermal equilibrium rather than cycling between two.

HRL has investigated possible non-eclipse orbits and has found that even despite the relatively low orbits under considerations, it is possible to achieve non-eclipse periods several times longer than the estimated lifetimes for these orbits. To attain these orbits only requires that a launch window constraint be placed on the mission. The satellite is launched 15 to 20 days before either the vernal or autumnal equinox (21 March or 21 September) into a polar orbit chosen such that on the day of the equinox, the orbital plane coincides with the terminator plane. At this point in time, the ecliptic and celestial poles of the earth are all in the terminator plane. The slow rotation of the terminator plane about the ecliptic poles causes a drift between the terminator plane and the orbital plane ($\sim 1^{\circ}$/day). However, simple calculations show that with this choice of launch time and orientation, it is possible to have non-eclipse periods in excess of 30 days even for orbital altitudes below 250 km.

Non-eclipse orbits could also be chosen using sun-synchronous orbits lying near the terminator plane, the non-eclipse period is then theoretically infinite. The foregoing shows, however, that with this minor constraint on launch time, the advantages of a non-eclipse orbit may be achieved while the self-calibration and full coverage aspects of the polar orbit are retained.

C. SPACECRAFT PARAMETERS

Because of the relatively low field strengths estimated for the higher order harmonics of the earth's field, the sensor must be made as large as possible. The arm length of the sensor is primarily determined by the maximum radius obtainable in the spacecraft, which, in turn, is determined by the payload envelope of the launch vehicle. If a Scout launch vehicle is used to keep costs down and reliability up, a number of launch shroud configurations that have been developed for this vehicle may be used. One of the largest in diameter is the 42-in. diameter shroud mentioned in the Scout users' handbook. The allowable payload diameter for this shroud is 96.5 cm (36 in.). The cylindrical portion of the payload envelope with this diameter is 84 cm (33 in.) long, which allows space for two cylindrical spacecraft 96 cm in. diameter by 42 cm thick. A very preliminary spacecraft design of this size is shown in Figs. 6 and 7. The sensor arm length with this spacecraft configuration is about 40 cm.

The front part of the payload envelope can be used for a spin-up and attitude control system that inserts the two spacecraft into orbit with the proper attitude and spin speed. After the payload attains orbit, the spin control mechanism increases the satellite spin speed to the desired rate (about 240 rpm) and orients the spin along the orbital track. After release of one spacecraft, the jets are used to torque the other spacecraft so that its spin vector is perpendicular to the first spacecraft. With the two spacecraft in this relative orientation, one craft measures the vertical gravity gradient and the cross-track horizontal gradient, while the other measures the along-track horizontal gradient and a redundant measurement of the cross-track gradient. After 1/4 of an orbit, the orientation of the two satellite spin axes relative to the orbital track changes, and the data output from the two sensors is interchanged. Although this is a relatively complex mode of data collection, it does allow for the measurement of more components of the gravity gradient at the same time. Most important, this mode of operation allows the cross-track gradient information to be obtained,

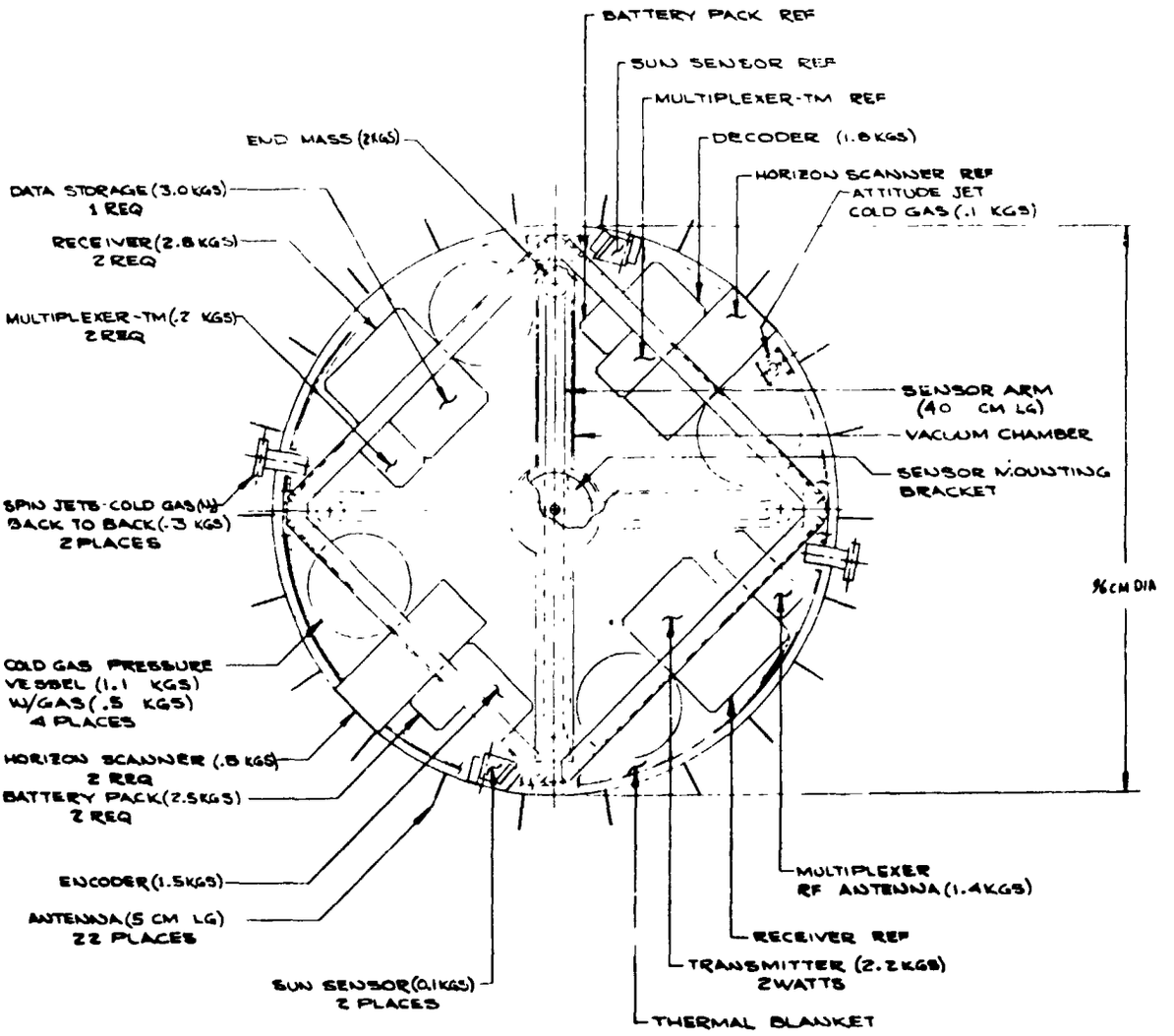

Fig. 6. Spacecraft Configuration for Earth Geodesy Experiment. (Plan View).

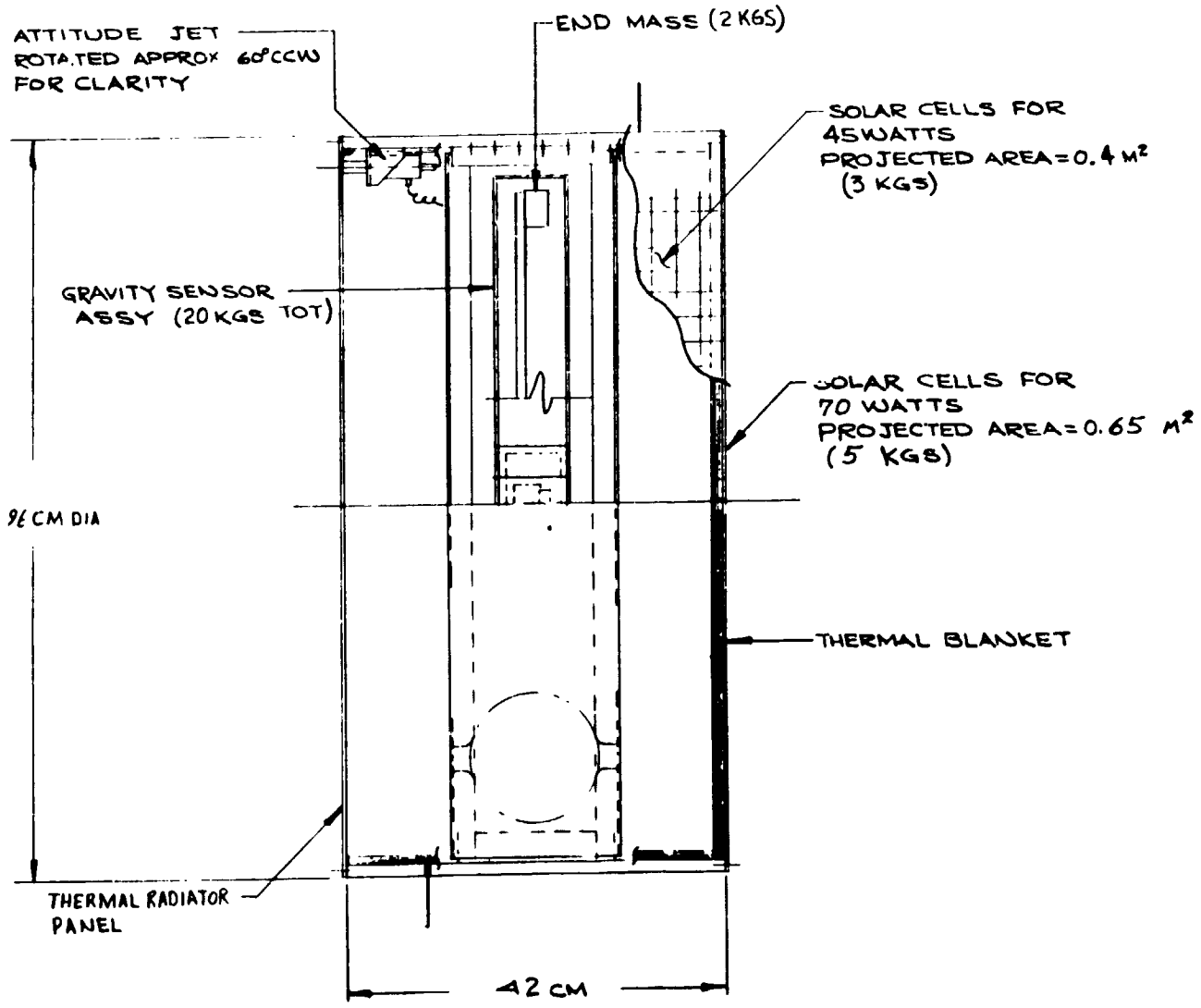

Fig. 7. Spacecraft Configuration for Earth Geodesy Experiment. (Side View).

which can be used to tie the data together across the orbital tracks. The cross-track gradient along one track can be used to predict the gravity field at the next track. This closure property of the data sets can be used to eliminate drift errors.

A simpler version of the experiment is to launch a single satellite and torque the spacecraft spin axis so that it lies in the plane of the orbit. The advantages of this mode of operation are that the spin axis of the spacecraft does not change orientation with respect to the orbit, and the drag torques remain constant. In this orientation, the gradiometer measures the difference between the vertical gradient and the along-track horizontal gradient, and their orientation with respect to the local vertical.

A major interaction of the sensor and the satellite is the dynamical interaction of the two mechanical structures. In its work prior to the contract, HRL performed a dynamic analysis of the interaction of the sensor and the spacecraft (see Attachment B). For the design phase of the contract, HRL improved this analysis for the specific mission and sensor design. A report of this work constitutes Appendix C.

As a result of this dynamic analysis, HRL determined a number of spacecraft parameters that should be controlled. The spacecraft transverse moments of inertia should be the same to 1%, and the alignment of the spacecraft spin axis and the direction of the sensor torsional axis should be aligned to within 10^{-3} radians (the position of the center of mass of the sensor is not critical), and the spacecraft coning angle should be kept below 10^{-5} radians with nutation dampers.

The results of the analysis are summarized in Table I, which shows the significant gradiometer errors caused by sensor-satellite dynamics. The table shows the sources of the error signals, their frequency, and their equivalent amplitude in EU.

The dc torques between the sensor arms do not generate any steady state signals because of the finite resistance across the transducer. Those terms at or near the spin frequency will be cut by a factor of greater than 100 by the integrating circuits of the electronics.

TABLE V

Significant Gradiometer Errors Due to Sensor Satellite Dynamics

Error Ouputs	Frequency	Equivalent Amplitude (EU)
Rotational Field Driving Function $(\omega_i\omega_j)$	dc	40
	$2\sqrt{k_1k_2}\ \omega_s$	10^{-2}
Sum Mode Mismatch $(\dot{\omega}_k)$	dc	0.4
	$\sqrt{k_1k_2}\ \omega_s$	10^{-1}
Mass Unbalance $(\Gamma_{\mu max})$	dc	5×10^5
	ω_s	5
	dc	20

T368

where

ω_s = spin frequency

$\sqrt{k_1k_2}$ = 0.99

This leaves only one term, the second term of the rotational field driving function, which is on the threshold noise level and close to the sensor detection frequency. If this term is traced back to its origins, it is found to be strongly dependent on the spacecraft coning angle. Any increase in this angle above the assumed 10^{-5} radians will cause signals above 10^{-2} EU. This signal varies as the square of this coning angle.

Since the HRL design study effort, a complete and detailed Earth Physics Satellite design has been developed by JPL[1] which includes an extensive discussion of the desired satellite parameters and the methods of achieving them. The reader is referred to this study report for this more up-to-date design.

desired satellite parameters and the methods of achieving them. The reader is referred to this study report for this more up-to-date design.

D. SENSOR PARAMETERS

Most sensor parameters are determined by mission and spacecraft constraints. The desirability of obtaining 0.01 EU sensitivity indicates the need for a sensor arm length that is as long as possible. A sensor arm length 76 cm from center to center of the end masses (86 cm overall) was selected as the largest arm diameter possible for the 96-cm spacecraft diameter, which, in turn, is dictated by the Scout payload envelope of 106.5-cm diameter. The chosen arm end masses were 2 kg each, this weight considered as being reasonable for the size of the sensor.

The 35-sec sensor time constant was derived by using the time required for the spacecraft to pass through one resolution element at the nominal altitude of 270 km at the orbital velocity of 7.75 km/sec. This figure was considered a reasonable optimum between the 41 sec for 320-km altitude and the 29 sec for 220-km altitude. With this size, weight, and time constant for the sensor, the thermal noise caused by the Brownian motion of the sensor structure has an equivalent noise level of 0.007 EU. This ultimate lower limit was distressingly close to the design goal of 0.01 EU, but could not be lowered within the constraints imposed by the Scout payload envelope. This sensor system time constant is the smoothing time to be used in the sensor data preprocessing. The sensor output should be sampled approximately once every 1 to 5 sec to overcome digitalization noise, prevent aliasing, and pick up strong, short period signals resulting from dense localized anomalies.

The sensor frequency of operation is not critical and is set by conflicting requirements. This frequency should be as low as possible to ease the spin speed stress requirements on the satellite structure, and should be high as possible to avoid the low-frequency noise in the

electronics and for ease in laboratory testing, where it is difficult to obtain adequate vibrational and acoustic isolation for mechanical structures below 10 Hz. The selected design frequency is 8 Hz, which implies a spin speed of 240 rpm (4 rps) for the satellite; although fast, this speed is not unreasonable. As is mentioned in Section III, the measured sensor frequencies are about 5 Hz.

With the 8-Hz sensor frequency and 35-sec sensor time constant, τ the desired sensor quality factor, Q, is

$$Q = \pi f \tau = 800 \quad .$$

Previous work indicated there should be little problem in obtaining a Q of this value with a structure such as this, since Q's from 300 to 2000 had been formerly obtained. Section III shows that HRL did not achieve this Q level in the sensor, although a redesign should provide an increased Q.

SECTION III

GRADIOMETER DESIGN, FABRICATION, AND TEST

A. DESIGN CONCEPT

During the contract study phase, several problem areas were anticipated which had to be accounted for in the sensor design. Primary among these was the fact that to obtain usable data from a 270-km altitude satellite orbit, the gradiometer must have a basic resolution level of 0.01 EU ($\frac{3}{2}\frac{GM}{R3}$). This implies resolution of two parts per million in a background gradient field of 4500 EU. Therefore, several design areas of no great concern in previous sensor designs were considered significant for this application. These included:

1. Variations of resonant frequency and Q with temperature
2. Reduced sensitivity to magnetic gradients
3. Improved signal level
4. Reduced electronic noise
5. Reduced thermal noise
6. Reduced inertial loading sensitivity

The sensor design was therefore created with the foregoing items as primary bounding conditions.

It is recognized, of course, that long-term variations in the signal can be eliminated because the sensor is recalibrated each time it passes over the north or south pole. Only those signal errors in the same frequency spectrum as the data to be obtained are of concern, e.g., from the 10^{th} to 80^{th} spherical harmonic of the earth's field.

The design drawings are attached to this final report as an appendix (Appendix A). The breadboard sensor, as it was assembled, is shown in Fig. 8. Although there are no magnetic shielding covers

M8926

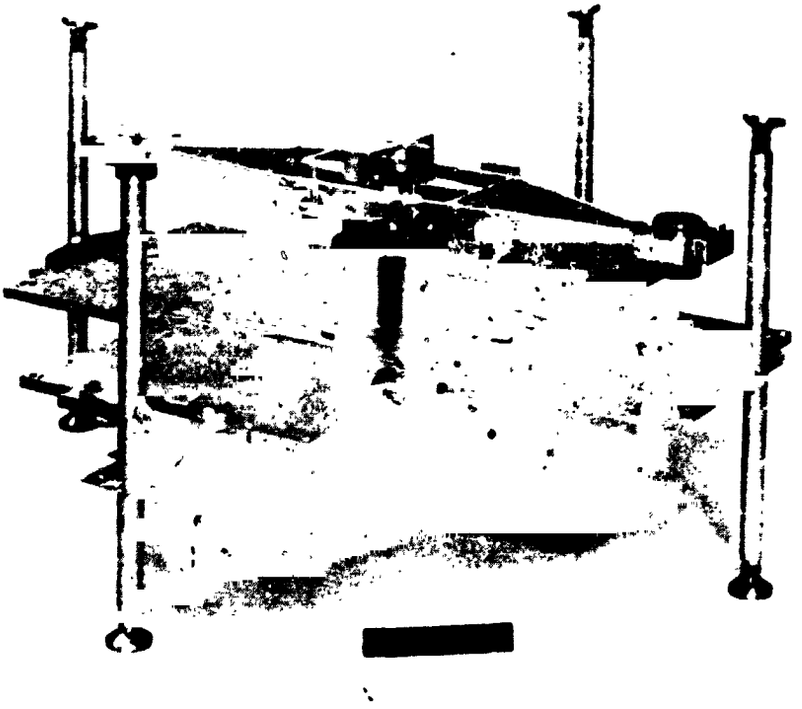

Fig. 8. Breadboard Sensor.

shown in the photograph, covers were designed that provide adequate magnetic shielding for the sensor (see Appendix F). This cover design is shown in drawings x1146, x1147, and x1149. The parts were not manufactured because of the high cost and because magnetic testing of the instrument was not planned under this contract. However, the design should provide the required magnetic shielding when the covers are lined with high permeability foil.

The transducer was designed to provide a very high voltage level by using large-size, piezoelectric, bender transducers. Most of the sensor damping was found to be in the piezoelectric of the transducer; this had an adverse effect on sensor Q by keeping it below 125. To obtain the desired 35-sec total time constant it is desirable to have a sensor Q as high as 625. Such a Q lowers the thermal noise from 0.015 EU to 0.007 EU.

It is suggested that for future models of this sensor, the amount of piezoelectric material be reduced. Such a reduction raises the Q and lowers the sensor scale factor, a trade off that leads to a more optimum unit and is one of the recommendations made in Section V.

The signal preamplifier was found to have an equivalent noise level of 0.002 EU equivalent, which was well inside the requirement (see Section III-A).

The size of the sensor, and to a large extent its weight, was determined by the thermal noise requirement. The breadboard was made deliberately heavy (≈70 lb) to allow experimental testing in a 1 g environment. For actual satellite operation, the weight could be probably cut to 1/3 of the present weight.

The arm design and its support structure were determined by requirements to minimize the inertial loading effects on the transducer (see Appendix D).

Materials were chosen to reduce sensor magnetic sensitivity and to minimize the termperature sensitivity effects (see Appendix G). Despite these efforts, HRL expected a considerable shift of resonant frequency with temperature and decided that additional control could

be provided by using one of the transducers as an adjustable spring damper system by padding it with resistance or capacitance. Results of these tests are contained in Sections III-G and III-H.

B. ASSEMBLY AND BALANCING

Once the manufactured parts were in house, assembly proceeded with very little problem. Some difficulty was experienced in assembly of the transducer into the support brackets and better fixturing would have simplified that effort.

Balancing of the arms of the first assembled sensor proved to be a difficult task. Data were inconsistent and varied with loading direction. The balance did not remain constant from day to day and balancing of the arms to within 0.003 in. of the center of support was unsuccessful.

Calculation of the stiffness of the transducer supporting structure (Fig. 9) disclosed that this structure was only a factor of 2 stiffer than the transducer itself. Deflections in the structure were suspected as being the cause of spurious signals from the transducer. Following redesign of the structure (Fig. 10), little difficulty in balancing the final sensor assembly to 0100014 in. (1 gram on the end of the arm).

C. ELECTRONICS

1. Amplifier Design

The signal amplifier is a low-noise instrumentation amplifier consisting of an FET input section, a main amplifier section, and a signal adder section. The electrical schematic is shown in Fig. 11. The parts list follows.

The FET input section consists of a matched pair of low-noise FET's with shunting diodes on the gates for overload protection against large signals.

M8684

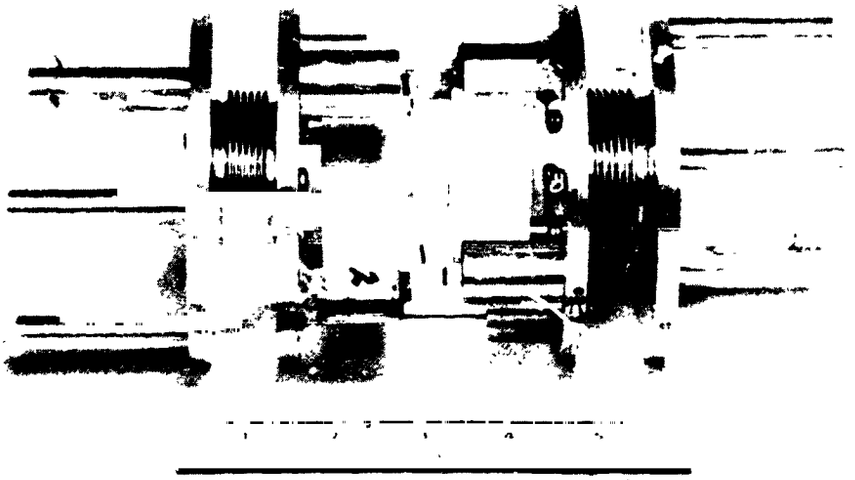

Fig. 9. Transducer Supporting Structure.

M8972

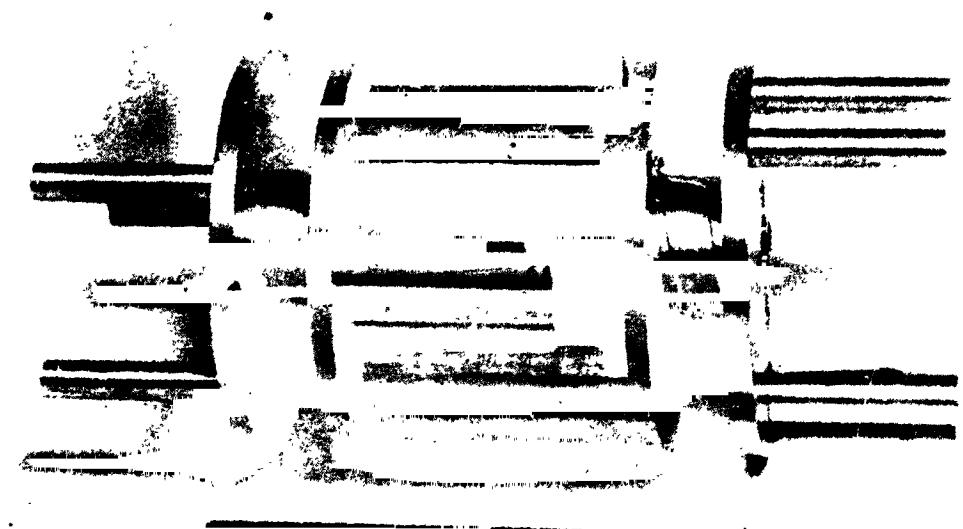

Fig. 10. Redesign of Transducer Supporting Structure.

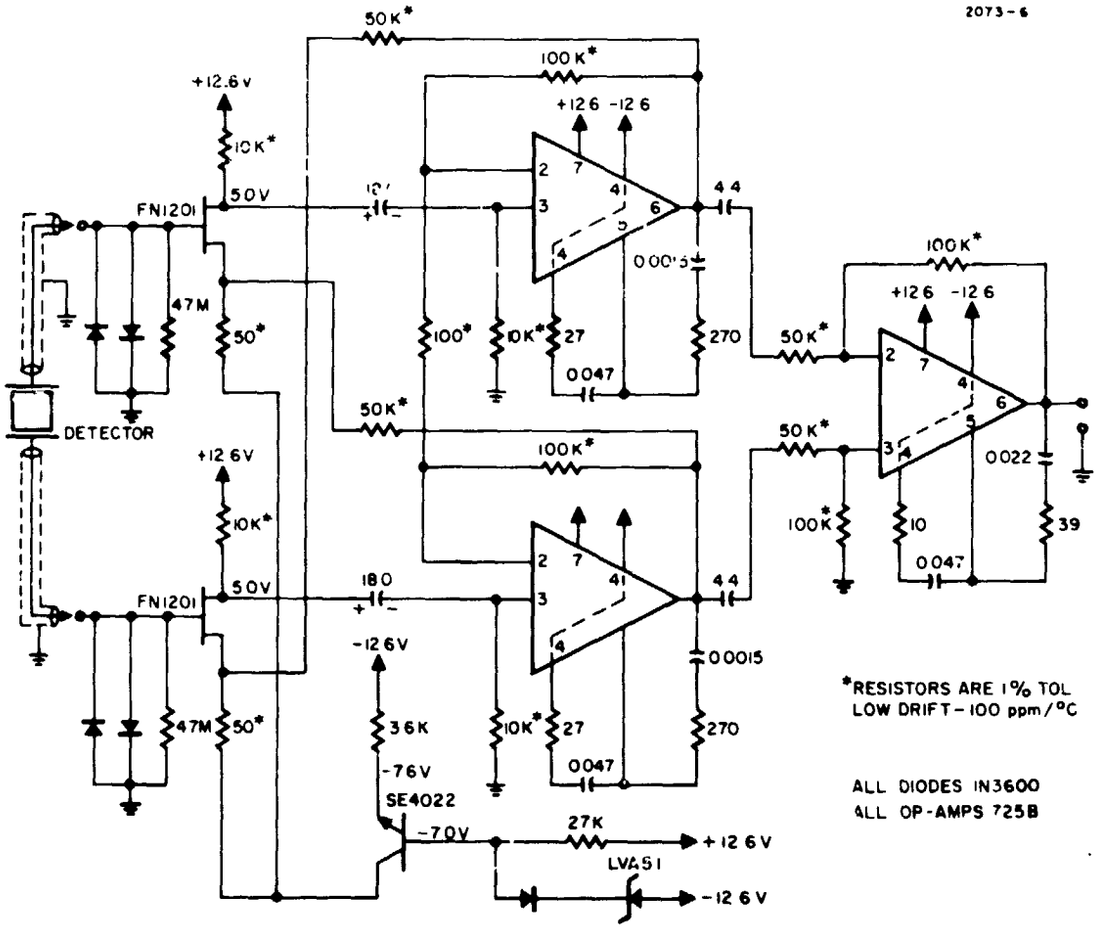

Fig. 11. Preamplifier Electrical Schematic.

TABLE II

Electronic Parts List

Number	Part	Mil Type	PO Number	Vendor	Remarks
1	725C				Stock
2	725B		01-479465-8	48174	
2	FN1201		01-477046-6	41372	Matched Sets
4	IN3600			-	Stock
2	18 µfd Elec Caps	CS13	01-479511-8	96104	
4	2.2 µfd			-	Stock (Eric)
3	0.047 µfd	CK06	01-479644-6	41372	
1	0.022 µfd	CK06	01-479644-6	41372	
2	0.0015 µfd			-	Stock
4	100K ohm 1%	RNR60D	01-479645-6	41372	
2	50K ohm 1%	RNR60D	01-479645-6	41372	
2	25K ohm 1%	RNR60D	01-479645-6	41372	
2	10K ohm 1%	RNR60D	01-479645-6	41372	
1	5K 1%	RNR60D	01-479645-6	41372	
1	500 1%	RNR60D	01-479645-6	41372	
2	27 Carbon				Stock
2	270 Carbon				Stock
1	39 Carbon				Stock
1	10 Carbon				Stock
2	4.7M Carbon				Stock
1	PCB		01-276236-1	Century Graphics	

The main amplifier section consists of two low-drift Op-amps with negative feedback coupled to the source leads of the input FET's for gain stabilization.

The last section consists of a low-drift Op-amp operated as a subtractor for differential signal addition and common mode rejection.

2. Amplifier Tests

Gain, noise, temperature, and voltage tests were run on the electronics package. The nominal amplifier gain is 1815 over the bandwidth from 1.5 to 500 Hz. The common mode rejection is better than 90 dB from 4 to 500 Hz with a value of 94 dB at 8 Hz. The shorted electronic noise level was measured and shows the expected variation with frequency (see Fig. 12). The noise is flat at 14 $nV/Hz^{1/2}$ from 20 to 500 Hz and shows the expected 1/f behavior below 20 Hz. The noise level is 35 nV at the operating frequency of 5.78 Hz with a 1-Hz bandwidth or an input noise characteristic of 35 $nV/\sqrt{Hz}$. If a total time constant of τ_T = 35 sec is assumed, the effective bandwidth would be

$$B = \frac{1}{2\tau} = 1.4 \times 10^{-2} \text{ Hz}$$

and the input noise with a 35-sec integration time would be 4.3 nV. Using the scale factor of S = 2 μV/EU calculated in Section III-D, the electronic noise equivalent gradient is

$$\left(\Gamma_{ij}\right)_{amp} = \frac{N}{\sqrt{B}\ S} = 0.002 \text{ E}$$

An additional long integration time test was run on the amplifier with shorted input. In this case, the output signal was run directly into the data processing electronics, and a noise trace was run, using

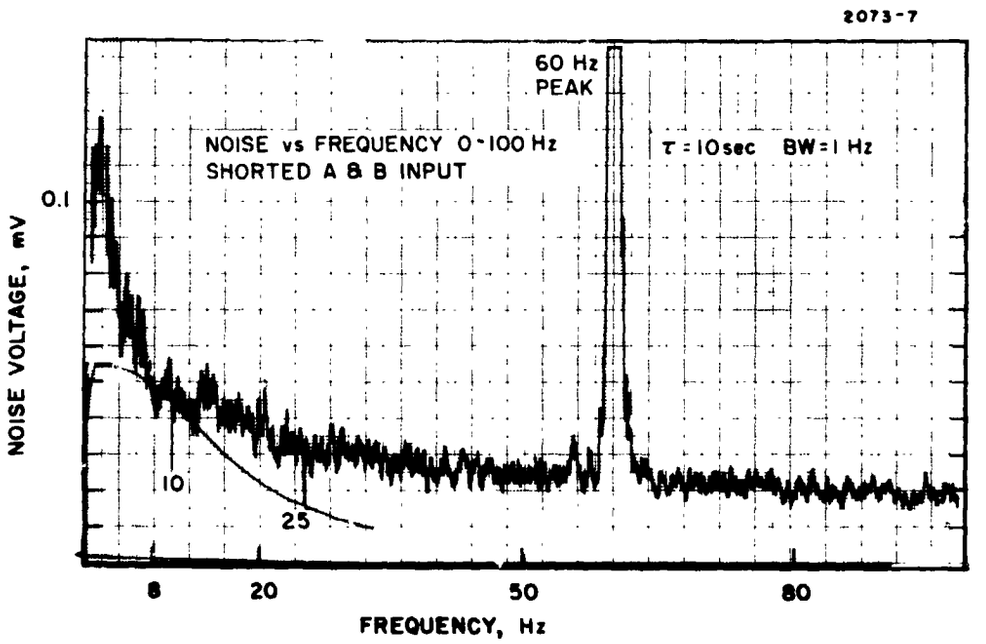

Fig. 12. Noise Output Versus Frequency.

an integration time of 31 sec. This noise curve is shown in Fig. 13. Here the output of the amplifier was $V_n = 0.075$ mV (rms). Using a total gain of G = 18, 150 and a transducer scale factor of 2 μV/EU (see Section III-D), the equivalent noise input level can be calculated at

$$(\Gamma_{ij})_{amp} = \frac{V_n}{GS} = 0.002 \text{ EU}.$$

D. SENSOR SCALE FACTOR

1. Expected Sensor Scale Factor

The expected sensor scale factor can be calculated by evaluating the expected moment on the transducer for a 1 EU gradient input and its resultant voltage output by formulas from the piezoelectric catalogues.

The torque level for a 1-EU input gradient is

$$T = \eta I_{zz} \Gamma_{(1 \text{ EU})} = 6.08 \times 10^{-3} \text{ dyn-cm}$$

where

η is the arm efficiency factor = 97.4%

I_{zz} is the arm polar moment of inertia = 6.24×10^6 gm-cm^2

Γ is the input gradient = 10^{-9} sec^{-2}.

This torque appears as a force at the end of the transducer where 1/2 FL = T. The transducer scale factor is given in the piezoelectric handbook as

$$\frac{V}{FL} = \frac{3}{4} \frac{g_{31}}{WT}$$

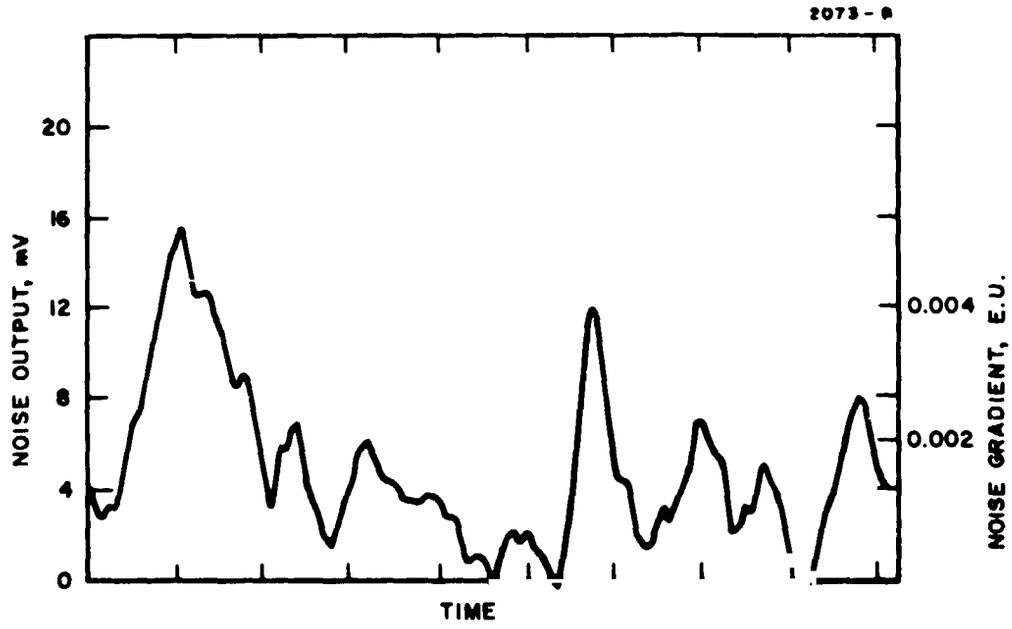

Fig. 13. Amplifier Noise (Input Shorted).

where

$g_{31} = 11.4 \times 10^{-3}$ for the material (channelite 5500)

W = 1 in. = 0.0254 m

T = 0.232 in. = 0.00589 m

L = 3 in. = 0.0762 m.

Therefore,

$$\frac{V}{FL} = 57.15 \text{ V/n-m.}$$

Now the force at the end of the transducer is

$$F = \frac{T}{1/2L} = 4 \times 10^{-4} \text{ dyn}$$

and $FL = 3.04 \times 10^{-3}$ dyn cm $= 3.04 \times 10^{-10}$ n-m; consequently, the voltage output for a 1-EU input $V = V/FL\,(FL) = 1.73 \times 10^{-8}$ V/EU. This assumes nonresonant operation. With a Q of 125, V/r would be $(1.73 \times 10^{-8})\,(125) = 2.17 \times 10^{-6}$ V/EU.

2. Sensor Scale Factor Test

a. Test Setup

The sensor was calibrated for scale factor by adding a known mass to the end of one arm thereby creating a deliberate center-of-mass unbalance in that arm. The sensor was then subjected to linear vibration perpendicular to its spin axis and also perpendicular to the mass unbalance vector. The input acceleration level was

measured by calibrated geophones and the sensor output was noted through the data readout electronics.

Geophone Output	V_g	= 12.5 mV (O-p)
Geophone Scale Factor	S_g	= 56 V/in./sec (@5.78 Hz)
Unbalance Weight	U	= 81 g at 15 in. = 3086.1 gm-cm
Sensor Resonant Frequency	f	= 5.78 Hz
Sensor Output	V_o	= 9.5 mV (gauge 1) (O-p)
		= 11.25 mV (gauge 2) (O-p)
		= 10.0 mV (O-p) avg.

b. Input Acceleration Calculation

The input peak acceleration car be calculated from the geophone output and scale factor

$$a_{peak} = \frac{V_g}{S_g} (2\pi f) = 8.1 \times 10^{-3} \text{in./sec}^2 = 2.06 \times 10^{-2} \text{cm/sec}^2.$$

c. Torque Scale Factor Calculations

The torque on arm 1 is given by

$$T_{1\,peak} = U\, a_{peak} = 63.5 \text{ dyn-cm}$$

while the torque on arm 2 is zero

$$T_2 = 0.$$

The ratio of sensor output voltage to peak input difference torque is therefore

$$\frac{V_o}{T_1 - T_2} = 1.575 \times 10^{-4} \text{ V/dyn-cm.}$$

d. Gradient Scale Factor Calculations

For a point mass gravitational anomaly (mass M, at distance R), the difference in torque on the two arms of a rotating gravitational gradiometer is given by

$$T_1 - T_2 = 2\eta C(\Gamma_{ij}) \sin 2\omega t$$

where C is a single arm polar inertia (6.24×10^6 gm-cm^2 for this sensor)

η = arm efficiency factor (0.97 for this sensor)

$\Gamma_{ij} = \frac{3}{2} \frac{GM}{R^3}$ an equivalent gradient. $= 10^{-9}$ sec^{-2} for 1 EU .

(This equation has been developed in Hughes literature many times before.)

The peak torque-gradient conversion for a 1-EU signal (Γ_{ij}) can now be determined:

$$(T_1 - T_2)_{1 \text{ EU (peak)}} = 1.21 \times 10^{-2} \text{ dyn-cm.}$$

The scale factor can now be calculated, combining the torque and gradient scale factors

$$S_s = (T_1 - T_2)_{\text{peak 1 EU}} \times \frac{V_o}{T_1 - T_2} = 1.91 \times 10^{-6} \text{ V/EU}$$

or approximately 2 μV/EU.

This is very close to the theoretical value calculated in Section III-D-1.

E. SENSOR NOISE LEVEL

1. Thermal Noise

The sensor thermal noise is calculated, using the equation

$$\overline{\sigma}_s = \frac{2}{\eta} \frac{2kT}{C\tau_1\tau_t}$$

where τ_1 is the sensor time constant ($Q/\pi f$) and τ_t is the total (filtered) time constant (35-sec max).

The final sensor Q was 126 and f was 5.78 Hz; therefore

$$\tau_1 = 7 \text{ sec},$$

and

$$\overline{\sigma}_s = \frac{2}{0.97} \frac{8 \times 10^{-14}}{6.24 \times 10^6 (7)(35)} = 0.015 \text{ EU}$$

It should be pointed out that $\overline{\sigma_s}$ is defined as the gradient equivalent thermal noise standard deviation, based on the following torque equation for a gradiometer rotating in the x-y plane:

$$T_1 - T_2 = \eta C \left\{[(\Gamma_{yy} - \Gamma_{xx}) + \sigma_s] \sin 2\omega t + (2\Gamma_{xy} + \sigma_c) \cos 2\omega t\right\}$$

where η and C are as previously defined.

Γ_{yy}, Γ_{xx}, and Γ_{xy} are components of the general gravitational gradient tensor, and $\overline{\sigma_c}$ is equal to $\overline{\sigma_s}$ (but statistically independent). (The total sensor output thermal noise $\overline{\sigma_c} + \overline{\sigma_s} = \sqrt{2}\,\overline{\sigma}_s = 0.0212$ EU)

The preceding definition implies that if operation on the output signal is conducted in such a way as to obtain Γ_{ij} (as previously defined, $3GM/2R^3$), the thermal noise level on this signal will be $\sigma_s/2$, or 0.007 EU. The following illustrative example is given in proof of this statement.

Example:

A spherical anomaly of 10^{16} kg whose center is at 300 km distance from the gradiometer along the y axis has the gradient components

$$\Gamma_{xx} = \Gamma_{zz} = -\frac{GM}{R^3} = -0.025 \text{ EU}$$

and

$$\Gamma_{yy} = +\frac{2GM}{R^3} = 0.05 \text{ EU}$$

$$(\Gamma_{xy} = 0).$$

Incorporating these values into the torque equation, a peak amplitude of

$$T_1 - T_2 = \eta C \left(\frac{3GM}{R^3} \pm \sqrt{2}\,\bar{\sigma}_s\right) = 4.54 \times 10^{-4} \pm 1.28 \times 10^{-4} \text{ dyn-cm}$$

is obtained. If this torque difference is multiplied by the voltage-to-torque ratio developed earlier (1.575×10^{-4} V/dyn-cm), an output voltage of

$$V_o = 71.5 \text{ nV} \pm 20.2 \text{ nV}.$$

is obtained. If this signal is phase split by a phase sensitive demodulation scheme, using the x and y axes as references, the sine and cosine components of this output voltage are

$$V_{os} = 71.5 \text{ nV} \pm 14.3 \text{ nV}$$

and

$$V_{oc} = \pm 14.3 \text{ nV}.$$

If V_{os} alone is now evaluated for the equivalent gradient and equivalent noise (Γ_{ij}) by dividing mean voltage, and standard deviation by the sensor scale factor ($S_s = 1.91\ \mu\text{V/EU}$),

$$\Gamma_{ij} = 0.0375 \text{ EU} \pm 0.0075 \text{ EU}$$

is derived where the mean gradient is equal to $3GM/2R^3$, and the noise gradient is equal to $\sigma_s/2$ as expected.

2. Isolated Noise

To check its noise level, the sensor was mounted on a pneumatically supported vibration isolation table. Data were taken for a 15-min run, using a 31-sec integration time. The noise data are shown in Fig. 14. The RMS of these data is 8 mV, which is equivalent to a transducer output of $0.008/1815 = 4.4 \times 10^{-6}$ V or 2.2 EU (equivalent).

It should be noted that this sensor was only moderately isolated from floor noise (resonant frequency of the suspension being in the 1- to 2-Hz region), and there was no acoustic isolation provided. The sensor output would increase by several orders of magnitude with the sounds of door slams or heavy footfalls. It would be anticipated that at least a 2 order of magnitude vibration level reduction in a spacecraft environment would be expected. (Vibration level on the table was approximately 10^{-5} g RMS.)

F. RESONANT FREQUENCY AND Q DETERMINATION

The first test performed on the sensor after assembly was that of running a frequency sweep by using the second transducer as a driver to excite the sensor arms in the gradient detection mode and sweep the excitation frequency to obtain a resonant frequency curve. This test was performed on both sensor assemblies with the two different transducer support structures.

The resultant Q curves are shown in Figs. 15 and 16. The first curve is with the old, weaker, transducer support structure and has a natural frequency of 4.59 Hz with a Q of 138. The second curve (final version of the sensor) has a resonant frequency of 5.65 Hz and a Q of 126. The resonant frequency difference is directly attributable to the modification of the transducer support structure. Although the Q in both these tests was greater than 125, a repetition of this value of Q was never achieved in later tests. Throughout the temperature

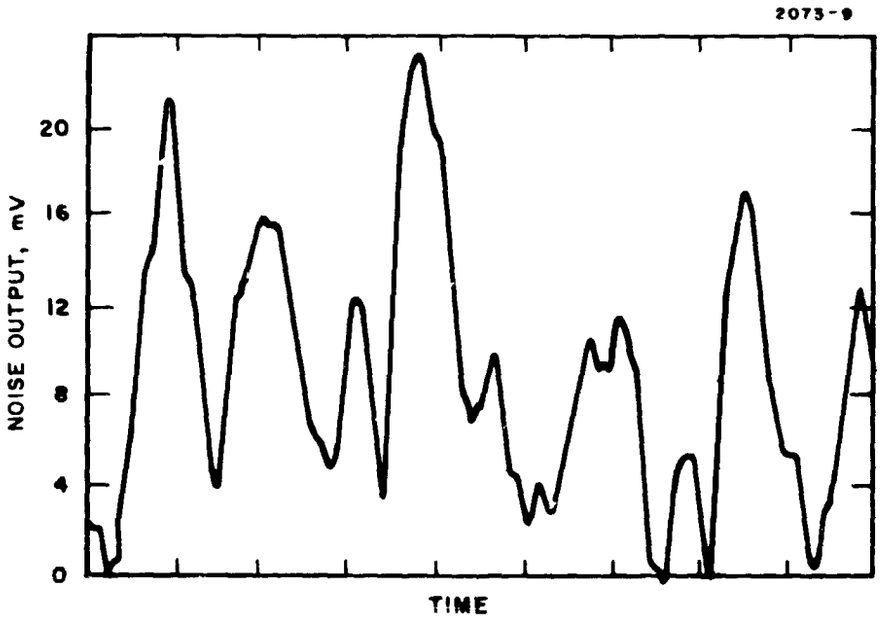

Fig. 14. Amplifier Noise (81-gram Unbalance).

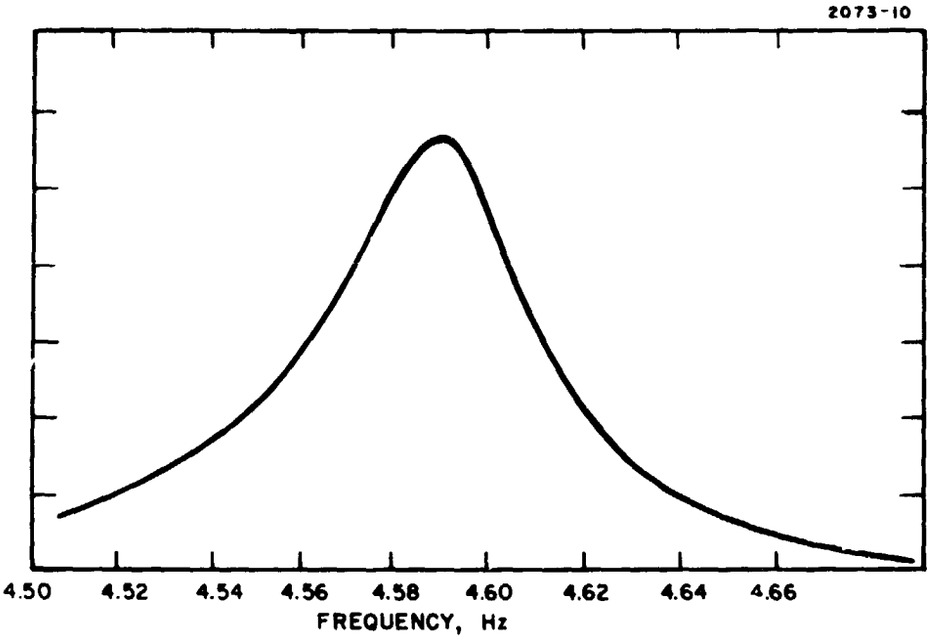

Fig. 15. Sensor Q Curve (Old Transducer).

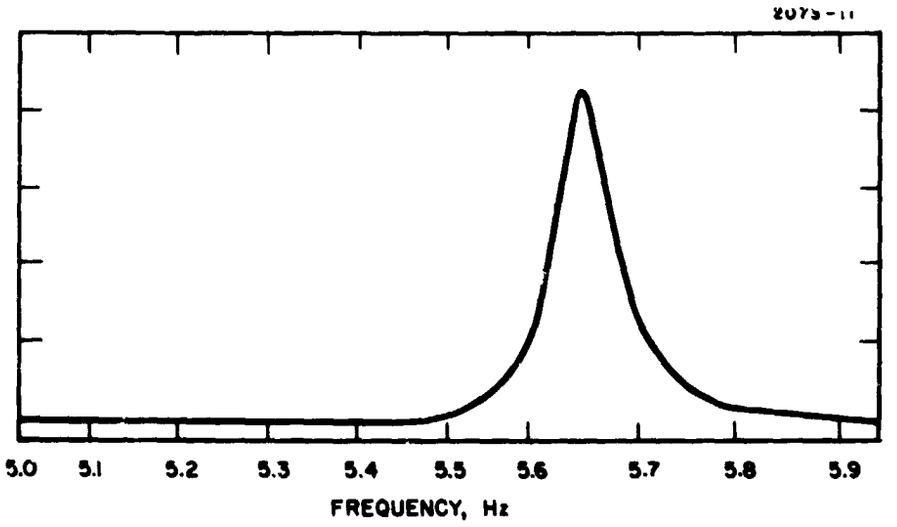

Fig. 16. Sensor Q Curve (New Transducer).

tests, the Q was between 70 and 85 at room temperature. The theory is that after the sensor was physically handled and moved, the bonding between the transducer halves was fractured in places, and certain cement joints and bond lines possibly weakened. The sensor stops were set to $\pm 3^{\circ}$, but the sensor was roughly handled during moving, and this 3° limit may have been exceeded by actual bending of the stop support structure.

G. TEMPERATURE TESTS

Once the resonant frequency of the sensor was determined, detailed temperature tests were conducted on the gradiometer. The capacitive drive was used to excite the resonant mode, and resonant frequency curves were run with the sensor temperature stabilized at $23.5^{\circ}C$, $30^{\circ}C$, $35^{\circ}C$, $40^{\circ}C$, and $50^{\circ}C$. These curves were run on both models of the sensor (old and new transducer support structures). The data are shown in Figs. 17 and 18. Results of both tests are nearly the same. The frequency shift rate is 0.043 Hz/$^{\circ}$C for the older sensor and 0.038 Hz/$^{\circ}$C for the newer one. This shift rate difference amounts to a percentage of $\approx 0.66\%/^{\circ}C$. Q shift for the older sensor was $3.5/^{\circ}C$ at the highest part of the temperature range and for the newer, $1.24/^{\circ}C$. These shifts are easily compensable by the transducer padding methods discussed in Section III-H.

H. FREQUENCY TUNING

The sensor internal electromechanical parameters were calculated using a capacitive load across one of the transducers, then the response of the sensor to various resistive and capacitive loads was determined; finally, the calculations were checked by using a 1 megohm resistor across the transducer and comparing the actual Q and f_n with those calculated values.

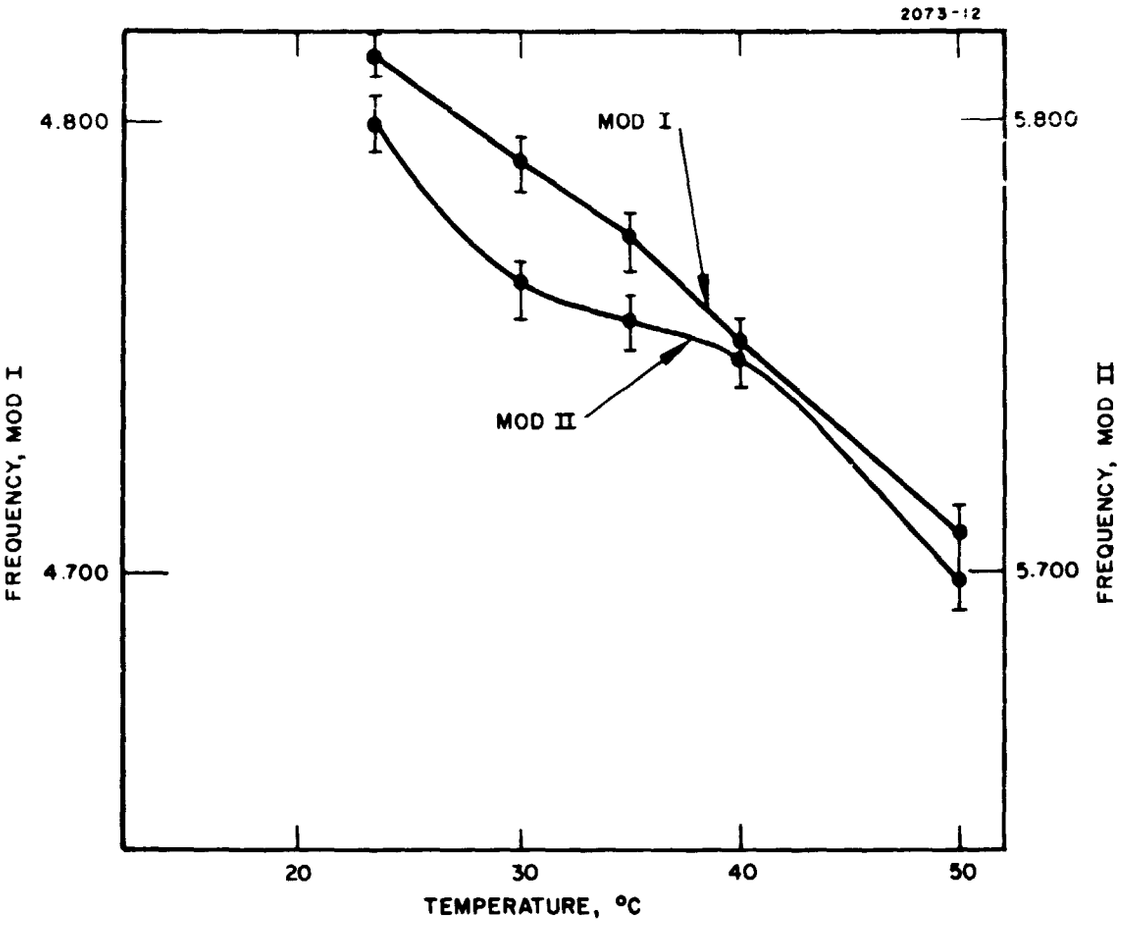

Fig. 17. Sensor Resonant Frequency Versus Temperature.

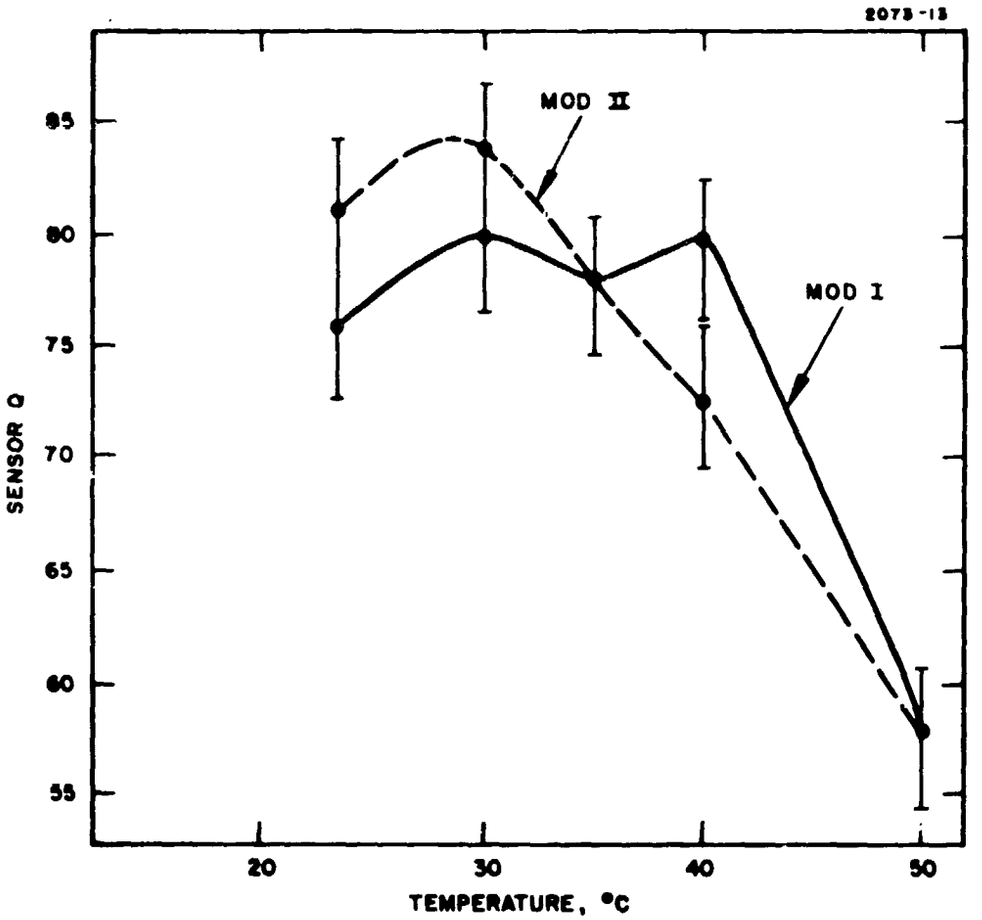

Fig. 18. Sensor Q Versus Temperature.

With no loading the old sensor parameters were

$$f_{n_1} = 4.816 \text{ Hz}, \quad Q = 60 .$$

Adding a 0.05 mf capacitor across one transducer the parameters changed to

$$f_{n_2} = 4.783 \text{ Hz}, \quad Q = 49 .$$

The equivalent electromechanical circuit can be modeled as shown in Fig. 19.

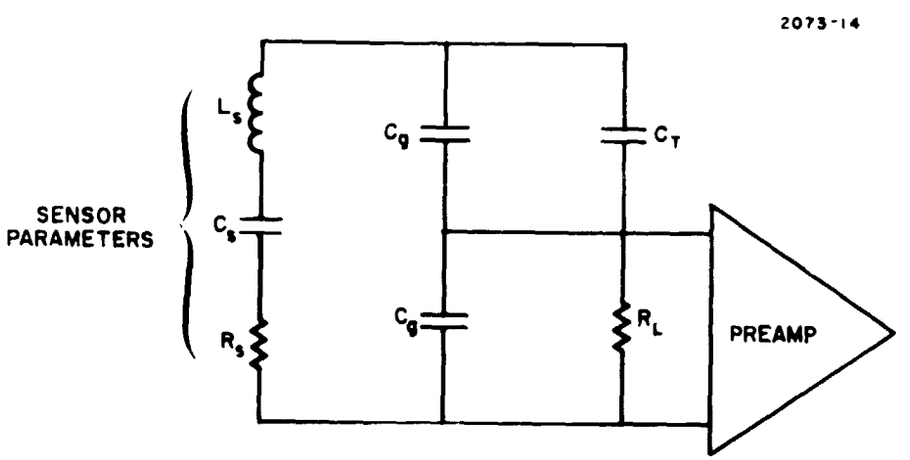

Fig. 19. Equivalent Electromechanical Circuit Model.

which when simplified into a series circuit becomes

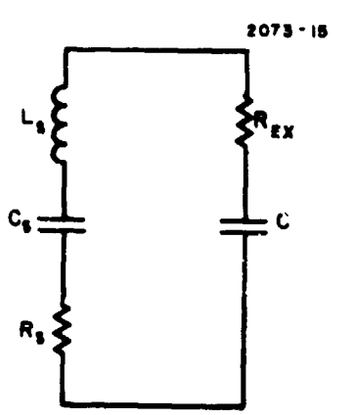

Fig. 20. Model Simplified into Series Circuit.

where C varies, depending on the value of C_T. (When C_T is zero, $C = 6.461 \times 10^{-9}$ F; when $C_T = 0.05$ mF, $C = 11.016 \times 10^{-9}$ F.) The general equation

$$\omega^2 = \frac{1}{LC} \qquad \text{in the two cases (with and without } C_T)$$

can now be used where C is the total capacitance of the circuit to solve for C_S and L_S

$$C_S = 2.207 \times 10^{-10} \text{ F} \qquad L_S = 5.133 \times 10^{6} \text{ H}$$

Using the equation

$$R = \frac{\omega L}{Q} \qquad (R_{EX} = 653,290\Omega \text{ for } R_L = 10 \text{ M})$$

Solving the equation gives

$$R_S = 1.937 \times 10^{6}\,\Omega$$

Curves can now be constructed, showing the effect of any tuning capacitor on the natural frequency, and any resistor on Q. For these curves, the new sensor natural frequency (untuned) of 5.75 Hz was assumed. (The new C_s was therefore calculated as 150×10^{-12} F.) These curves are shown in Figs. 21 and 22.

I. COMPENSATION REQUIREMENTS

If the slopes of the two tuning curves are now calculated at what appears to be convenient generating points ($C_T = 10^{-8}$ F, $R_T = 100$ K Ω), it is found that

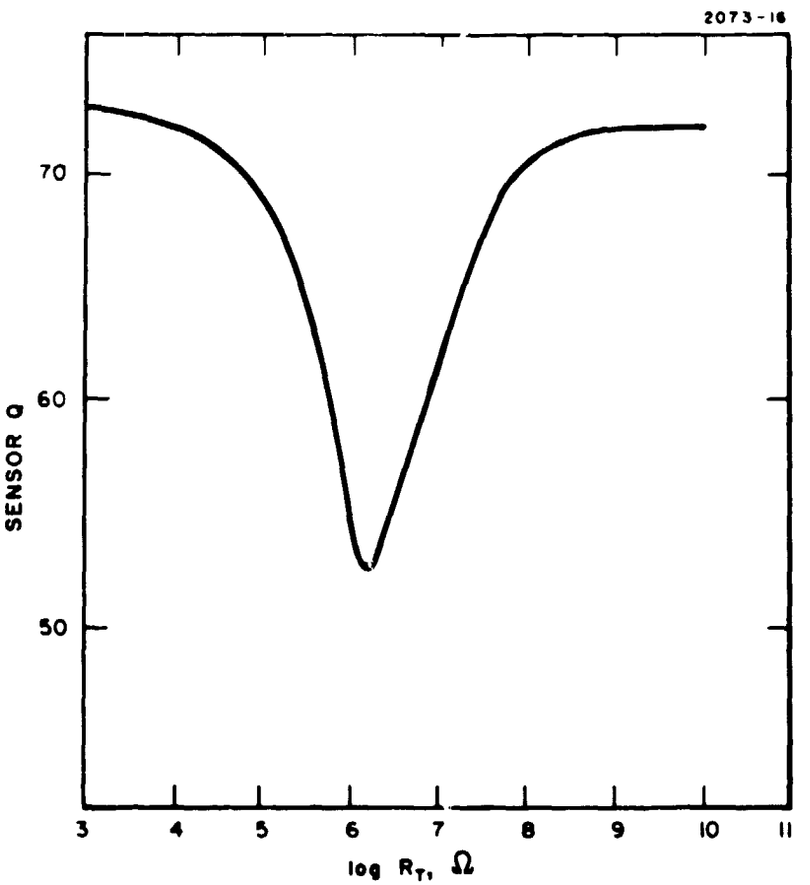

Fig. 21. Resistance Versus Sensor Q.

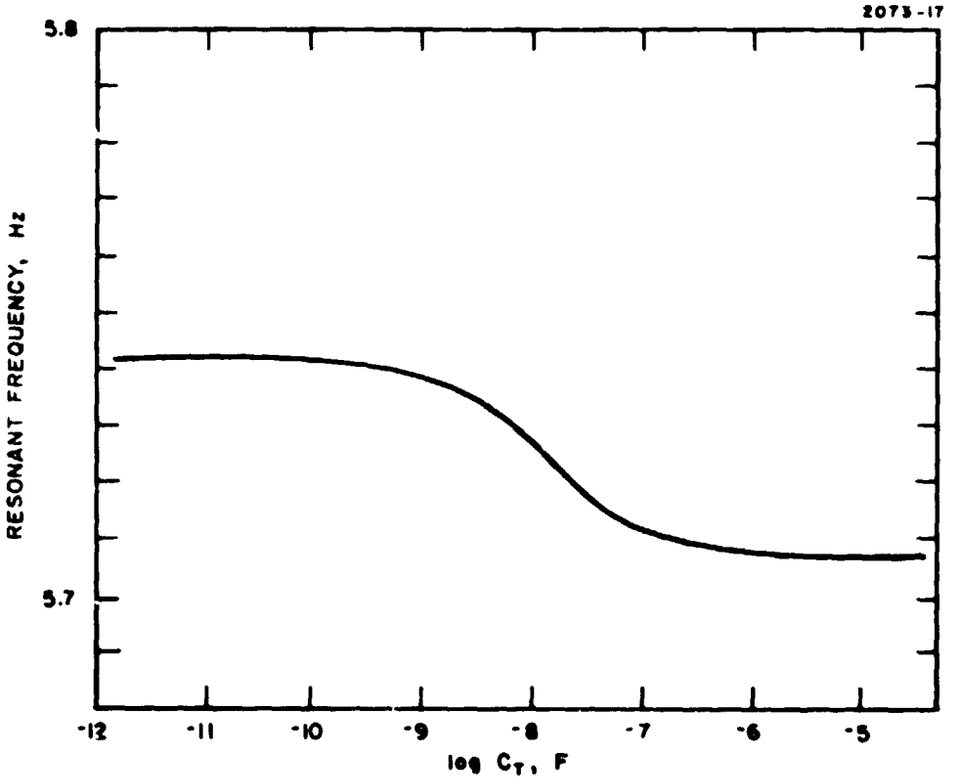

Fig. 22. Capacitance Versus Resonant Frequency.

$$\frac{\partial \omega}{\partial C_T} = -0.85 \times 10^{-6} \text{ Hz/pF}$$

and

$$\frac{\partial Q}{\partial R_T} = -2.1 \times 10^{-5}/\Omega$$

The requirement of maintaining an accuracy of 0.01 EU in the presence of a 4500-EU signal ($3GM/2R^3$) has already been noted as implying an overall amplitude measurement accuracy of 2 ppm. This requirement can be used to establish th resolution required on the tuning components of the tuning circuit. Amplitude is a direct function of Q; therefore, a 2-ppm variation in Q represents a 2-ppm variation in amplitude. This 2-ppm requirement on Q, therefore, necessitates a resolution in the tuning resistor of

$$\Delta R = \frac{2 \times 10^{-6} \times Q}{2.1 \times 10^{-5}} \Omega$$

$$\Delta R = 5.75 \Omega \text{ out of } 10^5 \Omega$$

which should be attainable.

The amplitude variation with natural frequency is somewhat more complex because this variation is also a function of Q.

The steady state amplitude near resonance is given by

$$X = \frac{\frac{P_o}{K}}{\sqrt{\left(\frac{1}{Q}\right)^2 + \left[1 - \left(\frac{\omega}{\omega_n}\right)^2\right]^2}}$$

at resonance

$$X_R = \frac{P_o}{K} Q$$

Therefore,

$$\frac{X_R}{X_0} = Q\sqrt{\left(\frac{1}{Q}\right)^2 + \left[1 - \left(\frac{\omega}{\omega_n}\right)^2\right]^2}$$

Now, if $1 - (\omega/\omega_n)^2$ is a small number, then

$$\left[\left(\frac{1}{Q}\right)^2 + \left[1 - \left(\frac{\omega}{\omega_n}\right)^2\right]^2\right]^{1/2} \approx \frac{1}{Q} + \frac{1}{2}\left(1 - \left(\frac{\omega}{\omega_n}\right)^2\right)^2 Q$$

and

$$\frac{X_R}{X} = Q\left[\frac{1}{Q} + \frac{1}{2}\left[1 - \left(\frac{\omega}{\omega_n}\right)^2\right]^2 Q\right]$$

$$= 1 + \frac{1}{2}Q^2\left[1 - \left(\frac{\omega}{\omega_n}\right)^2\right]^2$$

or in terms of deviations from the resonant condition,

$$1 + \frac{\Delta X}{X_R} = 1 + \frac{1}{2}Q^2\left[1 - \left(\frac{\omega_n + \Delta\omega}{\omega_n}\right)^2\right]^2$$

$$\frac{\Delta X}{X_R} = \frac{1}{2}Q^2\left[1 - \left(1 + \frac{\Delta\omega}{\omega_n}\right)^2\right]^2 = \frac{1}{2}Q^2\left[1 - 1 + 2\frac{\Delta\omega}{\omega_n}\right]^2 = Q^2\left(\frac{\Delta\omega}{\omega_n}\right)^2$$

$$\frac{\Delta X}{X_R} = Q^2\left(\frac{\Delta\omega}{\omega_n}\right)^2$$

if $\Delta X/X_R$ must be held to 2 ppm then

$$\frac{\Delta\omega}{\omega_n} = Q^{-1}\sqrt{\frac{\Delta X}{X_R}} = 1.4 \times 10^{-3}Q^{-1}$$

or in tabular form:

Q	$\frac{\Delta\omega}{\omega_n}$
50	2.8×10^{-5}
100	1.4×10^{-5}
200	7.1×10^{-6}
400	3.5×10^{-6}
600	2.4×10^{-6}

With a high Q system (Q = 600) $\Delta\omega/\omega_n$ must be held to ≈ 2 ppm which implies a frequency resolution of

$$\Delta f = 2 \times 10^{-6}\ \omega_n = 1.6 \times 10^{-5}\ \text{Hz} \quad .$$

The slope of the frequency versus capacitive curve was 0.85×10^{-6} Hz/pF which implies a capacitance resolution of $\Delta C = 19$ pF. Again, one which appears feasible.

SECTION IV

CONCLUSIONS

In this report, a set of mission and spacecraft parameters has been established that appear to be within the state of the art. Additionally, supporting studies by JPL indicate the attractiveness of such a mission as an alternate and/or verification test for the radar altimeter earth physics satellite. It has also been shown that such a gradiometer mission is feasible. The gradiometer design parameters are such that with some modification a resolution of 0.01 EU at 35-sec integration time could be reliably obtained from such an instrument operating in a spinning spacecraft.

Certain aspects of the sensor design need further study. Primary among these is the desirability of reducing sensor damping in order to improve the sensor Q and thereby obtain an improvement in sensor thermal noise threshold. The adjustment of Q and resonant frequency by padding a piezoelectric spring was demonstrated, but an effective system to provide the adjustment of the tuning components has yet to be designed.

SECTION V

RECOMMENDATIONS

As a result of its experience with the breadboard model of the rotating gravity gradiometer, HRL has seven principal recommendations for future work on the sensor.

1. The amount of piezoelectric in the transducer structure should be reduced by half to two-thirds and replaced by aluminum to raise the natural frequency to 8 Hz or more, and probably increase the Q significantly. This ratio should be adjusted to obtain best signal to noise, as when the piezoelectric material is reduced, the voltage output per EU drops.

2. The bellows method of decoupling the transducer structure from the arms (except for the desired torsional coupling) failed. Because bellows have a number of undesirable cross-coupling modes, a better design solution is needed.

3. The electronics for frequency and Q control of the sensor (See Section III-H) should be constructed and tested.

4. The vertical separation of the center of masses of the two arms caused some cross-coupling problems. A design concept that brings the centers of mass of the arms closer together, but retains the biaxial torsional suspension for each arm, was recently developed by HRL under Air Force Contract F19628-72-C-0222, and should be considered for the next NASA design.

5. The arm length and end masses of the sensor should be increased as much as possible to lower the sensor thermal noise level well below the desired 0.01 EU threshold sensitivity level. This would imply the use of a different launch vehicle than the Scout.

6. The proposed magnetic shielding should be fabricated and its effectiveness demonstrated in the laboratory.

7. A very low frequency (0.1 Hz) vacuum enclosed isolation suspension should be designed and fabricated so that the thermal and electronic noise level of the sensor can be demonstrated on the ground.

This test could be combined with a gradient detection test using rotating masses in the vicinity of the sensor to calibrate the sensor by gravitational torque excitation rather than the mass unbalance torque excitation method used in the completed program.

There are a number of recommended areas of study for the spacecraft, such as the development of adequate methods for measurement and control of temperature, spin speed, attitude, spacecraft dynamics, and data digitalization and reduction. These are adequately discussed in the JPL study.

REFERENCES

1. "Earth Physics Satellite – Gravity Gradiometer Study," Report 760-70, Jet Propulsion Laboratory, Pasadena, Calif., 17 May 1972.

2. W. M. Kaula, An Introduction to Planetary Physics, John Wiley & Sons, New York, 1968, p. 77.

3. Mark L. Sandson and William E. Strange, "An Evaluation of Gravity Gradients at Altitude," 53rd Annual AGU Meeting, Washington, D. C., April 1972.

4. Bernard H. Chovitz, James R. Lucas, and Foster Morrison, "Gravity Gradients at 300 Km Altitude," 53rd Annual AGU Meeting, Washington, D. C., April 1972.

5. R. J. Glaser and E. J. Sherry, "Comparison of Satellite Gravitational Techniques," AGU International Symposium on Earth Gravity Models and Related Problems," St. Louis University, St. Louis, Missouri, 16-18 August 1972.

6. B. L. Swenson, "Orbit Selection Considerations for Earth Resources Observations," NASA TMX-2156, February 1971.

7. J. C. King, "Swathing Patterns of Earth-Sensing Satellites and Their Control by Orbit Selection and Modification," AAS Paper No. 71-353, AAS/AIAA Astrodynamics Specialists Conference 1971, Ft. Lauderdale, Florida, 17-19 August 1972.

APPENDIX A

DESIGN DRAWINGS, PARTS LIST AND ASSEMBLY INSTRUCTIONS

APPENDIX A

ASSEMBLY INSTRUCTIONS

I. SUBASSEMBLIES

1. Transducer Assembly

a. Preparation of Transducers (L-B-936308)

Using an exacto knife or equivalent, remove 3/8 x 1.0 in. of plating at each end of the transducer (mounting areas). Sand clean with 320 grade silicon carbide paper. Silver is to be removed from both sides at both ends. No conductivity is to remain on transducers at mounting areas. Cement 0.015 x 0.250 in. phenolic strips to each side at ends of transducer. Cement 0.015 x 0.060 in. phenolic strips across edge of transducer to prevent shorting to mount. Accurately measure slot of mount and cement brass shimstock (selected X.125) to sides of previously mounted phenolic to provide not more than 0.001 in. or less than 0.0005 in. side clearance. This ensures perpendicularity and parallelism of transducer to support arms. Note 60°C max for cure.

b. Preparation of Plate Support (L-C-936315)

Remove balance weights to allow accessibility while cementing transducers in position. Cement 0.020 enameled wire in 0.062 holes, leaving approximately 1 in. exposed each end. Remove enamel from each end, but no closer than 0.050 of part body, to ensure infinite resistance. Clip outboard ends to 1/4 in. after tinning. Inboard ends are to be clipped to convenience when attaching to gauge after assembly of gauges to support arms. Balance weights are to remain off until completion of transducer assembly.

c. Assembly of Transducers to Plate (L-C-936314)

Clean parts in acetone. Assemble support plate, using bolts and spacers. Check parallelism to 0.001 in. at edge of plate; dress spacers until this dimension is achieved. Check fit of transducers with shims in their respective slots. They must fit smoothly and without distortion. Orient transducers to slots so that center terminal strip is located in short post slot adjacent to cemented wire terminal. Using wooden shims and wedges, block transducers to position. Do not wedge tightly. Transducers should be sufficiently free to allow removal with shims in place. For convenience, one gauge may be cemented in place per operation. After fit is established and transducer end is coated with epoxy, it may be inserted in place and cured for two hours at 50° to 60°C. When both gauges are initially set, a tinkers dam (coated with release agent) is inserted in slot to hold additional epoxy. Slot is to be filled flush with o.d. of support. Cure temperature is 60°C. Gravitational forces require a separate curing operation at each end. Central terminal strip of gauges is soldered to 0.020 in. wire and flushed before final epoxy operation is performed. Connect both sides of transducers in parallel to adjacent terminal with 0.005-in. diameter enameled wire. Install counter weights, using Locktite-G on threads. Tighten securely and leave in secure storage until ready to complete assembly.

d. Preparation of Adapter Arm (L-D-936323)

Install posts with large dia diametrically to the C/L of two smaller dia posts. Use Locktite-G on threads. On large dia post, slots must match holes in plate. Cement 2 pieces of 0.020-in. dia wire in place. Allow 1/4-in. max overhang at the plate end. Allow min of 1/2 in. at post end for attachment of flexural leads.

e. Transducer – Final Assembly of Supporting Elements

Add supporting plate (L-D-936323) to transducer plate (L-C-936315), using spacer. Orientation of support plate is with C/L of larger dia post aligned with C/L of shorter transducer support. Check concentricity on level block of each of the four plates at four

points on each circumference to max of 0.002 TIR misalignment. Further errors of parallelism will be corrected during attachment of sensor arms.

2. Sensor Arm Assembly

Insert arm weights with arbor press. If hole diameter is on low end of tolerance and diameter of weight is on high end, the arm can be heated to max of 78°C for relief. Caution: Apply heat by oven only. Uneven or pinpoint heating will distort arm. Place arm in secure storage until needed for final assembly.

3. Installation of Transducer Assembly in Housing

Insert assembly in housing. Orientation is established by holes in each end of housing. Use small parallel clamp to secure transducer in housing and prevent damage by impact. Place in secure storage until needed for final assembly.

Note: Use acetone for final degreasing and cleaning of all parts and assemblies. Connect transducer leads to plate terminals.

II. FINAL SENSOR ASSEMBLY

Mount support plate on leg supports and orient with base terminals that are outside evacuation area seals, facing up. Mount transducer housing assembly in such a manner that ends are equidistant from C/L of plate. Install torsion bar to housing. Note: Make certain that dowel is slide fit; otherwise, disassembly can become difficult.

Using 4.5-in. blocks, place on support plate in such a manner that the ends of arms are supported. The sensor arm may be lowered over torsion bar. Note: Do not mate arm hole to torsion bar diameter or allow it to bend. When arm is in place, torsion bar support plate may be added to assembly. An error of 0.005 in. to 0.010 in. will be

absorbed by glue line. Use sufficient epoxy to form a barrier at inboard end of enjoinment. Note: Refrain from using excessive cement; otherwise, it may drip down on sensor. Once lower end is sealed off, remaining void may be filled and surplus removed with razor blade. Cure at room ambient for min of 16 hr. Very carefully lower arm onto register and dowel, and secure.

Note: Locking screw and supports must be in place before attaching arms or rotating sensor assembly. Rotate plate 180^{o} and perform like operation to other arm. When both arms are secured, orthogonally measure clearance of adapter arm post to arm. Note: Make certain weight of transducer assembly is resting on lower arm. Measure each post clearance and divide shim into two equal parts; a ±0.0005-in. difference is allowed. Distortion of transducer assembly must be held to absolute minimum. Total value of each pair of shims should not exceed ±0.0005 in. of measured gap.

III. FINAL ASSEMBLY

Install capacitor drive. Set gap at 0.020 in. ±0.002 in. with sensor arms locked Release arm lock and check clearances. If error appears, reset stops until released position is same as locked position.

IV. DISASSEMBLY – REMOVAL OF TRANSDUCER ASSEMBLY

Orient sensor with housing cover up and release transducer from both arms. Remove bolts from torsion bar and arm. Block arm above register with 4.5-in. blocks after removal of arm locking brackets. Exercise caution in removal of screws in torsion bar case flange. Release torque from two screws in torsion bar support and leave sufficient torque to hold position. Remove remaining screws. Remove original two screws without exerting force on torsion bar.

Insert two razor blades, diametrically opposite each other, between torsion bar and case. Tap lightly if necessary. Lift sufficiently to insert two screwdrivers or case jacks and remove. Caution: Do not apply any force on support. Secure end of torsion bar to support with strip of tape and place in a secure storage. Disconnect transition wires. Remove housing cover. Transducer now may be safely removed from housing. Normally, it is not necessary to disturb opposite arm. If required, the same procedures apply.

V. REASSEMBLY – REPLACE TRANSDUCER ASSEMBLY

Clean cavity of housing. Insert transducer assembly, replace cover, and remove tape from torsion bar. With blocks in place, lower arm and torsion bar into place. Use light hand pressure to push torsion register into place. Replace screws in torsion bar support and lightly torque into position, avoiding as much as possible any preload. Secure torsion bar flange to housing. Lightly tap to provide nominal preload condition. Torque all screws tightly. Replace arm and secure to flange. Secure transducer to arms. Use same procedure as in final assembly. Reconnect transition wires and re-establish capacitor drive gap.

X 1136-28

PARTS LIST

MODEL LE 7363216

TITLE EARTH ORBITTING GRAVITY GRADIOMETER ASSY

DATE 12-29-72 REV NEXT ASS'Y

BY THEO SHEET 1 OF 2 SHEETS

ITEM	NOMENCLATURE	SIZE	DRAWING NUMBER 1 2 3 4 5 6 7 8 9 10 11 12	DWG CHG	QTY/ASSY
1	EARTH ORBITTING - GRAVITY GRADIOMETER ASSY	E	L E 9 3 6 3 2 6	A	1
2	SUPPORT PLATE - 8 NE G. GRAD	E	L E 9 3 6 3 2 5	B	1
3	INSERT - SCR TND 10-32 MS21209-F1-15		C O M M		64
4	INSERT - SCR TND 8-32 MS21209-C0820		C O M M		48
5	INSERT - SCR TND 1/4-20 MS21209-C4-15		C O M M		14
6	CAPACITANCE DRIVE ASSY	C	L C 9 3 6 3 2 2	-	2
7	BRACKET - CAPACITANCE DRIVE	C	L C 9 3 6 3 2 0	-	2
8	INSERT - TND 4-40 MS21209-C0415		C O M M		4
9	BRACKET, ANGULAR ADJUSTMENT	C	L C 9 3 6 3 1 9	-	2
10	INSERT MS21209-F1-15		C O M M		8
11	SPACER, INSULATOR	C	L C 9 3 6 3 1 8	A	2
12	PLATE, CAPACITANCE DRIVE	C	L C 9 3 6 3 1 7		2
13	TERMINAL 1582-1		C O M M		2
14	SEALING COMPOUND MIL-S-22473		C O M M		AR
15	SUPPORT, CAPACITANCE DRIVE	C	L C 9 3 6 3 2 1		4
16	SCREW 4-40 MS16995-10		C O M M		4
17	SCREW 10-32 MS16996-9		C O M M		4
18	SCREW 10-32 MS16996-10		C O M M		4
19	WASHER B48-103		C O M M		4
20	WEIGHT - 2 KG	B	L B 9 3 6 3 0 7	A	4
21	SUPPORT, TORSION SHAFT	C	L C 9 3 6 3 1 3	-	1
22	SUPPORT, LIMIT ADJUSTING SCR	C	L C 9 3 6 3 1 6	-	4
23	ARM, 130 ELASTIC	D	L D 9 3 6 3 2 4	A	2

PARTS RECORD

ASSEMBLY S/N _____

ER/PO NO	QUAN/ORD	ORD	CHG LTR	DUE	RECD	PART S/N

ASSEMBLY S/N _____

ER/PO NO	QUAN/ORD	ORD	CHG LTR	DUE	RECD	PART S/N

ASSEMBLY S/N _____

ER/PO NO	QUAN/ORD	ORD	CHG LTR	DUE	RECD	PART S/N

X1136-29

PARTS LIST

MODEL L-E-936926

TITLE EARTH ORBITTING GRAVITY GRADIOMETER ASSY

DATE 12-29-72 | REV | NEXT ASS'Y

BY THEO | SHEET 2 OF 2 SHEETS

ITEM	NOMENCLATURE	SIZE	DRAWING NUMBER 1	2	3	4	5	6	7	8	9	10	11	12	CHG LTR	QTY/ASSY
1	HOUSING - TRANSDUCER	D		L	D	9	9	6	3	0	6				A	1
2																
3																
4	CAP SCREW MS16995-19					C	O	M	M							6
5	DOWEL PIN MS9330-180					C	O	M	M							4
6	INSERT MS21209-F1-15					C	O	M	M							16
7	INSERT MS21209-C0615					C	O	M	M							6
8	SHAFT, TORSION	C		L	C	9	3	6	3	1	2				-	2
9	SCREW, BALANCING	B		L	B	9	3	6	3	1	0	-	1		-	4
10	SCREW, BALANCING	B		L	B	5	3	6	3	1	0	-	2		-	16
11	TRANSDUCER ASSY	C		L	C	9	3	6	3	1	4				A	2
12	PLATE SUPPORT-TRANSDUCER ASSY	C			L	C	9	3	6	5	1	5			B	4
13	BENDER TRANSDUCER	B			L	B	9	3	6	3	0	8			-	4
14	CAP SCREW MS16996-14					C	O	M	M							4
15	ADHESIVE, EPOXY EC2214					C	O	M	M							AR
16	TRAVEL LIMIT ADJUSTMENT SCR	B		L	B	9	3	6	3	0	9				-	2
17																
18	NUT 3/8-24 MS35650-3385				C	O	M	M								4
19	SCREW 10-32 MS51034-63				C	O	M	M								4
20	SCREW 10-32 MS35214-5				C	O	M	M								12
21	SCREW 1/4-20 MS35214-77				C	O	M	M								6
22	SCREW 1/4-20 MS35214-71				C	O	M	M								6
23	SCREW 10-24 MS35202-40				C	O	M	M								8
24	NUT 10-32 MS35650-305				C	O	M	M								4
25	SCREW 8-32 MS35214-42				C	O	M	M								8
26	WIRE 16 GA W16878				C	O	M	M								AR
27																
27	ADAPTER PLATE - ARM TO BELLOW	D		L	D	9	3	6	3	2	3				-	1

PARTS RECORD

ASSEMBLY S/N _____

ITEM	ER/PO NO.	QUAN/ORD	ORD	CHG LTR	DUE	RECD	PART S/N
1							
2							
3							
4							
5							
6							
7							
8							
9							
10							
11							
12							
13							
14							
15							
16							
17							
18							
19							
20							
21							
22							
23							
24							
25							
26							
27							

ASSEMBLY S/N _____

ITEM	ER/PO NO.	QUAN/ORD	ORD	CHG LTR	DUE	RECD	PART S/N
1							
2							
3							
4							
5							
6							
7							
8							
9							
10							
11							
12							
13							
14							
15							
16							
17							
18							
19							
20							
21							
22							
23							
24							
25							
26							
27							

ASSEMBLY S/N _____

ITEM	ER/PO NO.	QUAN/ORD	ORD	CHG LTR	DUE	RECD	PART S/N
1							
2							
3							
4							
5							
6							
7							
8							
9							
10							
11							
12							
13							
14							
15							
16							
17							
18							
19							
20							
21							
22							
23							
24							
25							
26							
27							

REVISIONS				
ZONE	LTR	DESCRIPTION	DATE	APPROVED
	A	ADDED .12 CHAM	6-9-72	

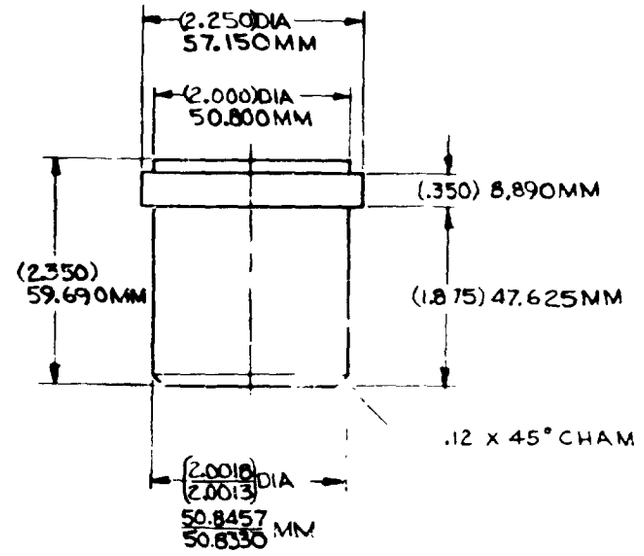

QTY REQD	CODE IDENT	PART NO OR IDENTIFYING NO.	NOMENCLATURE OR DESCRIPTION	FIND NO
		PARTS LIST		

2. REMOVE ALL BURRS AND SHARP EDGES TO .03 RADIUS MAXIMUM.
1. TOLERANCES: .XXX ± (.002) .051 MM
.XX ± (.03) .76 MM

NOTES, UNLESS OTHERWISE SPECIFIED:

EXCEPT AS NOTED DIM ARE IN INCHES
XXX XX ANGLES ~~.010 .08~~ ± 0°30'
MATERIAL MALLORY 1000

DR [illegible] Jan 72
CHK.
APPD

HUGHES

WEIGHT - 2 KG

NEXT ASSY	USED ON
APPLICATION	

SIZE	CODE IDENT NO	REV
B	82577	A

SCALE 1/1

X .12 - 1A

FORM [illegible] DIETERICH-POST [illegible]

99

REVISIONS				
ZONE	LTR	DESCRIPTION	DATE	APPROVED

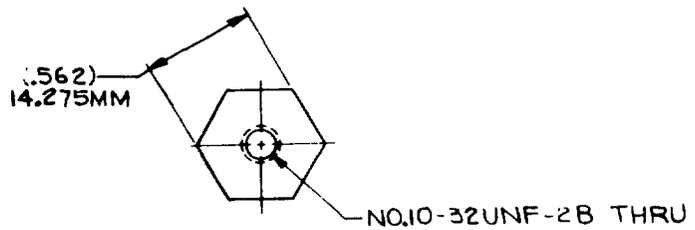

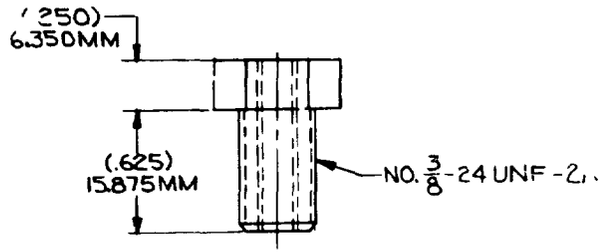

QTY REQD	PART OR IDENTIFYING NO	NOMENCLATURE OR DESCRIPTION	ITEM NO
		LIST OF MATERIALS	

2. TOLERANCES: .XXX ±(.010) .254MM
.XX ±(.03) .76MM

1. REMOVE ALL BURRS AND SHARP EDGES TO(.03)R .076MM MAXIMUM.

NOTES, UNLESS OTHERWISE SPECIFIED:

NEXT ASSY	USED ON
APPLICATION	

EXCEPT AS NOTED DIM. ARE IN INCHES SEE NOTE 2
XXX .XX ANGLES
±(.010) ±(.03) ±0°30'

MATERIAL
ROD, YEL BR, QQ-B-626, ALY 268, 1/2 HD

DR [illegible] 7 Jan 72
CHK [illegible]
APPD [illegible]

HUGHES — HUGHES AIRCRAFT COMPANY RESEARCH LABORATORIES MALIBU, CALIFORNIA

TRAVEL LIMIT ADJUSTMENT SCREW

SIZE	CODE IDENT NO		REV
B	82577	L-B-93 0309	

SCALE 2/1 SHEET 1 OF 1

FORM 11063-CS-RL 9-68 DIETERICH-POST 1000H

X1129-29

REVISIONS				
ZONE	LTR	DESCRIPTION	DATE	APPROVED

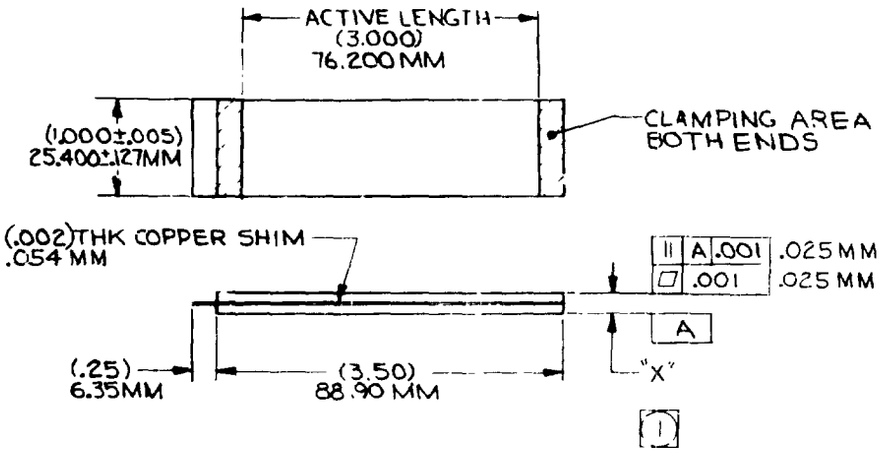

DASH NO.	DIM. "X"
-1	(.184±.004) 4.764±.102 MM
-2	(.232±.004) 5.893±.102 MM

SPECIFICATION CONTROL DWG

4. TOLERANCES: XXX ±(.010) .254MM
   XX ±(.03) .76 MM
3. OUTPUT IMPEDANCE: LESS THAN 1 MEG AT 8 HERTZ (CAPACITANCE: 20,000 PICOFARADS).
2. MAXIMUM ANGULAR DEFLECTION: 1°.
1. SELECT THICKNESS TO PROVIDE AN ANGULAR BENDING STIFFNESS OF 388 NEWTON-METERS/RADIAN ±10% (LINEAR BENDING STIFFNESS OF 1290 POUNDS/INCH).

NOTES, UNLESS OTHERWISE SPECIFIED:

QTY REQD	PART OR IDENTIFYING NO	NOMENCLATURE OR DESCRIPTION	ITEM NO

LIST OF MATERIALS

EXCEPT AS NOTED DIM ARE IN INCHES SEE NOTE 4
XXX ±.010 XX ±.03 ANGLES ±0°30'

MATERIAL
G 1500
OR
CHANNELITE
5500

DR [illegible] 19 JAN 72
CHK [illegible]
APPD [illegible] 1-22-73

L-C 936314
NEXT ASSY | USED ON
APPLICATION

HUGHES AIRCRAFT COMPANY
RESEARCH LABORATORIES
MALIBU, CALIFORNIA

HUGHES

BENDER TRANSDUCER

SIZE	CODE IDENT NO		REV
B	82577	L-B-[illegible]	

SCALE 1/1 SHEET 1 OF 1

X1130-29

FORM 11063-CS-RL 9-68 DIETERICH-POST 1000H

TABULATION		
DASH NO.	SCREW THD	DIMENSION "X"
-1	1/4-28 UNF-3A	(.075) 1.905 MM (.064) 1.626 MM
-2	8-32 UNC-3A	(.054) 1.371 MM (.045) 1.143 MM

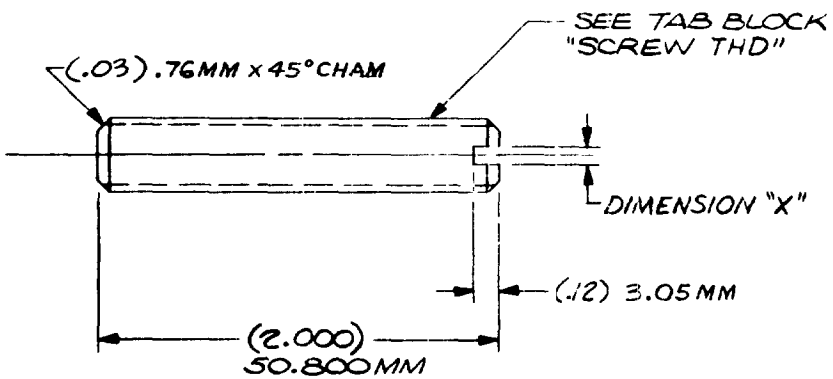

REVISIONS				
ZONE	LTR	DESCRIPTION	DATE	APPROVED

QTY REQD	CODE IDENT	PART NO. OR IDENTIFYING NO	NOMENCLATURE OR DESCRIPTION	FIND NO.
PARTS LIST				

2. PHOSPHOR BRONZE, QQ-B-750 COMP A, HARD
1. TOLERANCES: .XXX ±(.010) .254 MM
.XX ±(.03) .76 MM
NOTES: UNLESS OTHERWISE SPECIFIED

EXCEPT AS NOTED DIM. ARE IN INCHES SEE NOTE 1
.XXX .XX ANGLES ±(010) ±(03) ±0°30'

MATERIAL SEE NOTE 2

NEXT ASSY | USED ON
APPLICATION

DR Cook 2/6/72
CHK C. COMSTOCK 2-14-72
APPD

HUGHES AIRCRAFT COMPANY
RESEARCH LABORATORIES
MALIBU, CALIFORNIA

SCREW, BALANCING

SIZE B | CODE IDENT NO. 82577 | LB-13[illegible]

SCALE NONE | SHEET 1 OF 1

FORM 11063-CS-RL 9-68 DIETERICH-POST 1000H

X1145-21

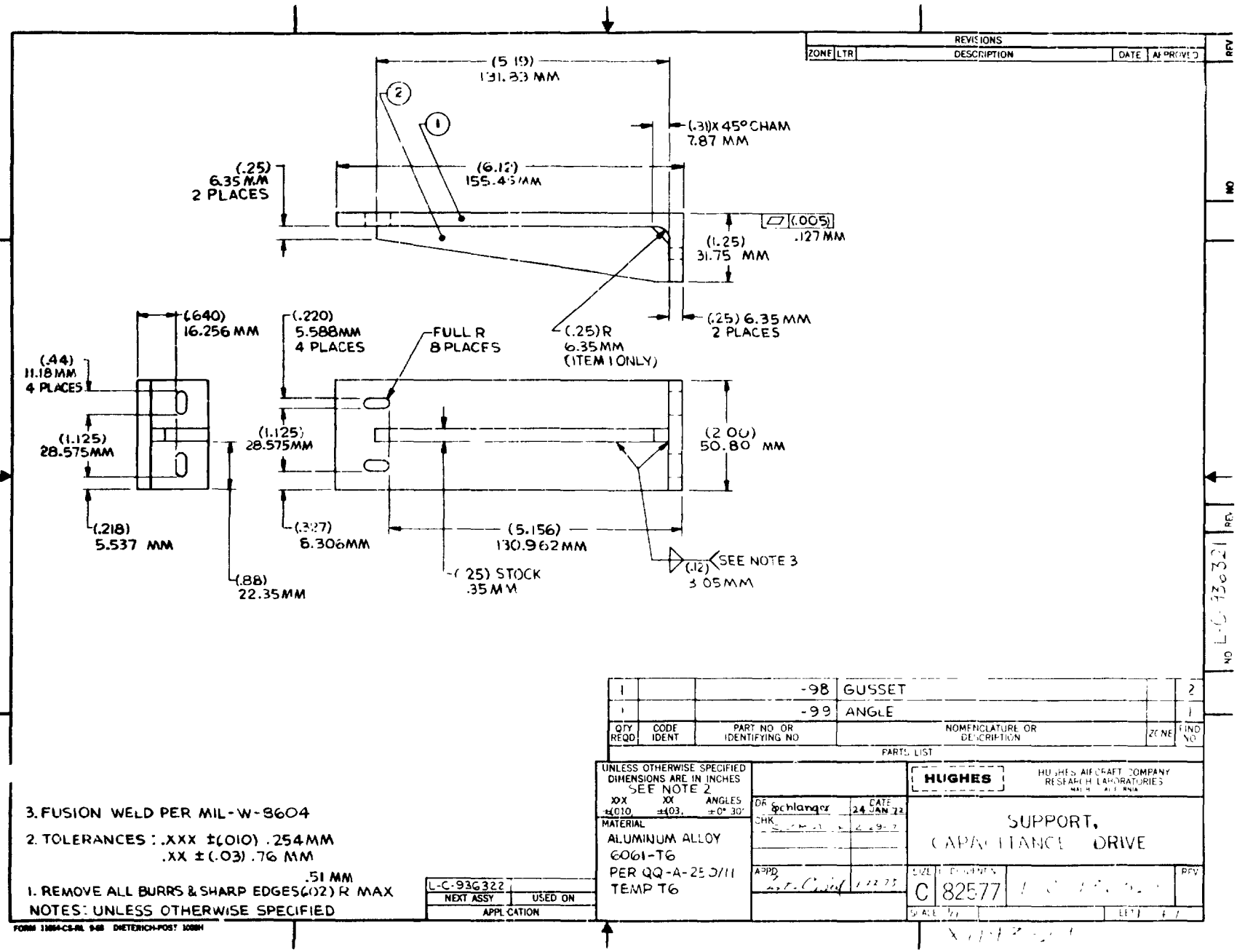
REVISIONS
ZONE LTR DESCRIPTION DATE APPROVED
(5.19)
131.83 MM
(.31) X 45° CHAM
7.87 MM
(.25)
6.35 MM
2 PLACES
(6.12)
155.45 MM
(.005)
.127 MM
(1.25)
31.75 MM
(.25) 6.35 MM
2 PLACES
(.640)
16.256 MM
(.220)
5.588MM
4 PLACES
FULL R
8 PLACES
(.25) R
6.35MM
(ITEM 1 ONLY)
(.44)
11.18MM
4 PLACES
(1.125)
28.575MM
(1.125)
28.575MM
(2.00)
50.80 MM
(.218)
5.537 MM
(.327)
8.306MM
(5.156)
130.962MM
(.88)
22.35MM
(.25) STOCK
.35MM
(.12)
3.05MM
SEE NOTE 3
70
1 -98 GUSSET 2
1 -99 ANGLE 1
QTY REQD | CODE IDENT | PART NO OR IDENTIFYING NO | NOMENCLATURE OR DESCRIPTION | ZONE | FIND NO
PARTS LIST
UNLESS OTHERWISE SPECIFIED DIMENSIONS ARE IN INCHES SEE NOTE 2
XX ±.010 XX ±.03 ANGLES ±0° 30'
MATERIAL
ALUMINUM ALLOY
6061-T6
PER QQ-A-250/11
TEMP T6
DR Schlanger DATE 24 JAN 72
CHK
APPD
HUGHES
HUGHES AIRCRAFT COMPANY
RESEARCH LABORATORIES
SUPPORT,
CAPACITANCE DRIVE
SIZE C
DWG NO 82577
REV
SCALE
SHEET
L-C-936322
NEXT ASSY
USED ON
APPLICATION
3. FUSION WELD PER MIL-W-8604
2. TOLERANCES: .XXX ±(.010) .254MM
.XX ±(.03) .76 MM
1. REMOVE ALL BURRS & SHARP EDGES (.02) R MAX .51 MM
NOTES: UNLESS OTHERWISE SPECIFIED
FORM 1088-CS-RL 9-68 DIETERICH-POST 1088H
NO L-C-936321
REV

REVISIONS				
ZONE	LTR	DESCRIPTION	DATE	APPROVED

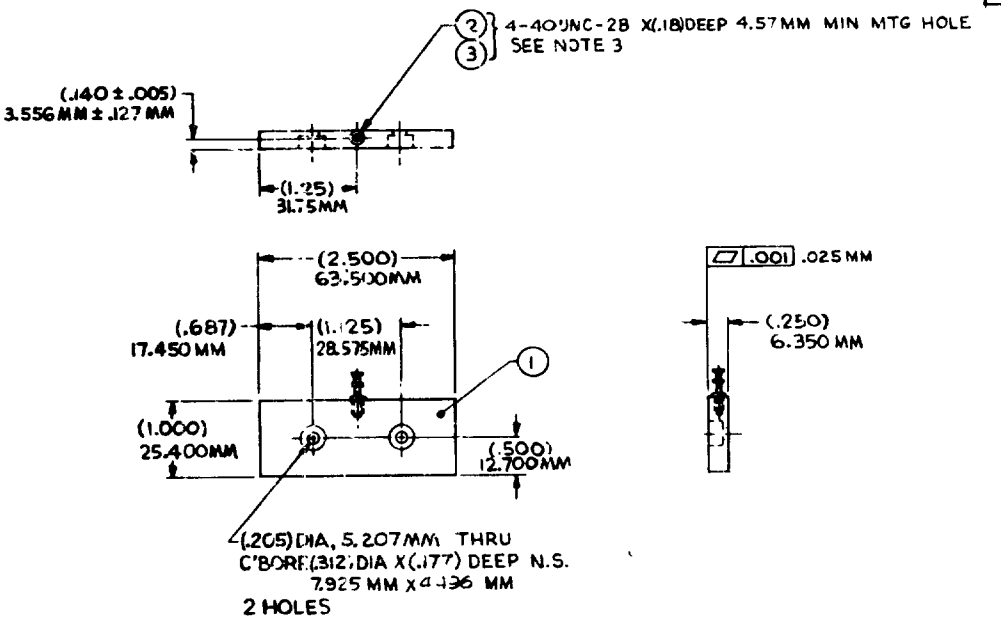

AS REQD		MIL-S-22473	SEALING COMPOUND, GRADE C		3
1	71279	1582-1	TERMINAL, SOLDER, TURRET		2
1		-99	PLATE, CAPACITOR		1
QTY REQD	CODE IDENT	PART NO OR IDENTIFYING NO	NOMENCLATURE OR DESCRIPTION	ZONE	FIND NO

PARTS LIST

3. ITEM 2 & 3 TO BE INSPECTED FOR ELECTRIC CONTINUITY
2. TOLERANCES: .XXX ± (.010) .254 MM
.XX ± (.03) .76 MM
.51 MM
1 REMOVE ALL BURRS & SHARP EDGES (.02) R MAX
NOTES: UNLESS OTHERWISE SPECIFIED

L-C-936322	
NEXT ASSY	USED ON
APPLICATION	

UNLESS OTHERWISE SPECIFIED DIMENSIONS ARE IN INCHES SEE NOTE 2
XXX ±(0.0) X° ±(03) ANGLES ±0° 30'
MATERIAL
ALUMINUM ALLOY 6061-T6 PER QQ-A-250/11 TEMP T6

		DATE
DR	SCHLANGER	26 JUL 72
CHK	COOK	2-3-73
APPD		2/23/73

HUGHES AIRCRAFT COMPANY
RESEARCH LABORATORIES
MALIBU, CALIFORNIA

PLATE,
CAPACITANCE DRIVE

SIZE	CODE IDENT NO		REV
C	82577	L-C-936317	
SCALE 1/1		SHEET 1 OF 1	

X-142-29

FORM 11854-CS-RL 9-65 DIETZGEN-POST 10004

L-C-936317 REV
L-C-936317 REV
L-C-936317 NO

REVISIONS				
ZONE	LTR	DESCRIPTION	DATE	APPROVED
	A	090 WAS 032		

A REV

LC-936318 NO

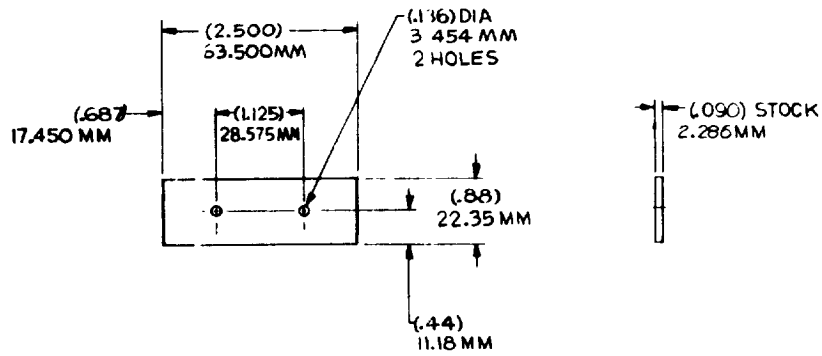

72

A REV

LC-936318 NO

QTY REQD	CODE IDENT	PART NO OR IDENTIFYING NO	NOMENCLATURE OR DESCRIPTION	ZONE	FIND NO

PARTS LIST

UNLESS OTHERWISE SPECIFIED DIMENSIONS ARE IN INCHES SEE NOTE 1

XXX ±(010)	XX ±(03)	ANGLES ±0° 30'

MATERIAL
NYLON
(POLYAMIDE)
GRADE E PER
MIL-M-20693

		DATE
DR	Schlange	2-25-72
CHK	E. Comstock	2-25-72
APPD		1-22-73

HUGHES AIRCRAFT COMPANY
RESEARCH LABORATORIES
MALIBU, CALIFORNIA

SPACER,
INSULATOR

SIZE	CODE IDENT NO	DRAWING NO	REV
C	82577	LC-936318	A

SCALE 1/1 SHEET 1 OF 1

LC-936322
NEXT ASSY | USED ON
APPLICATION

1. TOLERANCES: .XXX ± (.010) .254 MM
.XX ± (.03) .76 MM
NOTES: UNLESS OTHERWISE SPECIFIED

X1141-2

FORM 11654-CS-RL 9-69 DIETZGEN-POST 36BH

REVISIONS				
ZONE	LTR	DESCRIPTION	DATE	APPROVED

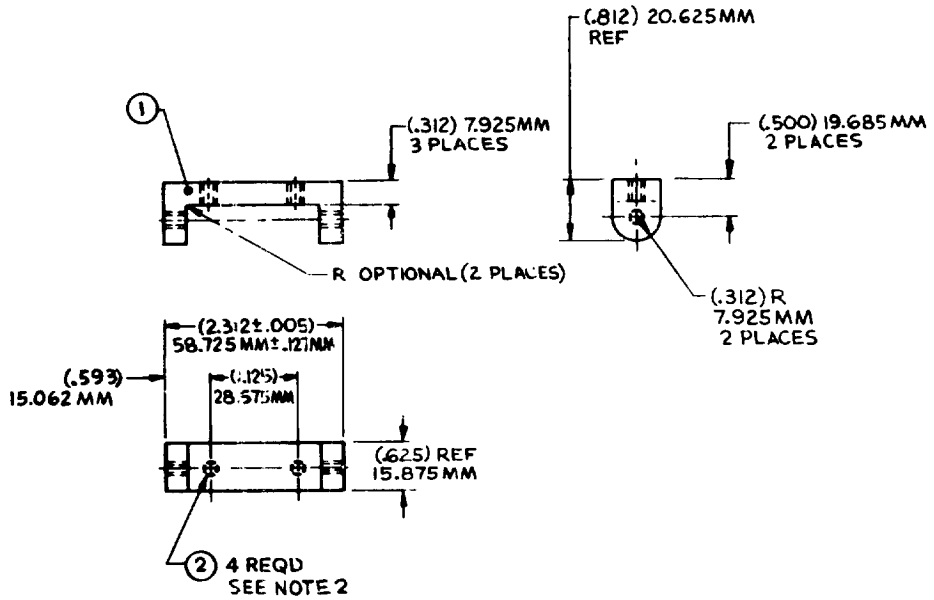

QTY REQD	CODE IDENT	PART NO OR IDENTIFYING NO	NOMENCLATURE OR DESCRIPTION	ZONE	FIND NO
4		MS 21209-F1-15	INSERT, THREADED		2
1		-99	BRACKET, ANGULAR ADJUSTMENT		1

PARTS LIST

3. TOLERANCES: .XXX ± (.010) .254 MM
.XX ± (.03) .76 MM

2. INSTALL ITEM 2 PER MS 33646

1. REMOVE ALL BURRS & SHARP EDGES (.02) R MAX .51 MM

NOTES: UNLESS OTHERWISE SPECIFIED

L-C-93G322
NEXT ASSY | USED ON
APPLICATION

UNLESS OTHERWISE SPECIFIED DIMENSIONS ARE IN INCHES
SEE NOTE 3
XXX ±(.010) XX ±(.03) ANGLES ±0° 30'

MATERIAL
ALUMINUM ALLOY
6061-T6
PER QQ-A-250/11
TEMP T6

		DATE
DR Schwager		21-JAN-72
CHK C.STOMSTOCK		2-25-72
APPD		11 12 73

HUGHES
HUGHES AIRCRAFT COMPANY
RESEARCH LABORATORIES
MALIBU, CALIFORNIA

BRACKET,
ANGULAR ADJUSTMENT

SIZE	CODE IDENT NO		REV
C	82577	L-C-93G319	

SCALE: 1/1 SHEET 1 OF 1

X1140-29

NO L-C-93G322 REV

FORM 11004-C8-RL 9-68 DIETZGEN-POST 30004

REVISIONS				
ZONE	LTR	DESCRIPTION	DATE	APPROVED

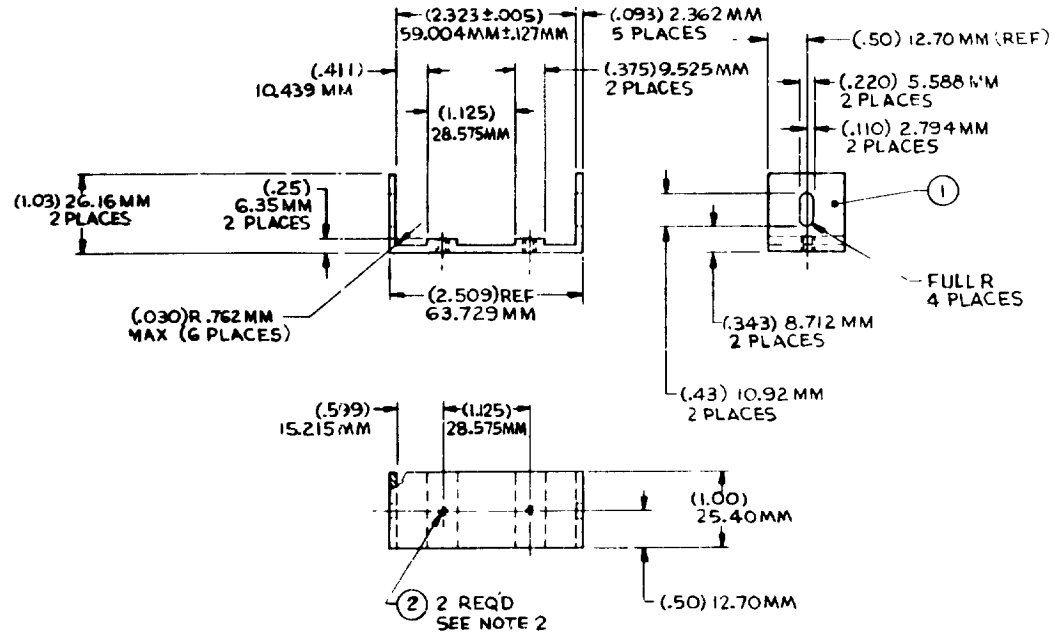

QTY REQD	CODE IDENT	PART NO OR IDENTIFYING NO	NOMENCLATURE OR DESCRIPTION	ZONE	FIND NO
2		MS21209-C0415	INSERT, THREADED, 4-40 CRES		2
1		-99	BRACKET, CAPACITOR		1

PARTS LIST

3 TOLERANCES: .XXX ± (.010) .254 MM
.XX ± (.03) .76 MM

2. INSTALL ITEM 2 PER MS 33646

1. REMOVE ALL BURRS & SHARP EDGES (.02) .51 MM R MAX

NOTES: UNLESS OTHERWISE SPECIFIED

NEXT ASSY	USED ON
APPLICATION	

UNLESS OTHERWISE SPECIFIED DIMENSIONS ARE IN INCHES
SEE NOTE 3
XXX ±(010) XX ±(03) ANGLES ±0° 30'

MATERIAL
ALUMINUM ALLOY
6061-T6
PER QQ-A-250/11
TEMP T6

ER [illegible] DATE 24 JAN 72
CHK [illegible]
APPD [illegible]

HUGHES
HUGHES AIRCRAFT COMPANY
RESEARCH LABORATORIES
MALIBU, CALIFORNIA

BRACKET-CAPACITANCE
DRIVE

SIZE C | DRAWING NO 82577 | REV

SCALE 1/1 | SHEET 1 OF 1

X1123-29

REV

NO L-C-136220

REV

NO L-C-136220

7.4

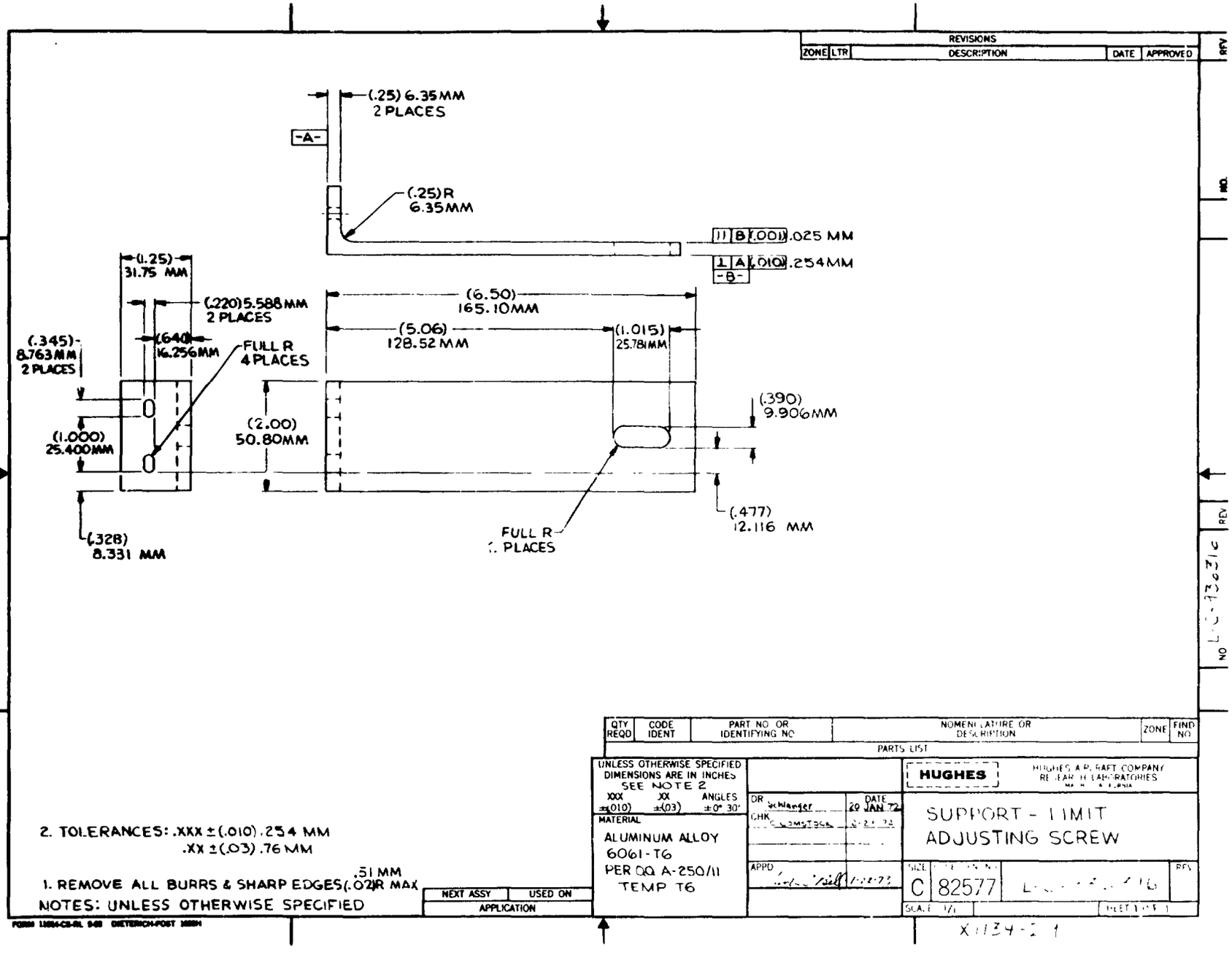
REVISIONS
ZONE LTR DESCRIPTION DATE APPROVED
REV
(.25) 6.35 MM
2 PLACES
-A-
(.25) R
6.35 MM
(.001) .025 MM
(.010) .254 MM
-B-
(1.25)
31.75 MM
(.220) 5.588 MM
2 PLACES
(.640)
16.256 MM
(.345)
8.763 MM
2 PLACES
FULL R
4 PLACES
(6.50)
165.10 MM
(5.06)
128.52 MM
(1.015)
25.781 MM
(1.000)
25.400 MM
(2.00)
50.80 MM
(.390)
9.906 MM
(.328)
8.331 MM
FULL R
PLACES
(.477)
12.116 MM
2. TOLERANCES: .XXX ±(.010) .254 MM
.XX ±(.03) .76 MM
1. REMOVE ALL BURRS & SHARP EDGES (.02) .51 MM R MAX
NOTES: UNLESS OTHERWISE SPECIFIED
NEXT ASSY
USED ON
APPLICATION
QTY REQD
CODE IDENT
PART NO OR IDENTIFYING NO
NOMENCLATURE OR DESCRIPTION
ZONE
FIND NO
PARTS LIST
UNLESS OTHERWISE SPECIFIED DIMENSIONS ARE IN INCHES SEE NOTE 2
XXX ±(010) XX ±(03) ANGLES ±0° 30'
MATERIAL
ALUMINUM ALLOY 6061-T6 PER QQ A-250/11 TEMP T6
DR Schlanger 29 JAN 72
CHK
APPD
HUGHES
HUGHES A.P. CRAFT COMPANY RESEARCH LABORATORIES
SUPPORT - LIMIT ADJUSTING SCREW
SIZE C
82577
SCALE 1/1
SHEET 1 OF 1
REV
NO L-133216
X1134-2 1

REVISIONS				
ZONE	LTR	DESCRIPTION	DATE	APPROVED
	A	REVISED & REDRAWN		

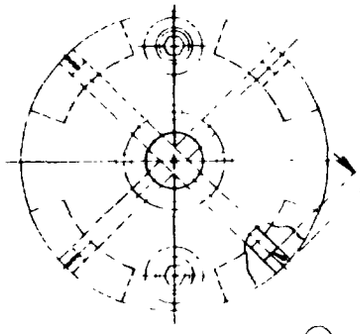

(250) BETWEEN EDGE OF SUPPORT & TRANSDUCER
6.530 MM
2 PL

(T) BOTH ENDS

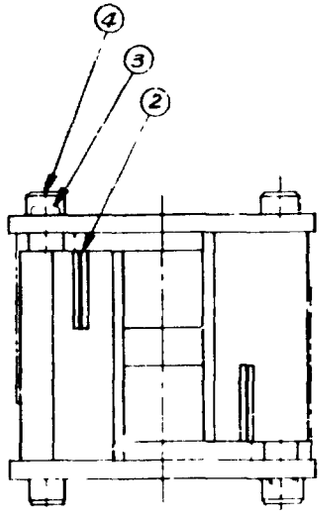

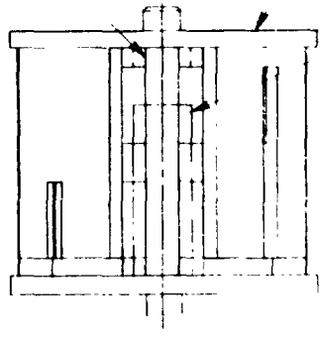

(3)

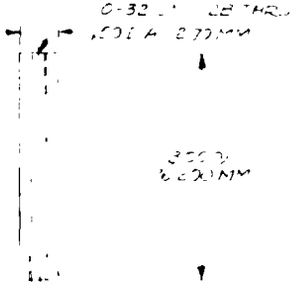

DETAIL-29

QTY REQD	CODE IDENT	PART NO OR IDENTIFYING NO	NOMENCLATURE OR DESCRIPTION	ZONE	FIND NO
(1)	A/R		ADHESIVE, EPOXY		5
2					4
2					3
4			TRANSDUCER, BENDER		2
2					1

PARTS LIST

4 AFTER REMOVE ITEMS 4 & -29 PART REPLACE ITEM 3
3 AFTER ADHESIVE HAS CURED REMOVE ITEMS 4 & -29 PART
2 TOLERANCE: XXX ± (010) 254 MM.
(1) BOND PER FED-MMMA-132 USING ITEM 5 POSITION AS SHOWN, 2 PLACES.
NOTES UNLESS OTHERWISE SPECIFIED.

NEXT ASSY	USED ON
APPLICATION	

UNLESS OTHERWISE SPECIFIED DIMENSIONS ARE IN INCHES

XXX	XX	ANGLES
± 010	± 03	± 0° 30

MATERIAL

		DATE
DR		
CHK		
APPD		

HUGHES — HUGHES AIRCRAFT COMPANY RESEARCH LABORATORIES

TRANSDUCER ASSY

SIZE	CAGE CODE	DWG NO	REV
C	82577	C-936314	A

SCALE — SHEET

X1:3/-29

C-936318

C-936314 NO

A REV

A REV

76

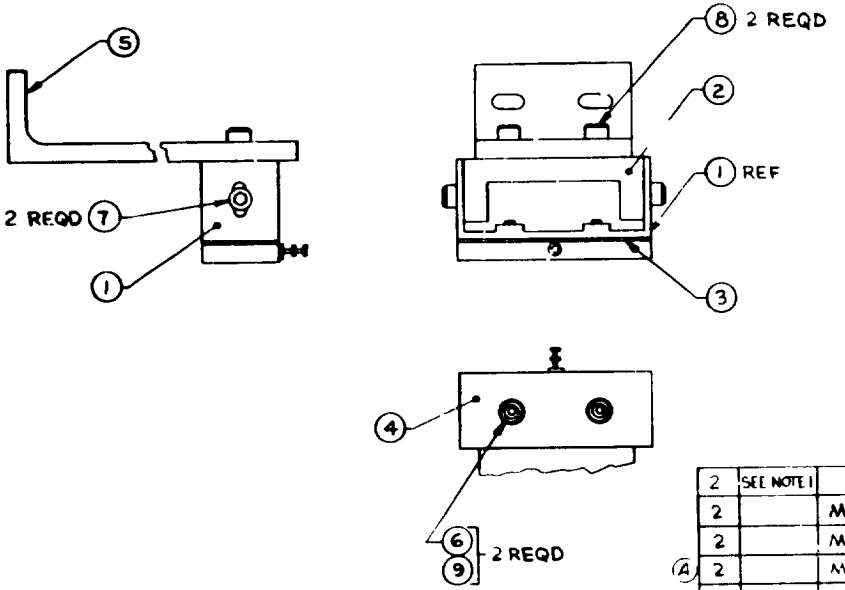

REVISIONS				
ZONE	LTR	DESCRIPTION	DATE	APPROVED

QTY REQD	CODE IDENT	PART NO OR IDENTIFYING NO	NOMENCLATURE OR DESCRIPTION	ZONE	FIND NO
2	SEE NOTE 1	848-103	WASHER SHOULDER INSULATED		9
2		MS16996-10	SCREW, CAP, 10-32 x .50LG, CRES		8
2		MS16996-9	SCREW, CAP, 10-32 x .38LG, CRES		7
(A) 2		MS16995-10	SCREW, CAP, 4-40 x .38LG, CRES.		6
1		L-C-936321	SUPPORT, CAPACITANCE DRIVE		5
1		L-C-936317	PLATE, CAPACITANCE DRIVE		4
1		L-C-936318	SPACER, INSULATOR		3
1		L-C-936319	BRACKET, ANGULAR ADJUSTMENT		2
1		L-C 936320	BRACKET, CAPACITANCE DRIVE		1

PARTS LIST

UNLESS OTHERWISE SPECIFIED DIMENSIONS ARE IN INCHES
XXX ± 010 XX ± 03 ANGLES ±0° 30'
MATERIAL

DR [illegible] DATE 22 AUG 73
CHK C. SOMSTOCK 2-69-74
APPD [illegible] 7-23-73

HUGHES HUGHES AIRCRAFT COMPANY RESEARCH LABORATORIES MALIBU, CALIFORNIA

CAPACITANCE DRIVE, ASSEMBLY

SIZE C | CODE IDENT NO 82577 | L-C-936322 | REV

SCALE 1/1 | SHEET 1 OF 1

NEXT ASSY | USED ON
APPLICATION

1. GRIES REPRODUCER CO. (162 BEECHWOOD AVE, NEW ROCHELLE, N.Y. 10801) OR EQUIV.

NOTES: UNLESS OTHERWISE SPECIFIED

X 1138-29

L-C-936322 REV

L-C-936322 REV

77

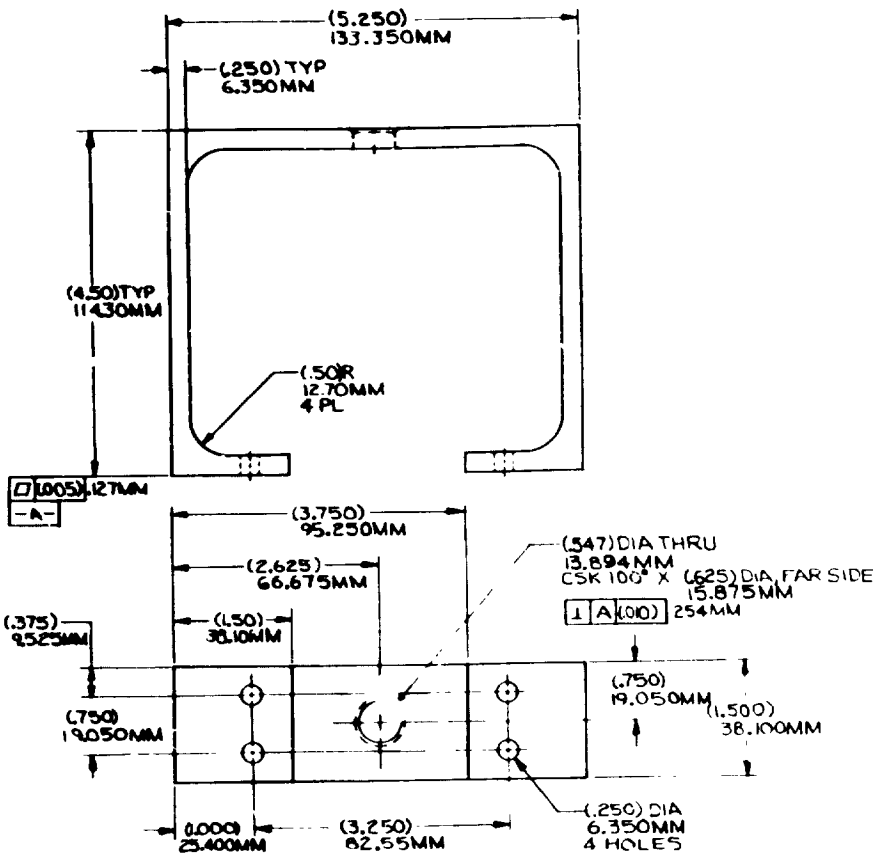

REVISIONS				
ZONE	LTR	DESCRIPTION	DATE	APPROVED

REV

NO.

78

QTY REQD	CODE IDENT	PART NO. OR IDENTIFYING NO.	NOMENCLATURE OR DESCRIPTION	ZONE	FIND NO.

PARTS LIST

UNLESS OTHERWISE SPECIFIED DIMENSIONS ARE IN INCHES

XXX	XX	ANGLES
±(.010)	±(.03)	±0° 30'

MATERIAL
ALUMINUM ALLOY
6061-T6
PER QQ-A-250/11
TEMPER

DRN [signature] DATE

APPD [signature]

HUGHES

SUPPORT [illegible] BRACKET

SIZE C | 82577

NEXT ASSY | USED ON

APPLICATION

2. REMOVE ALL BURRS AND SHARP EDGES TO .03 RADIUS MAXIMUM.
1. TOLERANCES: .XXX ± (.010) .254 MM
.XX ± (.03) .76MM

NOTES, UNLESS OTHERWISE SPECIFIED:

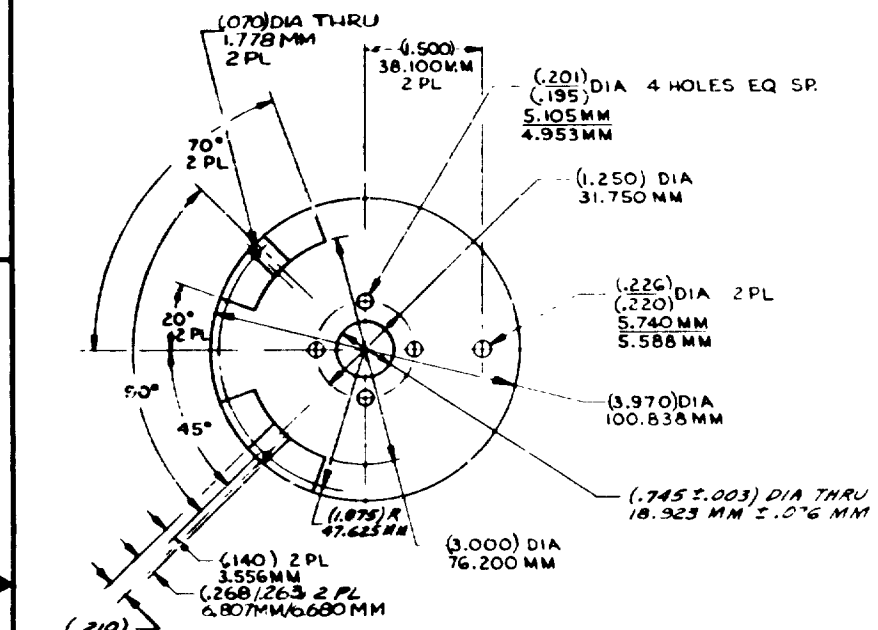

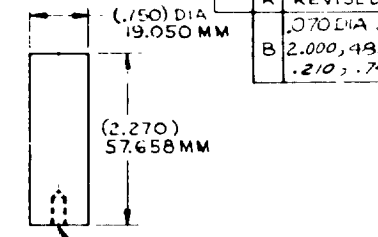

DETAIL ITEM (2)

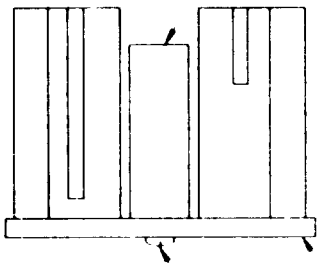

(2)

10-32 x .250 12.70MM LG. P.H. SCREW
BRASS PT NO. MS35338-55

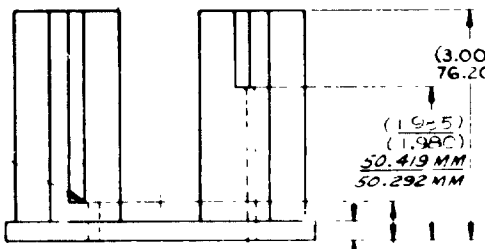

DETAIL ITEM (1)
VIEW ROTATED 90° CW

REVISIONS				
ZONE	LTR	DESCRIPTION	DATE	APPROVED
-	A	REVISED & REDRAWN	5-7-72	
		.070 DIA REL ADDED, TOPS MAC	10 22-72	
	B	2.000, .485 WAS .480), ADDED 1.875 R, .210, .745 DIA), .668/.263 WAS .280		

QTY REQD	CODE IDENT	PART NO. OR IDENTIFYING NO.	NOMENCLATURE OR DESCRIPTION	Z	FIND NO.
		PART LIST			

UNLESS OTHERWISE SPECIFIED DIMENSIONS ARE IN INCHES
SEE NOTE 2
XXX ±.010 XX ±.03 ANGLES ±0° 30'

MATERIAL
ITEM 1 ALUM A. 6061-T6 PER QQ A 225/8 TEMP TG
ITEM 2 BRASS PER QQ ... COND ... HARD

DR [illegible] DATE
CHK
APPD

NEXT ASSY | USED ON
APPLICATION

HUGHES

[illegible]

SIZE C | 82577 | REV B

SCALE 1 | SHEET

2. TOLERANCES: XXX ±(.010) .254 MM
.XX ±(.03) .76 MM
1. REMOVE ALL BURRS & SHARP EDGES (.03) .76 MM R. MAX
NOTES: UNLESS OTHERWISE SPECIFIED

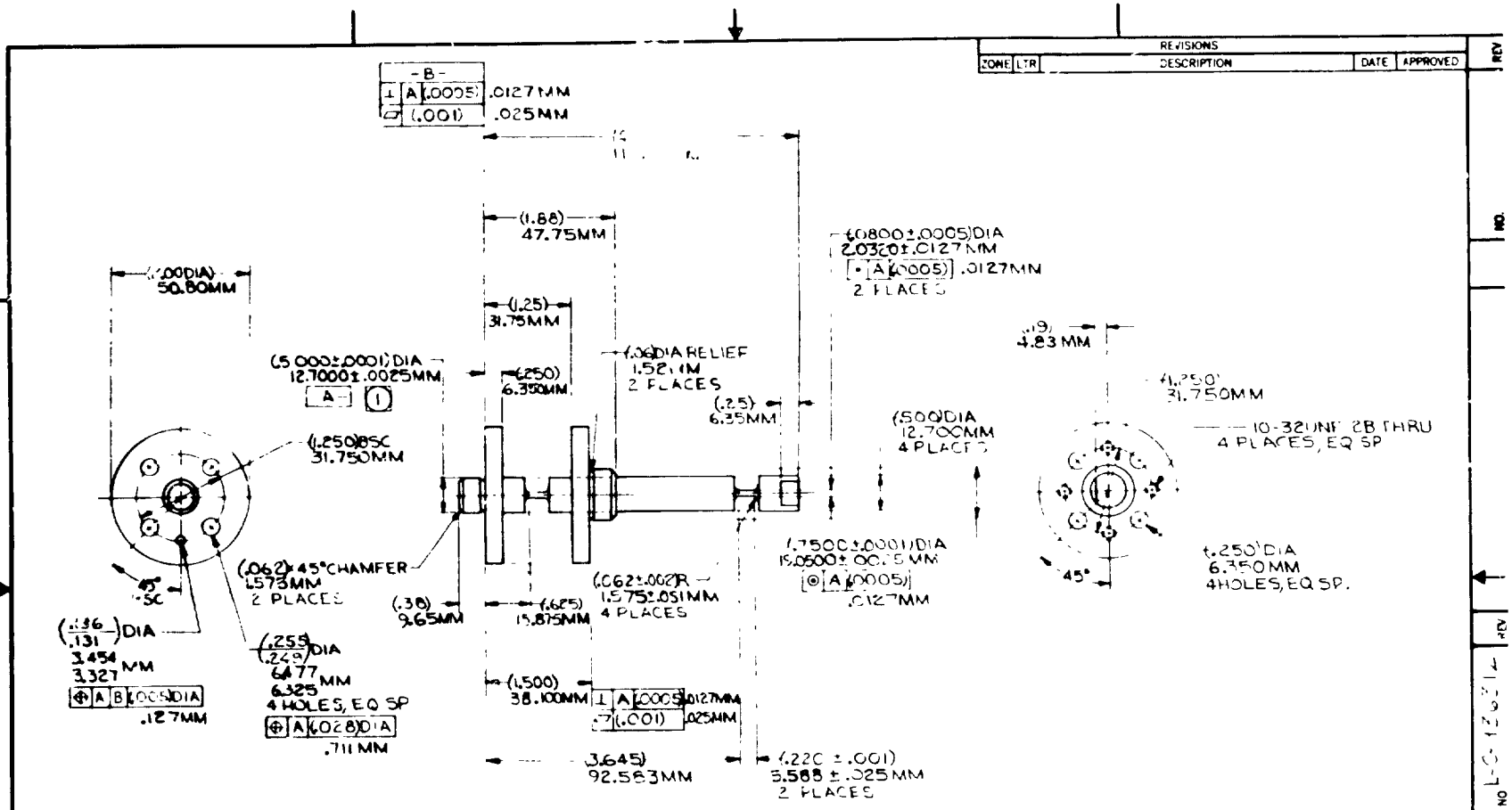

5 TOLERANCES .XXX±(.01).254MM
.XX±(.03).76MM

4. ALL SURFACES WITH TOLERANCES LESS THAN ± 001 SHALL HAVE 8 FINISH OR BETTER.

3 HEAT TREAT-PRECIPITATION HARDEN AT (600-625°F) 315.56°-329.45°C FOR 2 HOURS PER MIL-H-7199A.

2 CRITICAL DIMENSIONS TO BE MACHINED AFTER HEAT TREAT, MATERIAL NOT TO EXCEED (300°F) 148.89°C DURING MACHINING.

1 (5000)12.7000 MM DIA HOLDS FOR (38)965MM DIMENSION ONLY.

NOTES, UNLESS OTHERWISE SPECIFIED:

REVISIONS				
ZONE	LTR	DESCRIPTION	DATE	APPROVED

QTY REQD	CODE IDENT	PART NO OR IDENTIFYING NO	NOMENCLATURE OR DESCRIPTION	ZONE	FIND NO

PARTS LIST

UNLESS OTHERWISE SPECIFIED DIMENSIONS ARE IN INCHES SEE NOTE 5

XXX	XX	ANGLES
±(.01)	±(.03)	±0° 30'

MATERIAL
BeCu, (BERYLCO 25) COND HRD, QQ-C-530

DRN DATE
CHK
APPD

NEXT ASSY | USED ON
APPLICATION

HUGHES
HUGHES AIRCRAFT COMPANY
RESEARCH LABORATORIES

SHAFT, TORSION

SIZE C | DRAWING NO 82577 | REV

SCALE 1:1 | SHEET 1 OF 1

X-125-29

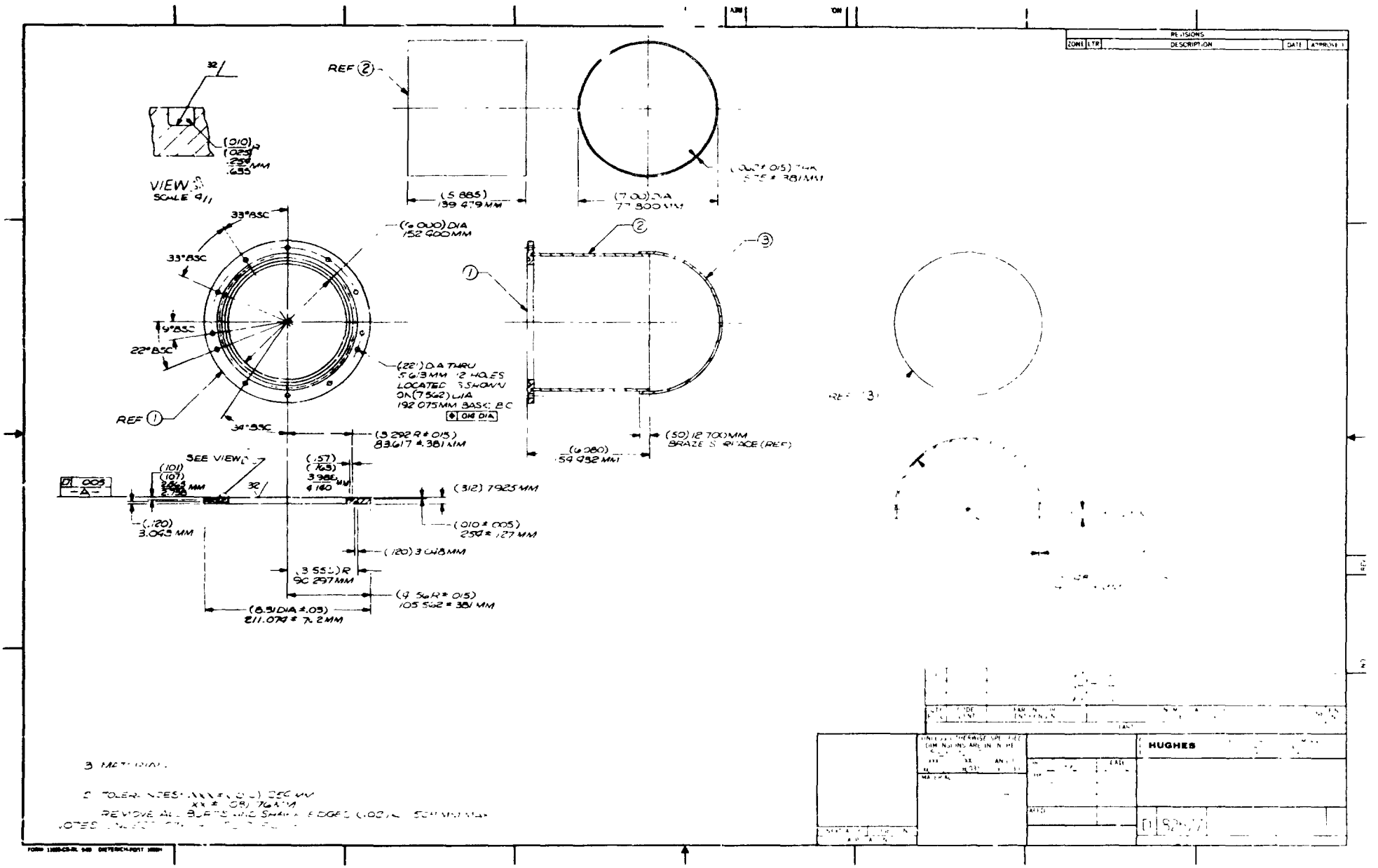

3 METRIC

5 TOLERANCES: XXX ± (.010) .25 MM
XX ± (.03) .76 MM
REMOVE ALL BURRS AND SHARP EDGES (.02) R .50 MM MAX

NOTES

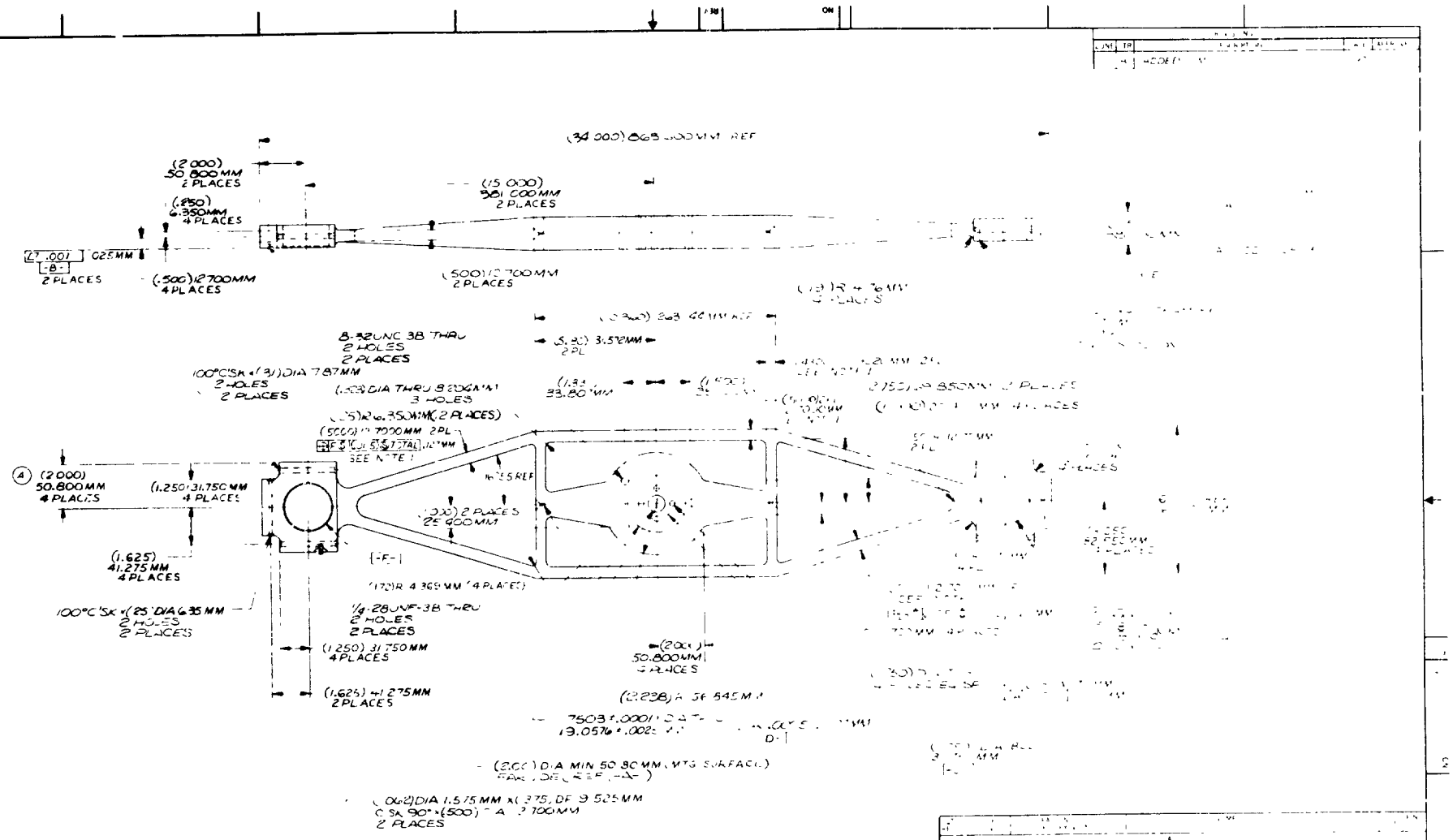

4. DIMENSIONS TO BE SYMMETRICAL ABOUT DATUM -D- & -E- WITHIN (.002) .051MM TOTAL
3. TEMPER (LEADER TO FINAL MACHINING) 24HR @ 400°F

2 PLACE DECIMALS: .xxx ± (.010) .254MM
.xx ± (.03) .76MM

1. WEB THICKNESS TO BE CONSTANT WITHIN ± (.001) .025MM 8 PLACES
NOTES: UNLESS OTHERWISE SPECIFIED

HUGHES

82

ZONE	LTR	REVISIONS DESCRIPTION	DATE	APPROVED
-	A	ADDED .745 DIA		
	B	PART NO OF ITEM 1 THRU 3 WAS X1133-29-1, X1133-29-2 & X1133-29-3 RESP. IN BLOCK NEXT ASSY WAS		

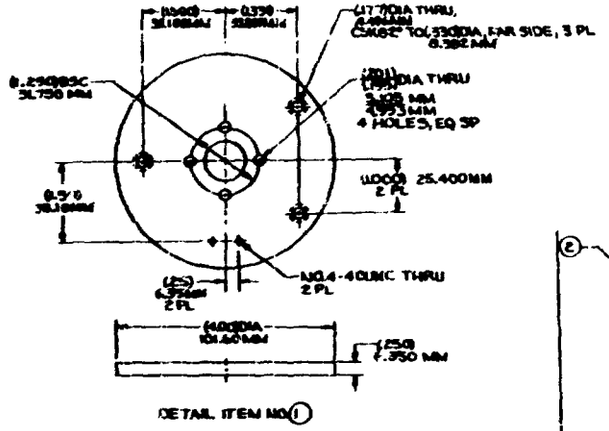

DETAIL ITEM NO. (1)

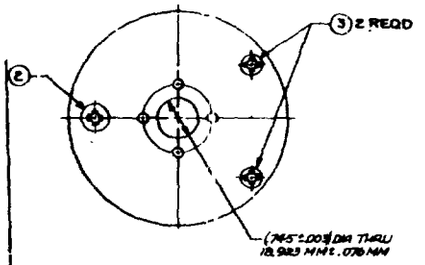

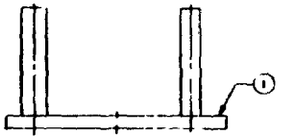

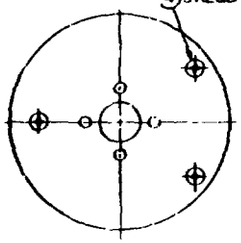

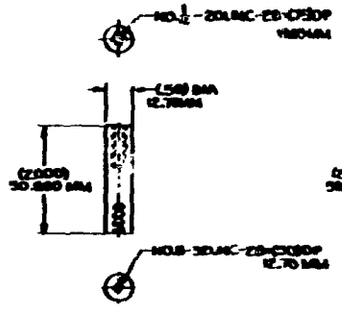

DETAIL ITEM NO. (2)

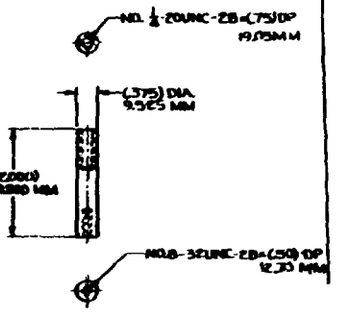

DETAIL ITEM NO. (3)

ITEM NO	QTY REQD	CODE IDENT	PART NO OR IDENTIFYING NO	NOMENCLATURE OR DESCRIPTION	ZONE	FIND NO
3		AN505U8R10	NO.8-32(.625)15.875MM LG SCR, F H, BR			4
2		L-D-936323-3	POST			3
1		L-D-936323-2	POST			2
1		L-D-936323-1	PLATE			1

PARTS LIST

2. TOLERANCES: .XXX ±(.010) .254 MM
.XX ± (.03) .76 MM
1. REMOVE ALL BURRS AND SHARP EDGES TO (.03) .762 MM R MAX.

NOTES, UNLESS OTHERWISE SPECIFIED:

UNLESS OTHERWISE SPECIFIED DIMENSIONS ARE IN INCHES
XXX ±(.010) XX ±(.03) ANGLES ±0° 30'

MATERIAL
ITEMS 1, 2, AND 3 - AL ALLOY 6061-T6 PER QQ-A 225/8, TEMPER T6

NEXT ASSY | USED ON APPLICATION

DRAWN | DATE 1/4/72
CHK L. CHRISTENSEN | 2/1/72
APPD | DATE

HUGHES AIRCRAFT COMPANY RESEARCH LABORATORIES MALIBU, CALIFORNIA

ADAPTER PLATE - ARM TO BELLOWS

SIZE D | CODE IDENT NO 82577 | L-D-936323 | REV A

SCALE 1/1 | SHEET 1 OF 1

X1133-29

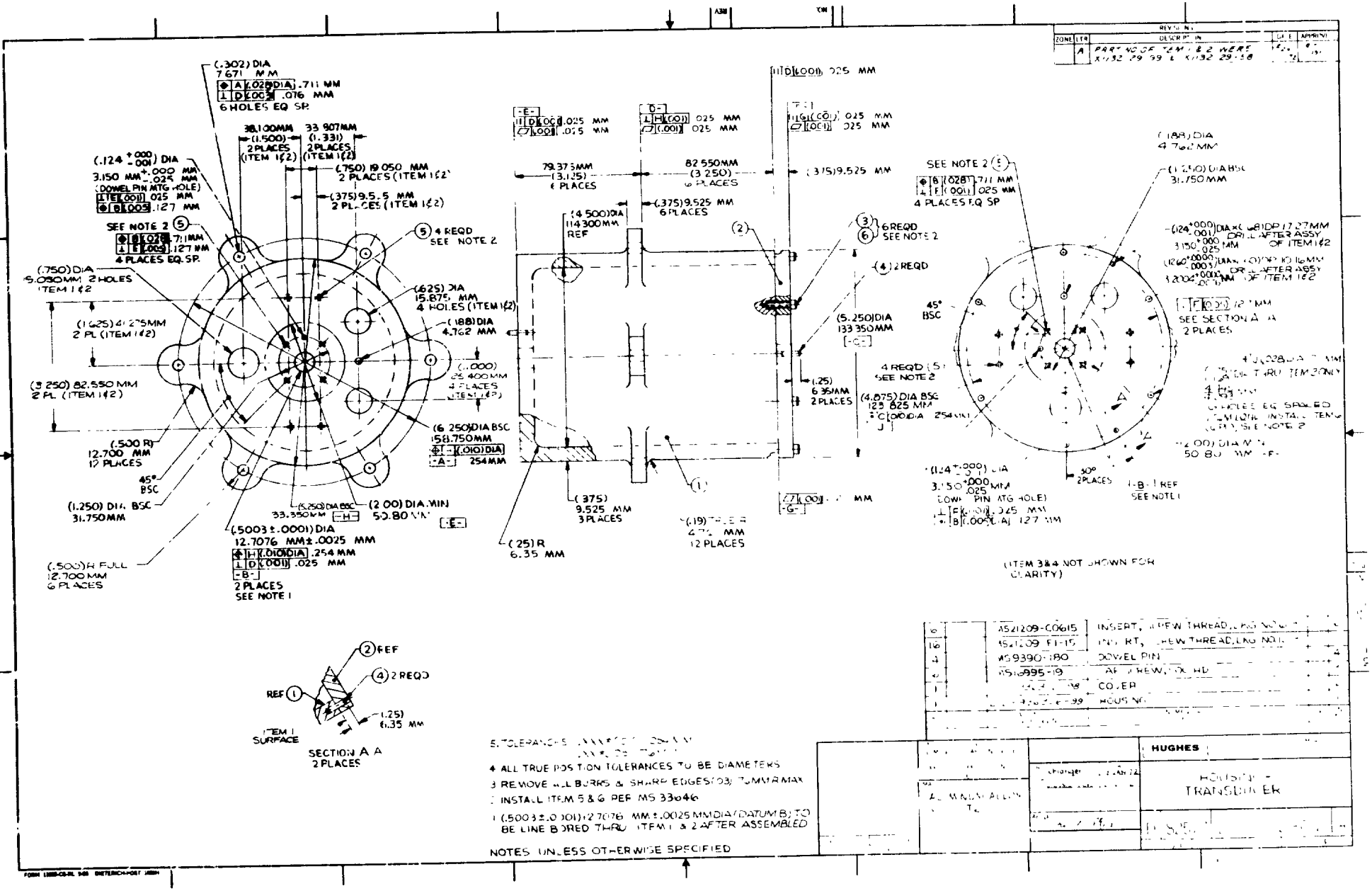
REVISIONS
ZONE LTR DESCRIPTION DATE APPROVED
A PART NO OF ITEM 1 & 2 WERE X1132 29 99 & X1132 29 98
(.302) DIA 7.671 MM
6 HOLES EQ SP
38.100MM (1.500) 2 PLACES (ITEM 1&2)
33.907MM (1.331) 2 PLACES (ITEM 1&2)
(.124 +.000 -.001) DIA 3.150 MM +.000 -.025 MM (DOWEL PIN MTG HOLE)
SEE NOTE 2
4 PLACES EQ SP
(.750) DIA 19.050 MM 2 PLACES (ITEM 1&2)
(.375) 9.525 MM 2 PLACES (ITEM 1&2)
4 REQD SEE NOTE 2
(.750) DIA 19.050MM 2 HOLES ITEM 1&2
(.625) DIA 15.875 MM 4 HOLES (ITEM 1&2)
(.188) DIA 4.762 MM
(1.625) 41.275MM 2 PL (ITEM 1&2)
(3.250) 82.550 MM 2 PL (ITEM 1&2)
(.000) 25.400MM 3 PLACES ITEM 1&2
(6.250) DIA BSC 158.750MM
(.500 R) 12.700 MM 12 PLACES
45° BSC
(1.250) DIA BSC 31.750MM
(5.250) DIA BSC 133.350MM
(2.00) DIA MIN 50.80 MM
(.5003 ±.0001) DIA 12.7076 MM ±.0025 MM
2 PLACES SEE NOTE 1
(.500) R FULL 12.700 MM 6 PLACES
79.375MM (3.125) 6 PLACES
82.550MM (3.250) 6 PLACES
(.375) 9.525 MM 6 PLACES
(4.500) DIA 114.300MM REF
6 REQD SEE NOTE 2
2 REQD
(5.250) DIA 133.350MM
(.25) 6.35MM 2 PLACES
4 REQD SEE NOTE 2
(4.875) DIA BSC 123.825 MM
(.375) 9.525 MM 3 PLACES
(.25) R 6.35 MM
(.19) THRU 4.7 MM 12 PLACES
SEE NOTE 2
4 PLACES EQ SP
(1.250) DIA BSC 31.750MM
(.188) DIA 4.762 MM
(.124 +.000 -.001) DIA 3.150 +.000 -.025 MM (DOWEL PIN MTG HOLE)
45° BSC
30° 2 PLACES
SEE SECTION A A 2 PLACES
SEE NOTE 1
(ITEM 3&4 NOT SHOWN FOR CLARITY)
SECTION A A 2 PLACES
ITEM 1 SURFACE
REF
2 REQD
(.25) 6.35 MM
AS21209-C0615 INSERT, SCREW THREAD, LOCKING
AS21209-F1-15 INSERT, SCREW THREAD, LOCKING
MS9390-180 DOWEL PIN
MS9995-19 SCREW, SOCKET HD
COVER
HOUSING
4. ALL TRUE POSITION TOLERANCES TO BE DIAMETERS
3. REMOVE ALL BURRS & SHARP EDGES (.03) .76MM R MAX
2. INSTALL ITEM 5 & 6 PER MS 33546
1. (.5003 ±.0001) 12.7076 MM ±.0025 MM DIA (DATUM B) TO BE LINE BORED THRU ITEM 1 & 2 AFTER ASSEMBLED
NOTES UNLESS OTHERWISE SPECIFIED
HUGHES
HOUSING - TRANSDUCER

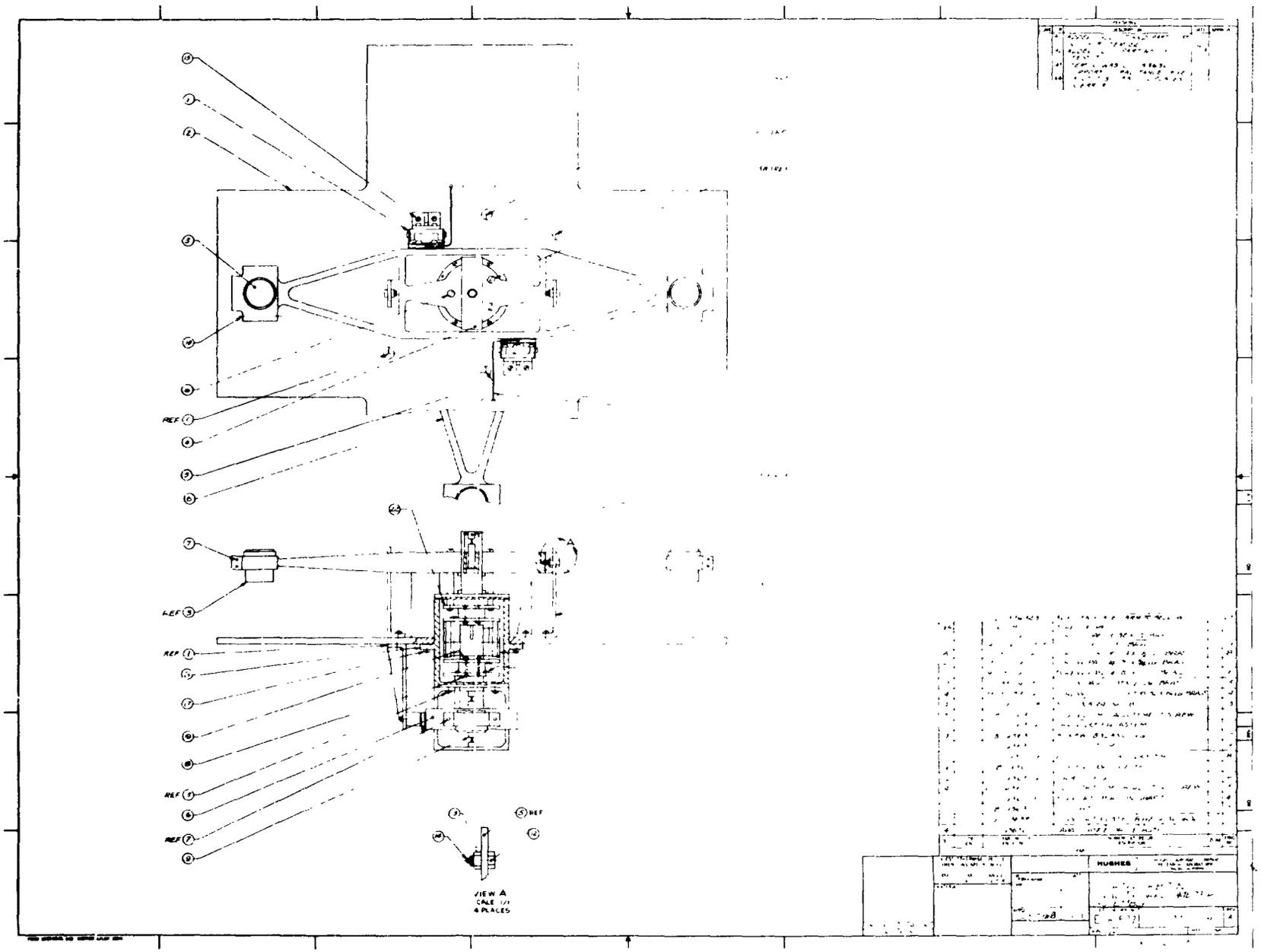
REF
REF
REF
REF
REF
REF
VIEW A
SCALE 1/1
4 PLACES
HUGHES

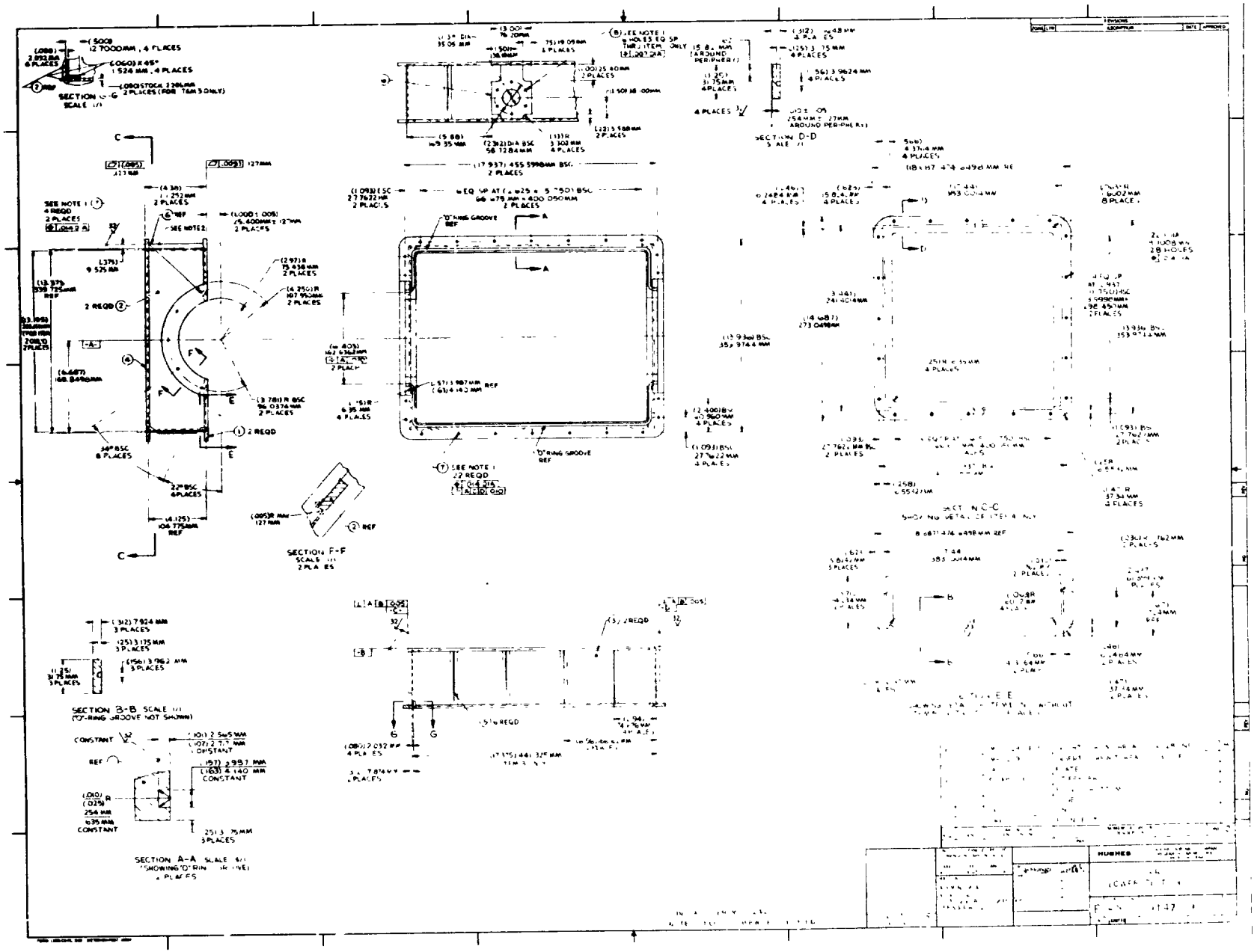
SECTION G-G
SCALE 1/1
SECTION D-D
SCALE 1/1
SECTION F-F
SCALE 1/1
2 PLACES
SECTION B-B SCALE 1/1
("O"-RING GROOVE NOT SHOWN)
SECTION A-A SCALE 6/1
SHOWING "O" RING
4 PLACES
SECTION C-C
SHOWING DETAILS OF ITEM 4 ONLY
HUGHES

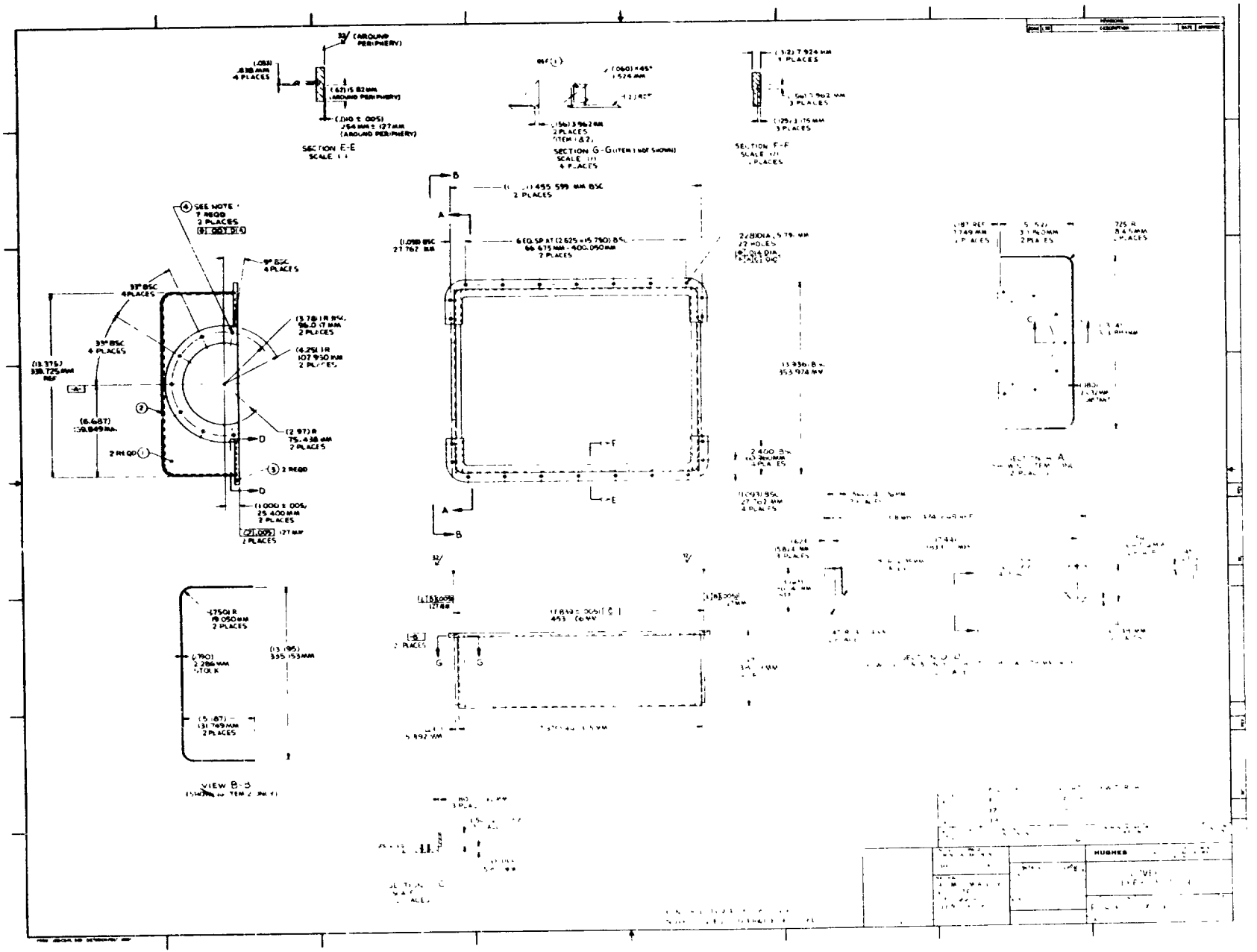

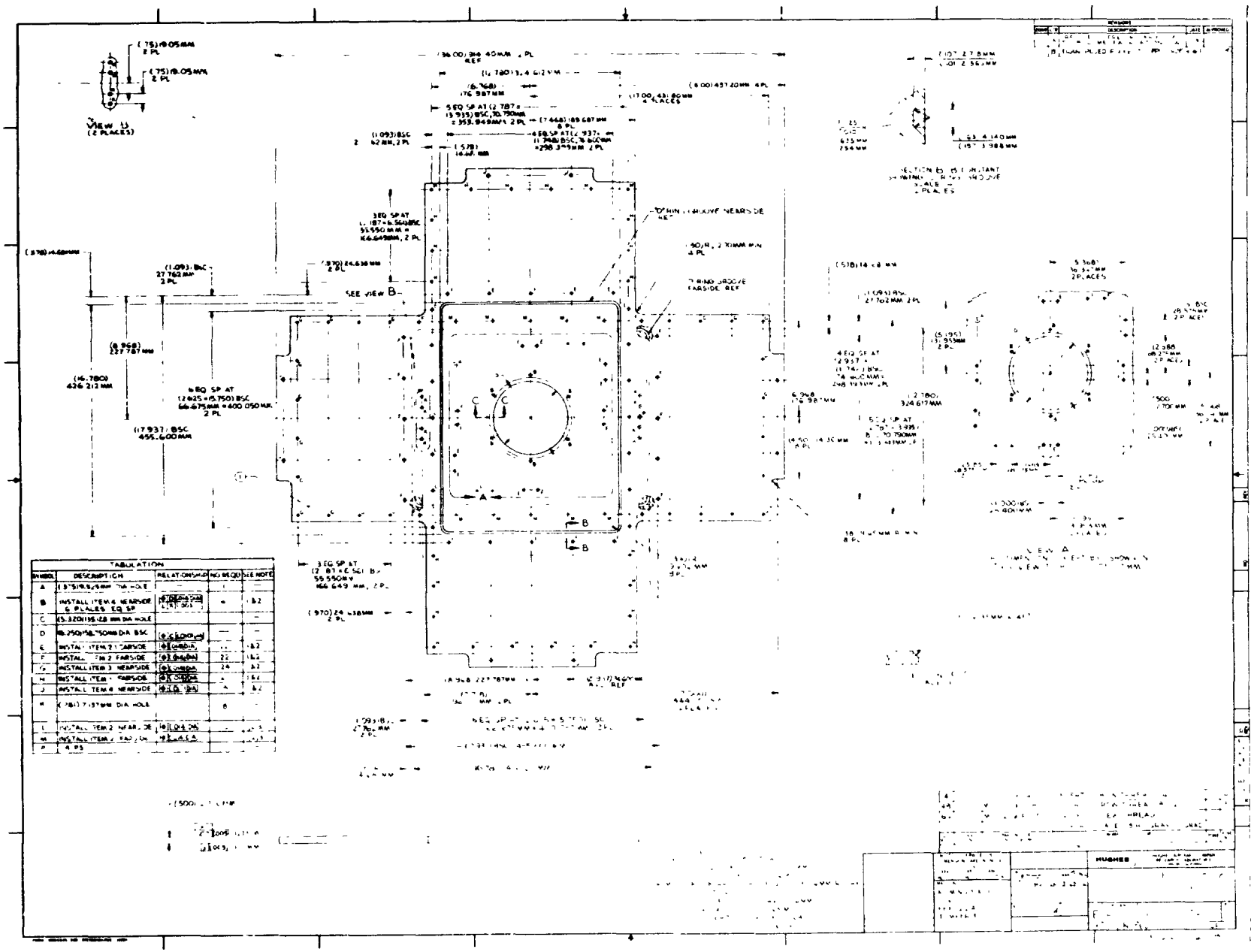
VIEW B
SEE VIEW B
TABULATION
SYMBOL
DESCRIPTION
RELATIONSHIP
NO REQ'D
SEE NOTE
A
B
C
D
E
F
G
H
J
K
L
M
P
INSTALL ITEM 4 NEARSIDE
6 PLACES EQ SP
INSTALL ITEM 2 NEARSIDE
INSTALL ITEM 2 FARSIDE
INSTALL ITEM 3 NEARSIDE
INSTALL ITEM 3 FARSIDE
INSTALL ITEM 4 NEARSIDE
INSTALL ITEM 2 NEAR SIDE
INSTALL ITEM 3 FAR SIDE
4 PLS
HUGHES

APPENDIX B

DEVELOPMENT OF A ROTATING GRAVITY GRADIOMETER FOR EARTH ORBIT APPLICATIONS

1 September 1971

DEVELOPMENT OF A ROTATING GRAVITY GRADIOMETER FOR EARTH ORBIT APPLICATIONS*†

by

Robert L. Forward
Principal Investigator

Exploratory Studies Department
Hughes Research Laboratories
Malibu, California 90265

---

* Reprint of a paper presented at the Advanced Applications Flight Experiments (AAFE) Principal Investigators' Review, 5-6 Oct 1971, NASA-Langley Research Center, Hampton, Virginia.

† Prepared under Contract NAS 1-10945.

ABSTRACT

Improvements in the knowledge of the earth's gravitational field would be of great value to the scientific fields of geology, geodesy and geophysics, and would have significant applicatic to orbital mechanics, navigation, guidance, earth dynamics, and mineral prospecting. The usual techniques of surface surveys with gravimeters have been augmented in recent years with orbital surveys using data derived from doppler tracking of satellites. These techniques have improved our knowledge significantly, but both are entering the regime of diminishing returns in terms of cost, time and effort required to obtain new data. Gravity gradient instrumentation for directly measuring the variations in the earth's gravity field from orbit has been under development for a number of years, but has not yet emerged into flight hardware status. Computer studies and experimental demonstrations with real gravitational fields in the laboratory have shown that a rotating gravity gradiometer flown in low earth orbit would be able to significantly improve our knowledge of the earth's gravitational field. Such instrumentation, flight proven for near-earth orbit mission, would also have wide application for measurement of the gravity fields of the moon, the terrestrial planets, the finer details of the outer planets and their satellites, and would significantly improve the scientific return from Comet/Asteroid Rendezvous and Docking (CARD) missions. The objective of this project in the AAFE program is to study the instrumentation and mission parameters required for improved measurement of the earth's gravity field from near earth orbit, design and fabricate a sensor optimized for this mission regime, and show by operational demonstrations of laboratory prototype hardware that the instrumentation requirements are attainable. The work on the project commenced on 22 June 1971. The mission studies are nearing completion, and the design parameters for the sensor are emerging. This paper is a preliminary report of the studies to date, combined with a summary report of relevant experimental and analytical studies carried out prior to the commencement of the project.

ROTATING GRAVITY GRADIOMETER

Method of Operation

The rotating gravity gradient sensor that has been developed at the Hughes Research Laboratories is a device for measurement of the second order gradient of the total gravity potential field.[1] The sensor configuration consists of a resonant cruciform mass-spring system with a torsional vibrational mode (see Fig. 1). In operation, the sensor is rotated about its torsionally resonant axis at an angular rate ω which is exactly one-half the torsional resonant frequency. When a gravitational field is present, the differential forces on the sensor resulting from the gradients of the gravitational field excite the sensor structure at twice the rotation frequency.[2] The differential torque ΔT between the sensor arms at the doubled frequency is coupled into the central torsional flexure. The strains in this flexure are sensed with piezoelectric strain transducers which provide an electrical output.

Since the rotating gravity gradiometer moves through the gravity gradient field and obtains a continuous sample of the field components in its plane of rotation, the output of the gradiometer contains two independent measurements of certain components of the gravity gradient field tensor. The two measurements appear as two sinusoidal signals in quadrature

$$\Delta T = \frac{m\ell}{4}^2 \left[(\Gamma_{xx} - \Gamma_{yy}) \cos 2\omega t + 2\Gamma_{xy} \sin 2\omega t \right] . \qquad (1)$$

One output is a measurement of the difference between two of the diagonal components and the other measures the cross product component of the gravity gradient tensor in the coordinate frame of the sensor. Alternatively, the output can be represented as an amplitude which measures the difference between the principal components of the gradient tensor and a phase angle that represents the orientation of the reference frame of the principal gradients to the sensor reference frame.

$$\Delta T = \frac{m\ell}{4}^2 (\Gamma_{\xi\xi} - \Gamma_{\eta\eta}) \cos (2 \quad 2\alpha) . \qquad (2)$$

For the simple example shown in Fig. , the differential torque induced by the mass M at the distance R is

$$\Delta T = \frac{3}{4} \frac{GM\, m\ell}{R^3}^2 \cos 2\omega t . \qquad (3)$$

The angular resonant deflection between the two quadrupoles of the sensor rotating at one-half its torsional resonant frequency with an associated quality factor Q is therefore

$$\phi = \frac{2\,\Delta T Q}{I\,(2\omega)^2} = 3\,\frac{GM}{R^3}\,\frac{Q}{(2\omega)^2} \sin 2\omega t , \qquad (4)$$

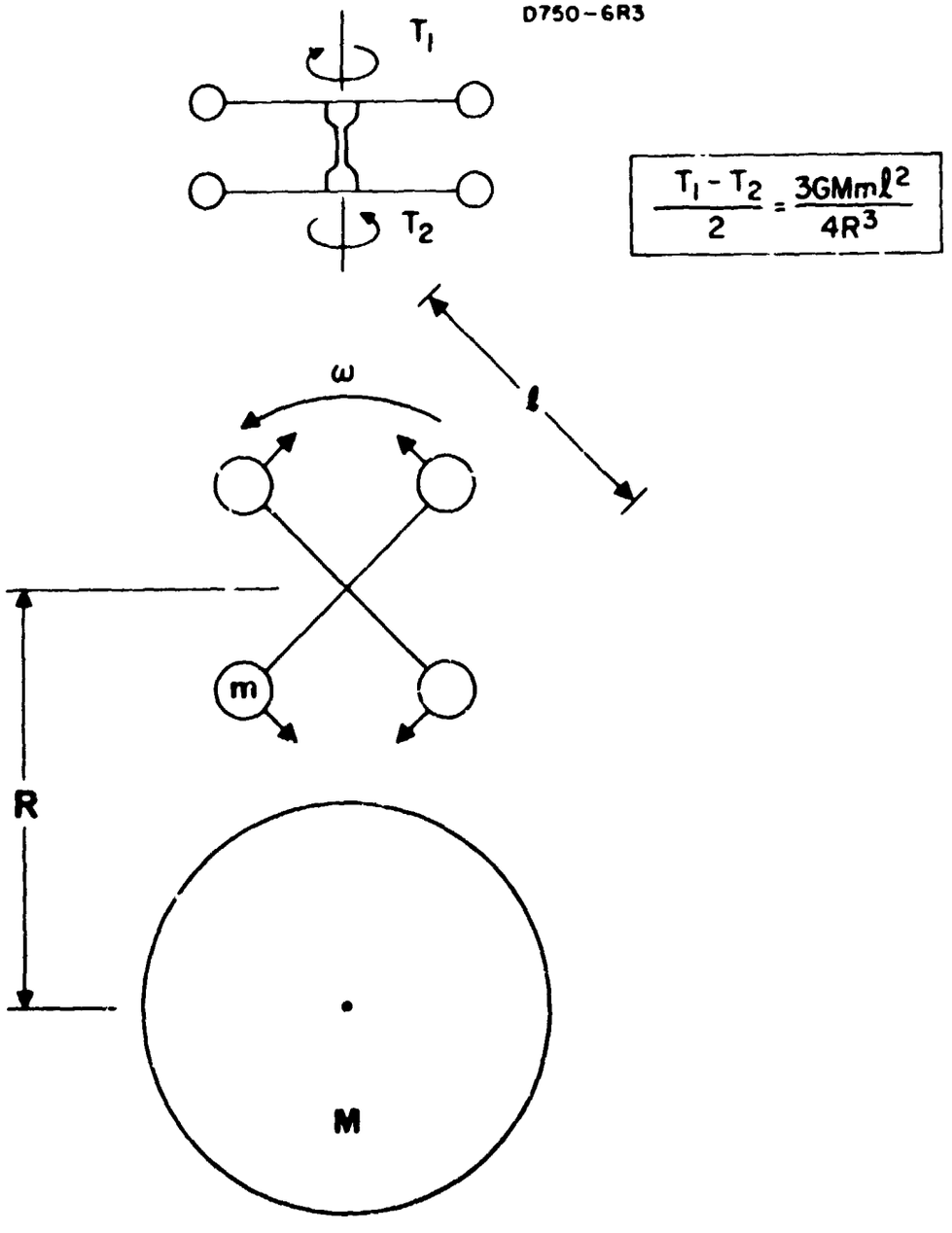

Fig. 1. Method of Operation of Torsional Gravity Gradiometer.

where $I = ml^2/2$ is the quadrupole inertia. The angle θ is extremely small. Surface gradients produced by the earth will produce angular deflections of $\theta \sim 3 \times 10^{-6}$ rad in typical orbital torsional sensor designs, while useful threshold signals of 10^{-11} gal/cm (0.01 Eötvös unit (E.U.)) produce angular responses of 10^{-11} rad.

Although these deflections are small, they are easily measured by utilizing piezoelectric strain transducers attached to the torsional flexure.[1] The threshold deflections of 10^{-11} rad produce voltage outputs of 10^{-8} V from typical transducers. These voltage levels are easily measured by modern amplifiers.

Present Development Status

The ultimate objective of our work on rotating gravitational gradient sensors is the development of a class of rugged sensors of high sensitivity and precision which may be used to measure accurately and rapidly the details of the gravity field during airborne or orbital surveys and as a component in an inertial guidance system to remove the effects of gravitational anomalies on the ultimate system performance.

The objectives of the research program initiated in 1962 was to investigate the engineering feasibility of the basic concept, to develop sensor structures which would operate a high sensitivity level both in free fall and in 1 G environment, to measure the sensor's sensitivity to gravitational fields, and to investigate the sources of noise produced by the rotation of the sensor. A torsionally flexible structure utilizing piezoelectric readout was found to be a suitable design and offers a significant improvement over other possible gradiometer designs. It has demonstrated the capability of being operated in an earthbound laboratory environment (see Fig. 2) while still maintaining a high sensitivity and low signal-to-noise ratio. The present noise level of this sensor is ±1 E.U. (1σ at an integration time of 10 sec) and is limited by background noise in the laboratory. Using this sensor, we recently carried out an experimental simulation where we measured in real time gravity gradient fields that had exactly the same magnitude and time variation as the gravity gradient signals that would be expected from an orbiting vehicle around the moon.[1]

Figure 3 shows the output of the sensor during the passage at 60 cm distance of two masses spaced 62 cm apart. The first mass was 14.4 kg and the second was 15.5 kg. The two gravity signals are resolved and it is possible to see the magnitude difference in the two masses. The three curves are the total signal amplitude, the sine output, and the cosine output. The dotted lines are the predicted outputs from the computer simulation.

At the present time, the development effort on the sensor is heading in two different directions. One program, sponsored by the Air Force, is for the development of an airborne gravity gradient measurement system. The major thrust of the development effort is to design a suitable hard mounted bearing and drive system that will spin a compact sensor (10 cm diameter) at the desired speed without introducing excessive amounts of noise and to design a

Fig. 2. Rotating Gravity Gradiometer Suspension and Drive System and Test Masses.

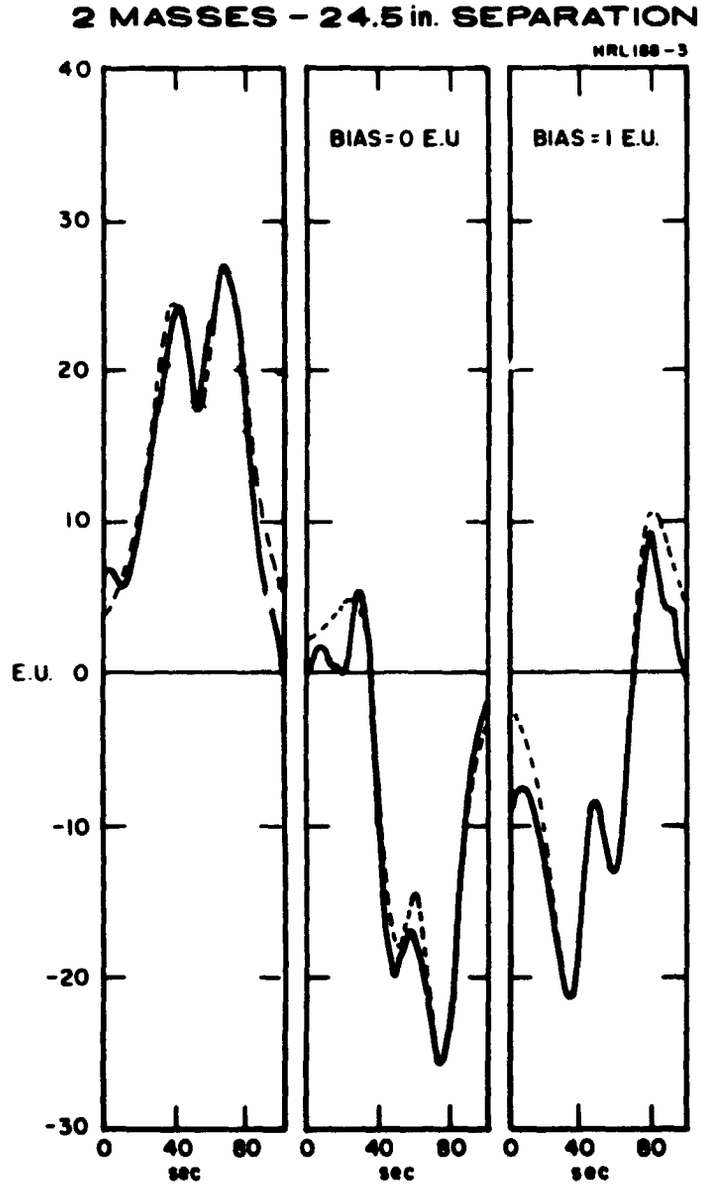

Fig. 3. Sensor Amplitude, Sine and Cosine Response to Flyby of 14.4 kg and 15.5 kg Masses at 24 in. Miss Distance.

vibration and rotation isolation system that will isolate the sensor system from the aircraft noise and motion. The noise level of our present system (see Fig. 4) is about 6 E.U. with a 30 sec integration time.[3] The goal of the program is to develop a gradiometer system capable of measuring gravitational gradients at the 1 E.U. level with a 10 sec integration time on a moving base, such as an aircraft or submarine. A similar design is being considered for deep space planetary and CARD missions.[4]

The other program, under NASA sponsorship through the AAFE program, is for the design of an earth orbiting gravity gradient measurement system.[5] For the orbital case, the optimum method is to fabricate a sensor with a relatively low resonant frequency (2 to 8 Hz) and very long arms, attach it directly to the spacecraft and spin the spacecraft itself at the desired spin speed (1 to 4 rev/sec). This mode of operation has two significant advantages. There are no bearing noise problems that are the primary source of difficulty in earthbound operation, and most important, since the spacecraft is rotating along with the sensor, the gravity gradient field of the spacecraft is stationary in the frame of reference of the sensor and the sensor does not sense the gravity field of the spacecraft, only the gravity gradient field of the earth. We have fabricated some prototype designs (Fig. 5) optimized for lunar orbital use and calibrated the sensor with ac gravitational fields from a dynamic gravity field generator. The measured noise level[6] of 5 E.U. at 30 sec was limited not by the sensor but by the difficulty of isolating room vibrations at this low frequency (2 Hz). The objective of the AAFE program is to develop a sensor system optimized for earth orbit applications and capable of measuring gravitational gradients at the 0.01 E.U. level with a 35 sec integration time.

Gradiometer Noise Limit

The fundamental sensitivity of any sensor is determined by the thermal noise limitation. For the past ten years, we have been developing gravitational sensors working near their thermal noise limit.[7,8] Because this basic limit is dependent upon energy considerations, its calculation depends only upon very general parameters of the sensor, such as its temperature, mass, effective length, and time of integration. The results can then be applied to all gravity gradient sensors, regardless of their detailed design.

In our torsional sensor the thermal signal-to-noise energy ratio is obtained by comparing the gravitational gradient signal energy in each of the two orthogonal outputs of the sensor to the 1/2 kT of thermal noise in each of the two degrees of freedom of the sensor.

The minimum gradient that can be measured in each output of a thermally limited sensor with an effective arm radius r and total effective mass m, is:

$$\Gamma = \frac{GM}{R^3} = \frac{4}{\eta \tau r} \left(\frac{kT}{m}\right)^{1/2} , \qquad (5)$$

M7447

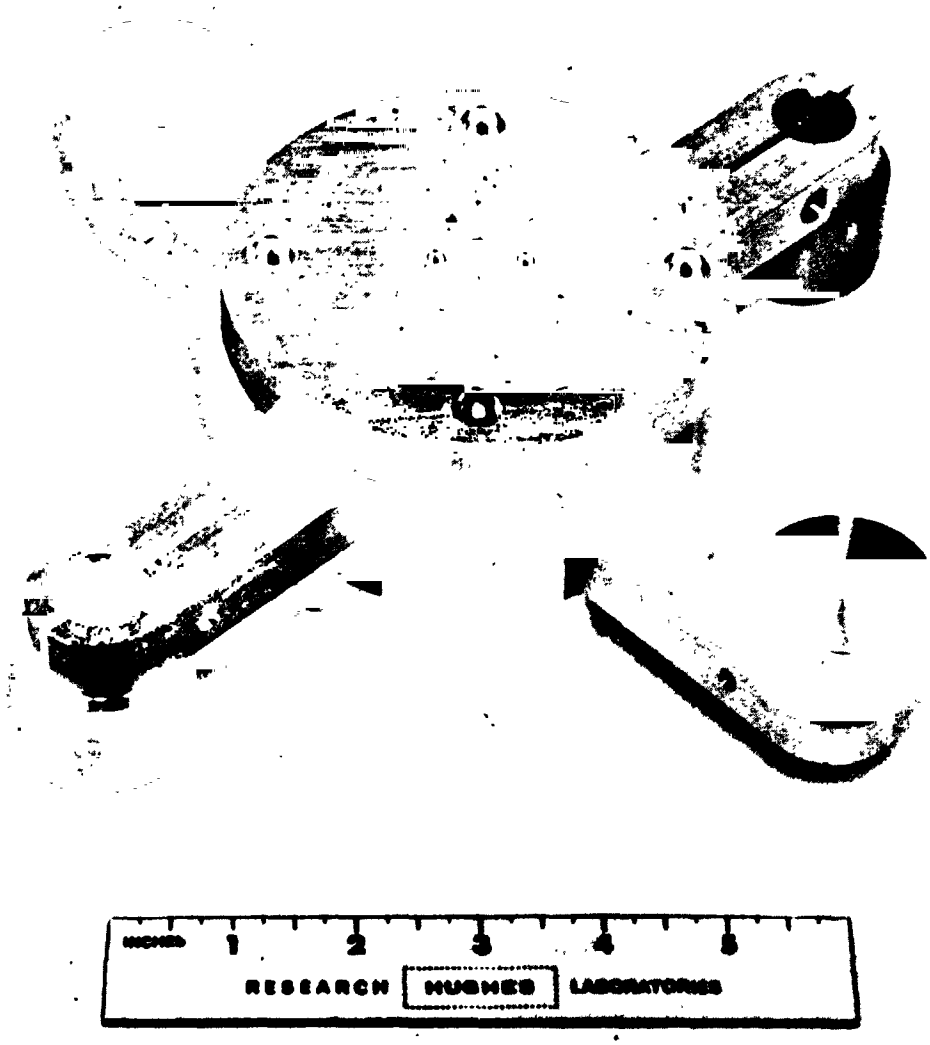

Fig. 5. 2 Hz Sensor Design for Lunar Orbiter.

where $\tau = 2Q/\omega$ is the 1/e time constant of the sensor and η is the ratio of the quadrupole inertia to the total inertia of each arm.

For what might be the desired sensor for earth geodesy,[5] one with a total arm mass of 8 kg (2 kg each), an $\eta = 0.95$, and an arm radius of 40 cm, the thermal noise equation gives us a kT limit of 0.007 E.U. for a 35 sec integration time. We should be able to obtain a measured noise very close to this thermal noise limit with a properly designed structure and electronic matching circuit.[5, 7, 8]

EARTH GRAVITY MEASUREMENTS WITH ORBITING GRADIOMETERS

Harmonic Representation of the Earth's Geoid

An objective of geodesy is to determine the variations of the earth's gravitational potential, which can be expressed in terms of spherical harmonics:

$$V = \frac{GM}{r}\left[1 + \sum_{n=2}^{\infty}\left(\frac{a}{r}\right)^{n}\sum_{m=0}^{\infty} P_{nm}(\sin\phi)\{C_{nm}\cos m\lambda + S_{nm}\sin m\lambda\}\right]$$

where a is the mean radius of the earth, P_{nm} is the normalized Legendre polynomial, C_{nm} and S_{nm} are the coefficients of the harmonic terms, and (r, ϕ, λ) are the coordinate positions of the instrument.

In the present satellite geodesy programs, orbital perturbation methods of obtaining the gravitational potential harmonics have led to the determination of the harmonics through the fourteenth degree and order.[9] In theory, this technique can be extended to obtain all higher orders of the gravitational potential; however, it is anticipated that it will be difficult to obtain the higher order components.[10]

The advantage of gradiometer techniques in obtaining the higher order harmonics of the earth's gravitational field is straightforward. Terms with increasing n correspond to small scale features on or near the surface. Although the contribution of these harmonic components to the gravitational potential is quite small, their contribution to the gravitational force gradient at a point above them is a substantial fraction of the gravitational gradient of the entire earth.

A typical term in the gravitational potential

$$V_{nm} = \frac{GM}{a}\left(\frac{a}{r}\right)^{n+1} P_{nm}(\sin\phi)\, C_{nm}\cos m\lambda \qquad (6)$$

gives rise to a radial gravity of

$$g_r = \frac{\partial V}{\partial r} = (n+1)\frac{GM}{a^2}\left(\frac{a}{r}\right)^{n+2} P_{nm}\, C_{nm}\cos m\lambda \qquad (7)$$

and a radial gravity gradient of

$$\Gamma_{rr} = \frac{\partial^2 V}{\partial r^2} = (n+1)(n+2)\frac{GM}{a^3}\left(\frac{a}{r}\right)^{n+3} P_{nm}\, C_{nm}\cos m\lambda \ . \qquad (8)$$

For the radial doppler velocity we take the time integral of the radial acceleration

$$\Delta v_r = \int g_r dt = \frac{n+1}{n} \frac{GM}{av} \left(\frac{a}{r}\right)^{n+2} P_{nm} C_{nm} \sin m\lambda \qquad (9)$$

where we have used the fact that the maximum spatial periodic variation (m=n) has a time variation due to the orbital velocity v given by

$$\cos_{max} m\lambda = \cos n\lambda = \cos\left(n\frac{x}{a}\right) = \cos\left(\frac{nv}{a} t\right) \quad . \qquad (10)$$

If we assume that the strength of the harmonic components follows the statistical law[11] $\bar{S}_{nm} \sim \bar{C}_{nm} \sim 10^{-5}/n^2$, and that (2n+1) terms contribute to each order, we can calculate the doppler velocity, gravity and gravity gradient as a function of the harmonic order. These are plotted in Fig. 6 for 250 km altitude.

The doppler velocity data in Fig. 6 are correct, although they differ by two orders of magnitude from what would be calculated from Fig. 5-7, page 5-28 of the Williamstown report,[10] as presently published. In recent correspondence, William M. Kaula has brought attention to the fact that the right hand ordinate of Fig. 5-7 in the Williamstown report should read 10^{-2} mm/sec rather than mm/sec.

Figure 6 gives the rms strength of the signals at each harmonic order averaged over the entire orbit. If we assume a maximum sensor integration time of about 30 sec, which is determined by the time it takes the measurement system to pass through one resolution element (250 km), then there will be approximately 170 independent samples of each of the higher harmonic orders per orbit. The accuracy of determination of the rms harmonic component would therefore be the measurement system sensitivity for the 30 sec interval divided by 13, the square root of the number of samples per orbit. Thus, a 0.01 E.U. gradiometer system would be capable of better than an 8% measurement of the higher orders out to degree 75.

Figure 6 indicates that if satellite-to-satellite doppler tracking techniques attain their anticipated sensitivity level of 0.05 mm/sec at 30 sec, doppler tracking will be able to extract gravity data up to degree 50, and if a gravity gradiometer with an 0.01 E.U. sensitivity at 30 sec can be flown it will contribute significant information out to degree 75. The comparative signal-to-noise of the two techniques crosses over at degree 35. We thus see that the two techniques are complementary rather than competitive since below degree 35 doppler tracking has a better signal level while above degree 35 the gradiometer gives better data.

The average strength of the higher order gravity variations predicted in Fig. 6 and Fig. 5-7 of the Williamstown report use a statistical model based on the autocovariance analysis of a large variety of samples of gravimetry,[12] and are estimated to be correct within ±30%. A statistical model assumes that the phases of the various harmonics are not correlated, whereas

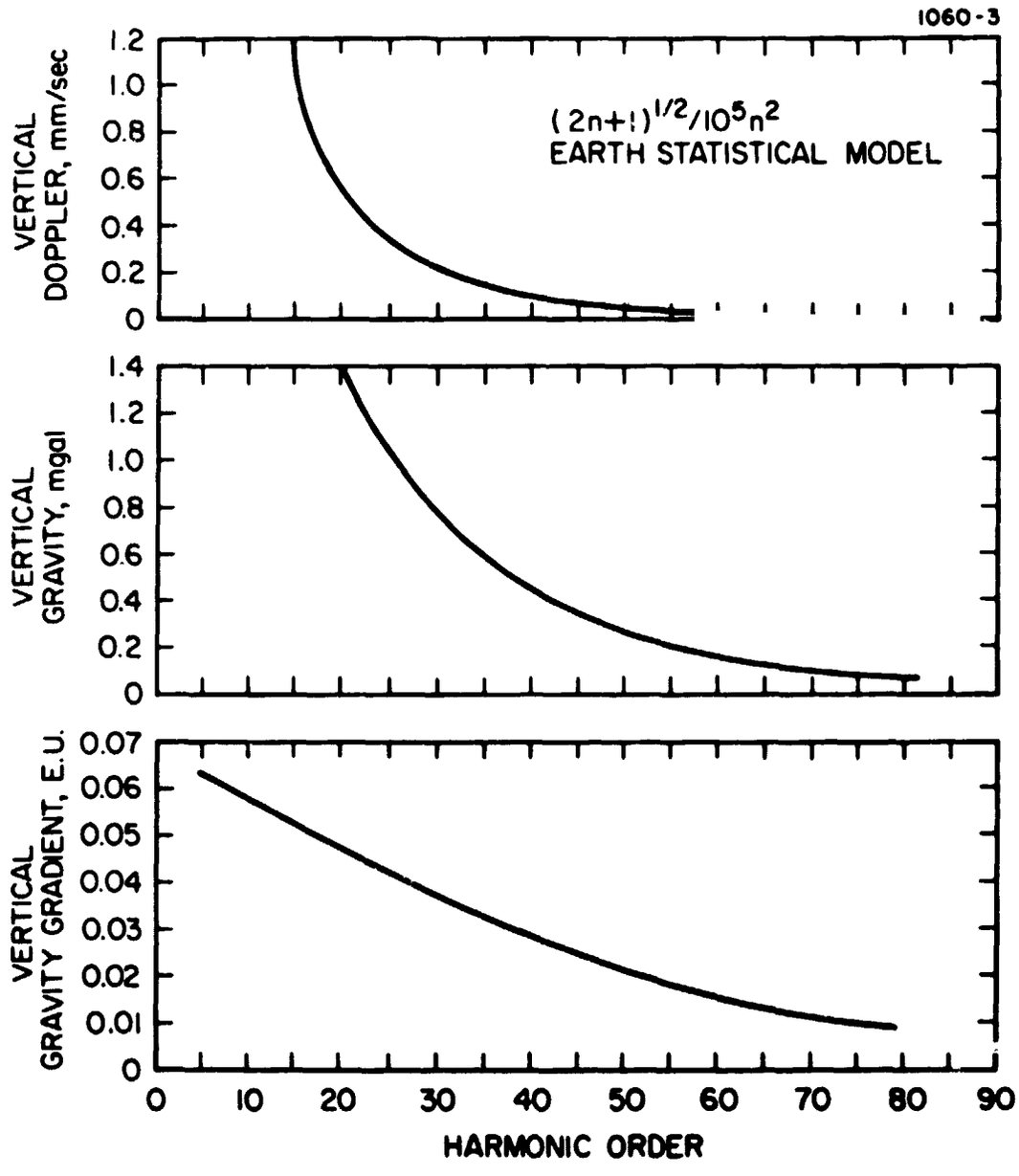

Fig. 6. Vertical Doppler, Velocity Gravity and Gravity Gradient at 250 km Orbit.

we might expect some correlation in phases to occur at the position of significant geophysical anomalies, such as mountain ranges. To obtain some feeling for this possibility, we have also looked at the gravity fields to be expected at altitude for reasonable mass anomalies on the surface.

Localized Anomalies

Although a statistical analysis of the gravity field contributions of the various harmonic orders can give us a general idea of the rms signal strengths averaged over an orbit, it does not give us a good picture of the time history of the signals expected over specific anomalies where the phases of the harmonic orders combine to produce an impulse type response. In an attempt to get a better feeling of the signals to be expected from localized anomalies, a massive disc mass model was used to generate gravity data and the signals expected for both a single disc and a periodic array of discs were calculated.

For the single disc model we chose a disc radius of 150 km or disc diameter of 300 km. The disc mass was chosen so that the gravity at the surface was 10 mgal. A plot of the results is shown in Fig. 7, which indicates that a disc with diameter 300 km, thickness 15 km, mass of 1.7×10^{16} kg and density difference of 0.016 gm/cc will create at an altitude of 250 km the following signals:

- Vertical gravity of 1.5 mgal peak
- Vertical gravity gradient variation of 0.11 E.U.
- Vertical doppler velocity shift of 1.0 mm/sec.

The analysis of a single disc is, however, not a close analogy to the periodic variation in the gravity field that is implied by the usual harmonic representation of the field. The disc model analysis was therefore expanded to a calculation of the signals expected over a periodic array of positive and negative disc anomalies. The mass (positive or negative) was assumed the same as in the single disc analysis. The curves in Fig. 8 are extrapolations of the data from the center portion of the disc array to eliminate end effects. The periodic signals were

- Vertical gravity ±0.65 mgal
- Vertical gravity gradient ±0.1 E.U.
- Vertical doppler velocity shift ±0.08 mm/sec.

We notice that the gravity gradient magnitude is almost the same as for the single disc. This is because the gravity gradient signal, being the spatial derivative of the acceleration, has a sharp cutoff, and the signal from an adjacent disc of opposite mass acutally contributes slightly to the total signal. The magnitude of the periodic vertical gravity signal has decreased slightly from

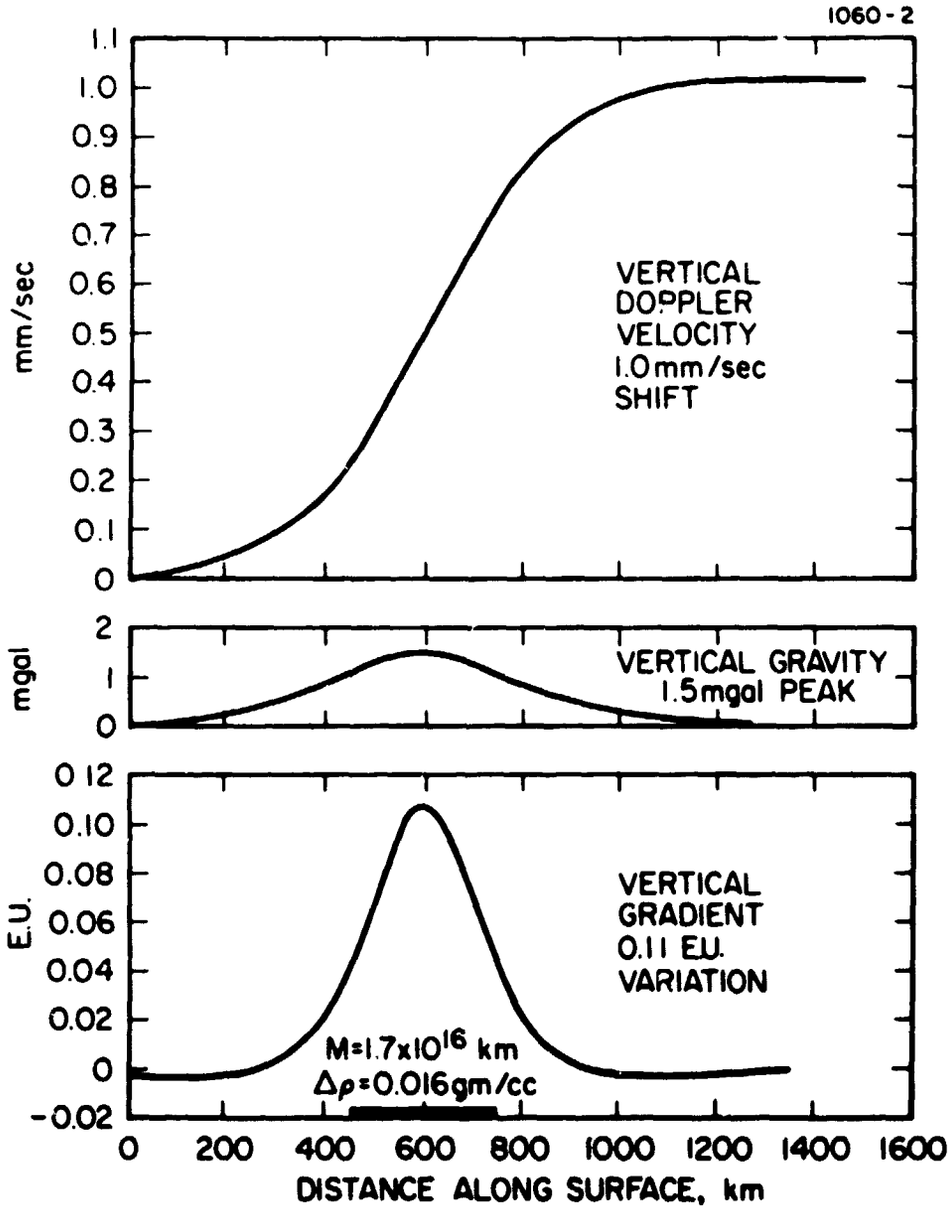

Fig. 7. Gravity Signals of Single 300 km Diameter Disc at 250 km Altitude.

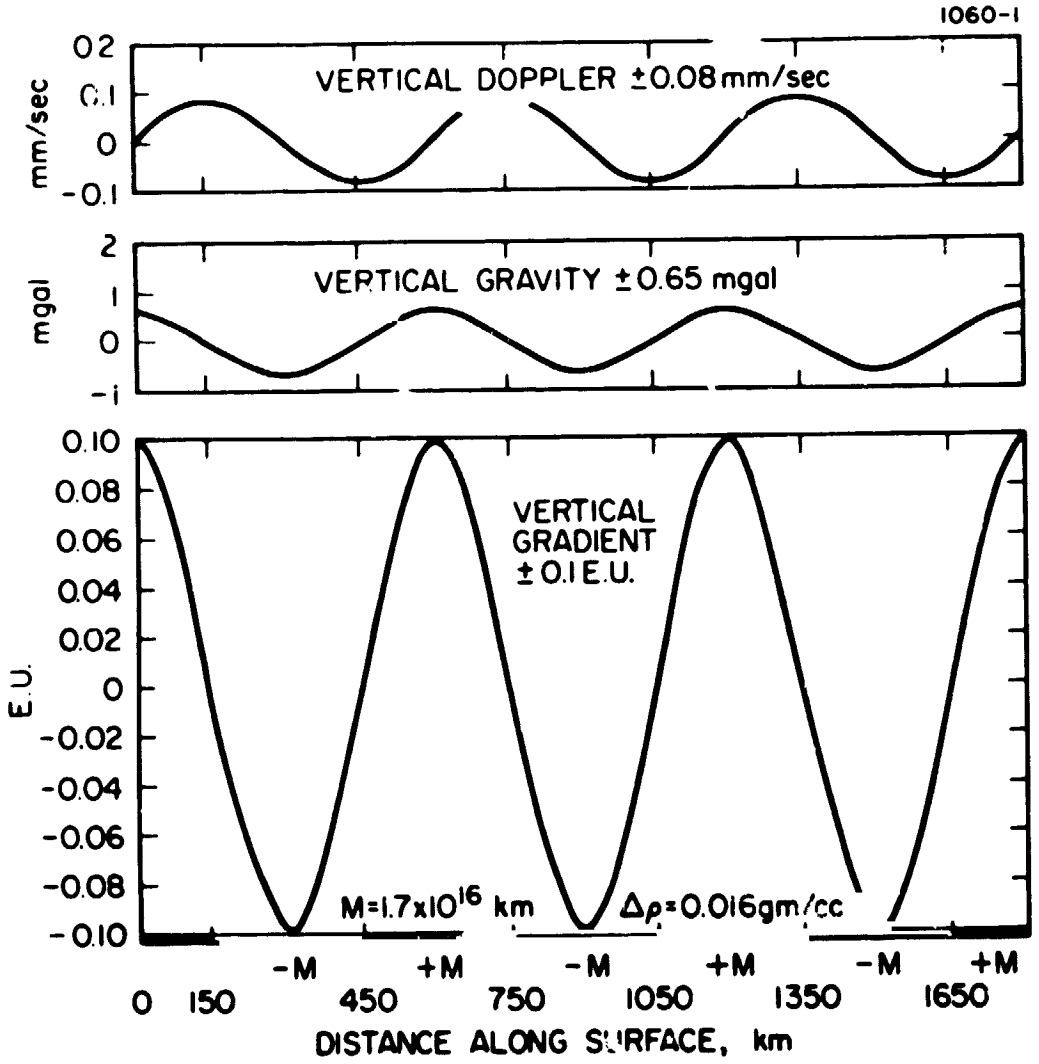

Fig. 8. Gravity Signals at 250 km Altitude from Periodic Disc Array.

the single disc signal. The broad signature of the vertical gravity signal causes signals from adjacent discs of opposite sign to partially cancel.

Finally, notice the very large decrease, over an order of magnitude, in the vertical doppler velocity signal from the single disc case to the periodic disc case. This is because the doppler velocity signal is the integral of the acceleration signal and the integration tends to smooth out the periodic variation that we are looking for.

MISSION AND DESIGN STUDIES

Introduction

We have found in our research that the design of a gravity gradiometer is often strongly dependent upon the particular mission and using vehicle. This is especially true for this application to earth geodesy. The size and operational parameters of the sensor are strongly determined by the orbital altitude and inclination, mission lifetime, and the requirements of geodesy. The sensor, in turn, has an effect on the spacecraft, especially the requirements for spin speed and attitude control. We have carried out some preliminary mission studies, and are beginning to define a set of mission, sensor and spacecraft parameters that are compatible with the overall mission objective of the accurate measurement of the earth's gravity field.

The presently envisioned mission would use a Scout with a 42 inch payload shroud to launch two orthogonally oriented, spin stabilized satellites into a 330 km circular polar orbit some 15-20 days before the vernal or autumnal equinox. Each satellite would carry an 8 kg, 80 cm diameter gradiometer with a sensitivity of 0.01 E.U. at 35 sec integration time. The orbital lifetime would be short, but during that time we would obtain at least two complete maps of the vertical gradient and the horizontal gradients, both along and across the orbital track, with a resolution of about 270 km (540 km wavelength or degree 75).

Orbital Parameters

To map the higher order harmonics of the earth's gravity field, it would be desirable to have the measurements take place at as low an orbit as possible. Because of the mathematical characteristics of the potential field, the resolution of any gravity measurement at altitude is roughly equivalent to the altitude. This is because the field strength of the gravity contributions due to the higher orders begins to fall off exponentially with altitude when the half wavelength becomes less than the altitude. However, a low orbit has a very short lifetime due to atmospheric drag, and a short lifetime makes it difficult to obtain the complete coverage of the earth that is also desired.

What is needed is a low orbit with orbital parameters such that the orbital tracks interleave so complete coverage is obtained in a period shorter than the orbital lifetime, and where the track spacing is matched to the swath width (equal to the altitude). It turns out that there does exist a set of orbital parameters that fits these requirements fairly well. At an orbital altitude of 270 km, there exists what is called an "integer orbit."[13,14] The orbital track repeats upon itself after exactly 16 orbits. This can be a polar orbit, with 16 orbits per sidereal day or a sun synchronous orbit (at a slightly different altitude and inclination) with 16 orbits per solar day. If the altitude is slightly higher or lower, then the orbital track drifts so that the 16th orbit is displaced to one side or the other of the first track. These offset orbits finally begin to repeat after a number of days when the drift has caused the satellite track to overlap the second ground track. There are two of these orbits that are of interest to us. They repeat after about 5 days, and their track spacing is

approximately equal to the altitude. One is a polar orbit at about 320 km which repeats after 79 orbits and the other is a polar orbit with altitude of 220 km which repeats after 81 orbits. The track spacing between the half arcs for both orbits is approximately 250 km, so that there is a good match between the track spacing and the swath width.

In reality, the orbital altitudes will decay due to drag, so that these simple orbital path models will not be followed exactly. We presently envisage launching into a 330 km polar orbit and allowing the altitude to decay through these two altitudes where we get overlapping coverage. We have chosen a polar orbit rather than a sun synchronous orbit in order to obtain full coverage of the earth and to provide for calibration points twice per orbit at the two poles. The orbital lifetime estimated for the mission is somewhere around 30-50 days. The time spent near 320 km would be long enough to obtain good coverage of the earth at that resolution (640 km wavelength or degree 62). As the altitude decreases, we will get better and better resolution. We should get a substantial amount of coverage at around 220 km altitude with excellent resolution (440 km wavelength or degree 90) but we will lose some coverage due to the rapidly decreasing altitude and the fact that the track spacing at the equator of 250 km is slightly larger than the sensor resolution.

Non-Eclipse Orbits

It would be desirable to launch the gradiometer satellites into a polar orbit of the earth which will not cause the satellites to be eclipsed by the earth throughout the mission. The advantages of the non-eclipse orbit are the weight reduction and reliability increase available by elimination of batteries for electrical power during the eclipse portion of the flight. Also, the thermal control system required for the sensor would only have to contend with one state of thermal equilibrium rather than cyling between two. We have investigated possible non-eclipse orbits and find that even despite the relatively low orbits under considerations it is possible to achieve non-eclipse periods several times longer than the estimated lifetimes for these orbits. To attain these orbits only requires that a launch window constraint be placed on the mission. The satellite is launched 15-20 days before either the vernal or autumnal equinox (21 May or 21 Sept) into a polar orbit chosen such that on the day of the equinox, the orbital plane coincides with the terminator plane. At this point in time, the ecliptic poles and the celestial poles of the earth are all in the terminator plane. The slow rotation of the terminator plane about the ecliptic poles will cause a drift between the terminator plane and the orbital plane ($\sim 1^{\circ}$/day). However, simple calculations show that with this choice of launch time and orientation, it is possible to have non-eclipse periods in excess of 30 days even for orbital altitudes below 250 km[15].

Non-eclipse orbits could also be chosen using sun-synchronous orbits lying near the terminator plane, and then the non-eclipse period is theoretically infinite. However, the above shows that with this minor constraint on launch time we can achieve the advantages of a non-eclipse orbit while keeping the self-calibration and full coverage aspects of the polar orbit.

Launch Vehicle and Spacecraft Configuration

Because of the relatively low field strengths estimated for the higher order harmonics of the earth's field, it is necessary to make the sensor as large as possible. The arm length of the sensor is primarily determined by the maximum radius obtainable in the spacecraft, which in turn is determined by the payload envelope of the launch vehicle. If we limit ouselves to a Scout launch vehicle in o.der to keep costs down and reliability up, we can use a number of launch shroud configurations that have been developed for this vehicle. One of the largest in diameter is the 42 inch diameter shroud mentioned in the Scout users handbook. The allowable payload diameter for this shroud is 96.5 cm (36 in). The cylindrical portion of the payload envelope with this diameter is 84 cm (33 in) long, which would allow space for two cylindrical spacecraft 96 cm diameter by 42 cm thick. A very preliminary spacecraft design of this size is shown in Figs. 9 and 10. The sensor arm length with this spacecraft configuration would be about 40 cm.

The front part of the payload envelope could be used for a spin-up and attitude control system which would be used to insert the two spacecraft into orbit with the proper attitude and spin speed. After the payload had attained orbit, the spin control mechanism would increase the satellite spin speed to the desired rate (about 240 rpm) and orient the spin along the orbital track. After release of one spacecraft, the jets would be used to torque the other spacecraft so that its spin vector was perpendicular to the first spacecraft. With the two spacecraft in this relative orientation, one would be measuring the vertical gravity gradient and the cross-track horizontal gradient, while the other would be measuring the along-track horizontal gradient and a redundant measurement of the cross-track gradient. After 1/4 of an orbit, the orientation of the two satellite spin axes relative to the orbital track would change, and the data output from the two sensors would be interchanged. Although this is a relatively complex mode of data collection, it does allow for the measurement of more components of the gravity gradient at the same time. Most importantly, this mode of operation allows us to obtain the cross-track gradient information which can be used to tie the data together across the orbital tracks. The cross-track gradient along one track can be used to predict the gravity field at the next track. This closure property of the data sets can be used to eliminate drift errors.

A simpler version of the experiment would be to launch a single satellite and to torque the spacecraft spin axis so that it lies in the plane of the orbit. The advantages of this mode of operation would be that the spin axis of the spacecraft would not change orientation with respect to the orbit and the drag torques would remain constant. In this orientation, the gradiometer would measure the difference between the vertical gradient and the along-track horizontal gradient and their orientation with respect to the local vertical.

Sensor Parameters

Most of the sensor parameters have been determined by the mission and spacecraft studies to date, although a few remain to be determined. The sensor

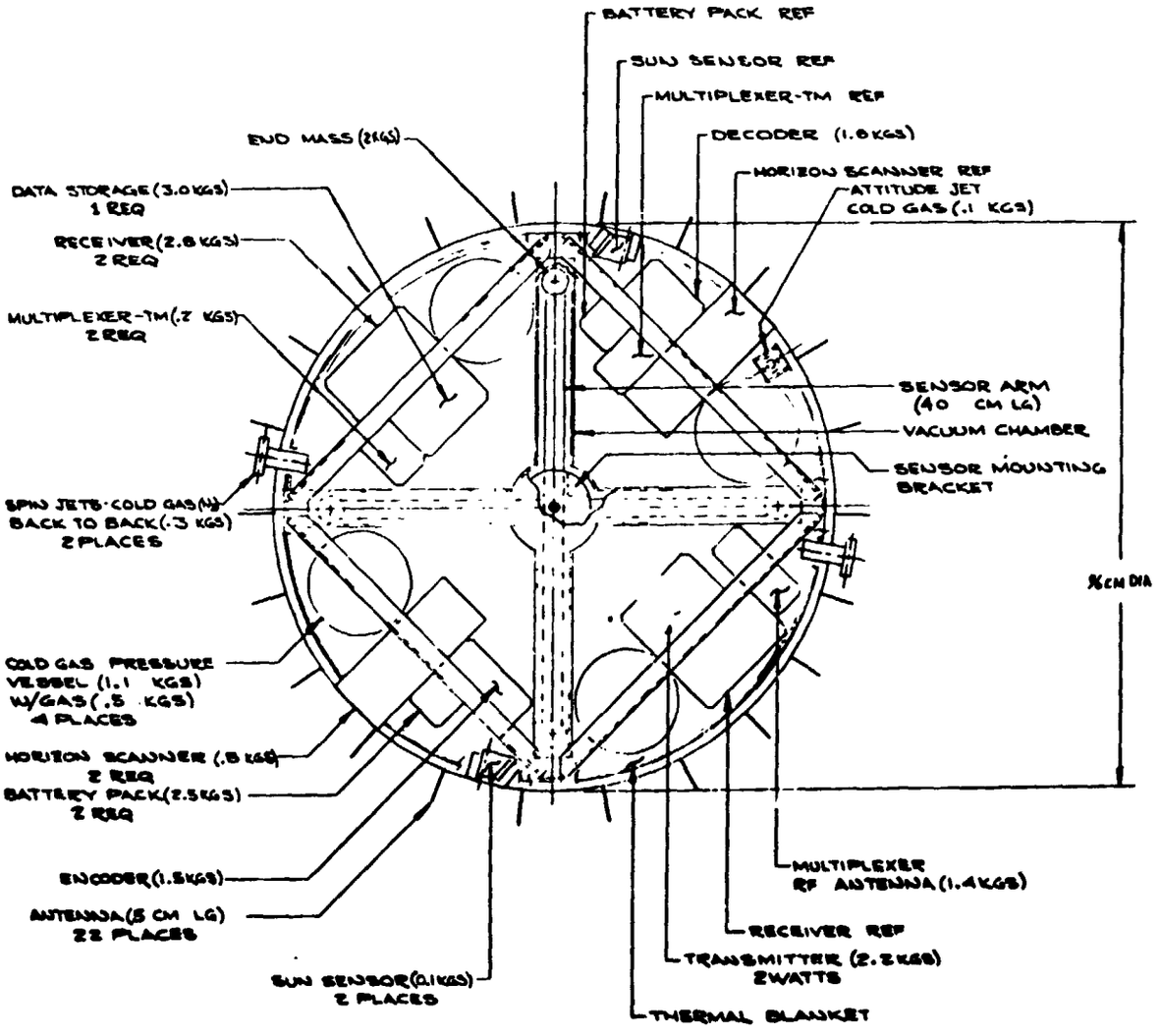

Fig. 9. Spacecraft Configuration for Earth Geodesy Experiment. (Plan View).

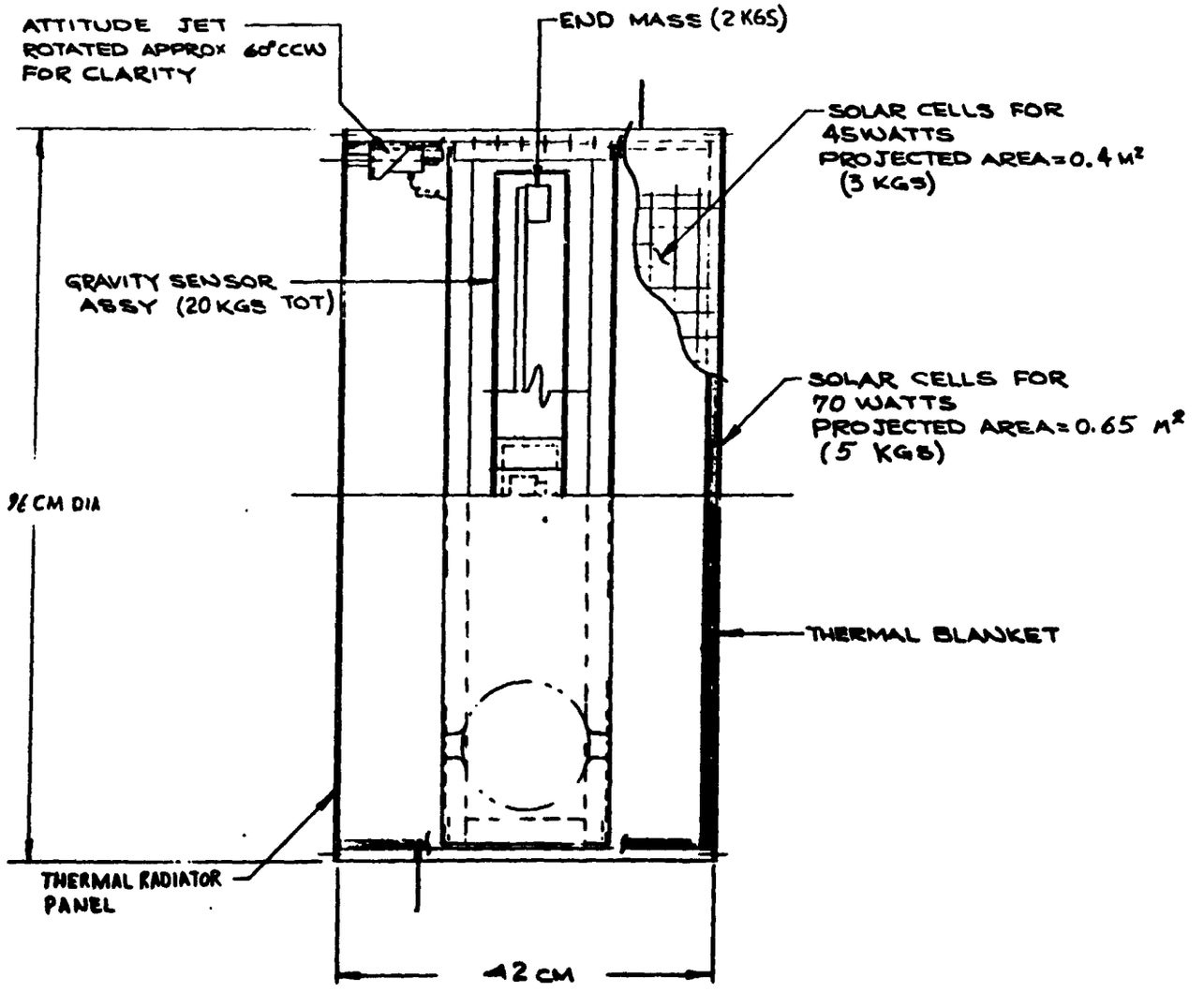

Fig. 10. Spacecraft Configuration for Earth Geodesy Experiment. (Side View).

arm length has been chosen at 40 cm radius (80 cm diameter) as the largest arm radius possible for the 96 cm spacecraft diameter, which in turn is dictated by the Scout payload envelope. The arm end masses have been chosen at 2 kg each as a reasonable weight for the size of the sensor and the payload capability of the Scout booster. The sensor time constant has been chosen at 35 sec by using the time required for the spacecraft to pass through one resolution element at the nominal altitude of 270 km and orbital velocity of 7.75 km/sec. This figure was chosen as a reasonable optimum between the 41 sec for 320 km altitude and the 29 sec for 220 km altitude. This sensor system time constant is the smoothing time that will be used in the sensor data preprocessing. The sensor output will be sampled more often than this (every 1-5 sec) to overcome digitalization noise, to prevent aliasing, and to pick up strong, short period signals due to dense localized anomalies.

The major sensor parameter that is yet to be determined is the sensor resonant frequency. We are presently completing a study of the interaction of the spacecraft dynamics with the sensor dynamics and the choice of the resonant frequency will probably be determined as a result of optimization studies carried out using this dynamics interaction study. It is suspected, however, that the frequency of the sensor will be about 8 Hz, which implies a spacecraft spin speed of 240 rpm (4 rps).

CONCLUSION

We have carried out preliminary studies of the application of the rotating gravity gradiometer to the measurement of the gravitational field of the earth from orbit. Although the studies are still in their preliminary phases, a sensor design and mission profile have emerged that show promise of substantially improving our knowledge of the earth's field. The studies will continue with the objective of determining the optimum sensor, spacecraft and mission parameters. These will then be used in the design, fabrication and test of a laboratory prototype to show that the instrumentation requirements are attainable.

ACKNOWLEDGMENTS

Although the responsibility for the content of this paper is mine, it contains contributions from many people. I especially want to thank C. C. Bell, P. M. LaHue and E. F. Mallove for their contributions and comments.

REFERENCES

1. Bell, C.C., R. L. Forward and H. P. Williams, "Simulated Terrain Mapping with the Rotating Gravity Gradiometer," Proc. Symposium on Dynamic Gravimetry, 115-128, Fort Worth, Texas, 1970.

2. Forward, R. L., "Rotating Gravitational and Inertial Sensors," Proc. AIAA Unmanned Spacecraft Meeting, 346-351, Los Angeles, California, 1965.

3. Rouse, D.W., "Continued Experimental Program – Hard Bearing Gradiometer Development Project" Research Report 446, Hughes Research Labs, Malibu, Calif., July 1971.

4. Forward, R.L., "Gravitational Field Measurements of Planetary Bodies with Gravity Gradient Instrumentation" AAS/AIAA Astrodynamics Specialists Conf., Ft. Lauderdale, Fla. 17-19 August 1971.

5. Forward, R.L., "Geodesy with Orbiting Gravity Gradiometers" Use of Artifical Satellites in Geodesy, AGU Monograph (to be published) of AGU Symposium 19-21 April 1971, Washington, D.C.

6. Bell, C.C. "Gravity Gradient Study" Final Report NAS 8-24788, Hughes Research Labs, Malibu, Calif., July 1971.

7. Forward, R.L. "Detectors for Dynamic Gravitational Fields," Ph. D. Thesis, Dept. of Physics, University of Maryland, 1965.

8. Forward, R.L., D. Berman and L. R. Miller, "Thermal Noise Limited Operation of Dynamic Gravitational Detectors," Bull. Am. Phys. Soc., 13, 513, 1968.

9. Rapp, R.H., "Gravitational Potential of the Earth Determined From a Combination of Satellite, Observed and Model Anomalies," J. Geophys. Res., 73, 6555-6562, 1968.

10. Kaula, W.M., Ed., The Terrestrial Environment, Solid-Earth and Ocean Physics, Williams College Study Report, NASA-ERC and MIT-Measurement Systems Laboratory, Cambridge, Mass., 1969.

11. Kaula, W.M., An Introduction to Planetary Physics, Wiley and Sons, New York, 1968.

12. Kaula, W.M. "Determination of the Earth's Gravitational Field," Rev. Geophysics, 1, 507-551, 1963.

13. Swenson, B.L., "Orbit Selection Considerations for Earth Resources Observations" NASA TM X-2156, Feb 1971.

14. King, J.C., "Swathing Patterns of Earth-Sensing Satellites and their Control by Orbit Selection and Modification", AAS Paper No. 71-353, AAS/AIAA Astrodynamics Specialists Conference 1971, Ft. Lauderdale, Florida 17-19 August 1971.

15. Mallove, E.F. (personal communication).

APPENDIX C

AN IMPROVED DYNAMIC ANALYSIS OF THE SECOND ORDER GRADIOMETER

HUGHES RESEARCH LABORATORIES
Malibu, California

a division of hughes aircraft company

Research Report 451

AN IMPROVED DYNAMIC ANALYSIS OF THE SECOND ORDER GRADIOMETER*

Eugene F. Mallove

February 1972

*This work was partially supported under Contract NAS 1-10945.

TABLE OF CONTENTS

LIST OF ILLUSTRATIONS

LIST OF TABLES

ABSTRACT

Prior analysis has established that error signals generated in a Hughes Rotating Gravity Gradiometer (RGG) mounted in a spin stabilized satellite can be classified as three types: angular rate errors, angular acceleration errors, and mass unbalance errors. Equations of motion are developed for a dynamic model of the sensor satellite system, and errors are evaluated using parameters developed for an Earth orbiting experiment. The errors are shown to produce inaccuracies less than 0.01 E.U. for such a system.

I. INTRODUCTION

The purpose of this report is to present a more general, improved version of the dynamic analysis of the Hughes rotating gravity gradiometer mounted in a spinning satellite in planetary orbit. The original Hughes analysis was published in Research Report 441, Dynamic Analysis of the Second Order Gradiometer, by R.W. Peterson, July 1971.

This analysis is preceded by a discussion and justification of the changes and generalizations stated in the Peterson report. It then completes a dynamic analysis with the new assumptions, makes some numerical assumptions about the sensor-satellite configuration, and develops numerical values for the errors generated by each of the dynamic sources.

Evaluations of aerodynamic torque and aerodynamic drag are also made and included in the analysis.

In conclusion, it is shown that dynamic interaction problems may be overcome with judicious control of sensor-satellite parameters.

II. TECHNICAL DISCUSSION

A. Point of Departure from Previous Analyses

Peterson's approach to the evaluation of the effects of satellite dynamics on the function of the gradiometer appears to be a very useful analytical road. However, some of the assumptions made are open to question.

I have accepted Peterson's basic model of the gradiometer, the assumption of infinite rigidity about the $\bar{k}$ axis, and the ignoring of cross products of inertia. But I must disagree with the form of the inertia tensors for each gradiometer arm which Peterson proposes.

Peterson has:

$$\bar{\bar{\Phi}}_1 = \begin{bmatrix} I_1 & 0 & 0 \\ 0 & 0 & 0 \\ 0 & 0 & I_1 \end{bmatrix} \quad \text{and} \quad \bar{\bar{\Phi}}_2 = \begin{bmatrix} 0 & 0 & 0 \\ 0 & I_2 & 0 \\ 0 & 0 & I_2 \end{bmatrix}$$

Equations (3) and (4), RR 441

This form of the principal inertia tensor assumes that each arm is dumbbell-like as in the following diagram:

1403-1

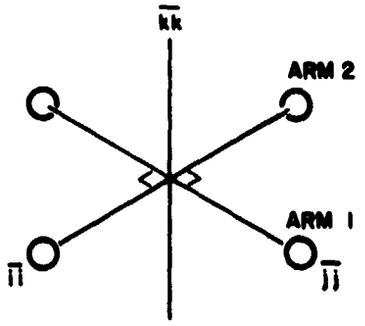

However, even the dumbbell model fails to be represented by Peterson's suggested tensors, because the principal moment about $\overline{jj}$ for Arm 1 is neglected, and the principal moment about $\overline{ii}$ for Arm 2 is ignored as well.

I suggest that the principal inertia tensors for the arms be kept as general as possible, in line with the diagram.

1403-2

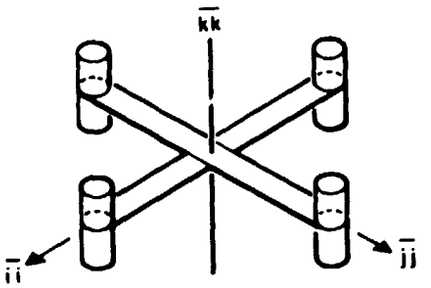

The general inertia tensors I have chosen keep general conformity with Peterson's notation but use superscripts to indicate principal axis:

$$\underline{\text{Arm 1}} \quad \bar{\bar{\Phi}}_1 = \begin{bmatrix} I_1^1 & 0 & 0 \\ 0 & I_1^2 & 0 \\ 0 & 0 & I_1^3 \end{bmatrix} \qquad \underline{\text{Arm 2}} \quad \bar{\bar{\Phi}}_2 = \begin{bmatrix} I_2^1 & 0 & 0 \\ 0 & I_2^2 & 0 \\ 0 & 0 & I_2^3 \end{bmatrix}$$

Peterson's* coefficients become:

$$\alpha_1 = \frac{D_1}{I_1^3} \qquad \beta_1^2 = \frac{K_1}{I_1^3}$$

$$\alpha_2 = \frac{D_2}{I_2^3} \qquad \beta_2^2 = \frac{K_2}{I_2^3}$$

$$\alpha_{12} = \frac{D_1 + D_2}{I_1^3 + I_2^3} \qquad \beta_{12}^2 = \frac{K_1 + K_2}{I_1^3 + I_2^3}$$

*RR 441, p. 6.

$$\frac{\omega_0}{Q} \simeq D_0 \left[\frac{I_1^3 + I_2^3}{I_1^3 I_2^3}\right] + \left[\frac{D_1 + D_2}{I_1^3 + I_2^3}\right]$$

$$\omega_0^2 = K_0 \left[\frac{I_1^3 + I_2^3}{I_1^3 I_2^3}\right] + \left[\frac{K_1 + K_2}{I_1^3 + I_2^3}\right]$$

Peterson's equivalent gradient signal (eq. (20)) becomes (with the new tensor forms):

$$\Gamma_e = \left(\frac{\omega_0^2}{Q}\right) \frac{(S^2 + \alpha_2 S + \beta_2^2)\left(\frac{M_1}{I_1^3}\right) - (S^2 + \alpha_1 S + \beta_1^2)\left(\frac{M_2}{I_2^3}\right)}{(S^2 + \alpha_{12} S + \beta_{12}^2)\left(S^2 + \frac{\omega_0}{Q} S + \omega_0^2\right)} \quad (1)$$

The most significant changes come in through the torques M_1 and M_2 which must now be rewritten.

Pecerson's eqs. (15) and (21) become:

$$\left.\begin{aligned} M_1 &= \bar{k} \cdot \bar{M}_{g1} + \bar{k} \cdot \bar{M}_{\mu 1} - [I_1^3 \dot{\omega}_k + I_1^2\, \omega_i \omega_j - I_1^1\, \omega_i \omega_j] \\ M_2 &= \bar{k} \cdot M_{g2} + \bar{k} \cdot \bar{M}_{\mu 2} - [I_2^3 \dot{\omega}_k + I_2^2\, \omega_i \omega_j - I_2^1\, \omega_i \omega_j] \end{aligned}\right\}$$

$$\frac{M_1}{I_1^3} = \Gamma_{ij}^1 + \Gamma_{\mu 1} - \dot{\omega}_k + \left[\frac{I_1^1 - I_1^2}{I_1^3}\right] \omega_i \omega_j$$

$$\frac{M_2}{I_2^3} = \Gamma_{ij}^2 + \Gamma_{\mu 2} - \dot{\omega}_k + \left[\frac{I_2^1 - I_2^2}{I_2^3}\right] \omega_i \omega_j$$

where

$$\Gamma^1_{ij} = \frac{\bar{k} \cdot \bar{M}_{g1}}{I_1^3} \qquad \Gamma_{\mu 1} = \frac{\bar{k} \cdot \bar{M}_{\mu 1}}{I_1^3}$$

$$\Gamma^2_{ij} = \frac{\bar{k} \cdot \bar{M}_{g2}}{I_2^3} \qquad \Gamma_{\mu 2} = \frac{\bar{k} \cdot \bar{M}_{\mu 2}}{I_2^3} \quad .$$

Let

$$\frac{I_1^1 - I_1^2}{I_1^3} = \gamma_1 \quad \text{and} \quad \frac{I_2^1 - I_2^2}{I_2^3} = \gamma_2 \quad .$$

Equation (2) is the resulting expression for Γ_e. This equation is analogous to Peterson's eq. (23). As in Peterson's analysis we take the mass unbalance terms to be of opposite sign for the maximum error (i.e., $\Gamma_{\mu 1} = -\Gamma_{\mu 2} = \Gamma_{\mu max}$). However, I see no reason to make $\Gamma^1_{ij} = -\Gamma^2_{ij}$ as in Peterson's analysis.

$$\Gamma_e = \frac{\frac{\omega_0^2}{Q}}{(s^2 + \alpha_{12}s + \beta_{12}^2)\left(s^2 + \frac{\omega_0}{Q}s + \omega_0^2\right)} \Bigg[\underbrace{\left[s^2(\gamma_2 - \gamma_1) + s(\alpha_1\gamma_2 - \alpha_2\gamma_1) + (\beta_1^2\gamma_2 - \beta_2^2\gamma_1)\right]\omega_i\omega_j}_{\text{Gravity Gradient Signal}}$$

$$+ \underbrace{\left[s^2(\gamma_1 - \gamma_2) + s(\alpha_2\gamma_1 - \alpha_1\gamma_2) + (\beta_2^2\gamma_1 - \beta_1^2\gamma_2)\right]\omega_i\omega_j}_{\text{Rotational Field Error}}$$

$$+ \underbrace{\left[s^2(2) + s(\alpha_2 + \alpha_1) + (\beta_2^2 + \beta_1^2)\right]\Gamma_{\mu max}}_{\text{Mass Unbalance Error}}$$

$$+ \underbrace{\left[(\alpha_1 - \alpha_2)s + (\beta_1^2 - \beta_2^2)\right]\dot{\omega}_k}_{\text{Angular Acceleration Error}} \Bigg] \qquad (2)$$

The three gradient error sources (as identified by Peterson) are:

- Rotational field $\omega_i\omega_j$
- Arm mass unbalance $\Gamma_{\mu max}$
- Sum mode mismatch $(\beta_1^2 - \beta_2^2)\dot{\omega}_k$ acting on angular acceleration input $\dot{\omega}_k^1$.

Only $\dot{\omega}_k$ affects Γ_e exactly as in Peterson's analysis. Note also that a dc error of the form $(\beta_2^2\gamma_1 - \beta_1^2\gamma_2)$ now appears as a result of having $\gamma_1 \neq 1$ and $\gamma_2 \neq 1$. There is still a potential large error due to excitation of frequency β_2.

I have followed Peterson's basic approach of estimating the satellite motions in the principal inertial axes of the satellite and then transferring the effects of these motions to the sensor in terms of the orientation of the sensor with respect to the principal inertial axes of the satellite and with respect to the center of mass of the satellite. But I have radically altered the expression for $\omega_i\omega_j$ and $\dot{\omega}_k$ found by Peterson by incorporating essential changes in the dynamical analysis. By far, the most fundamental change is to include the effect of the satellite's precession. I believe Peterson has inadvertently eliminated this effect by calling the nodal angle zero (an angle which he calls ϕ, p. 10 of RR 441). In order for the satellite to precess, the nodal angle, defined by the intersection of the satellite's equatorial plane with the (approximately) invariable momentum plane and by some arbitrary direction in the momentum plane, must be cyclic at the precession frequency.

Peterson also makes the assumption that a special relation holds among the satellite's principal moments, A, B, and C. He assumes $k_1 = k_2$ or $(C-B)/A = (C-A)/B$. The latter implies $C = A + B$, which seems quite arbitrary. Peterson later estimates $k_3 = (B-A)/C = 0.1$, which, with his former assumption, implies $A = 0.45$ and $B = 0.55$ if C is 1.0. I

have chosen instead to assume general principal moments, A, B, and C even though I feel that choosing A = B would be practical enough. I have chosen a precession frequency expression based on the coning angle θ, spin frequency ω_s, and principal inertial moments A, B, and C. Strictly speaking, a torque-free body exhibits uniform precession only if A = B (A and B are transverse moments of inertia). However, since the body is in this case not torque-free (due to aerodynamic torque) and A will probably nearly equal B, I have confidence in estimating a uniform precession. Essentially, I have considered a uniformly precessing satellite and superimposed aerodynamic torque on its motion. I have also considered the effect of the linear acceleration caused by aero-drag on the mass unbalance error terms. In this analysis, I have chosen to ignore the solar radiation torque, the magnetic torque, or the micrometeorite impact torque. With the exception of the magnetic torque, calculations would show that the latter torques would be less than the gravity gradient and the aerodynamic torques in near earth orbit. The following points summarize my changes to Peterson's dynamic analysis of gravity gradient effects:

- **Do not assume (C-B)/A = (C-A)/B.**
- **Assume general principal satellite moments C > B > A.**
- **Include effect of aerodynamic torque on spin: M_z = aerodynamic torque.**
- **Include satellite precession.**
- **Change to conventional Euler angle notation.**
- **Include linear acceleration from aerodynamic drag.**

B. Dynamic Analysis

1. General Equations

The local orbital coordinates are X, Y, and Z; Y aligned with local vertical, Z normal to orbit plane, and X tangent orbit, as illustrated in Fig. 1.

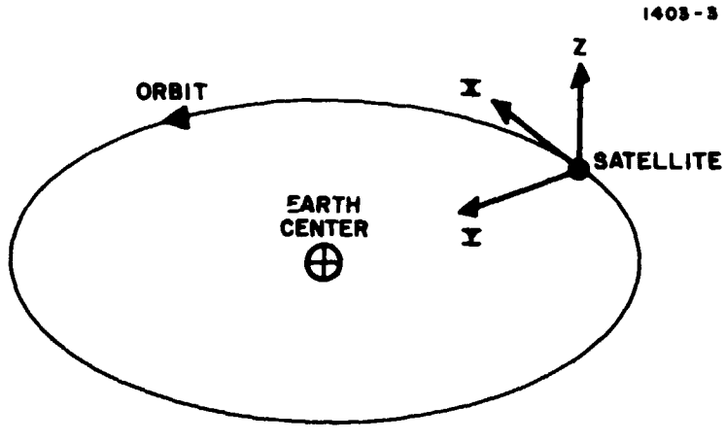

Fig. 1. Local Orbital Path Coordinates.

The principal axes of the satellite are x, y, and z which are related to the approximately inertial space frame axes X, Y, and Z by the Euler angles ψ, θ, and ϕ. The geometrical relationship of these angles and the axes is shown in Fig. 2.

The spin of the satellite, which is approximately constant at $\dot{\omega}_s$, is about the z principal axis and describes the angular motion $\dot{\phi}$. The Z axis is not only normal to the orbit plane but describes the constant direction of the satellite angular momentum vector for torque-free motion. The angle θ is the coning angle of the satellite precession. For torque-free motion, $\dot{\theta} = 0$. The angle ψ describes the satellite's precession; $\dot{\psi}$ is the precession frequency. (Note: Peterson calls ψ, ϕ and then considers $\phi = 0$, implying no precessional motion.)

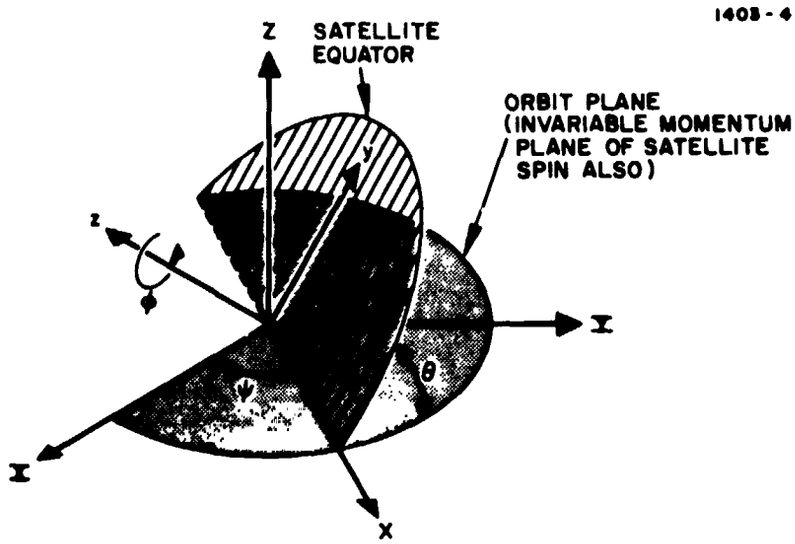

Fig. 2. Euler Angle Relationship of Satellite to Inertial Space Coordinates.

The standard transformation between the space axes and the principal inertia axes is:

$$\begin{bmatrix} X \\ Y \\ Z \end{bmatrix} = \begin{bmatrix} (\cos\phi\cos\psi - \sin\phi\cos\theta\sin\psi) & (-\sin\phi\cos\psi - \sin\psi\cos\theta\cos\phi) & (\sin\theta\cos\psi) \\ (\cos\phi\sin\psi + \sin\phi\cos\theta\cos\psi) & (-\sin\phi\sin\psi + \cos\phi\cos\theta\cos\psi) & (-\sin\theta\cos\psi) \\ (\sin\theta\sin\phi) & (\sin\theta\cos\phi) & (\cos\theta) \end{bmatrix} \begin{bmatrix} \bar{x} \\ \bar{y} \\ \bar{z} \end{bmatrix}$$

The Euler dynamic equations describing the satellite motion under gravity gradient torque alone are contained in Peterson's eq. (26):

$$\bar{\Phi}_s \cdot \dot{\bar{\omega}} + \bar{\omega} \times [\bar{\Phi}_s \cdot \bar{\omega}] = 3\Omega_0^2 [Y \times (\bar{\Phi}_s \cdot Y)]$$

$$\bar{\omega} = \begin{bmatrix} \omega_x \\ \omega_y \\ \omega_z \end{bmatrix} = \text{inertial angular velocity of the satellite in principal axes coordinates}$$

$$\bar{\bar{\Phi}}_s = \begin{bmatrix} A & 0 & 0 \\ 0 & B & 0 \\ 0 & 0 & C \end{bmatrix} = \text{principal inertia tensor of the satellite}$$

$$\Omega_0^2 = \frac{GM_\oplus}{R_0^3}$$

R_0 = satellite distance from center of Earth
$M_\oplus$ = mass of Earth
Ω_0 = angular velocity of satellite in orbit
$\Omega_0 << \omega_s$

For surface orbit R_0 = 6,371 km, $\Omega_0^2 = 1.54 \times 10^{-6}$ sec^{-2}.

The dynamical regime of the satellite includes only small coning precession angles, $\theta << 1$. Hence, cos $\theta \approx 1$. We therefore can approximate $\bar{Y}$: (Note that $\phi = \omega_s t$ and later that $\psi = \dot{\omega} t$.)

$$\bar{Y} = \begin{bmatrix} (\cos \omega_s t \sin\psi + \sin\omega_s t \cos\psi) & \bar{x} \\ (-\sin \omega_s t \sin\psi + \cos\omega_s t \cos\psi) & \bar{y} \\ -\theta \cos\psi & \bar{z} \end{bmatrix} = \begin{bmatrix} \sin(\omega_s t + \psi) & \bar{x} \\ \cos(\omega_s t + \psi) & \bar{y} \\ -\theta \cos\psi & \bar{z} \end{bmatrix}$$

$\bar{Y} \times (\bar{\bar{\Phi}}_s \cdot \bar{Y})$ is found by the determinant:

$$\begin{bmatrix} \bar{x} & \bar{y} & \bar{z} \\ \sin(\omega_s t + \psi) & \cos(\omega_s t + \psi) & -\theta\cos\psi \\ A \sin(\omega_s t + \psi) & B \cos(\omega_s t + \psi) & -C\theta\cos\psi \end{bmatrix}$$

$$\bar{Y} \times (\bar{\bar{\Phi}}_s \cdot \bar{Y}) = \begin{bmatrix} (B - C)\ \theta\cos\psi\ \cos(\omega_s t + \psi) & \bar{x} \\ (C - A)\ \theta\cos\psi\ \sin(\omega_s t + \psi) & \bar{y} \\ (B - A)\ \cos(\omega_s t + \psi)\ \sin(\omega_s t + \psi) & \bar{z} \end{bmatrix}$$

$$\bar{\bar{\Phi}}_s \cdot \dot{\bar{\omega}} + \bar{\omega} \times (\bar{\bar{\Phi}}_s \cdot \bar{\omega}) = \begin{bmatrix} (A\dot{\omega}_x + C\omega_y\omega_z - B\omega_y\omega_z) & \bar{x} \\ (B\dot{\omega}_y + A\omega_x\omega_z - C\omega_x\omega_z) & \bar{y} \\ (C\dot{\omega}_z + B\omega_x\omega_y - A\omega_x\omega_y) & \bar{z} \end{bmatrix} .$$

The resulting dynamical equations are:

$$\begin{aligned} \dot{\omega}_x + k_1\omega_z\omega_y &= -3\Omega_0^2 k_1\theta\ \cos\psi\ \cos(\omega_s t + \psi) \\ \dot{\omega}_y - k_2\omega_z\omega_x &= 3\Omega_0^2 k_2\theta\ \cos\psi\ \sin(\omega_s t + \psi) \\ \dot{\omega}_z + k_3\omega_x\omega_y &= (3/2)\ \Omega_0^2 k_3 \sin 2(\omega_s t + \psi) \quad , \end{aligned}$$

where

$$\begin{aligned} k_1 &= \frac{C - B}{A} \\ k_2 &= \frac{C - A}{B} \\ k_3 &= \frac{B - A}{C} \quad . \end{aligned} \tag{3}$$

To solve these highly nonlinear equations would be impossible without some simplifying assumptions. I have solved the first two equations for ω_x and ω_y by first assuming ω_z approximately constant, $\omega_z = \omega_s$. Then the product $\omega_x\omega_y$ may be substituted in the ω_z equation and ω_z will be known. Because the solution for ω_z is done after ω_x and ω_y are found, there is an opportunity to include the predominant effect of aerodynamic torque, which is a decrease in the spin

angular velocity. The ω_z equation for gravity gradient and aerodynamic torque is:

$$\dot{\omega}_z + k_3\omega_x\omega_y = \frac{3}{2}\ \Omega_0^2 k_3 \sin 2(\omega_s t + \psi) + \frac{M_z}{C}$$

where

M_z = aerodynamic torque about z axis.

After the approximation $\omega_z = \omega_s$ has been made, the x and y equations are in matrix form:

$$\begin{bmatrix} S & k_1\omega_s \\ -k_2\omega_s & S \end{bmatrix} \begin{bmatrix} \omega_x \\ \omega_y \end{bmatrix} = \begin{bmatrix} -3\Omega_0^2 k_1\theta \cos\psi \cos(\omega_s t + \psi) \\ 3\Omega_0^2 k_2\theta \cos\psi \sin(\omega_s t + \psi) \end{bmatrix}, \quad (4)$$

where $s = d/dt$.

Solving for ω_x and ω_y indicates that the equations to be solved are a second order linear differential equation in ω_x and a second order linear differential equation in ω_y. The homogeneous part of the solution is found from the simple solutions to the following equations:

$$(S^2 + k_1k_2\omega_s^2 S)\omega_x = 0$$

$$(S^2 + k_1k_2\omega_s^2 S)\omega_y = 0$$

The homogeneous solutions are of the form

$$\omega_x = C_1 \sin \sqrt{k_1k_2}\omega_s t + C_2 \cos \sqrt{k_1k_2}\omega_s t$$

$$\omega_y = C_3 \sin \sqrt{k_1k_2}\omega_s t + C_4 \cos \sqrt{k_1k_2}\omega_s t$$

The above must also solve the original homogeneous equations:

$$\dot{\omega}_x + k_1\omega_s\omega_y = 0$$

$$\dot{\omega}_y - k_2\omega_s\omega_x = 0 \quad .$$

To find the relationship between the coefficients of the homogeneous part of the solution, we combine the last two equations and obtain:

$$C_1 \sqrt{k_1k_2}\omega_s \cos \sqrt{k_1k_2}\omega_s t - C_2 \sqrt{k_1k_2}\omega_s \sin \sqrt{k_1k_2}\omega_s t$$

$$+ C_3k_1\omega_s \sin \sqrt{k_1k_2}\omega_s t + C_4k_1\omega_s \cos \sqrt{k_1k_2}\ \omega_s t = 0$$

$$C_3 \sqrt{k_1k_2}\omega_s \cos \sqrt{k_1k_2}\omega_s t - C_4 \sqrt{k_1k_2}\omega_s \sin \sqrt{k_1k_2}\omega_s t$$

$$- C_1k_2\omega_s \sin \sqrt{k_1k_2}\omega_s t - C_2k_2\omega_s \cos \sqrt{k_1k_2}\omega_s t = 0 \quad .$$

We find that

$$\left.\begin{aligned} C_1 \sqrt{k_1k_2} + C_4k_1 &= 0 \\ C_1k_2 + C_4 \sqrt{k_1k_2} &= 0 \end{aligned}\right\} \Rightarrow C_4 = \frac{-\sqrt{k_1k_2}}{k_1} C_1 \quad ,$$

and

$$\left.\begin{aligned} C_3k_1 - C_2 \sqrt{k_1k_2} &= 0 \\ C_3 \sqrt{k_1k_2} - C_2k_2 &= 0 \end{aligned}\right\} \Rightarrow C_3 = \frac{\sqrt{k_1k_2}}{k_1} C_2 \quad .$$

Thus, the resulting homogeneous solutions are:

$$\omega_x = C_1 \sin \sqrt{k_1k_2}\omega_s t + C_2 \cos \sqrt{k_1k_2}\omega_s t$$

$$\omega_y = \frac{-\sqrt{k_1k_2}}{k_1} C_1 \cos \sqrt{k_1k_2}\omega_s t + \frac{\sqrt{k_1k_2}}{k_1} C_2 \sin \sqrt{k_1k_2}\omega_s t$$

C_1 and C_2 are arbitrary. The nonhomogeneous part of the solution for ω_x and ω_y may be determined by the method of undetermined coefficients. The following assumed forms of ω_x and ω_y (nonhomogeneous) were used successfully. (A, B, and C are not inertia tensor members.)

$$\omega_y = A \sin\psi \sin(\omega_s t + \psi) + B \cos\psi \cos(\omega_s t + \psi)$$

$$\omega_x = C \sin\psi \cos(\omega_s t + \psi) + D \cos\psi \sin(\omega_s t + \psi) \quad . \tag{6}$$

Differentiating the above terms of ω_x and ω_y (remember, $\psi = \dot{\psi}t$):

$$\dot{\omega}_y = A\dot{\psi} \cos\psi \sin(\omega_s t + \psi) + A(\omega_s + \dot{\psi}) \sin\psi \cos(\omega_s t + \psi)$$

$$- B\dot{\psi} \sin\psi \cos(\omega_s t + \psi) - B(\omega_s + \dot{\psi}) \cos\psi \sin(\omega_s t + \psi)$$

$$\dot{\omega}_x = C\dot{\psi} \cos\psi \cos(\omega_s t + \psi) - C(\omega_s + \dot{\psi}) \sin\psi \sin(\omega_s t + \psi)$$

$$- D\dot{\psi} \sin\psi \sin(\omega_s t + \psi) + D(\omega_s + \dot{\psi}) \cos\psi \cos(\omega_s t + \psi) \quad .$$

Substituting the ω_x, ω_y, and $\dot{\omega}_x$, $\dot{\omega}_y$ forms into the nonhomogeneous differential equations for ω_x and ω_y we get:

$\dot{\omega}_x$ equation

$$\text{cos cos: } C\dot{\psi} + D(\omega_s + \dot{\psi}) + k_1\omega_s B = -3\Omega_0^2 k_1 \theta$$

$$\text{sin sin: } -C(\omega_s + \dot{\psi}) - D\dot{\psi} + k_1\omega_s A = 0$$

$\dot{\omega}_y$ equation

$$\text{cos sin: } A\dot{\psi} - B(\omega_s + \dot{\psi}) - k_2\omega_s D = 3\Omega_0^2 k_2 \theta$$

$$\text{sin cos: } A(\omega_s + \dot{\psi}) - B\dot{\psi} - k_2\omega_s C = 0 \quad . \tag{7}$$

The latter equations may be put in matrix form for easier visibility of the solutions:

$$\begin{bmatrix} 0 & k_1\omega_s & \dot{\psi} & (\omega_s + \dot{\psi}) \\ k_1\omega_s & 0 & -(\omega_s + \dot{\psi}) & \dot{\psi} \\ \dot{\psi} & -(\omega_s + \dot{\psi}) & 0 & -k_2\omega_s \\ \omega_s + \dot{\psi} & -\dot{\psi} & -k_2\omega_s & 0 \end{bmatrix} \begin{bmatrix} A \\ B \\ C \\ D \end{bmatrix} = \begin{bmatrix} -3\Omega_0^2 k_1\theta \\ 0 \\ 3\Omega_0^2 k_2\theta \\ 0 \end{bmatrix}$$

Adding the first two rows: $(A + B)\, k_1\omega_s + (D - C)\, \omega_s = -3\Omega_0^2 k_1\theta$. Subtracting row 3 from row 4: $(A + B)\omega_s + k_2\omega_s(D - C) = -3\Omega_0^2 k_2\theta$. Solving for $(A + B)$ and $(D - C)$:

$$A + B = \frac{-3\Omega_0^2\theta k_2\,(1 - k_1)}{\omega_s(1 - k_1k_2)}$$

$$D - C = \frac{-3\Omega_0^2\theta\, k_1(1 - k_2)}{\omega_s\,(1 - k_1k_2)} \qquad (9a)$$

Adding rows 3 and 4:

$$(A - B)\,(\omega_s + 2\dot{\psi}) - k_2\omega_s\,(C + D) = 3\Omega_0^2 k_2\theta \quad .$$

Subtracting row 1 from row 2:

$$(A - B)\, k_1\omega_s - (\omega_s + 2\dot{\psi})\,(C + D) = 3\Omega_0^2 k_2\theta \quad .$$

Solving for $(A - B)$ and $(C + D)$:

$$A - B = \frac{3\Omega_0^2 k_2\theta\,[k_1\omega_s - (\omega_s + 2\dot{\psi})]}{[k_2k_1\omega_s^2 - (\omega_s + 2\dot{\psi})^2]}$$

$$C + D = \frac{-3\Omega_0^2 k_1\theta\,[k_2\omega_s - (\omega_s + 2\dot{\psi})]}{[k_2k_1\omega_s^2 - (\omega_s + 2\dot{\psi})^2]} \quad . \qquad (9b)$$

2. Estimate of Precession Frequency ψ

The nonhomogeneous parts of ω_x and ω_y involve $\psi = \dot{\psi}t$ as arguments of sines and cosines; hence, it is important to know $\dot{\psi}$. Even though our satellite is not torque-free, we can get an estimate of $\dot{\psi}$ by examining torque-free motion.

With the assumption that $\dot{\theta} = 0$, the angular velocities and accelerations in terms of Euler angles are:

$$\left.\begin{aligned} \omega_x &= \dot{\psi}\sin\theta\sin\phi \\ \omega_y &= \dot{\psi}\sin\theta\cos\phi \\ \omega_z &= \dot{\phi} + \dot{\psi}\cos\theta = \omega_s \end{aligned}\right\} \qquad \left.\begin{aligned} \dot{\omega}_x &= \ddot{\psi}\phi\sin\theta\cos\phi \\ \dot{\omega}_y &= -\ddot{\psi}\phi\sin\theta\sin\phi \\ \dot{\omega}_z &= 0 \quad . \end{aligned}\right\}$$

Taking one of the torque-free Euler dynamical equations:

$$A\dot{\omega}_x + \omega_x\omega_z (C - B) = 0 \quad .$$

Substituting the values of $\dot{\omega}_x$, ω_x, and ω_z above:

$$A\ddot{\psi}\phi\sin\theta\cos\phi + [\ddot{\psi}\phi\sin\theta\cos\psi + \dot{\psi}^2\sin\theta\cos\theta\cos\phi](C - B) = 0 \; .$$

The result is:

$$\dot{\psi} = \left(\frac{A + C - B}{B - C}\right)\frac{\dot{\phi}}{\cos\theta}$$

Since $\theta << 1$ and $\dot{\phi} = \omega_s$:

$$\dot{\psi} \simeq \left(\frac{A + C - B}{B - C}\right)\omega_s \qquad (10)$$

Note that for $C > B > A$, $\dot{\psi} < 0$ for $\dot{\omega}_s > 0$. This means that our satellite will undergo retrograde precession.

3. Evaluating the Product $\omega_x\omega_y$

The product $\omega_x\omega_y$ is present in the gradient error driving functions $\dot{\omega}_k$ and $\omega_i\omega_j$, so it is important to evaluate.

First, we simplify the nonhomogeneous parts of ω_x and ω_y with the basic trigonometric relationships:

$$\sin \frac{p+q}{2} \cos \frac{p-q}{2} = \frac{1}{2}(\sin p + \sin q)$$

$$\sin \frac{p-q}{2} \cos \frac{p+q}{2} = \frac{1}{2}(\sin p - \sin q)$$

$$\cos \frac{p+q}{2} \cos \frac{p-q}{2} = \frac{1}{2}(\cos p + \cos q)$$

$$\sin \frac{p+q}{2} \sin \frac{p-q}{2} = \frac{1}{2}(\cos q - \cos p) \quad ,$$

if $\frac{p+q}{2} = \psi$ and $\frac{p-q}{2} = \omega_s t + \psi$ then $p = (\omega_s t + 2\psi)$

and $q = -\omega_s t$.

The simplified equations are:

$$\omega_y = \frac{A}{2}[\cos \omega_s t - \cos(\omega_s t + 2\psi)] + \frac{B}{2}[\cos(\omega_s t + 2\psi) + \cos \omega_s t]$$

$$\omega_x = \frac{C}{2}[\sin(\omega_s t + 2\psi) - \sin \omega_s t] + \frac{D}{2}[\sin(\omega_s t + 2\psi) + \sin \omega_s t] \quad . \qquad (11)$$

Thus (nonhomogeneous solutions):

$$\left.\begin{aligned} \omega_y &= \frac{A + B}{2} \cos\omega_s t - \frac{A - B}{2} \cos(\omega_s t + 2\psi) \\ \omega_x &= \frac{C + D}{2} \sin(\omega_s t + 2\psi) + \frac{D - C}{2} \sin \omega_s t \end{aligned}\right\} \tag{12}$$

These equations make use of the relationships between A, B, C, and D previously derived.

Adding the homogeneous parts to the nonhomogeneous parts of ω_x and ω_y and solving for the product $\omega_x\omega_y$:

$$\begin{aligned} \omega_x\omega_y = {} & \frac{(A + B)\ (C + D)}{4} \cos \omega_s t \sin (\omega_s t + 2\psi) \\ & + \frac{(A + B)\ (D - C)}{4} \cos \omega_s t \sin \omega_s t \\ & + \frac{(A + B)}{2} C_1 \cos \omega_s t \sin \sqrt{k_1 k_2}\omega_s t \\ & + \frac{(A + B)}{2} C_2 \cos \omega_s t \cos \sqrt{k_1 k_2}\omega_s t \\ & - \frac{(A - B)\ (C + D)}{4} \cos (\omega_s t + 2\psi) \sin (\omega_s t + 2\psi) \\ & - \frac{(A - B)\ (D - C)}{4} \cos (\omega_s t + 2\psi) \sin \omega_s t \\ & - \frac{(A - B)}{2} C_1 \cos (\omega_s t + 2\psi) \sin \sqrt{k_1 k_2}\omega_s t \\ & - \frac{(A - B)}{2} C_2 \cos (\omega_s t + 2\psi) \cos \sqrt{k_1 k_2}\omega_s t \\ & - \frac{\sqrt{k_1 k_2}}{k_1} C_1 (\cos \sqrt{k_1 k_2}\omega_s t) \left(\frac{C + D}{2}\right) \sin (\omega_s t + 2\psi) \\ & - \frac{\sqrt{k_1 k_2}}{k_1} C_1 \frac{(D - C)}{2} \cos \sqrt{k_1 k_2}\omega_s t \sin \omega_s t \\ & - \frac{\sqrt{k_1 k_2}}{k_1} C_1^2 \cos \sqrt{k_1 k_2}\omega_s t \sin \sqrt{k_1 k_2}\omega_s t \end{aligned}$$

$$- \frac{\sqrt{k_1 k_2}}{k_1} C_1 C_2 \cos^2 \sqrt{k_1 k_2}\,\omega_s t$$

$$+ \frac{\sqrt{k_1 k_2}}{2k_1} C_2 (C + D) \sin \sqrt{k_1 k_2}\,\omega_s t \sin (\omega_s t + 2\psi)$$

$$+ \frac{\sqrt{k_1 k_2}}{2k_1} C_2 (D - C) \sin \sqrt{k_1 k_2}\,\omega_s t \sin \omega_s t$$

$$+ \frac{\sqrt{k_1 k_2}}{k_1} C_1 C_2 \sin^2 \sqrt{k_1 k_2}\,\omega_s t + \frac{\sqrt{k_1 k_2}}{k_1} C_2^2$$

$$\cos \sqrt{k_1 k_2}\,\omega_s t \sin \sqrt{k_1 k_2}\,\omega_s t \quad . \tag{13}$$

By using the sine and cosine relationships already described, it is possible to reduce each term of the expanded $\omega_x \omega_y$ expression to a recognizable frequency combination of sines and cosines.

The full expansion of $\omega_x \omega_y$ is:

$$\omega_x \omega_y = \frac{(A + B)(C + D)}{8} [\sin 2(\omega_s t + \psi) + \sin 2\psi)]$$

$$+ \frac{(A + B)(D - C)}{8} \sin 2\omega_s t - \frac{(A - B)(C + D)}{8}$$

$$\sin (2\omega_s t + 4\psi) - \frac{(A - B)(D - C)}{8} [\sin 2(\omega_s t + \psi)$$

$$- \sin 2\psi] - \frac{\sqrt{k_1 k_2}}{2k_1} C_1^2 \sin(2\sqrt{k_1 k_2}\,\omega_s t)$$

$$- \frac{\sqrt{k_1 k_2}}{k_1} C_1 C_2 \cos (2\sqrt{k_1 k_2}\,\omega_s t)$$

$$+ \frac{(A + B)}{4} C_1 [\sin (1 + \sqrt{k_1 k_2})\,\omega_s t - \sin (1 - \sqrt{k_1 k_2})\,\omega_s t]$$

$$+ \frac{(A+B)}{4} C_2 \left[\cos\left(1 + \sqrt{k_1 k_2}\right) \omega_s t + \cos\left(1 - \sqrt{k_1 k_2}\right) \omega_s t\right]$$

$$- \frac{\sqrt{k_1 k_2}\,(D - C)\, C_1}{4k_1} \left[\sin\left(1 + \sqrt{k_1 k_2}\right) \omega_s t + \sin\left(1 - \sqrt{k_1 k_2}\right) \omega_s t\right] + \frac{\sqrt{k_1 k_2}\,(D - C)\, C_2}{4k_1} \left[\cos\left(1 - \sqrt{k_1 k_2}\right) \omega_s t - \cos\left(1 + \sqrt{k_1 k_2}\right) \omega_s t\right] + \frac{\sqrt{k_1 k_2}}{2k_1} C_2^2 \sin\left(2\sqrt{k_1 k_2}\, \omega_s t\right)$$

$$- \frac{(A - B)}{4} C_1 \left[\sin\left(2\psi + \left(1 + \sqrt{k_1 k_2}\right) \omega_s t\right) - \sin\left(2\psi + \left(1 - \sqrt{k_1 k_2}\right) \omega_s t\right)\right]$$

$$- \frac{(A - B)}{4} C_2 \left[\cos\left(2\psi + \left(1 + \sqrt{k_1 k_2}\right) \omega_s t\right) + \cos\left(2\psi + \left(1 - \sqrt{k_1 k_2}\right) \omega_s t\right)\right]$$

$$- \frac{\sqrt{k_1 k_2}(C + D)\, C_1}{4k_1} \left[\sin\left(2\psi + \left(1 + \sqrt{k_1 k_2}\right) \omega_s t\right) + \sin\left(2\psi + \left(1 - \sqrt{k_1 k_2}\right) \omega_s t\right)\right]$$

$$+ \frac{\sqrt{k_1 k_2}(C + D) C_2}{4K_1} \left[\cos\left(2\psi + \left(1 - \sqrt{k_1 k_2}\right) \omega_s t\right) - \cos\left(2\psi + \left(1 + \sqrt{k_1 k_2}\right) \omega_s t\right)\right] . \qquad (14)$$

4. Angular Misalignment of Gradiometer; Calculation of $\omega_i \omega_j$ and $\dot{\omega}_k$

Following Peterson's formulation, the gradiometer case axes $\bar{I}$, $\bar{J}$, and $\bar{K}$ are assumed to be canted with respect to the satellite principal axes by the matrix relation:

$$\begin{bmatrix} \bar{i} \\ \bar{j} \\ \bar{k} \end{bmatrix} = \begin{bmatrix} 1 & 0 & -\alpha \\ 0 & 1 & \beta \\ \alpha & -\beta & 1 \end{bmatrix} \begin{bmatrix} \bar{x} \\ \bar{y} \\ \bar{z} \end{bmatrix}$$

β and α are small angles

$$\alpha << 1$$

$$\beta << 1 \quad .$$

For a better understanding of the geometry of this relation, I have separated the above matrix into a product of two matrices that perform the rotations of the $\bar{x}$, $\bar{y}$, and $\bar{z}$ axes into the $\bar{i}$, $\bar{j}$, and $\bar{k}$ axes shown in the following.

$$\begin{bmatrix} 1 & 0 & -\alpha \\ 0 & 1 & \beta \\ \alpha & -\beta & 1 \end{bmatrix} \approx \begin{bmatrix} 1 & 0 & 0 \\ 0 & 1 & \beta \\ 0 & -\beta & 1 \end{bmatrix} \begin{bmatrix} 1 & 0 & -\alpha \\ 0 & 1 & 0 \\ \alpha & 0 & 1 \end{bmatrix}$$ Note: $\alpha\beta << 1$

1405-5

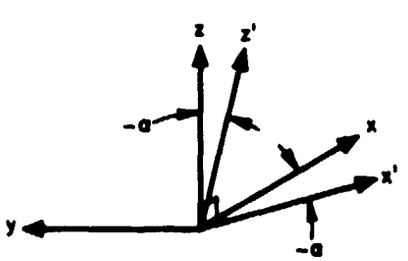

ROTATION ABOUT Y AXIS

1405-6

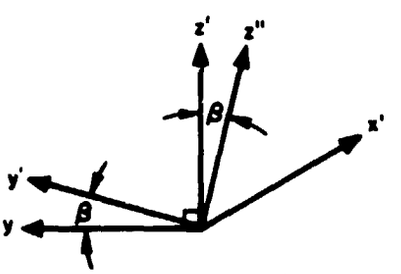

ROTATION ABOUT X' AXIS

The angular misalignment results in the following relations:

$$\left.\begin{aligned} \omega_i &= \omega_x - \alpha\omega_z \\ \omega_j &= \omega_y + \beta\omega_z \\ \omega_k &= \omega_z + \alpha\omega_x - \beta\omega_y \end{aligned}\right\} \text{ and } \left.\begin{aligned} \dot{\omega}_i &= \dot{\omega}_x - \alpha\dot{\omega}_z \\ \dot{\omega}_j &= \dot{\omega}_y + \beta\dot{\omega}_z \\ \dot{\omega}_k &= \dot{\omega}_z + \alpha\dot{\omega}_x - \beta\dot{\omega}_y \end{aligned}\right\} .$$

By multiplying $\omega_i\omega_j$, we have the useful relation:

$$\omega_i\omega_j = \omega_x\omega_y + \omega_z(\beta\omega_x - \alpha\omega_y) - \alpha\beta\,\omega_z^2$$

where

$$\omega_z = \omega_s \tag{15}$$

From the previous expansion of $\omega_x\omega_y$, we can list the amplitudes and frequencies of the rotational field driving function $\omega_i\omega_j$, as shown in Table I.

Finding the sum mode mismatch driving function $\dot{\omega}_k$ involves the two equations

$$\dot{\omega}_k = \dot{\omega}_z + \alpha\dot{\omega}_x - \beta\dot{\omega}_y \tag{16a}$$

$$\dot{\omega}_z = \frac{3}{2}\,\Omega_0^2 k_3 \sin 2(\omega_s t + \psi) + \frac{M_z}{C} - k_3\omega_x\omega_y\,. \tag{16b}$$

The sum mode mismatch driving function therefore contains all of the frequency components that the rotational field function had, except their amplitudes are multiplied by the factor k_3. However, it also contains the additional components listed in Table II.

C. Aerodynamic Torque About Spin Axis

According to a technical analysis by K.R. Johnson on* the effect of aerodynamic torque on satellite rotation, the torque caused by the differences in velocities with respect

*"The Effect of Dissipative Aerodynamic Torques on Satellite Rotation" by K.R. Johnson, Journal of Spacecraft and Rockets, Volume 5, No. 4, April 1968, page 408.

TABLE I

Rotational Field Driving Function, $\omega_i \omega_j$

Frequency	Amplitudes of Components
dc	$\alpha\beta\omega_s^2$
ω_s	$\omega_s\alpha \left(\frac{A+B}{2}\right)$; $\omega_s\beta \left(\frac{D-C}{2}\right)$
$2\omega_s$	$\frac{(A+B)(D-C)}{8}$
$2\dot{\psi}$	$\frac{(A+B)(C+D)}{8}$; $\frac{(A-B)(D-C)}{8}$
$\sqrt{k_1k_2}\ \omega_s$	$\beta\omega_s C_1$; $\beta\omega_s C_2$; $\frac{\sqrt{k_1k_2}}{k_1}\omega_s\alpha C_1$; $\frac{\sqrt{k_1k_2}}{k_1}\omega_s\alpha C_2$
$2\sqrt{k_1k_2}\omega_s$	$\frac{\sqrt{k_1k_2}}{2k_1} C_1^2$; $\frac{\sqrt{k_1k_2}}{k_1} C_1C_2$; $\frac{\sqrt{k_1k_2}}{2k_1} C_2^2$
$(1+\sqrt{k_1k_2})\omega_s$	$\frac{A+B}{4} C_1$; $\frac{A+B}{4} C_2$; $\frac{\sqrt{k_1k_2}(D-C)C_1}{4k_1}$; $\frac{\sqrt{k_1k_2}(D-C)C_2}{4k_1}$
$(1-\sqrt{k_1k_2})\omega_s$	$\frac{A+B}{4} C_1$; $\frac{A+B}{4} C_2$; $\frac{\sqrt{k_1k_2}(D-C)C_1}{4k_1}$; $\frac{\sqrt{k_1k_2}(D-C)C_2}{4k_1}$
$2(\omega_s+\dot{\psi})$	$\frac{(A+B)(C+D)}{8}$; $\frac{(A-B)(D-C)}{8}$
$(\omega_s+2\dot{\psi})$	$\omega_s\beta \frac{(C+D)}{2}$; $\omega_s\alpha \frac{(A-B)}{2}$
$2(\omega_s+2\dot{\psi})$	$\frac{(A-B)(C+D)}{8}$
$2\dot{\psi}+(1+\sqrt{k_1k_2})\omega_s$	$\frac{A-B}{4} C_1$; $\frac{A-B}{4} C_2$; $\frac{\sqrt{k_1k_2}(C+D)C_1}{4k_1}$; $\frac{\sqrt{k_1k_2}(C+D)C_2}{4k_1}$
$2\dot{\psi}+(1-\sqrt{k_1k_2})\omega_s$	$\frac{A-B}{4} C_1$; $\frac{A-B}{4} C_2$; $\frac{\sqrt{k_1k_2}(C+D)C_1}{4k_1}$; $\frac{\sqrt{k_1k_2}(C+D)C_2}{4k_1}$

T364

TABLE II

Additional Components of Sum Mode Driving Function, $\dot{\omega}_k$

Frequency	Amplitudes of Components
dc (actually exponentially decreasing)	$\frac{M_z}{C}$ (C = principal moment of satellite about z axis)
$2(\omega_s + \dot{\psi})$	$\frac{3}{2}\Omega_0^2 k_3$
$\sqrt{k_1 k_2}\omega_s$	$\alpha C_1 \sqrt{k_1 k_2}\omega_s$; $\alpha C_2 \sqrt{k_1 k_2}\omega_s$; $\beta C_1 K_2 \omega_s$; $\beta C_2 k_2 \omega_s$
$(\omega_s + 2\dot{\psi})$	$\alpha \frac{(C + D)(\omega_s + 2\dot{\psi})}{2}$; $\beta \frac{(A - B)(\omega_s + 2\dot{\psi})}{2}$
ω_s	$\alpha \frac{(D - C)}{2} \omega_s$; $\beta \frac{(A + B)}{2} \omega_s$

T365

to the atmosphere of different portions of a rotating satellite causes secular variations in the precession rate, spin rate, and coning angle. I have chosen to integrate into my analysis only the secular variation in spin rate caused by aerodynamic torque. The choice was only based on the desire for simplicity and the fact that the coning angle and precession rate change introduce "perturbations on perturbations."

Johnson's eq. (44) indicates the time variation of spin rate.

$$\dot{\phi} = \dot{\phi}_0 e^{-t/\tau_\phi} ,$$

where $\dot{\phi}_0$ is the initial spin, ω_s and τ_ϕ is a parameter to be defined below.

Hence,

$$\ddot{\phi} = \frac{-\dot{\phi}_0}{\tau_\phi} e^{-t/\tau_\phi}$$

$$\left.\frac{M_z \text{ (aero)}}{C}\right|_0 = \ddot{\phi}_0 = \frac{-\dot{\phi}_0}{\tau_\phi} = \frac{-\omega_s}{\tau_\phi} .$$

Johnson indicates that his $\dot{\phi}$ formulation for a cylindrical satellite holds only when a parameter p, which he defines, is either greater than 2 or less than 1.

$$p = \frac{3R^2A}{(R^2 + r_0^2)C}$$

R = radius of cylinder

r_0 = half of satellite length

A = transverse moment of inertia

C = z axis moment of inertia.

For our proposed satellite designed to fit into the Scout upper stage, R = 38 cm, r_0 = 20 cm. Hence, p = 2.36 (A/C). Depending on our A/C ratio, the analysis may or may not be valid. Assuming

$$\frac{A}{C} > \frac{2}{2.36} ,$$

an unlikely configuration due to stability considerations, or

$$\frac{A}{C} < \frac{1}{2.36}$$

we proceed to determine $\ddot{\phi}$.

According to Johnson,

$$t_{\phi} = \frac{3C}{4\rho V_0 r_0 R\ (3R^2)\ \langle \sin \delta \rangle_{av}}$$

ρ = upper atmospheric density

V_0 = satellite orbital velocity

$\langle \sin \delta \rangle_{av}$ = the average over one precession period of the angle between the satellite spin axis and the direction of air flow

I used the following values to determine $\ddot{\phi}_0$:

$\dot{\phi}_0$ = 4 Hz

$\langle \sin \delta \rangle_{av} \approx 1 \quad (\delta \approx \pi/2)$

$\rho = 2 \times 10^{-13}$ gm/cm^3 (@ 240 km altitude)

$V_0 = 7.4 \times 10^5$ cm/sec

r_0 = 20 cm

R = 38 cm

C = 7.1 kg m^2

$$\ddot{\Phi}_0 = \frac{-4(2 \times 10^{-13})(7.4) \times 10^5)(7.6 \times 10^2)(4.33 \times 10^3)}{3(7.1)}$$

$$\ddot{\Phi}_0 = 9 \times 10^{-9} \text{ rad/sec}^2 = \left.\frac{M_z}{C}\right|_0 . \qquad (17)$$

D. Arm Mass Unbalance Driving Function

$\Gamma_{\mu max}$ is produced by the linear acceleration of the gradiometer center of mass acting on the individual offsets of center of mass for each arm from the pivot center. The basic correction to Peterson's derivation which I would make is the inclusion of the effect of aerodynamic drag. Peterson's model has the gradiometer center of mass offset from the satellite center of mass by the vector $\bar{\ell}$. Peterson's expression for the linear acceleration of the sensor center of mass is then:

$$\bar{a} = \dot{\bar{\omega}} \times \bar{\ell} + \bar{\omega} \times [\bar{\omega} \times \bar{\ell}]$$

$$\bar{\ell} = \begin{bmatrix} \ell_i \\ \ell_j \\ \ell_k \end{bmatrix} \text{ and } \bar{\omega} = \begin{bmatrix} \omega_i \\ \omega_j \\ \omega_k \end{bmatrix} \quad \text{(coordinatized in sensor case axes)}$$

The effect of aerodynamic drag would come in as an additional term:

$$\bar{a} = \bar{a}_D + \dot{\bar{\omega}} \times \ell + \bar{\omega} \times [\bar{\omega} \times \bar{\ell}] .$$

Peterson's expression for $\Gamma_{\mu max}$ needs no change:

$$\Gamma_{\mu max} = \frac{m}{I} [\bar{k} \cdot (\bar{\delta} \times \bar{a})] .$$

Where $I = I_1^3 \approx I_2^3$, m = mass of one gradiometer arm, and $\bar{\delta}$ is the offset of the sensor arm center of mass from the pivot center.

$$\bar{\delta} = \begin{bmatrix} \delta_i \\ \delta_j \\ \delta_k \end{bmatrix}$$

$\bar{a}_D$ is initially coordinatized in satellite principal axes and it must be put in sensor case axes:

$$\bar{a}_D = \begin{bmatrix} 1 & 0 & -\alpha \\ 0 & 1 & \beta \\ \alpha & -\beta & 1 \end{bmatrix} \begin{bmatrix} a_x \\ a_y \\ a_z \end{bmatrix}$$

The total linear acceleration of the gradiometer center of mass is:

$$\bar{a} = \begin{bmatrix} (a_x - \alpha a_z) + \dot{\omega}_j \ell_k - \dot{\omega}_k \ell_j + (\omega_i \omega_j \ell_j - \omega_j^2 \ell_i) - (\omega_k^2 \ell_i - \omega_i \omega_k \ell_k) \\ (a_y + \beta a_z) + \dot{\omega}_k \ell_i - \dot{\omega}_i \ell_k + (\omega_k \omega_j \ell_k - \omega_k^2 \ell_j) - (\omega_i^2 \ell_j - \omega_i \omega_j \ell_i) \\ (\alpha a_x - \beta a_y + a_z) + \dot{\omega}_i \ell_j - \dot{\omega}_j \ell_i + (\omega_i \omega_k \ell_i - \omega_i^2 \ell_k) - (\omega_j^2 \ell_k - \omega_j \omega_k \ell_j) \end{bmatrix} \begin{bmatrix} \bar{I} \\ \bar{J} \\ \bar{K} \end{bmatrix}$$

Peterson's analysis ignores the aerodynamic drag contribution to $\Gamma_{\mu max}$ which is:

$$(\Gamma_{\mu max})_{\text{Aero Drag}} = [\delta_i (a_y + \beta a_z) - \delta_j (a_x - \alpha a_z)]$$

The aerodynamic drag will be along the tangent to the orbit (approximately) in the direction of the negative X axis.

Ignoring precession and coning angle,

$$\begin{bmatrix} a_x \\ a_y \\ a_z \end{bmatrix} = \begin{bmatrix} \cos \omega_s t & \sin \omega_s t & 0 \\ -\sin \omega_s t & \cos \omega_s t & 0 \\ 0 & 0 & 1 \end{bmatrix} \begin{bmatrix} -a_x \\ 0 \\ 0 \end{bmatrix}$$

Hence,

$$(\Gamma_{\mu max})_{aero\ drag} = [\delta_i (a_x \sin \omega_s t) + \delta_j (a_x \cos \omega_s t)] \frac{m}{I} . \quad (18)$$

E. Graphical Evaluation of Error Terms

Figure 3 plots the magnitudes of seven complex functions, formed by replacing S by $j\omega$ versus frequency in rad/sec. ω_0^2/Q is indicated, as are $(\beta_{12}^2 - \omega^2 + j\omega\alpha_{12})$ and $(\omega_0^2 - \omega^2 + j\omega\,(\omega_0/Q))$. A combined curve of the three factors is formed. The three factors below are also plotted as:

Mass Unbalance: $(\beta_2^2 + \beta_1^2) - 2\omega^2 + j\omega(\alpha_1 + \alpha_2)$

Rotational Field: $(\beta_2^2\gamma_1 - \beta_1^2\gamma_2) - \omega^2(\gamma_1 - \gamma_2) + j\omega(\alpha_2\gamma_1 - \alpha_1\gamma_2)$

Angular Acceleration: $(\beta_1^2 - \beta_2^2) + (\alpha_1 - \alpha_2)j\omega$

In Fig. 4 the error numerators are multiplied by the combined curve to give the dimensionless frequency response.* To find the absolute error magnitudes at specific frequencies, it is only necessary to multiply the three curves by the magnitude of $\omega_i\omega_j$, $\dot{\omega}_k$, and $\Gamma_{\mu max}$, respectively.

*Reference the Appendix.

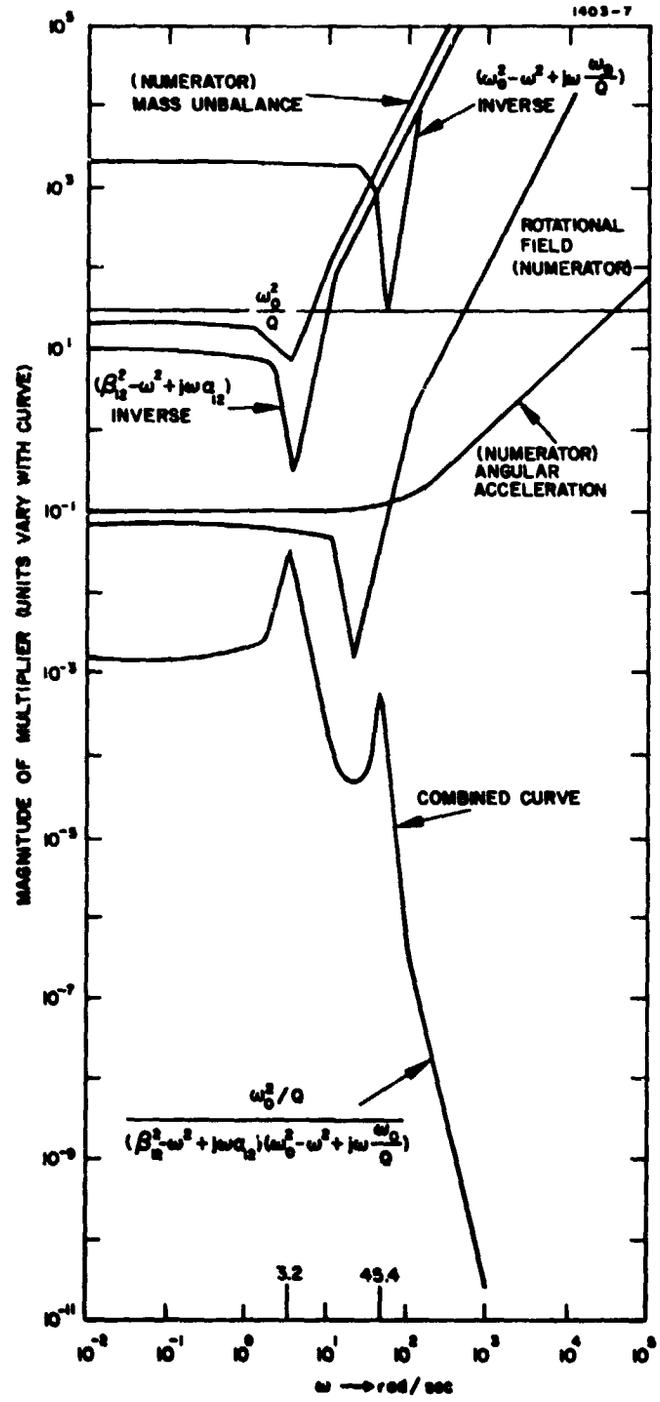

Fig. 3. Complex Functions in Dynamic Equations.

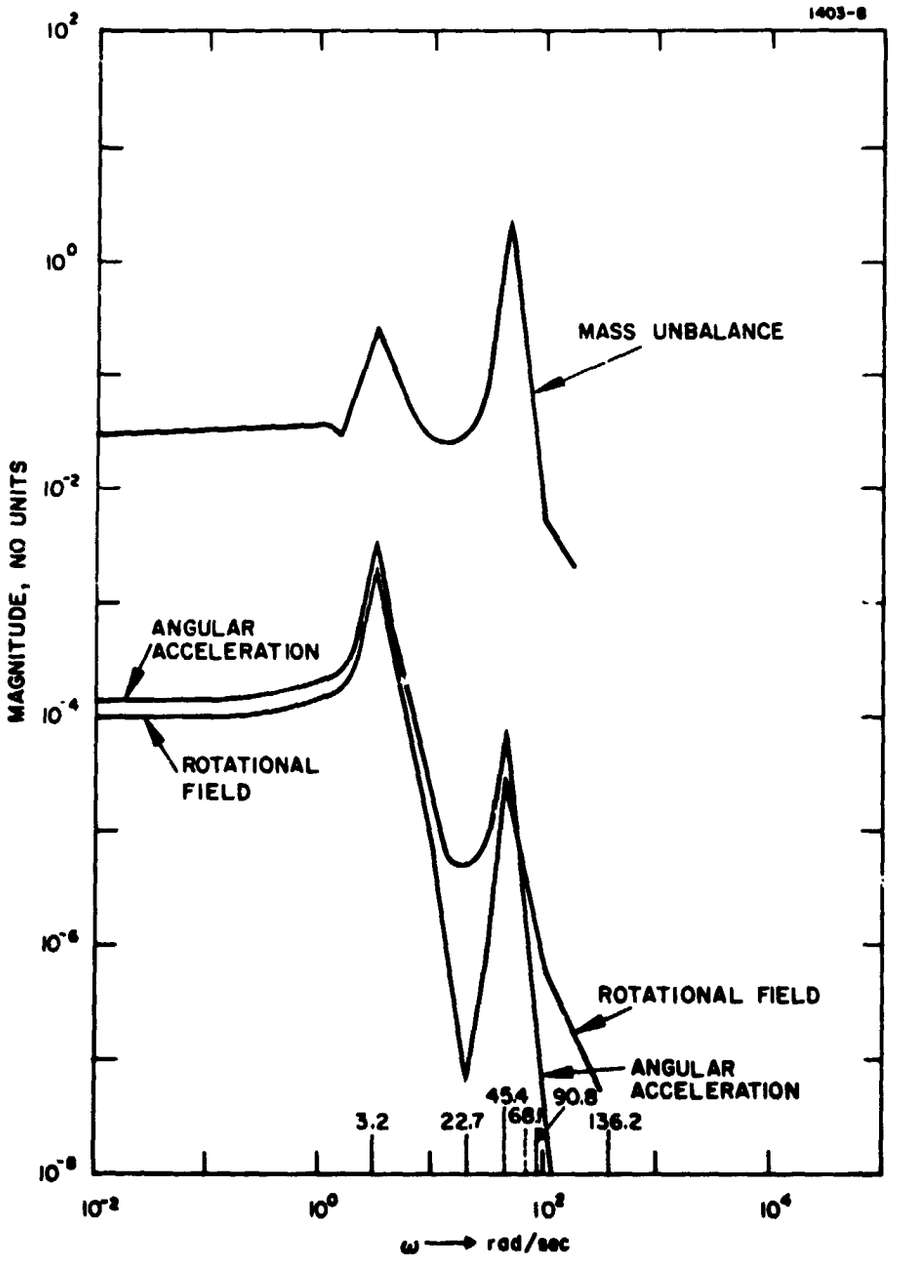

Fig. 4. Error Multipliers.

In order to construct Figs. 3 and 4, it was necessary to make numerical assumptions about the gradiometer system. While an effort was made to make reasonable estimates, the ideal gradiometer design process might include a computer evaluation of the errors under varying assumptions of parameters.

1. Design Assumptions

a. Sensor Assumptions

$I_1^3 \sim I_2^3 = 4.5 \times 10^6$ gram cm^2

$K_0 = 4.6 \times 10^9$ dyne cm/rad

$K_1 \sim K_2 = 4.6 \times 10^7$ dyne cm/rad

Q (untuned) = 70

$\omega_0 = 45.4$ rad/sec = 7.23 Hz

$\omega_0^2 = 2060$ sec^{-2}

$\omega_0/Q = 0.65$ sec^{-1}

$\frac{\omega_0^2}{Q} = 29.4$ sec^{-2}

$D_0 = 1.17 \times 10^6$ g cm^2/sec (From Above Assumptions Plus $D_1 \sim D_2 = (1/2)\ D_0$ and ω_0/Q Expression, Section II-A.)

$$D_1 \sim D_2 = \frac{1}{2} D_0 = 5.8 \times 10^5 \text{ g cm}^2/\text{sec}$$

$$\alpha_1 \sim \alpha_2 \sim \alpha_{12} = 0.13 \text{ sec}^{-1}$$

$$\beta_1^2 \sim \beta_2^2 \sim \beta_{12}^2 = 10.2 \text{ sec}^{-2}$$

$$\beta_1 \sim \beta_2 \sim \beta_{12} = 3.2 \text{ sec}^{-1}$$

$$\gamma_1 \sim \gamma_2 = 0.7$$

b. Difference Factor Assumptions

$$\gamma_1 - \gamma_2 = 2 \times 10^{-4} \text{ (1 g at 30 cm)}$$

$$\alpha_1 - \alpha_2 = (10^{-2})(0.13) = 1.3 \times 10^{-3} \text{ sec}^{-1}$$

$$\beta_1^2 - \beta_2^2 = 10^{-2} (10.2) = 0.102 \text{ sec}^{-2}$$

$$(\alpha_2\gamma_1 - \alpha_1\gamma_2) = 10^{-2} (0.13)(0.7) = 9 \times 10^{-4} \text{ sec}^{-1}$$

$$(\beta_2^2\gamma_1 - \beta_1^2\gamma_2) = 10^{-2} (10.2)(0.7) = 7 \times 10^{-} \text{ sec}^{-2}$$

c. Gradiometer – Satellite Assumptions

Misalignment: $\alpha = \beta = 10^{-3}$ rad

Coning Angle: $\theta = 10^{-5}$ rad

$$\Omega_0^2 = 1.5 \times 10^{-6} \text{ sec}^{-2}$$

$$\omega_s = 22.7 \text{ rad/sec}$$

$$\dot{\psi} \sim -2\omega_s = -45.4 \text{ rad/sec}$$

$$k_1 = \frac{C - B}{A}$$

$$k_3 = \frac{B - A}{C}$$

Assume $k_1 = 0.99$ and $k_3 = 0.01$; the result is that $A \simeq 0.497\ C$ and $B \simeq 0.507\ C$; then $k_2 = C - A/B \simeq 0.99$.

2. Angular Rate Error Evaluation

Before evaluating the error magnitudes, estimate the constants of eqs. 9(a) and 9(b):

$$\frac{1 - k_1}{1 - k_1 k_2} = \frac{1 - 0.99}{1 - (0.99)^2} = \frac{0.01}{0.02} = 0.5$$

$$(A + B) = (D - C) = \frac{-3\Omega_0^2 \theta k_2 (1 - k_1)}{\omega_s (1 - k_1 k_2)} = -10^{-12}\ \text{sec}^{-1}\ .$$

(Equality in the special case of $k_1 = k_2$) (19)

and

$$(A - B) = -(C + D) = \frac{[k_1 \omega_s - (\omega_s + 2\dot{\psi})](3\Omega_0^2 k_2 \theta)}{(k_2 k_1 \omega_s^2 - (\omega_s + 2\dot{\psi})^2)} = 10^{-12}\ \text{sec}^{-1} \quad (20)$$

Another set of constants which must be estimated is C_1 and C_2 that are connected with the homogeneous solution for ω_x and ω_y of eq. (13).

An estimate of the magnitude of both C_1 and C_2 comes from the standard expression for the magnitude of the transverse angular velocity of a torque-free body of revolution:*

* Introduction to Space Dynamics by William Tyrell Thomson, John Wiley & Sons (N.Y.) 1963.

$$\omega_{transverse} = \frac{C}{A}\ \omega_s \tan\theta$$

$$\simeq 2(25)(10^{-5})$$

$$\simeq 5 \times 10^{-4} \text{ rad/sec}$$

$$C_1 \sim C_2 \sim 5 \times 10^{-4} \text{ rad/sec} \quad . \tag{21}$$

From Table I, Fig. 4, and the preceding assumptions and estimates, we can construct Table III:

3. Angular Acceleration Error Evaluation

The angular acceleration error has all of the frequency components of Table III, but the amplitude of these error components is a factor of k_3(=0.01) less than the corresponding rotational field errors. In addition, the angular acceleration error includes the data of Table IV.

4. Mass Unbalance Error Evaluation

To find the mass unbalance errors it is reasonable to use Peterson's simplification (eq. (43) in RR 441), with a term added to take into consideration the effect of aerodynamic deceleration.

$$\Gamma_{\mu max} \leq \frac{m\delta\ell_k}{I_1^3}\ [\dot{\omega}_i + \dot{\omega}_j + (\omega_i + \omega_j)\omega_k]$$

$$+ \frac{m\delta\ell_{ij}}{I_1^3}\ [2\dot{\omega}_k + \omega_i^2 + \omega_j^2 + 2\omega_k^2 + 2\omega_i\omega_j]$$

$$+ \left.\frac{2\delta a_x m}{I_1^3}\right|_{@\ \text{Freq. } \omega_s}$$

(Last term is eq. (18) of this report.)

TABLE III

Rotational Field Errors

Error Frequency, rad/sec	Order of Magnitude of Amplitude	Multiplier (Fig. 4)	Error Equivalent	
			sec^{-2}	E.U.
dc = 0	10^{-6} $(4 \times 10^{2}) = 4 \times 10^{-4}$ sec^{-2}	10^{-4}	4×10^{-8}	40
$\omega_s = 22.7$	$10(10^{-3})(10^{-12}) = 10^{-14}$ sec^{-2}	10^{-7}	10^{-21}	10^{-12}
$2\omega_s = 45.4$	10^{-25} sec^{-2}	5×10^{-5}	5×10^{-30}	5×10^{-21}
$2\dot{\psi} = -90.8$	10^{-25} sec^{-2}	10^{-6}	10^{-31}	10^{-22}
$\sqrt{k_1 k_2}\,\omega_s = 22.5$	10^{-3} $(2 \times 10)(5 \times 10^{-4}) = 10^{-5}$ sec^{-2}	10^{-7}	10^{-12}	10^{-3}
$2\sqrt{k_1 k_2}\,\omega_s = 45.0$	$(5 \times 10^{-4})^2 = 2.5 \times 10^{-7}$ sec^{-2}	5×10^{-5}	10×10^{-12}	10^{-2}
$(1 + \sqrt{k_1 k_2})\,\omega_s = 45.2$	10^{-16} sec^{-2}	5×10^{-5}	5×10^{-21}	5×10^{-12}
$(1 - \sqrt{k_1 k_2})\,\omega_s = 0.227$	10^{-16} sec^{-2}	10^{-4}	10^{-20}	10^{-11}
$2(\omega_s + \dot{\psi}) = -45.4$	10^{-21} sec^{-2}	5×10^{-5}	5×10^{-26}	5×10^{-17}
$(\omega_s + 2\dot{\psi}) = -68.1$	$10(10^{-3})(10^{-10}) = 10^{-12}$ sec^{-2}	5×10^{-6}	5×10^{-18}	5×10^{-9}
$2(\omega_s + 2\dot{\psi}) = -136.2$	10^{-21} sec^{-2}	5×10^{-8}	5×10^{-29}	5×10^{-20}
$2\dot{\psi} + (1 + \sqrt{k_1 k_2})\,\omega_s = -45.6$	10^{-16} sec^{-2}	5×10^{-5}	5×10^{-21}	5×10^{-12}
$2\dot{\psi} + (1 - \sqrt{k_1 k_2})\,\omega_s = -90.6$	10^{-12} sec^{-2}	10^{-6}	10^{-22}	10^{-13}

T366

TABLE IV

Additional Components of Angular Acceleration Error

Frequency, rad/sec	Order of Magnitude of Amplitude	Multiplier	Error Equivalent	
			sec^{-2}	E.U.
dc = 0	10^{-8} sec^{-2}	10^{-4}	10^{-12}	10^{-3}
$2(\omega_s + \dot{\psi}) \simeq -45.4$	10^{-6} $(10^{-2}) = 10^{-8}$ sec^{-2}	10^{-4}	10^{-12}	10^{-3}
$\sqrt{k_1 k_2}\ \omega_s \simeq 22.5$	10^{-3} $(5 \times 10^{-4})(2 \times 10) = 10^{-5}$ sec^{-2}	10^{-5}	10^{-10}	10^{-1}
$(\omega_s + 2\dot{\psi}) \simeq -68.1$	10^{-3} $(10^{-10})(3 \times 10) = 3 \times 10^{-12}$ sec^{-2}	10^{-6}	3×10^{-18}	3×10^{-9}
$\omega_s = 22.7$	10^{-3} $(10^{-10})(10) = 10^{-12}$ sec^{-2}	10^{-5}	10^{-17}	10^{-8}

T367

m = Mass of one sensor arm

δ = Magnitude of sensor arm C.M. offset from pivot center

ℓ_k = Magnitude of sensor C.M. offset from spacecraft C.M. – k axis direction

ℓ_{ij} = Magnitude of sensor C.M. offset from spacecraft C.M. – i-j plane

a_x = Aerodynamic deceleration tangent to orbit

The dimensionless parameters

$$\frac{m\delta\ell_k}{I_1^3} \quad \text{and} \quad \frac{m\delta\ell_{ij}}{I_1^3}$$

should be approximately equal. Estimating their size:

$$m \sim 5 \text{ kg}$$

$$I_1^3 \sim 4.5 \times 10^6 \text{ g cm}^2$$

$$\delta \sim 10^{-2} \text{ cm}$$

$$\ell_k \sim \ell_{ij} \sim 1.0 \text{ cm} \quad .$$

$$\frac{m\delta\ell_k}{I_1^3} \sim \frac{m\delta\ell_{ij}}{I_1^3} \sim \frac{(5 \times 10^3)(10^{-2})(1)}{4.5 \times 10^6} \sim 10^{-5}$$

As indicated by the above $\Gamma_{\mu max}$ expression, there will be the full complement of rotational field and angular acceleration error frequencies but at amplitudes a factor of 2×10^{-5} times the Fig. 4 mass unbalance multipliers.

The error caused by aerodynamic drag has magnitude:

$$\left[\frac{2 \times (10^{-2})(5 \times 10^{3})}{4.5 \times 10^{6}}\right] (a_X)(5 \times 10^{-2}) \sim 5 \times 10^{-9} \text{ sec}^{-2} = 5 \text{ E.U.} \Bigg\} @\ \omega_s$$

where

$$(5 \times 10^{-2}) \approx \text{Mass unbalance multiplier at } \omega_s$$

and

$$a_X \approx \frac{1}{2} \frac{\rho V^2 A C_D}{M_{s/c}} = \frac{(2 \times 10^{-13})(7.4 \times 10^{5})^2 (3.04 \times 10^{3})}{6.85 \times 10^{4}}$$

$$\sim 5 \times 10^{-3} \text{ cm/sec}^2 \ ;$$

also, the $2\omega_k^2$ term in the $\Gamma_{\mu max}$ expression is dc and of magnitude:

$$10^{-5} (2\omega_s^2)(5 \times 10^{-2}) \sim 5 \times 10^{-4} \text{ sec}^{-2} = 5 \times 10^{5} \text{ E.U.}$$

The remaining mass unbalance errors are in the terms: $(\omega_i^2 + \omega_j^2)$, $(\omega_i + \omega_j)$, and $(\omega_i + \omega_j)\omega_k$. Rather than laboriously expanding the latter, it is easier to make certain observations. The magnitude of any error coming from $(\omega_i^2 + \omega_j^2)$ can be taken as roughly equal to the mass unbalance errors from $2\omega_i\omega_j$ which were explained previously. Also:

$$\omega_k(\omega_i + \omega_j) = \omega_s[\omega_x + \omega_y + (\beta - \alpha)\omega_s]$$

and

$$(\dot{\omega}_i + \dot{\omega}_j) = \dot{\omega}_x + \dot{\omega}_y + (\beta - \alpha)\ \dot{\omega}_z \ .$$

The $(\omega_x + \omega_y)\omega_s$ and $(\dot{\omega}_x + \dot{\omega}_y)$ parts each have amplitudes of the order of 10^{-12} due to the A, B, C, and D coefficients. The error caused by these terms will thus be of order 10^{-17} sec^{-2} for $(\dot{\omega}_x + \dot{\omega}_y)$ and 10^{-16} sec^{-2} for $\omega_s(\omega_x + \omega_y)$, times the Fig. 4 mass unbalance multipliers (all less than 1.0).

The remaining errors are $(\beta - \alpha)\omega_s^2$ and $(\beta - \alpha)\dot{\omega}_z$. $(\beta - \alpha)$ could be as small as 10^{-4} when $\alpha \sim \beta = 10^{-3}$. The error from $(\beta - \alpha)\omega_s^2$ would be dc and of order (10^{-4}) $(4 \times 10^2)(10^{-5})(5 \times 10^{-2})$ sec^{-2} = 2×10^{-8} sec^{-2} = 20 E.U. The errors from $(\beta - \alpha)\dot{\omega}_z$ will be $(10^{-4})(10^{-5}) = 10^{-9}$ times the amplitudes within $\dot{\omega}_z$. The latter amplitudes are listed in the second column of Table IV.

Summary of Mass Unbalance Errors
(values in sec^{-2})

- Less than (2×10^{-5}) x (column two, Table III) (from $\omega_i\omega_j$ terms)
- Less than 10^{-9} x (column two, Table IV) (From $(\beta - \alpha)\dot{\omega}_z$ terms)
- Aerodynamic drag: 5×10^{-9} @ ω_s
- Other dc errors:

  $2\omega_k^2$: 5×10^{-4}

  $(\beta - \alpha)\omega_k^2$: 2×10^{-8}

- Errors from $(\omega_x + \omega_y)\omega_s$: 10^{-14}
- Errors from $(\dot{\omega}_x + \dot{\omega}_y)$: 10^{-15}
- Errors from $(\omega_i^2 + \omega_j^2)$: less than (2×10^{-5}) x (column two Table III).

III. CONCLUSIONS

We may now look at this wealth of dynamic outputs and eliminate from consideration all these with magnitudes less than 0.01 E.U. (10^{-11} sec^{-2}) because these fall below the anticipated threshold noise level of the instrument.

The remaining outputs are listed in the following Table V.

TABLE V

Significant Gradiometer Errors Due to Sensor Satellite Dynamics

Error Ouputs	Frequency	Amplitude, Equivalent E.U.
Rotational Field During Function $(\omega_i\omega_j)$	dc	40
	$2\sqrt{k_1k_2}\ \omega_s$	10^{-2}
Sum Mode Mismatch $(\dot{\omega}_k)$	dc	0.4
	$\sqrt{k_1k_2}\ \omega_s$	10^{-1}
Mass Unbalance $(\Gamma_{\mu max})$	dc	5×10^5
	ω_s	5
	dc	20

T368

We observe that dc torques between the sensor arms do not generate any steady state signals because of the finite impedance across the transducer. In addition, those terms at or near the spin frequency will be cut by a factor of greater than 100 by the integrating circuits of the electronics.

This leaves only one term; term 2 of the rotational field driving function, which is on the threshold noise level and is close to the sensor detection frequency. If we trace this term back to its origins, we find that it is strongly dependent on θ (the coning angle). Any increase in this angle above the assumed 10^{-5} radians will cause signals above 10^{-2} E.U., which fluctuate as the square of this coning angle.

Therefore, it must be determined what control can be placed on θ to maintain it below 10^{-5} radians while data are being taken.

APPENDIX: DIMENSIONLESS FREQUENCY RESPONSE FUNCTIONS AS PLOTTED IN FIG. 4

Mass Unbalance

$$\frac{[S^2(2) + S(\alpha_1 + \alpha_2) + (\beta_1^2 + \beta_2^2)]\ \frac{\omega_0^2}{Q}}{(S^2 + \alpha_{12} S + \beta_{12}^2)\left(S^2 + \frac{\omega_0}{Q} S + \omega_0\right)} = \frac{[(\beta_2^2 + \beta_1^2) - 2\omega^2 + j\omega(\alpha_1 + \alpha_2)]\ \frac{\omega_0^2}{Q}}{(\beta_{12}^2 - \omega^2 + j\omega\alpha_{12})\left(\omega_0^2 - \omega^2 + j\omega\frac{\omega_0}{Q}\right)}$$

Rotational Field

$$\frac{\omega_0^2}{Q}\ \frac{[S^2(\gamma_1 - \gamma_2) + S(\alpha_2\gamma_1 - \alpha_1\gamma_2) + (\beta_2^2\gamma_1 - \beta_1^2\gamma_2)]}{(S^2 + \alpha_{12} S + \beta_{12}^2)\left(S^2 + \frac{\omega_0}{Q} S + \omega_0\right)} = \frac{[(\beta_2^2\gamma_1 - \beta_1^2\gamma_2) - \omega^2(\gamma_1 - \quad) + j\omega(\alpha_2\gamma_1 - \alpha_1\gamma_2)]\ \frac{\omega_0}{Q}}{(\beta_{12}^2 - \omega^2 + j\omega\alpha_{12})\left(\omega_0^2 - \omega^2 + j\omega\ \frac{\omega_0}{Q}\right)}$$

Angular Acceleration

$$\frac{[(\alpha_1 - \alpha_2)\ S + (\beta_1^2 - \beta_2^2)]\ \frac{\omega_0^2}{Q}}{(S^2 + \alpha_{12} S \quad \beta_{12}^2)\left(S^2 + \frac{\omega_0}{Q} S + \omega_0^2\right)} = \frac{[(\beta_1^2 - \beta_2^2) + (\alpha_1 - \alpha_2) j\omega]\ \frac{\omega_0^2}{Q}}{(\beta_{12}^2 - \omega^2 + j\omega\alpha_{12})\left(\omega_0^2 - \omega^2 + j\omega\ \frac{\omega_0}{Q}\right)}$$

APPENDIX D

AAFE ARM DESIGN

APPENDIX D

AAFE ARM DESIGN

Several requirements are imposed on the design of the arms of the rotating gravity gradiometer (Fig. D-1). Of primary importance is the fact that the structure must be isoelastic, i.e., the bending and longitudinal stiffnesses of the arm must be equal, and as large as practical. Also, the rotational stiffness (tangential motion of the end masses while the center is held fixed), as well as the flapping stiffness, i.e., rotation about an axis normal to the spin-axis, should be as large as practical.

For the AAFE sensor, it is desirable to have the ratio of arm width to length as small as possible to keep weight down and moment of inertia efficiency up, and to allow for electronic packaging space between the arms.

Several arm design configurations have been considered; the one described and analyzed herein, however, appears to best meet all the foregoing requirements.

A. LOAD ANALYSIS

1. Bending Load

P_B is the ma acceleration force acting on the arm end mass. The tensile force, R, in the upper arm strut causes a compressive force, F, in the upper support web. From the defined geometry, it can be seen that

$$R_B = \frac{\ell}{2h} P_B$$

$$T_B = \frac{b}{2h} P_B$$

$$F_B = \frac{P_B}{2}$$

2073-33

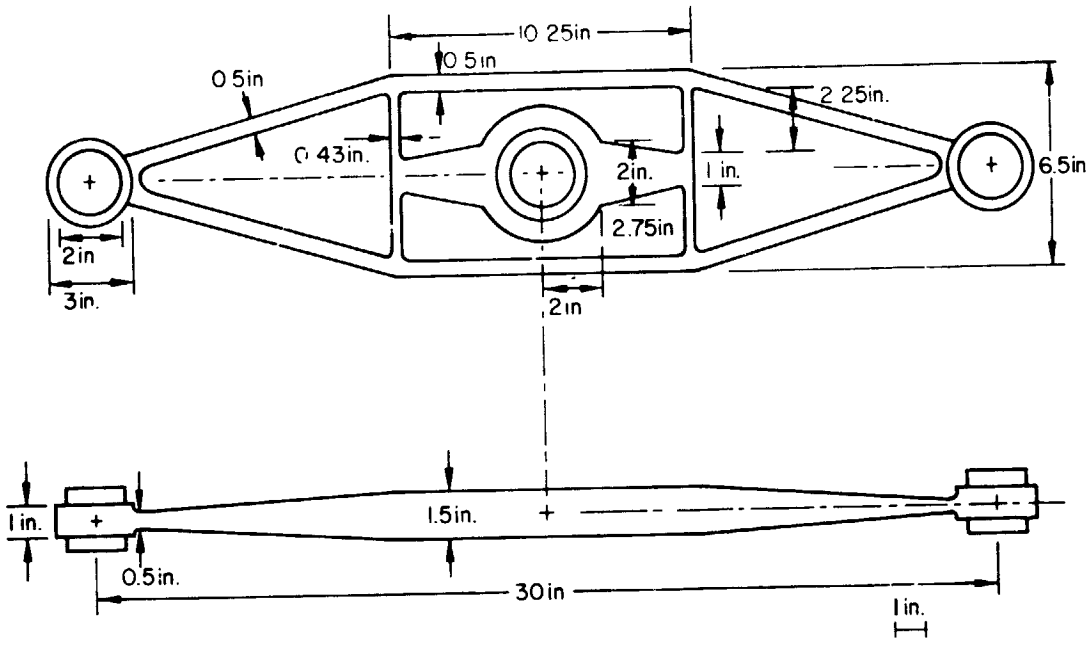

Fig. D-1(a). Sensor Arm Design.

M8707

Fig. D-1(b). Sensor Arm Photo.

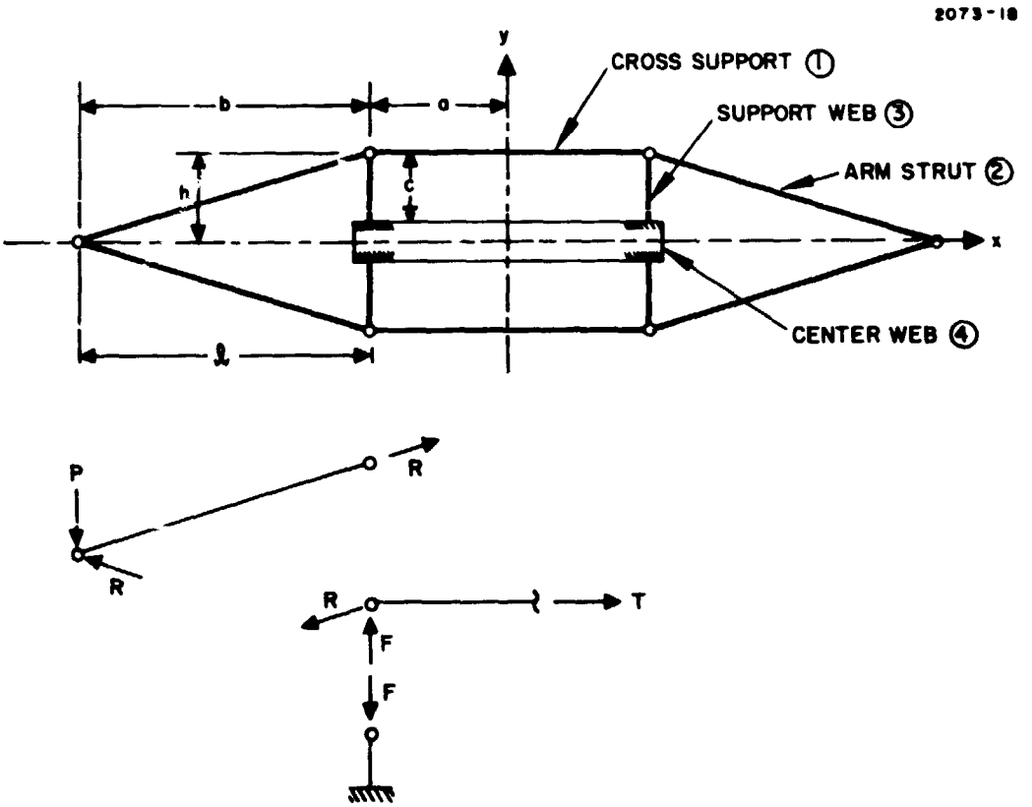

Fig. D-1(c). nsor Arm Schematic.

2. Longitudinal Load

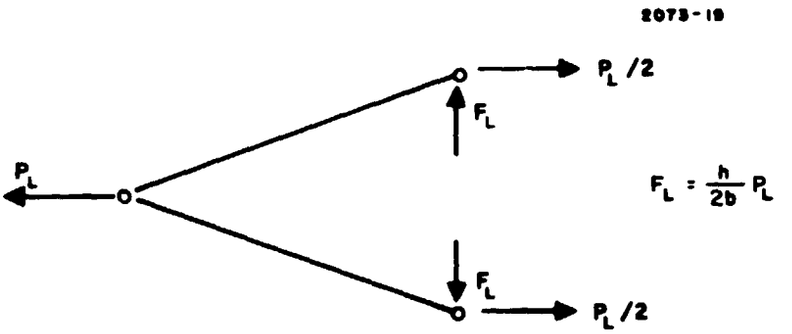

Fig. D-2. Longitudinal Loading Diagram.

For a longitudinal acceleration load, the cross support will carry no load. Each support web will bend to react with $P_L/2$ induced force. The tension in the arm strut is:

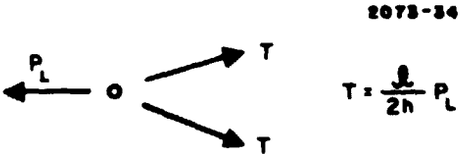

Fig. D-3. Arm Strut Tension Diagram.

B. DEFLECTION ANALYSIS

For a bending load, we may analyze only half the structure, since it is assumed symmetrical.

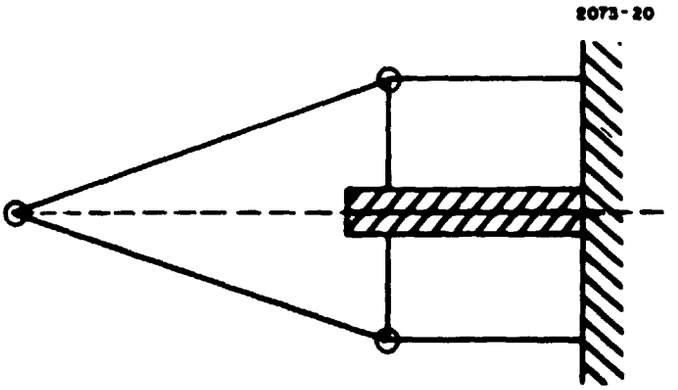

Fig. D-4. Schematic.

It will be assumed that the horizontal resistive force provided by bending of the support webs is negligible. Hence, the deflection picture may be composed of two portions: axial deflection of the cross supports plus axial deflection of the arm struts. The cross supports will contribute to the end vertical deflection as follows:

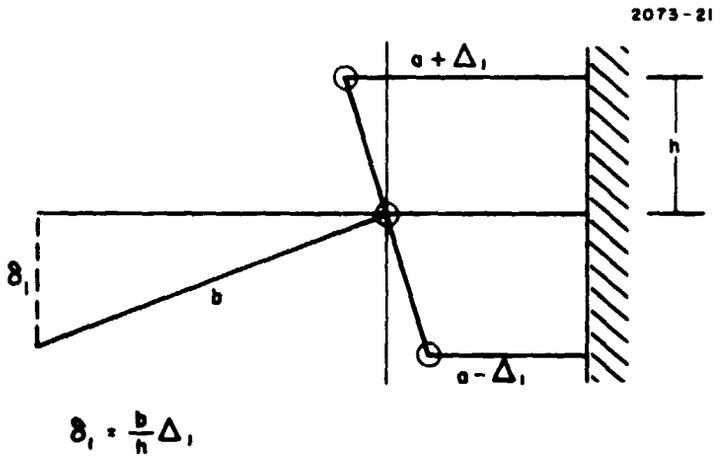

$$\delta_1 = \frac{b}{h}\Delta_1$$

Fig. D-5.
Bending Load Diagram.

To compute the end vertical deflection caused by axial deflection of the arm struts, note that the locus of the end point deflection is the intersection of two arcs of a circle swung from the point of attachment of the arm struts to the cross supports:

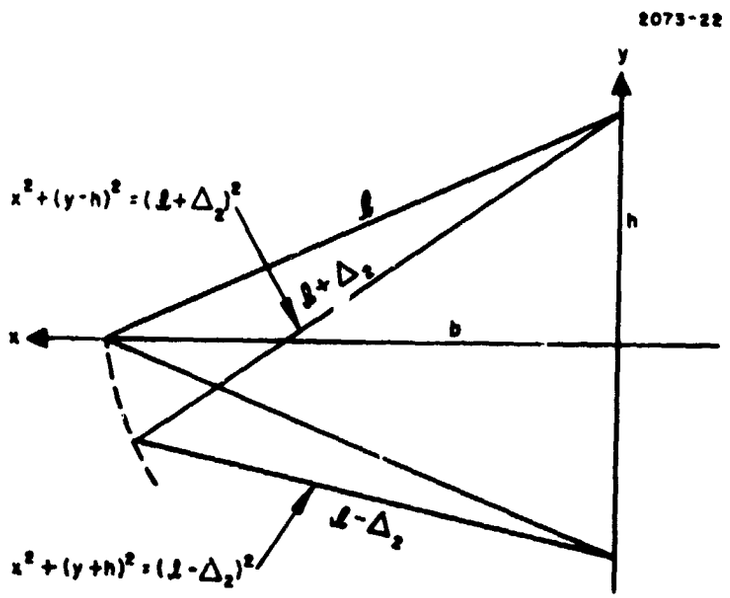

Fig. D-6.
Deflection Diagram.

Simultaneous solution of the equations of these circles yields

$$\delta_2 \triangleq y = -\frac{\ell}{h}\Delta_2$$

$$x = b\sqrt{1 - \left(\frac{\Delta_2}{h}\right)^2}$$

Note that the x component of this deflection is second order and therefore negligible.

The total vertical deflection of the arm end is therefore

$$\boxed{\delta_B = \delta_1 + \delta_2 = \frac{b}{h}\Delta_1 + \frac{\ell}{h}\Delta_2}$$

Δ_1 and Δ_2 can be computed in terms of the vertical load, P, as follows. The axial deflection of a member is $\Delta = P\ell/AE$ where

P = axial force

ℓ = length of member

A = cross section area

E = Young's modulus .

For a tapered member of the following dimension:

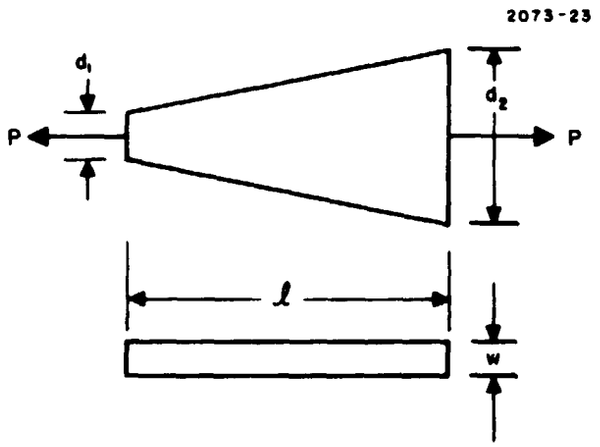

Fig. D-7. Tapered Member Dimension.

the axial deflection is given by:

$$\Delta = \frac{P\ell}{E(d_2 - d_1)\omega} \ln \frac{d_2}{d_1} \triangleq \frac{P\ell}{A_{eff} E}$$

$$A_{eff} = \frac{(d_2 - d_1)\omega}{\ln\left(\frac{d_2}{d_1}\right)}$$

Hence, Δ, is given by

$$\Delta_1 = \frac{T_a}{A_1 E} = \frac{ba}{2h A_1 E} P_B$$

and

$$\Delta_2 = \frac{R\ell}{A_2 E} = \frac{\ell^2}{2h A_2 E} P_B$$

The total vertical deflection δ_B is then:

$$\delta_B = \frac{b}{h} \Delta_1 + \frac{\ell}{h} \Delta_2$$

$$= \left(\frac{ab^2}{2h^2 A_1 E} + \frac{\ell^3}{2h^2 A_2 E} \right) P_B$$

$$\boxed{\delta_B = \frac{P_B}{2h^2 E} \left(\frac{ab^2}{A_1} + \frac{\ell^3}{A_2} \right)}$$

For longitudinal end loads, the deflections of the arm struts and the deflection of the support web comprise the total deflection. Because of symmetry, only half the structure need be analyzed.

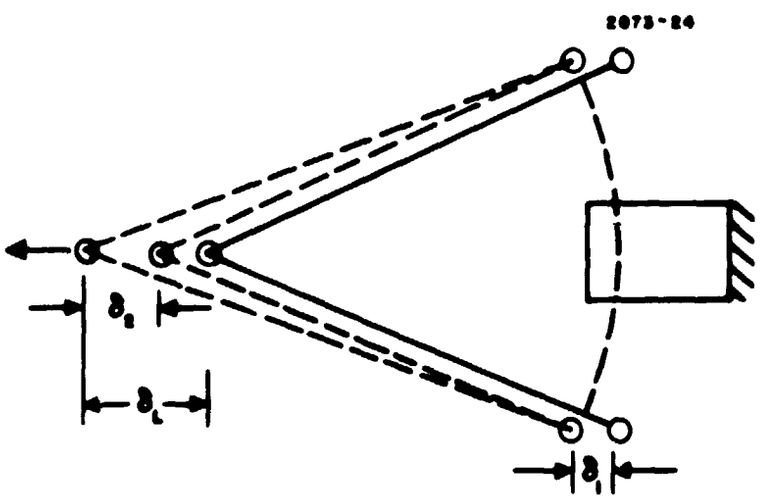

Fig. D-8. Total Deflection Diagram.

The total end deflection, δ_2, is composed of the support web bending deflection, Δ_1 plus the arm struts axial deflection, Δ_2.

The bending deflection, δ_1 is:

$$\delta_1 = \frac{P_L c^3}{6EI}$$

The deflection Δ_2 may be derived as follows:

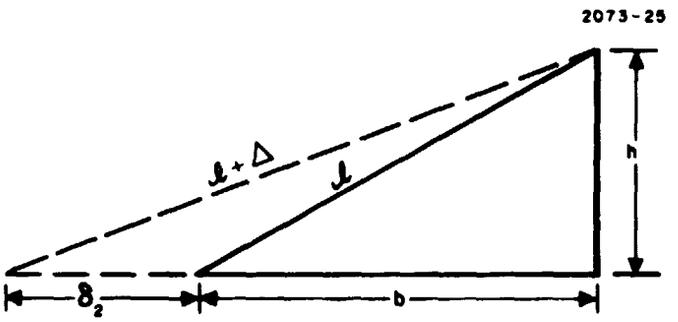

Fig. D-5. Deflection Diagram.

By using the Pythagorean theorem

$$(\ell + \Delta)^2 = (b + \delta_2)^2 + h^2$$

and

$$\ell^2 = b^2 + h^2 ,$$

subtracting, and ignoring the second order terms,

$$\delta_2 = \frac{\ell}{b} \Delta ,$$

Δ is now given by

$$\Delta = \frac{T\ell}{A_2 E} = \frac{P_L \ell^2}{2h\, A_2 E}$$

and δ_2 is

$$\delta_2 = \frac{\ell}{b} \cdot \frac{P_L \ell^2}{2h\, A_2 E} = \frac{P_L \ell^3}{2bh\, A_2 E}$$

$$\delta_L = \delta_1 + \delta_2 = \frac{P_L c^3}{6EI} + \frac{P_L \ell^3}{2bh\, A_2 E}$$

or

$$\boxed{\delta_L = \frac{P_L}{6E}\left(\frac{3\ell^3}{bhA_2} + \frac{c^3}{I}\right)}$$

where I is the section moment of inertia of the support web.

C. CROSS-SECTION PROPERTIES

2073-26

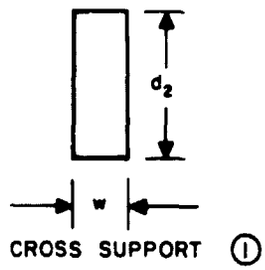

CROSS SUPPORT ①

$$A_1 = w\, d_2$$

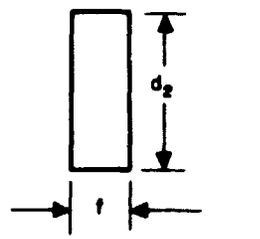

SUPPORT WEB ③

$$I = \frac{d_2\, t^3}{12}$$

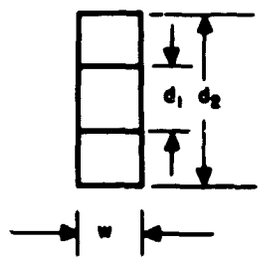

$$A_{2_{eff}} = \frac{(d_2 - d_1)\, w}{\ln\left(\frac{d_2}{d_1}\right)}$$

Fig. D-10. Tapered Member.

D. NUMERICAL EVALUATION

Assume the following arm dimensions:

$a = 5$ in. $\qquad f =$ to be determined

$b = 10$ in. $\qquad h = 3$

$c = 1.25$ in. $\qquad \ell = \sqrt{h^2 + b^2} = 11.18$ in.

$d_1 = 0.5$ in. $\qquad \omega = 0.5$ in.

$d_2 = 1.5$ in.

The width of the support web, f, will be determined by making $\delta_B = \delta_L$ for $P_B = P_L$, i.e., an isoelastic configuration. The cross-section properties are:

$$A_1 = w d_2 = 0.5 \times 1.5 = 0.75 \text{ in.}^2$$

$$A_{2_{eff}} = \frac{(1.5 - 0.5) \times 0.5}{\ln 3} = \frac{0.5}{1.1} = 0.455 \text{ in.}^2$$

$$I = \frac{d_2 f^3}{12} = \frac{1.5}{12} f^3 = 0.125 f^3 \text{ in.}^4 \text{ (f in in.)}$$

The end bending deflection is:

$$\frac{\delta_B}{P_{B/E}} = \frac{1}{2h^2}\left(\frac{ab^2}{A_1} + \frac{\ell^3}{A_2}\right) = \frac{1}{18}\left(\frac{500}{0.75} + \frac{\overline{11.18}^3}{0.455}\right)$$

$$= 0.0555\,(667 + 3,680) = 38 + 204 = 242 \text{ in.}^{-1}$$

204 — relative deflection of arm strut or 84.5%

38 — relative deflection of cross support or 15.5%

The end longitudinal deflection is:

$$\frac{\delta_L}{P_L/E} = \frac{1}{6}\left(\frac{3\ell^3}{bh\,A_2} + \frac{c^3}{I}\right) = \frac{1}{6}\left(\frac{3 \times \overline{11.18}^3}{10 \times 3 \times 0.455} + \frac{\overline{1.25}^3}{0.125\,f^3}\right)$$

$$= 0.1667\left(307 + \frac{15.625}{f^3}\right) = 51 + \frac{2.605}{f^3}$$

Equating the two normalized deflections

$$242 = 51 + \frac{2.605}{f^3}$$

or

$$f^3 = \frac{2.605}{242 - 51} = 0.01362$$

or

$$f = 0.239 \text{ in.}$$

$$\frac{\delta_L}{P_L/E} = 51 + 191 = 242$$

191 — relative deflection of support web or 79%

51 — relative deflection of arm strut or 21%.

Absolute spring ratio for aluminum arm:

$$K = \frac{P_L}{\delta_L} = \frac{P_L/E}{\delta_L} \times E = \frac{10 \times 10^6}{242} = 41,300 \text{ lb/in.}$$

$$f_n = \frac{1}{2\pi}\sqrt{\frac{K}{m}} = \frac{1}{2\pi}\sqrt{\frac{41,300 \times 454 \times 386}{2000}} = 303 \text{ Hz}.$$

E. ROTATIONAL STIFFNESS

2073-27

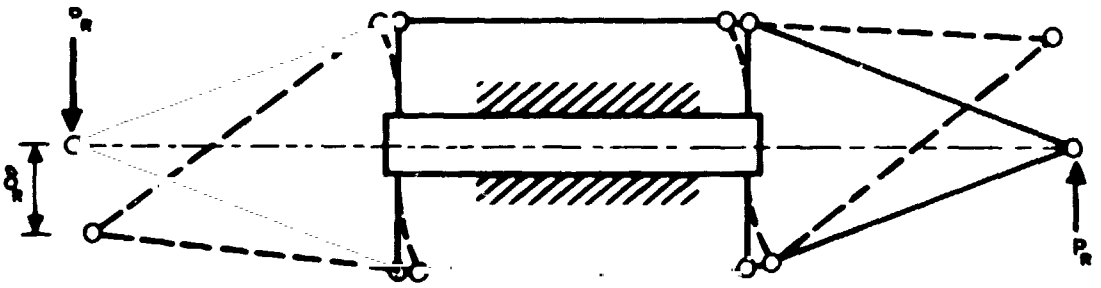

Fig. D-11. Moment Loading Bending Diagram.

For the indicated loading, the cross supports carry no load. Bending deflection of the support webs and axial deflection of the arm struts account for the total arm end point deflection, δ_R.

1. Loads Analysis

The loads induced in the structure are similar to those previously derived. The tension (or compression) in the arm struts is

$$R_R = \frac{\ell}{2h} P_R .$$

The force acting to bend the support webs is

$$F_R = \frac{b}{2h} P_R$$

2. Deflection Analysis

The total deflection of the arm end point, δ_R, is

$$\delta_R = \delta_1 + \delta_2$$

where

δ_1 = the vertical deflection of the arm end point caused by bending deflection of the support webs

δ_2 = the vertical deflection of the arm end point caused by axial deflection of the arm struts.

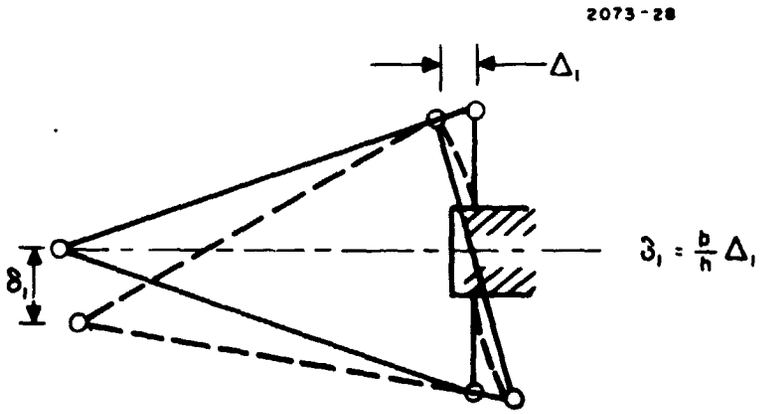

Fig. D-12. Bending Diagram.

δ_1 is computed as

$$\delta_1 = \frac{b}{h} \Delta_1$$

where

$$\Delta_1 = \frac{F_R c^3}{3EI} = \frac{b c^3}{6hEI} P_R$$

or

$$\delta_1 = \frac{b^2 c^3}{6h^2 EI} P_R .$$

δ_2 is computed as before, i. e.,

$$\delta_2 = \frac{\ell}{h} \Delta_2$$

where

$$\Delta_2 = \text{axial deflection of arm struts} = \frac{R\ell}{A_2 E} = \frac{\ell^2}{2hA_2 E} P_R$$

whence

$$\delta_2 = \frac{\ell^3}{2h^2 A_2 E} P_R$$

The total deflection is

$$\delta_R = \delta_1 + \delta_2 = \left(\frac{b^2 c^3}{6I} + \frac{\ell^3}{2A_2} \right) \frac{P_R}{Eh^2}$$

For the arm design parameters (see page 180), this rotational stiffness can be evaluated as follows:

$$I = 0.125\, f^3 = 0.125 \times 0.01362 = 0.001703 \text{ in.}^4$$

$$A_{2_{eff}} = 0.455 \text{ in.}^2$$

$$\frac{\delta_R}{P_{R/E}} = \frac{1}{h^2}\left(\frac{b^2 c^3}{6I} + \frac{\ell^3}{2A_2}\right) = \frac{1}{9}\left(\frac{100 \times \overline{1.25}^3}{6 \times 0.001703} + \frac{\overline{11.18}^3}{2 \times 0.455}\right)$$

$$= \frac{1}{9}\left(19,130 + 1535\right) = 2130 + 171 = 2301$$

171 — relative deflection of arm strut or 7.4%

2130 — relative deflection of support web or 92.6%.

Absolute spring rate (for aluminum):

$$K_R = \frac{P_R}{\delta_R} = \frac{P_{R/E}}{\delta_L} \times E = \frac{10 \times 10^6}{2301} = 4350 \text{ lb/in.}$$

Natural rotation mode frequency:

$$f_R = \frac{1}{2\pi}\sqrt{\frac{K}{m}} = \frac{1}{2\pi}\sqrt{\frac{4350 \times 454 \times 386}{2000}} = 98 \text{ Hz}.$$

F. MASS AND MOMENT OF INERTIA ANALYSIS

Weights and mass moments of inertia of all component parts of the structure are computed, assuming the arm material is aluminum with a weight density of 0.1 lb/in.^{3}.

1. Weight Estimate

a. Arm Strut

$$W = \rho V = 0.1 \times 9 \times \frac{1}{2} \times \frac{1.5 + 0.5}{2} = 0.45 \text{ lb}$$

b. Cross Support

$$W = \rho V = 0.1 \times 10.25 \times \frac{1}{2} \times 1.5 = 0.77 \text{ lb}$$

c. Support Web

$$W = \rho V = 0.1 \times 2.25 \times 0.430 \times 1.5 = 0.145 \text{ lb}$$

d. Central Web

1. Ring $W = 0.1 \times \frac{\pi}{4} \left(4.25^2 - 3^2\right) \times 1.5 = 1.07 \text{ lb}$

2. Webs $W = 2 \times 0.1 \times \frac{2+1}{2} \times 2.75 \times 1.5 = 1.24 \text{ lb}$

Total center web 2.31 lb

e. End Masses

$W = \frac{2000}{454} \times 2$ (includes aluminum ring) = 8.80 lb

f. Summary

	(lb)
Arm Struts	1.80
Cross Supports	1.54
Support Webs	0.58
Central Web	2.31
End Masses	8.80
Total Arm Weight	15.03 lb

2. Moment of Inertia Estimates

a. Arm Strut

Assume it is a line mass with linearly varying weight distribution over its length:

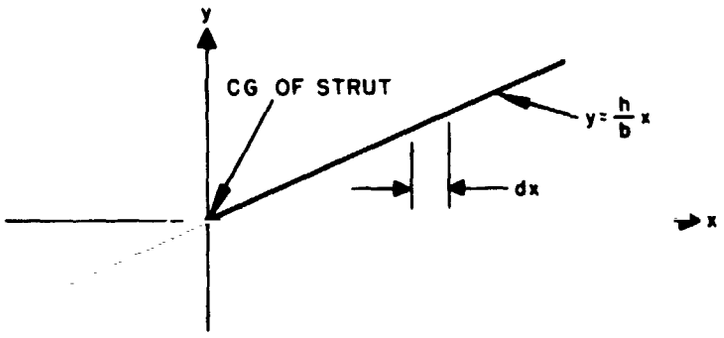

Fig. D-13. Mass Distribution Diagram.

$$I_{xx_o} = \int y^2\, dm \qquad dm = \rho A \frac{\ell}{h}\, dx \qquad m = \int dm = \frac{2}{3}\rho \ell A_o$$

$$A = A_o - \frac{A_o - A_h}{h}\, x = A_o \left[1 - \frac{r}{h}\, x\right]$$

$$\gamma \triangleq \frac{A_o - A_h}{A_o} = \text{taper ratio} = \frac{2}{3}$$

$$dm = \rho A_o \left[1 - \frac{\gamma}{h} x\right] \frac{\ell}{h} dx$$

$$I_{xx_o} = \frac{\ell}{h} \int_{-h/3}^{+2h/3} \left(\frac{h}{b}\right)^2 x^2 \rho A_o \left(1 - \frac{\gamma}{h} x\right) dx = 0.096 \rho A_o \frac{h^4 \ell}{b^2}$$

$$= 0.096 \times \frac{3}{2} m \frac{h^4}{b^2} = 0.096 \times \frac{3}{2} \times 0.45 \times \frac{3^4}{10^2} = 0.0525 \text{ lb-in.}^2$$

$$I_{xx} = I_{xx_o} + Wy^2 = 0.0525 + 0.45 \times \left(\frac{2}{3} \times 3\right)^2 = \underline{\underline{1.852 \text{ lb-in.}^2}}$$

$$I_{yy_o} = \int x^2 \, dm = \left(\frac{b}{h}\right)^2 I_{xx_o} = 0.0525 \left(\frac{10^2}{3^2}\right) = 0.583 \text{ lb-in.}^2$$

$$I_{yy} = I_{yy_o} + Wx^2 = 0.583 + 0.45 \times \left(5.125 + \frac{3}{3}\right)^2 = \underline{\underline{17.46 \text{ lb-in.}^2}}$$

Because of the "line mass" assumption, $I_{zz} = I_{xx} + I_{yy}$,

$$I_{zz} = 1.852 + 17.46 = \underline{\underline{19.31 \text{ lb-in.}^2}}$$

b. Cross Support

Assume a "line mass" distribution:

$$I_{xx_o} = 0$$

$$I_{xx} = mr^2 = 0.77 \times 3^2 = \underline{\underline{6.93 \text{ lb-in.}^2}}$$

$$I_{yy} = \frac{m\ell^2}{12} = \frac{0.77}{12} \times \overline{10.25}^2 = \underline{\underline{6.75 \text{ lb-in.}^2}}$$

$$I_{zz} = I_{xx} + I_{yy} = \underline{\underline{13.68 \text{ lb-in.}^2}}$$

c. Support Web

$$I_{xx} = \frac{m\ell^2}{12} + mr^2 = 0.145 \times \left[\frac{\overline{2.25}^2}{12} + \overline{1.625}^2\right] = \underline{\underline{0.44 \text{ lb-in.}^2}}$$

$$I_{yy} \cong mr^2 = 0.145 \times \overline{5}^2 = \underline{\underline{3.62 \text{ lb-in.}^2}}$$

$$I_{zz} \cong 0.44 + 3.62 = \underline{\underline{4.06 \text{ lb-in.}^2}}$$

d. Center Web

1. Ring

$$I_{xx} = I_{yy} = m\frac{r_1^2 + r_2^2}{4} = \frac{1.07}{4}\left(\overline{2.125}^2 + \overline{1.5}^2\right) = \underline{\underline{1.81 \text{ lb-in.}^2}}$$

$$I_{zz} = 2I_{xx} = \underline{\underline{3.62 \text{ lb-in.}^2}}$$

2. Webs (Both)

$$I_{xx} = m\frac{\ell^2}{12} = 1.24 \times \frac{2^2}{12} = \underline{\underline{0.41 \text{ lb-in.}^2}}$$

$$I_{yy} = m\frac{\ell^2}{12} + mr^2 = 1.24\left(\frac{\overline{2.75}^2}{12} + \overline{3.3}^2\right) = 14.28 \text{ lb-in.}^2$$

$$I_{zz} = 0.41 + 14.28 = \underline{\underline{14.69 \text{ lb-in.}^2}}$$

e. End Masses

1. Aluminum Arm End

$$W_{end} = \rho\frac{\pi}{4}\left(d_2^2 - d_1^2\right)\ell = \frac{\pi}{4}\left(3^2 - 2^2\right) \times 1.0 \times 0.1 = 0.392 \text{ lb}$$

$$I_{xx} = m\left[\frac{r_1^2 + r_2^2}{4} + \frac{\ell^2}{12}\right] = 0.392\left[\frac{\overline{1.5}^2 + \overline{1.0}^2}{4} + \frac{1^2}{12}\right] = \underline{\underline{0.351 \text{ lb-in.}^2}}$$

$$I_{yy} = I_{xx} + m\ell^2 = 0.351 + 0.392 \times \overline{15}^2 = \underline{\underline{88.55 \text{ lb-in.}^2}}$$

$$I_{zz} = m\frac{r_1^2 + r_2^2}{2} + m\ell^2 = 0.392\frac{\overline{1.5}^2 + \overline{1.0}^2}{2}$$

$$+ 0.392 \times \overline{15}^2 = \underline{\underline{88.84 \text{ lb-in.}^2}}$$

2. Tungsten Masses

$$W = 4.4 - 0.392 = 4.008 \text{ lb}$$

$$\ell = \frac{4W}{\rho\pi d^2} = \frac{4 \times 4.008}{0.6 \times \pi \times 2^2} = 2.125 \text{ in.}$$

$$I_{xx} = m\left(\frac{r^2}{4} + \frac{\ell^2}{12}\right) = 4.008\left(\frac{1^2}{4} + \frac{\overline{2.125}^2}{12}\right) = \underline{2.51 \text{ lb-in.}^2}$$

$$I_{yy} = I_{xx} + m\ell^2 = 2.51 + 4.008 \times \overline{15}^2 = \underline{904.31 \text{ lb-in.}^2}$$

$$I_{zz} = m\frac{r^2}{2} + m\ell^2 = 4.008\left(\frac{1^2}{2} + \overline{15}^2\right) = \underline{903.80 \text{ lb-in.}^2}$$

3. Moment of Inertia Summary

TABLE D-I

Moment of Inertia Summary

Item	Quantity	I_{xx}	I_{yy}	I_{zz}	I_{xx}	I_{yy}	I_{zz}
Arm Strut	4	1.85	17.46	19.31	7.40	69.80	77.30
Cross Support	2	6.93	6.75	13.68	13.86	13.50	27.36
Support Web	4	0.44	3.62	4.06	1.76	14.50	16.24
Center Web Ring	1	1.81	1.81	3.62	1.81	1.81	3.62
Center Webs	1	0.41	14.28	14.69	0.41	14.28	14.69
Alum. Arm End	2	0.35	88.55	88.84	0.70	177.10	177.68
Tungsten Masses	2	2.51	904.31	903.80	5.02	1808.62	1807.60
Totals for one arm					30.96	2099.61	2124.49

Inertia efficiency ratio:

$$\eta = \frac{I_{yy} - I_{xx}}{I_{zz}} = \frac{2099.61 - 30.96}{2124.49} = 97.4\%$$

APPENDIX E

DETERMINATION OF A NON-ECLIPSE ORBIT FOR GRADIOMETER SATELLITE

APPENDIX E

DETERMINATION OF A NON-ECLIPSE ORBIT FOR GRADIOMETER SATELLITE

A. SUMMARY

It appears possible to launch the gradiometer satellite into a polar orbit of the earth, which will not cause the satellite to be eclipsed by the earth even though only a relatively low orbit has been achieved. Depending on the orbit altitude, it is possible to achieve non-eclipse periods several times or more longer than the approximately one-week period necessary for complete surface coverage. The advantages of the non-eclipse orbit are the weight reduction and reliability increase associated with no dependence on chemical batteries. Also, because the gravity gradient sensor output is thermally sensitive, the required thermal control system would, therefore, have only one state of thermal equilibrium to contend with rather than cycling between two. The trade-off does not seem too severe. A launch window is created which previously was not a mission constraint.

Figure E-1 shows the earth at the time of the vernal equinox (around March 21). The [illegible] seen looking down from the north ecliptic pole (NEP). The [illegible]rth and south celestial poles (NCP and SCP) are each ~23-1/2° away fr[illegible] the a[illegible]ent ecliptic poles and at the times of vernal and autumnal equi[illegible]s lie on the terminator.

The terminator rotates [illegible] rclockwise about the polar axis to the ecliptic (passing through NE[illegible]) as the earth orbits the sun. The terminator rotates with the earth's orbital angular velocity, which is about 1°/day. Considering the time around the vernal equinox: If the satellite is placed in a polar orbit plane that coincides with the terminator plane at the time of the vernal equinox, then no eclipse of the satellite will occur at the time of the vernal equinox. If the satellite is launched into the latter orbit some days before the vernal equinox, the orbit plane and terminator plane intersect at an angle, θ, whose vertex is at the NEP (Fig. E-2).

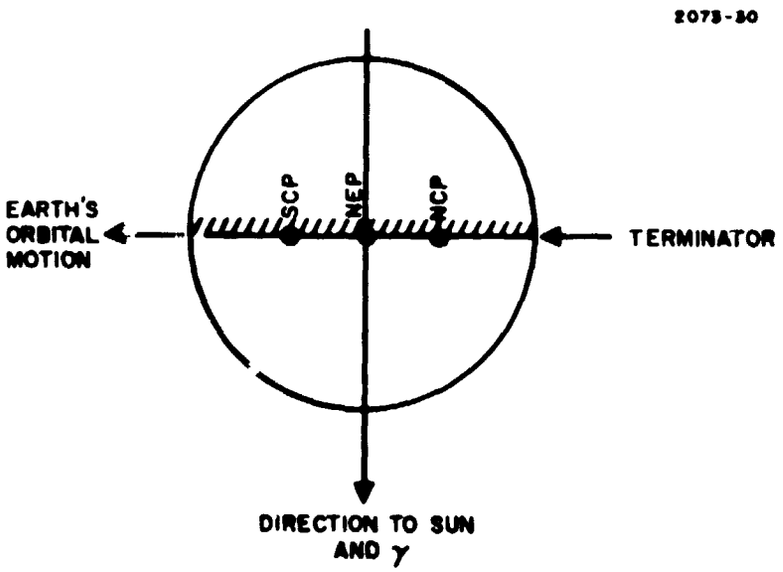

Fig. E-1. Earth at Vernal Equinox.

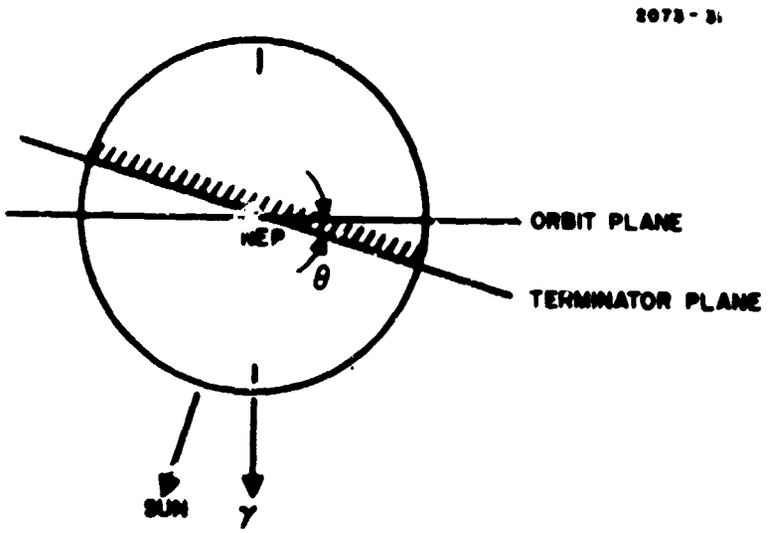

Fig. E-2. Earth Position Several Days Before Vernal Equinox.

The main question becomes: How large can θ be for a given altitude of the specified orbit with the satellite not eclipsed as it travels over the dark area of the earth? An answer to this question gives the non-eclipse period (maximum), which is centered at each equinox and is of duration:

$$\text{Time of non-eclipse} \cong \frac{2\theta^{\circ}}{1^{\circ}/\text{DAY}}$$

B. DETERMINING MAXIMUM θ

One method for finding θ_{max} is to project the circular orbit onto the terminator plane and determine if the projection anywhere dips within the circular intersection of the earth and terminator plane. This formulation tacitly assumes that the shadow of the earth is cylindrical when in reality the umbral shadow is conical with a cone half-angle of about 0.5°. However, since the cone half-angle is so small, the simple approximation of a cylindrical shadow will be used:

Let x_1, y_1 be the rectangular orbital coordinates of the satellite in the orbital plane (Fig. E-3). Then

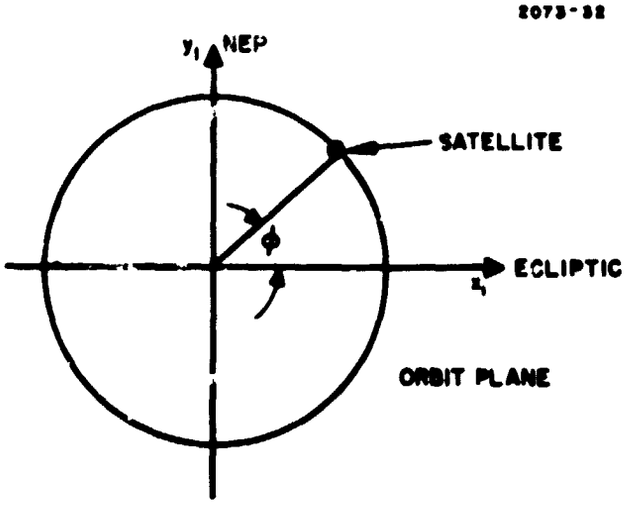

Fig. E-3.
Orbit Plane.

$x_1 = (R_o + h) \cos \phi$ $\quad$ R_o = Earth Radius = 6371 km

$y_1 = (R_o + h) \sin \phi$ $\quad$ h = Orbit Altitude

Let the terminator plane projections of these coordinates be x, y. Then

$$x = x_1 \cos \theta = (R_o + h) \cos \phi \cos \theta$$

$$y = y_1 = (R_o + h) \sin \phi$$

The condition for non-eclipse is:

$$\sqrt{x^2 + y^2} > R_o$$

which results in:

$$\left[\left(R_o + h\right)^2 \cos^2 \phi \cos^2 \theta + \left(R_o + h\right)^2 \sin^2 \phi\right]^{1/2} > R_o .$$

Squaring to get

$$\cos^2 \phi \cos^2 \theta + \sin^2 \phi > \frac{R_o^2}{\left(R_o + h\right)^2} .$$

Then

$$1 + \cos^2 \phi \left(\cos^2 \theta - 1\right) > \frac{1}{1 + \frac{2h}{R_o} + \frac{h^2}{R_o^2}}$$

Since $h^2/R_o^2 << 2\,h/R_o$, neglect h^2/R_o^2 and make approximation:

$$1 + \cos^2\phi\,(\cos^2\theta - 1) \gtrsim 1 - \frac{2h}{R_o}$$

The result is:

$$\cos^2\phi < \frac{2h}{R_o\,(1 - \cos^2\theta)} \qquad \text{(non-eclipse condition)}$$

Since $0 \leq \cos^2\phi \leq 1$, the non-eclipse condition must satisfy the most severe constraint:

$$\frac{2h}{R_o\,(1 - \cos^2\theta)} > 1$$

Hence,

$$\cos^2\theta > 1 - \frac{2h}{R_o}$$

$$|\cos\theta| > \left(1 - \frac{2h}{R_o}\right)^{1/2}$$

$$\boxed{|\cos\theta| \gtrsim \left(1 - \frac{h}{R_o}\right)} \qquad \text{(non-eclipse condition)}$$

The duration vs. altitude of non-eclipse orbits is shown in Table E-1.

TABLE E-1

Duration vs Altitude of Non-eclipse Orbits

h (km)	h/R_o	$(1 - h/R_o)$	θ°_{max}	Duration = $2\theta_{max}/1^\circ$/Day (Days)	
250	0.0392	0.9608	$16^\circ\ 6'$	32	
275	0.0431	0.9569	$16^\circ\ 53'$	34	
300	0.0471	0.9529	$17^\circ\ 39'$	35	Launch Window is Equal to Duration Minus Minimum Required Mission Time
325	0.0510	0.9490	$18^\circ\ 22'$	37	
350	0.0550	0.9450	$19^\circ\ 5'$	38	
375	0.0589	0.9411	$19^\circ\ 46'$	40	Launch Windows Occur Twice per Year
400	0.0629	0.9371	$20^\circ\ 26'$	41	

C. SOLAR CELL POWER GENERATION IN NON-ECLIPSE ORBIT

Since the satellite will have its spin axis perpendicular to the non-eclipse orbit plane, the bulk of the power will have to come from solar cells mounted on the sun-facing end of the cylinder (Fig. E-4).

The tentative 76 cm configuration to fit the internal diameter of Scout has a 4550 cm^2 area for the cylinder end. At 61.5×10^{-3} watts per cell, each of which has 4 cm^2 area, the power available from the end solar cells is:

$$P_{\substack{END \\ \theta=0^\circ}} = \frac{4550\ cm^2}{4\ cm^2/cell} \times \frac{61.5 \times 10^{-3}\ watts}{cell} = 70\ watts$$

For the θ excursions to be expected over mission lifetime resulting from terminator rotation, the latter power will decrease by $(1 - \cos\theta)$ or from 4 to 7% for 250- to '50-km orbits.

By contrast, were the current configuration to go into an eclipsing orbit with the sun vector perpendicular to the cylindrical wall, a substantial power available reduction would result. The rectangular cross section = 76 (40) = 3040 cm^2 leading to:

$$P = \frac{3040}{4550} \times 70 = 47 \text{ watts} .$$

The 47 watts would hardly be sufficient to operate the spacecraft and recharge batteries. But 70 watts should be sufficient for operation in a non-eclipse orbit.

APPENDIX F

RGG TORQUES RESULTING FROM PARAMAGNETIC ARMS

APPENDIX F

RGG TORQUES RESULTING FROM PARAMAGNETIC ARMS

A. INTRODUCTION

This section is based largely on Ref. F-1.

In the cgs electromagnetic system, the force on a magnetic pole is

$$F \equiv Hm \tag{F-1}$$

where

F = force on pole in dynes

H = field strength in oersteds

m = pole strength in emu.

The flux emanating from a magnetic pole is

$$\phi \equiv 4\pi m \text{ maxwells} \tag{F-2}$$

If a soft ferromagnetic or paramagnetic bar is introduced into a uniform field, the bar will align itself with that field, if the bar is unrestrained. Magnetic poles will be induced in the bar. If it is assumed that all the flux from the induced poles emanates from the end of the bar (an over-simplification, but it does provide simple equations with practically acceptable accuracies for relatively long bars), the flux balance will be

$$\phi_b - \phi_o = 4\pi m \tag{F-3}$$

where

ϕ_b = flux in the bar

ϕ_o = flux in the volume occupied by the bar with the bar removed

$4\pi m$ = flux caused by the induced poles in the bar.

Dividing Eq. (F-3) by the cross-section area of the bar, A:

$$\frac{\phi_b}{A} - \frac{\phi_o}{A} = \frac{4\pi m}{A} \qquad \text{(F-4)}$$

But, ϕ_b/A is defined

$$\phi_b/A \equiv B_b = \text{flux density in the bar}$$

and

$$\phi_o/A \equiv B_o = \text{flux density in free space}$$

and

$$B_o \equiv H \text{ in the emu system.}$$

Rewriting Eq. (F-4),

$$B_b - H = \frac{4\pi m}{A}$$

and

$$B_b = H + \frac{4\pi m}{A} \quad . \tag{F-5}$$

B. PERMEABILITY AND SUSCEPTIBILITY

Dividing Eq. (F-5) by H

$$\frac{B}{H} = 1 + \frac{4\pi m}{HA}$$

$$\mu \equiv \frac{B}{H} = 1 + \frac{4\pi m}{HA} \quad . \tag{F-6}$$

μ is defined in the emu system by Eq. (F-6). $\frac{m}{HA} \equiv K$ = the magnetic susceptibility of the substance of the bar. It is common in scientific work to define the susceptibility per unit mass χ,

$$\chi \equiv K\rho \tag{F-7}$$

where ρ is the density of the substance. χ is also frequently based on either the atomic weight χ_a or on the molecular weight χ_m. In this discussion, χ is based on density exclusively. Thus,

$$\mu = 1 + 4\pi K$$

$$= 1 + 4\pi\chi\rho \quad . \tag{F-8}$$

The permeability of some materials is shown in Table (F-I) from Ref. F-1, F-3, and F-5.

TABLE F-1

Magnetic Properties of Pure Materials

	$\chi \times 10^6$	ρ	μ
Aluminum	+0.63	2.68	1.0000212
Beryllium	-1.0	1.85	0.9999767
Copper	-0.086	8.96	0.9999900
Tungsten	+0.28	19.3	1.0000675
Uranium	+2.6	19.1	1.000624
Elgiloy			1.00005
Air			1.00000036
Permalloy			100,000
Iron, technically pure			6,500
Cast iron			600

C. TORQUE ON A BAR MAGNET

If a bar magnet of length, ℓ , with pole strengths, +m and -m, is introduced into a uniform field of strength, H, at an angle, θ , to the field, the following is derived from Eq. F-1 and the geometry

$$\text{Torque} = m\ell H \sin\theta \ . \qquad \text{(F-9)}$$

D. TORQUE ON A PARAMAGNETIC BAR

It is seen from Eq. (F-3)

$$\phi_b - \phi_o = 4\pi m \qquad \text{(F-3)}$$

that a pole of strenth, m, is induced in a bar when it is introduced into a field. From Eq. (F-6) for a field of H oersteds

$$\mu = 1 + \frac{4\pi m}{HA} \qquad \text{(F-6)}$$

or

$$\mu = 1 + \frac{4\pi m\ell}{HA\ell} = 1 + \frac{4\pi m\ell}{H\ \text{Vol}} \quad , \qquad \text{(F-10)}$$

or

$$H(\mu - 1) = \frac{4\pi m\ell}{\text{Vol}} \quad ,$$

and

$$m\ell = \frac{(\mu - 1)\ H\ \text{Vol}}{4\pi} \quad . \qquad \text{(F-11)}$$

This "magnet" of pole strength m and length ℓ can be substituted into Eq. (F-9) and

$$\text{Torque} = \frac{(\mu - 1)\ H^2\ \text{Vol}\ \sin\theta}{4\pi} \quad . \qquad \text{(F-12)}$$

Two elements have not been taken into account in the derivation of Eq. (F-12): the demagnetizing effect and the reduced projected area of the ends of the bar when the latter is not parallel the field. The reduced area coefficient is simply cos θ.

When the bar is introduced into the field, the induced poles tend to counteract the initial field. Thus, the effective field H is

$$H = H' - NKH = H' - N\chi\rho H \qquad \text{(F-13)}$$

where

H = effective field

H' = initial field in a vacuum

N = demagnetizing factor.

N varies from nearly zero for long thin rods to 4π for flat plates. For paramagnetic materials with mass susceptibilities in the ranges shown in Table F-I,

$$H \approx H'$$

even if N is as large as 4π, its maximum value.

Thus, the final torque equation for a paramagnetic bar introduced into a magnetic field of strength H is

$$\text{Torque} = \frac{(\mu - 1)\, H^2\, \text{Vol} \sin\theta \cos\theta}{4\pi} \qquad \text{(F-14)}$$

or

$$\text{Torque} = \chi\rho H^2\, \text{Vol} \sin\theta \cos\theta \qquad \text{(F-15)}$$

where

Torque = dyn cm

χ = emu units

ρ = g/cc

H = field strength in oersteds

E. FORCES ON A PARAMAGNETIC MASS IN NON-UNIFORM FIELD

The force on a homogeneous mass, M, in a non-uniform field is derived by Williams (Ref. F-1).

$$F = \chi M H \frac{dH}{dX}$$

F = dynes

χ = emn

M = mass

H = oersteds

dH/dx = oersteds/cm .

F. MAGNETIC TORQUES ON THE AAFE RGG

Torques can be introduced into the sensor either by the unequal attraction of the end masses or by the magnetic poles introduced in the paramagnetic arms. Because of the symmetry of the end masses, poles induced in them will not introduce torques.

The orbit of the AAFE sensor is such that the spin axis of the sensor is at all times orthogonal to the earth's spin axis. That is, the plane of the sensor arms lies in a longitudinal plane through the earth.

HRL notes state that "the earth can be considered as a dipole magnet with a pole strength of about 8.1×10^{25} emu. --- (The field gradient in a longitudinal plane) varies from about 0.005 γ/ft altitude at the equator to 0.01 γ/ft altitude at the poles."

Taking the worst case at the pole

$$\frac{dH}{dX} = 10^{-7} \text{ oersted/ft} \quad (1\ \gamma = 10^{-5} \text{ oersted})$$

$$\frac{dH}{dX} = 3.3 \times 10^{-9} \text{ oersted/cm} \quad . \qquad \text{(F-17)}$$

Since the gradient changes only by a factor of 2 to 1 as the sensor revolves around the earth, the maximum torque resulting from the field gradient occurs when the arms are at an angle, θ, to the field and the field differs because of the separation of the masses. The torque on one arm is

$$\text{Torque} = f_1\gamma_1 - f_2\gamma_2 = (f_1 - f_2)\,\gamma \cos\theta$$

$$= \left(\chi M_1 H_1 \frac{dH}{dX} - \chi M_1 H_2 \frac{dH}{dX}\right)\gamma \cos\theta$$

but

$$H_2 = H_1 + \gamma \sin\theta \frac{dH}{dX}$$

and

$$\text{Torque} = \chi M_1 \frac{dH}{dX}\,\gamma \cos\theta \left(H_1 - H_1 - \gamma \sin\theta \frac{dH}{dX}\right)$$

$$\text{Torque} = \chi M_1 \gamma^2 \cos\theta \sin\theta \left(\frac{dH}{dX}\right)^2 \quad . \qquad \text{(F-18)}$$

Even though M_1 and Y are large for this sensor, $\left(\frac{dH}{dX}\right)^2$ is so small that the torque caused by this effect is insignificant even in this sensor.

The induced pole alignment torque is from Eq. (F-15)

$$\text{Torque} = \chi \rho H^2 \text{ Vol } \sin\theta \cos\theta \qquad \text{(F-15)}$$

Assume

$\chi = 0.63 \times 10^{-6}$ for aluminum

$\rho = 2.68$ g/cc for aluminum

$H = 0.5$ oersted

Vol = 60 cm long x 7.5 cm thick x 5 cm wide

$= 2250 \text{ cm}^3$

$\theta = 45^\circ$

$$\text{Torque} = 0.63 \times 10^{-6} \times 2.68 \times 2.25 \times 10^3 \times 0.5^2 \times 0.707^2$$

$$\text{Torque} = 4.8 \times 10^{-4} \text{ dyn cm} \qquad \text{(F-19)}$$

because of paramagnetic aluminum arms.

The AAFE sensor has a polar moment of inertia for one arm of I = 0.622 N msec^2 and an inertia efficiency of about 97%. Thus the effective inertia, I_e, equals 0.6 N msec^2.

$$\text{Torque resulting from gradient} = I\Gamma_{ij} = I_e 3/2\, \Gamma_{eq}$$

$$\text{Torque} = 0.6 \times 3/2 \times 0.01 \times 10^{-9} = 9 \times 10^{-12} \text{ N m}$$

$$\text{Torque} = 9 \times 10^{-5} \text{ dyn cm} \qquad \text{(F-20)}$$

because of 0.01 EU gradient input.

Thus, the peak torque resulting from paramagnetic aluminum arms is 5.34 times the peak torque caused by the desired gravity gradient resolution. This torque will vary by a factor of about 2 to 1 while rotating around the earth.

Table F-I shows that it makes little difference whether aluminum or beryllium is used. The $\chi\rho$ product is essentially the same for both of them, but the polarity of the torque would be reversed.

Since the field strength will vary by about 2 to 1 as the sensor orbits the earth, it seems obvious that the sensor should have a magnetic shield. This is discussed in Section F-H of this appendix.

The altitude of the orbit, 250 to 300 km, puts the sensor generally in the Van Allen belt. Variations in this belt will also cause significant variations in H; therefore, magnetic shielding is again required.

G. EFFECTS OF FERROMAGNETIC IMPURITIES IN SENSOR ARMS

The effects of ferromagnetic impurities are exceedingly difficult to estimate. Iron seems to be an impurity in almost all commercial and even technically pure alloys. However, a number of compounds of iron and other ferromagnetic materials are only slightly paramagnetic. If the impurity is not in a combined form, the effect is particle size, heat treat, and cold work dependent.

The problem may be bounded by assuming that the iron inclusion has the permeability of cast iron; it is evenly dispersed and is 1% by weight.

$$\mu \text{ cast iron} \approx 600 = 1 + 4\pi\chi\rho$$

$$(\chi\rho) \text{ iron} = 599/4\pi = 47.7$$

If the iron is 1% by weight, the volume will be only

$$\text{Vol iron} = \text{Vol al} \times 0.01 \times 2.68/7.85$$

$$= \text{Vol al} \times 0.0034 \quad .$$

Assuming the susceptibilities add directly, the torque resulting from a 1% free iron impurity is

$$\text{Torque} = (\chi \, al \, \rho \, al + 0.0034 \; \chi_i \rho_i) H^2 \; \text{Vol} \sin\theta \cos\theta .$$

The torque is increased by a factor of approximately

$$\Delta \text{ Torque} \approx \frac{3.4 \times 10^{-3} \times 47.7}{0.63 \times 10^{-6}} = 2.6 \times 10^5 \quad .$$

The total peak torque will be

$$\text{Torque} = 4.8 \times 10^{-4} \cdot 2.6 \times 10^5 = 124 \text{ dyn cm} \qquad \text{(F-21)}$$

because of 1% free iron impurity in the AAFE aluminum arms and the earth's field.

H. MAGNETIC SHIELDING OF RGG

Since the AAFE sensor arms rotate in a longitudinal plane through the earth's field, the sensor can be shielded by a cylindrical shield with the axis of the cylinder along the spin axis of the sensor. The cylinder should be as long as convenient, but the ends need not be covered if the shield extends 5 or 6 in. beyond the arms.

Reference F-2, Section 5-33, states that the induction inside such a cylinder, B_i, is uniform and has the following ratio to the external field B:

$$\frac{B}{B_i} = \frac{4\mu b^2 + (\mu - 1)^2 (b^2 - a^2)}{4\mu b^2} \qquad \text{(F-22)}$$

where

μ = relative permeability of the shield. (This is the same as μ in emu units given in Table F-I and the previous equations.)

b = external radius of the shield

a = internal radius of the shield

For thin shields of thickness, t, and if $\mu \gg 1$, as any good shield will be, this can be approximated

$$\frac{B}{B_i} = 1 + \frac{0.5\,\mu\, t}{b} \quad . \qquad \text{(F-23)}$$

For the AAFE sensor, assume t = 0.01 in., b = 15 in. and $\mu = 10^4$. (Such high initial permeability will be quite difficult to obtain in practice.) For this condition

$$\frac{B}{B_i} = 1 + \frac{0.5 \times 10^4 \times 10^{-2}}{15}$$

$$= 4.35 \qquad \text{(F-24)}$$

The flux density inside the shield has been reduced by a factor of 4.35 to 1.

As was shown in Section F-G, since the induced RGG torque varies as the square of H (B and H are essentially equal in the arms and free space), this shield should reduce the induced paramagnetic torques to nearly acceptable values. However, since high initial permeability is difficult to obtain in situ, a shield thickness of 0.03 in. is recommended. This would theoretically provide a shielding factor of 10 and a magnetic torque reduction of 100.

One more calculation is required to ensure that the shield material is not saturated by the magnetic flux it is conducting around the shielded volume. It can be assumed that all the flux intercepted on one-half the cylinder face is concentrated and conducted through the shield.

$$\phi \text{ intercepted} = H \times 2b \times \ell$$

$$\text{Cross section area of shield } A. \qquad \text{(F-25)}$$

At the point of maximum flux density

$$A = 2t\,\ell \qquad \text{(F-26)}$$

$$B_{\text{shield}} = \frac{\phi}{A} = \frac{H2b\ell}{2t\ell}$$

$$= \frac{0.5 \times 15}{0.01} = 750 \text{ G} . \qquad \text{(F-27)}$$

This flux density is easily acceptable.

The shielding ratio for a spherical shell is also given in Ref. F-2 as

$$\frac{B}{B_i} = \frac{9\mu b^3 + 2(\mu - 1)^2 (b^3 - a^3)}{9\mu b^3} \qquad \text{(F-28)}$$

which can be approximated for these particular conditions as

$$\frac{B}{B_i} = 1 + 2/3\ \mu \frac{t}{b} \quad . \tag{F-29}$$

For a 0.03-in.-thick shell with $\mu = 10,000$, this is

$$\frac{B}{B_i} = 14.5 \text{ shielding ratio for a spherical shell.} \tag{F-30}$$

Thus a spherical shell provides a little more shielding.

It probably will be wise to cover the drum heads of the shield as a precaution.

It should be noted that multiple-layered shields provide better shielding than a single shield. This layering is significant only if the spacing between the layers is a significant fraction of the shield radius. In the present case, this is obviously impractical.

I. CONCLUSIONS

The AAFE RGG sensor should be designed as follows:

1. The aluminum arms should not have a relative permeability of greater than about 1.000050, and no ferromagnetic inclusions can be allowed.

2. The end masses must be symmetrical about an axis parallel to the sensor spin axis, i.e., cylindrical, as they are. The permeability can be as high as 1.001, but the end masses must be homogeneous. No ferromagnetic inclusions or residual magnetism can be allowed.

3. A magnetic shield approximately 0.03-in.-thick is required. This is visualized as a three-layer wrap of 0.010-in.-thick "Co-Netic" magnetic shielding tape. This tape is considered to have the necessary high initial permeabilities at the very low flux densities involved. This capability is being investigated. It should be noted that this tape in the 15-in. width weighs 0.62 lb/linear ft, and will add about 20 lb to the sensor. One telephone quote estimates the cost at $18/ft.

   The Rawson flux meter in the HRL laboratory has full-scale ranges from 0.0005 to 5.0 G. HRL, therefore, has no difficulty making tests to ensure that adequate shielding has been attained.

REFERENCES

F-1. Williams, S. R., Magnetic Phenomena, McGraw-Hill Book Company, 1931.

F-2. Gray, D. E., Editor, American Institute of Physics Handbook, Second Edition, McGraw-Hill Book Company, 1963.

F-3. Hallen, E., Electromagnetic Theory, Chapman & Hall, 1962.

F-4. Lobe, L. B., Fundamentals of Electricity and Magnetism, John Wiley and Sons, Inc., 1931.

F-5. Van Horn, Kent R., Editor, Aluminum-Properties, Physical Metallurgy and Phase Diagrams, American Society for Metals, Metals Park, Ohio, 1967.

APPENDIX G

TEMPERATURE SENSITIVITY OF A ROTATING GRAVITY GRADIOMETER FOR EARTH ORBIT APPLICATIONS

APPENDIX G

TEMPERATURE SENSITIVITY OF A ROTATING GRAVITY GRADIOMETER FOR EARTH ORBIT APPLICATIONS

HUGHES RESEARCH LABORATORIES
Malibu, California

a division of hughes aircraft company

Research Report 453

TEMPERATURE SENSITIVITY OF A ROTATING GRAVITY GRADIOMETER FOR EARTH ORBIT APPLICATIONS

Philip M. LaHue

Exploratory Studies Department

February 1972

TABLE OF CONTENTS

LIST OF ILLUSTRATIONS

ABSTRACT

In this report it is shown that a simple compensation or calibration approach to the reduction of the RGG sensor temperature sensitivity appears to be impractical. Automatic sensor compensation and adaptive tracking of the sensor natural frequency to the satellite rotation speed is proposed. This approacn appears to be feasible. Future work and necessary tests are discussed.

I. SENSOR DESCRIPTION

A. General Overview

The RGG sensor is composed of two isoelastic (in the plane perpendicular to the axis of rotation) arms that have concentrated masses at their extreme ends. These arms are attached to the case by end pivots, also called support pivots. The end pivots offer little torsional stiffness (they contribute approximately 1 Hz of the 8 Hz sensor resonant frequency) but they are quite rigid in the longitudinal and lateral directions.

The system main torsional stiffness is provided by two piezoelectric bimorph transducers arranged to operate in a pure bending mode. The use of the piezoelectric material to provide the main torsional stiffness is desired in this sensor, because the signal energy input is so low that most of it must be transformed by the piezoelectric transducers in order to obtain a usable output signal level.

B. Sensor Characteristics Summary (Preliminary)

The following sensor characteristics are summarized largely from the Monthly Progress Reports[1] and from the notes of C.C. Bell.

1. RGG

Arms:

Material	**Aluminum**
Radius to CG of mass	**0.381 m**

Mass:

Material	Sintered tungsten
Each end mass	2.0 kg

One Complete Arm with Masses:

Polar moment of inertia about spin axis	0.624 Nm sec^2
Mass of one complete arm	6.8 kg
Inertia efficiency = A-B/C ~	97%

Sensor Resonant Frequency 8 Hz

ω_n = 50.24 rad/sec

Sensor Stiffness

$$K_T = \omega_n^2(I/2) = \left(K_o + \frac{K_e}{2}\right) = 788 \text{ Nm/rad (6800 in lb/rad)}$$

K end pivots, each = $(6.28)^2 I$ = 24.6 Nm/rad (218 in lb/rad)

K transducers = 775.7 Nm/rad

K each transducer = 387.8 Nm/rad

2. Environment

Temperature

In pivot region	28°C ± 0.25°C
In arm region, initial	24°C + 1°C
gradually shifting to at the end of 30 days	15°C ± 1°C

Magnetic Field (approximate)

Horizontal at equator	0.6 G
Vertical at poles	0.7 G
Acceleration (any axis)	< 10^{-4} G
Spin Speed	4.0 rps

II. STATEMENT OF THE PROBLEM

The phase and amplitude of the output of the RGG is known to be extremely sensitive to operating temperature. This sensitivity is due to the variation in material dimensions, variation of the modulus of elasticity, and the variation of the transducer piezoelectric coefficients with temperature. It is shown in Ref. 2, p. 473, eq. (VI-N-15), that the undamped natural frequency of the sensor will change:

$$\frac{\Delta f}{f_o} = \delta = \frac{1}{2} \left(3\alpha_{pivot} + e_{o_{pivot}} - 2\alpha_{arms}\right) \Delta T \qquad (1)$$

where

α_{pivot} = temperature coefficient of linear expansion of the pivot material

α_{arm} = temperature coefficient of linear expansion of the arm material

$e_{o_{pivot}}$ = temperature coefficient of the modulus of elasticity of the pivot material

$\delta = \Delta f/f_o$, the change in frequency divided by the natural frequency.

The change in the sensor natural frequency due to (1) will cause a change in the amplitude of the output as shown by (2), if the rotation speed is maintained constant.

$$\frac{\Delta\theta_1}{\theta_o} = \left[\frac{1}{1 + 4Q^2\delta^2 + 2\delta}\right]^{1/2} - 1 . \qquad (2)$$

In addition to the amplitude reduction due to operating off the natural frequency of the sensor, the characteristic amplitude of the sensor itself changes due to variation in moment of inertia and spring rate. This change, again from Reference 1, p. 474, is:

$$\frac{\Delta\theta_2}{\theta_o} = (2\alpha_{arm} - 3\alpha_{pivot} - e_{o_{pivot}}) \Delta T \ . \qquad (3)$$

The total change in output amplitude is given by the sum of (2) and (3).

The above equations were derived on the basis of a single pivot material; piezoelectric materials and effects were neglected, and the inertia of the arm was assumed to be due to a concentrated mass at the end. For the proposed AAFE RGG, only the last assumption is completely valid. The supporting structure of this sensor is composed of metallic end pivots, which constitute approximately 1/64 of the total stiffness, and two piezoelectric bimorph benders, which provide approximately 63/64 of the total. Since no dimensions are involved in eqs. (1), (2), (3), or in their derivation, the contribution of each material can be proportioned and used directly. (Additional terms would have to be included in a final detailed design since the piezoelectric material is supported by still another material.)

A. Sample Temperature Amplitude Sensitivity Calculation

A sample calculation demonstrates the problem. Assume the arms are of aluminum,

$$\alpha_{arm} = 20 \times 10^{-6}/°C$$

the support pivots are of beryllium copper,

$$\alpha_{p1} = 16.6 \times 10^{-6}/°C$$

$$e_{0p1} = -350 \times 10^{-6}/°C$$

and the piezoelectric "pivots" are 4% $PbTiO_3$; 5.7% $CaTiO_3$; and 90.3% $BaTiO_3$. (Refer to the discussion of piezoelectric material characteristics in the following section of this report.)

$$\alpha_{p2} = 1 \times 10^{-6}/°C$$

$$e_{op2} = +400 \times 10^{-6}/°C \text{ (approximate)}$$

It is also assumed that the sensor $Q \sim 100$, and the temperature change is 1°C.

$$\delta = \frac{1}{2} [3\{(1/64)16.6 + (63/64)1\} - (1/64)350 + (63/64)400 - 2x20] \, 10^{-6}/°C$$

$$\delta \sim 1.75 \times 10^{-4}/°C \, . \qquad (4)$$

Substituting this value of δ into eq. (2), we have

$$1 = 1.0$$

$$4Q^2\delta^2 = 4 \times 10^4 \times 3 \times 10^{-8} = 1.2 \times 10^{-3}$$

$$2\delta = 2 \times 1.75 \times 10^{-4} = 0.3 \times 10^{-3}$$

$$\text{Total denominator of (2)} = 1.0015$$

and

$$\left[\frac{1}{1.0015}\right]^{1/2} \sim 1.0000-0.0007$$

Thus,

$$\frac{\Delta\theta_1}{\theta_o} = - 0.0007 = - 0.07\%/°C \ . \qquad (5)$$

This is the amplitude change due to sensor frequency change.

The characteristic amplitude change due to the sensor temperature change is found by substituting the same material temperature coefficients into eq. (3), and we find

$$\frac{\Delta\theta_2}{\theta_o} = [2x20-3\{(1/64)16.6 + (63/64)1\}$$

$$-(1/64)(-350)-(63/64)(400)]10^{-6} \ . \qquad (6)$$

$$\frac{\Delta\theta_2}{\theta_o} \sim - 3.5 \times 10^{-4} = - 0.035\%/°C$$

due to characteristic amplitude changes. The total amplitude change for a 1°C increase in temperature is

$$\frac{\Delta\theta}{\theta_o} = - 0.07 \ (-0.035) = - 0.105\%/°C. \qquad (7)$$

For the earth orbiting RGG it is desired to attain an accuracy of 0.01 E.U. in the presence of the earth gradient of approximately 2,250 E.U. or approximately four parts in 10^6. The above estimate shows a variation in sensor output amplitude of 1050 parts in 10^6 for a 1° temperature change.

The above calculations were carried out in detail to demonstrate the magnitude and difficulty of the problem. The dominant terms are those involving the temperature coefficient of the modulus of elasticity.

B. Temperature Coefficient of Modulus of Elasticity

For the metals, this coefficient is approximately linear, but it is poorly controlled and sensitive to alloying, heat treating, and cold working. However, in this sensor the effect of the varying modulus of elasticity of the metals is completely overshadowed by the effect of the piezoelectric materials, since the piezoelectric transducer provides almost all of the mechanical stiffness.

All of the constants of the piezoelectric ceramic materials vary with temperature. The dielectric constant, modulus of elasticity, and strain coupling coefficients all vary with temperature and age. The shape of the curves for some typical compositions is shown on pp. 3-104 and 3-105 of Reference 3 reproduced here for convenience as Fig. 1. It can be seen from these curves that the percent constant change per degree C change can be plus, minus, or zero, depending on the material and operating temperature.

In the previous example we picked the 4% $PbTiO_3$, 5.7% $CaTiO_3$, and 90.3% $BaTiO_3$ at 20°C operating temperature and found $(\Delta E/E)/°C$ to be approximately + 400 x 10^{-6}/°C. When this is compared to the curve of 8% $PbTiO_3$, 5.5% $CaTiO_3$, and 86.6% $BaTiO_3$, it is apparent that we cannot expect to predict the modulus of the piezoelectric ceramic or its temperature coefficient to better than ± 10%.

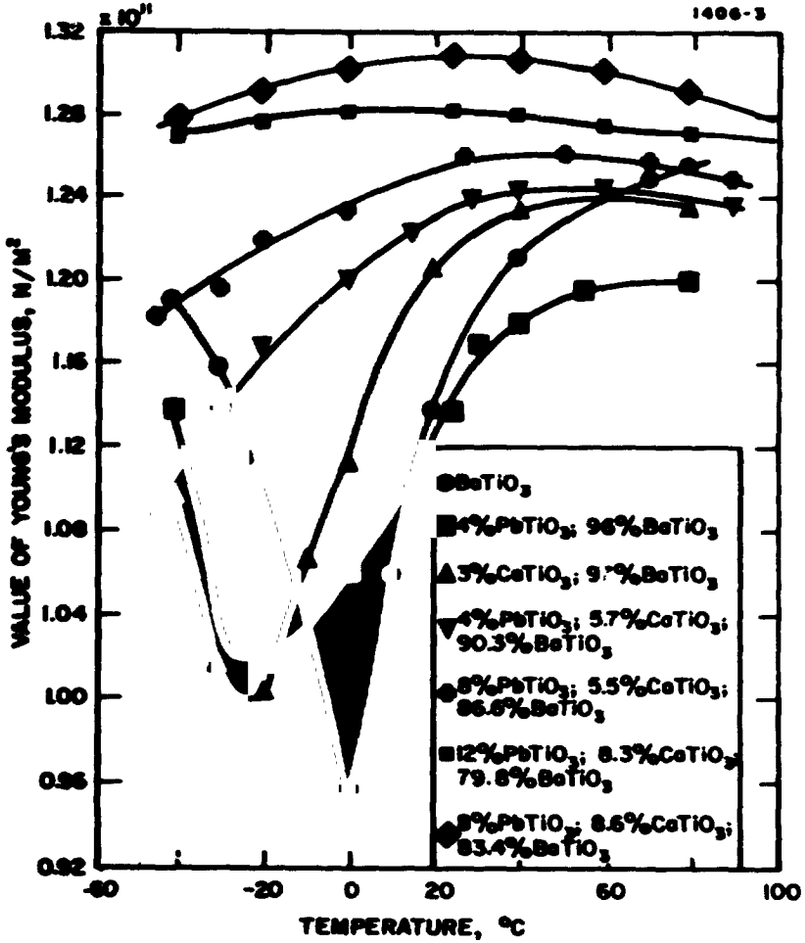

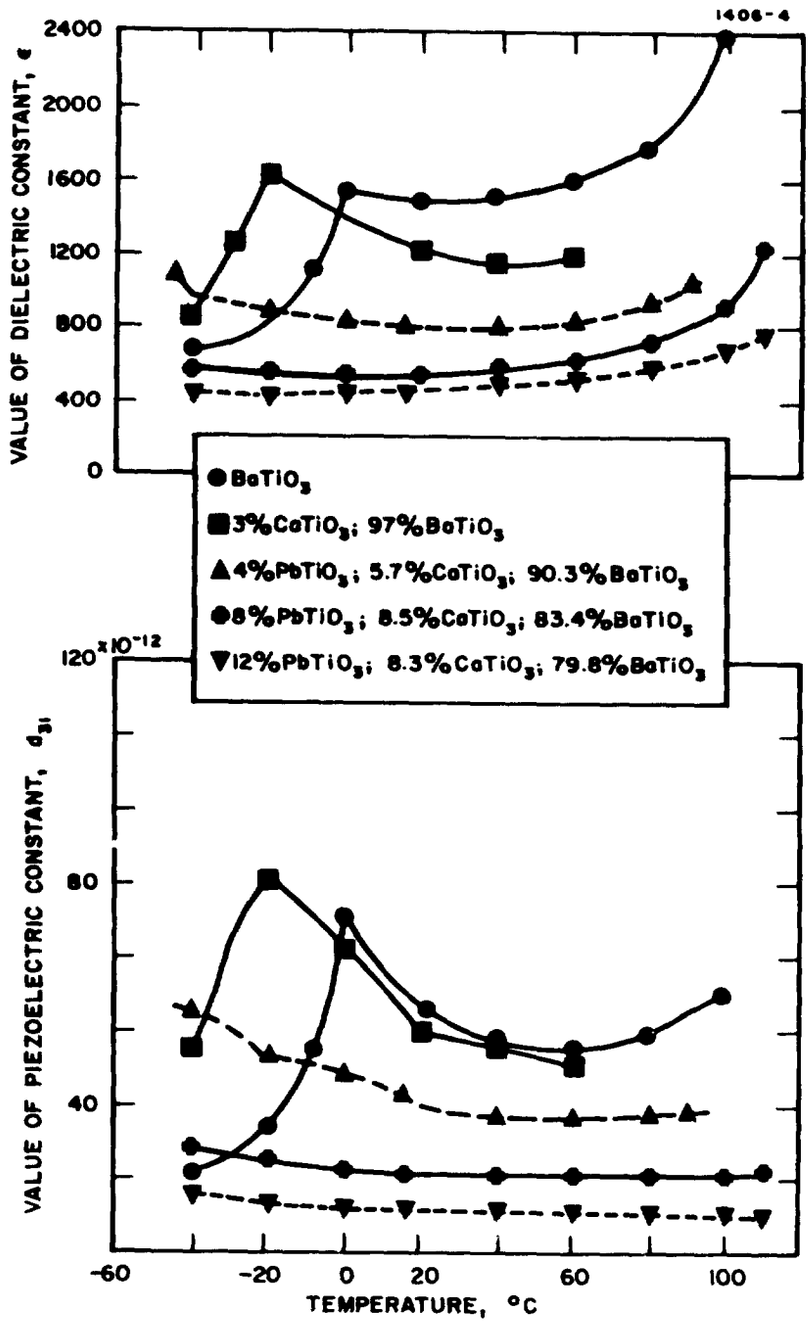

Fig. 1. Properties of Barium, Lead, and Calcium Titanate Ceramics as Functions of Temperature and Composition.

In view of these uncertainties it seems unlikely that a sensor can be designed with a temperature sensitivity uncertainty of less than about 100 x 10^{-6}/°C. Thus simple compensation or calibration along with closer temperature control appears to be impractical at this time.

III. AN RGG TEMPERATURE COMPENSATION METHOD

The equivalent circuit of the RGG sensor with two piezoelectric bimorph benders and the two sets of end pivots is shown in Fig. 2.

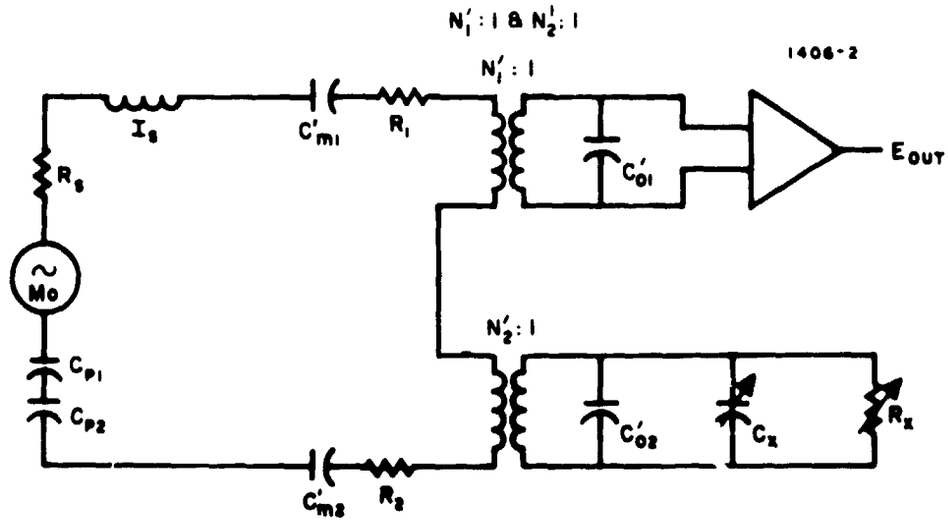

Fig. 2. Electrical Equivalent of RGG.

M_o	=	moment in sensor due to gravity gradient.
C_{p1}, C_{p2}	=	mechanical compliance for arm end pivots.
R_s	=	mechanical loss in sensor.
C'_{m1}, C'_{m2}	=	equivalent mechanical compliance of piezoelectric bimorph benders.
R_1, R_2	=	mechanical loss in piezoelectric bimorph benders.
C_{01}, C_{02}	=	capacitance of piezoelectric bimorph benders.
N'_1, N'_2	=	electromechanical transformation ratio of piezoelectric bimorph benders.
C_x	=	electrically variable capacitance.
R_x	=	electrically variable resistance.

In this circuit the mechanical compliance (C'_m) of the piezoelectric benders will vary with temperature as will C_{p1} and C_{p2}, I_s, M_o, and C'_{01} and C'_{02}. Figure 2 can be further simplified to Fig. 3, where all parameters e, R, L, and C are temperature sensitive. It is desired that the resonant frequency of Fig. 3 be equal to twice the spin speed of the satellite and the Q maintained constant. By adjusting the variable capacitor and the resistor independently these two objectives can be attained.

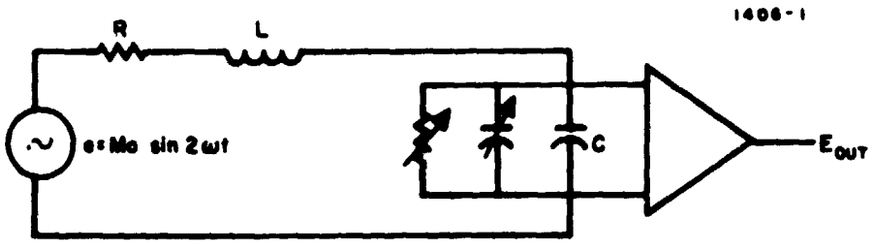

Fig. 3. Reduced Equivalent of Fig. 2.

IV. FUTURE WORK AND TESTS

The equivalent circuit of the bimorph benders must be analyzed in more detail and tests made to insure that the equivalent circuit adequately describes the physical system. Tests also need to be made with the variable R and C to insure that the Q and amplitude can be adjusted over the ranges required.

REFERENCES

1. Development of a Rotating Gravity Gradiometer for Earth Orbit Applications (AAFE), Contract NAS 1-10945, Hughes Research Laboratories, Monthly Progress Reports 1 through 6, July through December 1971.
2. Prototype Moving Base Gravity Gradiometer, Proposal 71M-1593/C3755, Part 2, Technical Proposal, Sept 1971, Hughes Research Laboratories.
3. American Institute of Physics Handbook, 2nd Edition, 1963, McGraw-Hill Book Company.

ATTACHMENT A*

GEODESY WITH ORBITING GRAVITY GRADIOMETERS

*This Attachment is included for information only and was not funded under the Contract.

HUGHES RESEARCH LABORATORIES
Malibu, California

a division of hughes aircraft company

Research Report 442

GEODESY WITH ORBITING GRAVITY GRADIOMETERS*

R.L. Forward
Exploratory Studies Department

July 1971

*Preprint of paper to be published in the AGU Monograph – Symposium on the Use of Artificial Satellites in Geodesy, 19-21 April 1971, Washington, D.C.

TABLE OF CONTENTS

LIST OF ILLUSTRATIONS

GEODESY WITH ORBITING GRAVITY GRADIOMETERS*

by

Robert L. Forward
Exploratory Studies Department
Hughes Research Laboratories
Malibu, California 90265

ABSTRACT

A new instrument for sensing of the earth's gravity field, the rotating gravity gradiometer, has been demonstrated in the laboratory. The gravity gradiometer measures the gradient of the gravity force field rather than the field itself. The sensor does not respond to acceleration and can operate in free fall or in accelerating environments where the usual gravity meters cannot work. A gradiometer in a spin stabilized satellite in a low polar orbit will make a significant contribution to the geodetic mapping program presently being carried out by satellite tracking, since it preferentially senses the higher harmonics (> 35) of the earth's field where the doppler tracking signals (revised Williamstown report) fall off rapidly.

*Preprint of paper to be published in the AGU Monograph – Symposium on the Use of Artificial Satellites in Geodesy, 19-20 April 1971, Washington, D.C.

I. DISCUSSION

A. Rotating Gravity Gradiometer

The rotating gravity gradient sensor that has been developed, Bell [1970], and operates daily in the Hughes Research Laboratories is a device for measurement of the second order gradient of the total gravity potential field. The sensor configuration consists of a resonant cruciform mass-spring system with a torsional vibrational mode (see Fig. 1). In operation, the sensor is rotated about its torsionally resonant axis at an angular rate ω which is exactly one-half the torsional resonant frequency. When a gravitational field is present, the differential forces on the sensor resulting from the gradients of the gravitational field excite the sensor structure at twice the rotation frequency, Forward [1965b]. Only the differential torque ΔT between the sensor arms at the doubled frequency is coupled into the sensor output.

For the simple example shown in Fig. 1, the differential torque induced by the mass M at the distance R is

$$\Delta T = \frac{3}{4} \frac{GM\, m\ell^2}{R^3} \sin 2\omega t \ . \qquad (1)$$

The angular resonant deflection between the two quadrupoles of the sensor rotating at one-half its torsional resonant frequency with an associated quality factor Q is therefore

$$\theta = \frac{2\, \Delta T Q}{I(2\omega)^2} = 3 \frac{GM}{R^3} \frac{Q}{(2\omega)^2} \cos 2\omega t \ , \qquad (2)$$

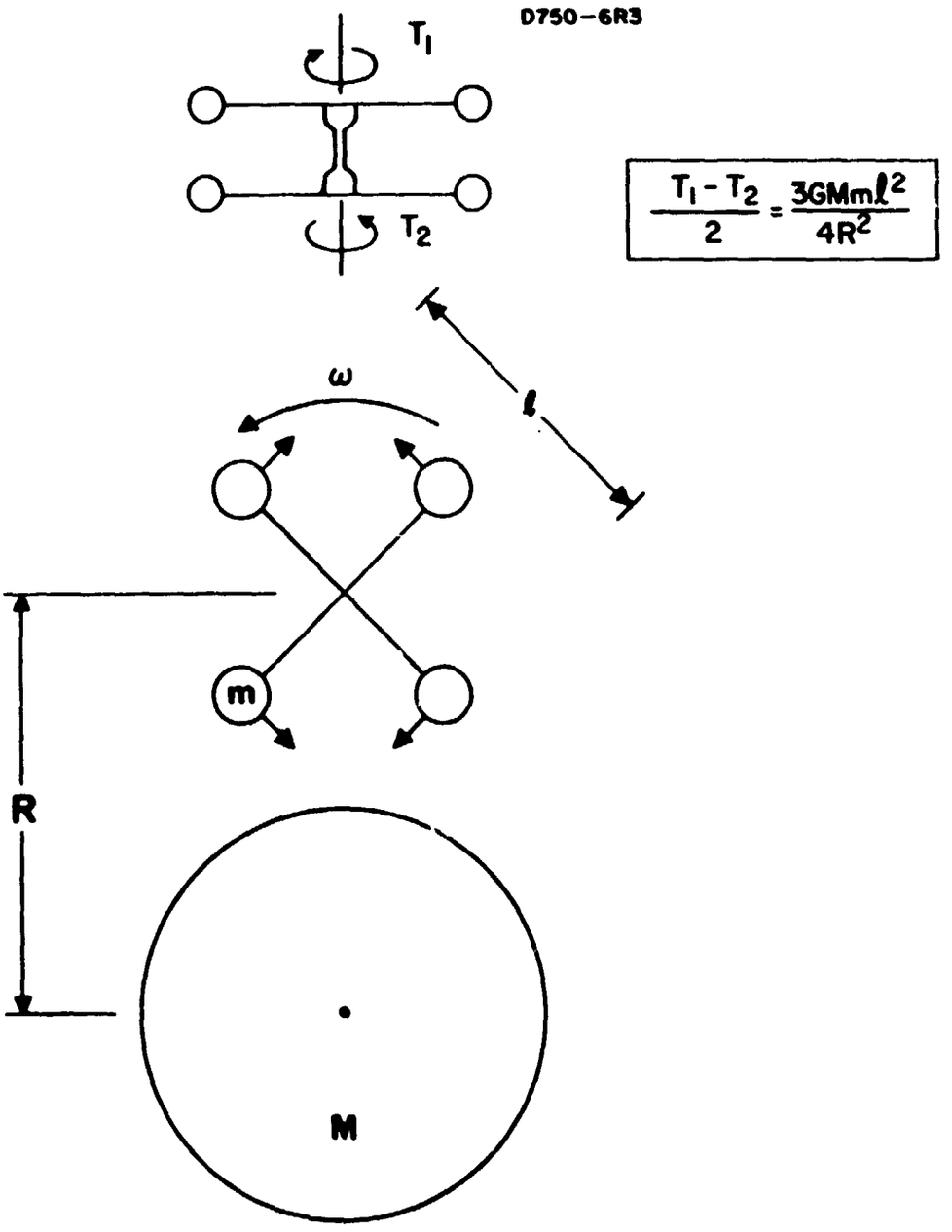

Fig. 1. Method of Operation of Torsional Gravity Gradiometer.

where $I = m\ell^2/2$ is the quadrupole inertia. The angle θ is extremely small. Surface gradients produced by the earth will produce angular deflections of $\theta \sim 3 \times 10^{-6}$ rad in typical orbital torsional sensor designs (see Fig. 2), while useful threshold signals of 10^{-11} gal/cm (0.01 Eötvös unit (E.U.)) produce angular responses of $\sim 10^{-11}$ rad.

Although these deflections are small, they are easily measured by utilizing piezoelectric strain transducers attached to the torsional flexure. The threshold deflections of 10^{-11} rad produce voltage outputs of 10^{-8} V from typical transducers. These voltage levels are easily measured by modern amplifiers.

B. Present Development Status

The ultimate objective of our work on rotating gravitational gradient sensors is the development of a class of rugged sensors of high sensitivity and precision which may be used to measure accurately and rapidly the details of the gravity field during airborne or orbital surveys and as a component in an inertial guidance system to remove the effects of gravitational anomalies on the ultimate system performance.

The objectives of the initial research programs were to investigate the engineering feasibility of the basic concept, to develop sensor structures which would operate at a high sensitivity level both in free fall and in 1 G environment, to measure the sensor's sensitivity to gravitational fields, and to investigate the sources of noise produced by the rotation of the sensor. A torsionally flexible structure utilizing

M 7402

Fig. 2. 2.75 Hz Orbital Sensor Design.

piezoelectric readout was found to be a suitable design and offers a significant improvement over other possible gradiometer designs (see extensive bibliography in Bell [1970]). It has demonstrated the capability of being operated in an earthbound laboratory environment (see Fig. 3) while still maintaining a high sensitivity and low signal-to-noise ratio. The present noise level of this sensor is ±1 E.U. (1 σ at an integration time of 10 sec) and is limited by background noise in the laboratory. Using this sensor, we recently carried out an experimental simulation where we measured *in real time* gravity gradient fields that had *exactly the same magnitude and time variation* as the gravity gradient signals that would be expected from an orbiting vehicle around the moon, Bell [1970].

At the present time, the development effort on the sensor is heading in two different directions. One program, sponsored by the Air Force, is for the development of an airborne gravity gradient measurement system. The major thrust of the development effort is to design a suitable hard mounted bearing and drive system that will spin the sensor at the desired speed without introducing excessive amounts of noise and to design a vibration and rotation isolation system that will isolate the sensor system from the aircraft noise and motion. The goal of the program is to develop a gradiometer system capable of measuring gravitational gradients at the 1 E.U. level with a 10 sec integration time on a moving base, such as an aircraft or submarine.

The other program, under NASA sponsorship, is for the design of an earth orbiting gravity gradient measurement system.

Fig. 3. Rotating Gravity Gradiometer Suspension and Drive System and Test Masses.

For the orbital case, the optimum method is to fabricate a sensor with a relatively low resonant frequency (2 to 8 Hz) (see Fig. 2), attach it directly to the spacecraft and spin the spacecraft itself at the desired spin speed (1 to 4 rev/sec), (see Fig. 4.) This mode of operation has two significant advantages. There are no bearing noise problems that are the primary source of difficulty in earthbound operation, and most importantly, since the spacecraft is rotating along with the sensor, the gravity gradient field of the spacecraft is stationary in the frame of reference of the sensor and the sensor does not sense the gravity field of the spacecraft, only the gravity gradient field of the earth. The objective of the program is to develop a sensor system capable of measuring gravitational gradients at the 0.01 E.U. level with a 30 sec integration time.

The effective resolution of a gradiometer at an altitude of 250 km is approximately 250 km. If a gradiometer were placed in a near polar orbit with suitably chosen orbital parameters, it would pass within 250 km of every point on the earth in 80 orbits, thus completely mapping the earth in 5 days.

C. Geodesy with Orbiting Gradiometers

The application of orbiting gravity gradient sensors to geodesy is straightforward. An objective of geodesy is to determine the variations of the earth's gravitational potential, which can be expressed in terms of spherical harmonics:

$$V = \frac{GM}{r}\left[1 + \sum_{n=2}^{\infty}\left(\frac{a}{r}\right)^{n}\sum_{m=0}^{\infty}P_{nm}(\sin\phi)\{C_{nm}\cos m\lambda + S_{nm}\sin m\lambda\}\right] \quad (3)$$

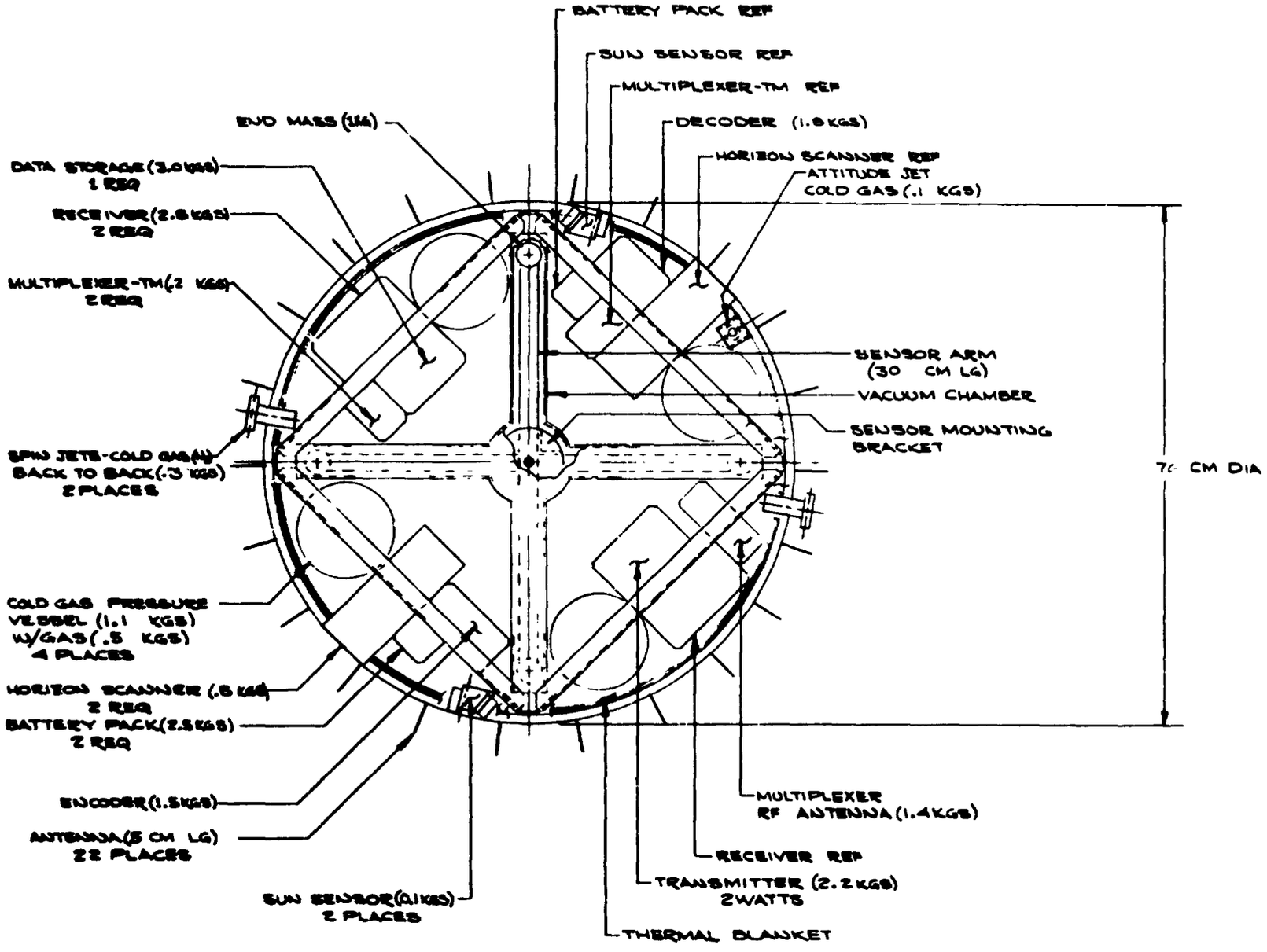

Fig. 4. Spacecraft Configuration for Earth Geodesy Experiment.

where a is the mean radius of the earth, P_{nm} is the normalized Legendre polynomial, C_{nm} and S_{nm} are the coefficients of the harmonic terms, and (r,ϕ,λ) are the coordinate positions of the instrument.

In the present satellite geodesy programs, orbital perturbation methods of obtaining the gravitational potential harmonics have led to the determination of the harmonics through the fourteenth degree and order, Rapp [1968]. In theory, this technique can be extended to obtain all higher orders of the gravitational potential; however, it is anticipated that it will be difficult to obtain the higher order components, Kaula [1969].

The advantage of gradiometer techniques in obtaining the higher order harmonics of the earth's gravitational field is straightforward. Terms with increasing n correspond to small scale features on or near the surface. Although the contribution of these harmonic components to the gravitational potential is quite small, their contribution to the gravitational force gradient at a point above them is a substantial fraction of the gravitational gradient of the entire earth.

To illustrate the behavior of the gravitational force gradient, let us examine the gradient which is predicted for higher orders of n. A typical term in the gravitational potential

$$V_{nm} = \frac{GM}{a}\left(\frac{a}{r}\right)^{n+1} P_{nm}(\sin\phi) C_{nm} \cos m\lambda \qquad (4)$$

gives rise to a radial gravity of

$$g_r = \frac{\partial V}{\partial r} = (n+1)\ \frac{GM}{a^2}\left(\frac{a}{r}\right)^{n+2} P_{nm}C_{nm}\cos\ m\lambda \qquad (5)$$

and a radial gravity gradient of

$$\Gamma_{rr} = \frac{\partial^2 V}{\partial r^2} = (n+1)(n+2)\ \frac{GM}{a^3}\left(\frac{a}{r}\right)^{n+3} P_{nm}C_{nm}\cos\ m\lambda\ . \qquad (6)$$

The present technique for measurement of the gravitational field from orbit utilizes doppler velocity tracking of the orbiting vehicle, either from the ground or from other spacecraft. The portion of the differential doppler velocity due to the higher orders of the gravitational field is given by the time integral of the acceleration field. For the radial doppler velocity we take the time integral of the radial acceleration

$$\Delta v_r = \int g_r dt = \frac{n+1}{n}\ \frac{GM}{av}\left(\frac{a}{r}\right)^{n+2} P_{nm}C_{nm}\ \sin\ m\lambda \qquad (7)$$

where we have used the fact that the maximum spatial periodic variation (m=n) has a time variation due to the orbital velocity v given by

$$\cos_{max}\ m\lambda = \cos\ n\lambda = \cos\left(n\ \frac{x}{a}\right) = \cos\left(\frac{nv}{a}\ t\right)\ .$$

If we assume that the strength of the components follows the statistical law $\bar{S}_{nm} \sim \bar{C}_{nm} \sim 10^{-5}/n^2$ Kaula [1968], and that (2n+1) terms contribute to each order, we can calculate the doppler velocity, gravity and gravity gradient as a function of the harmonic order. These are plotted in Fig. 5 for 250 km altitude.

The doppler velocity data in Fig. 5 are correct, although they differ by two orders of magnitude from what would be

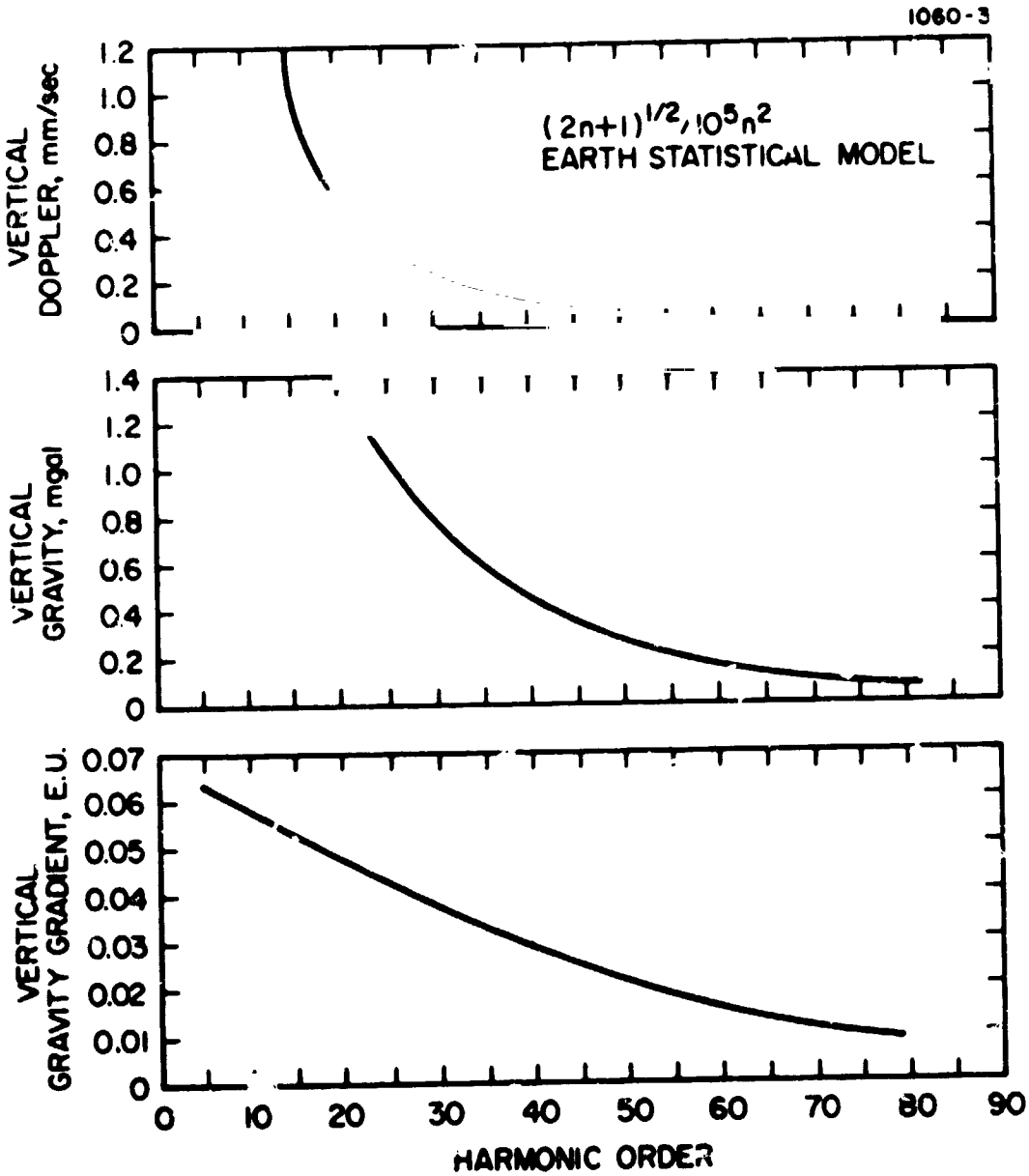

Fig. 5. Vertical Doppler Velocity Gravity and Gravity Gradient in 250 km Orbit.

calculated from Fig. 5-7, page 5-28 of the Williamstown report, Kaula [1969] as presently published. In recent correspondence, William M. Kaula has brought attention to tne fact that the right hand ordinate of Fig. 5-7 in the Williamstown report should read 10^{-2} mm/sec rather than mm/sec.

Figure 5 indicates that if satellite-to-satellite doppler tracking techniques attain their anticipated sensitivity level of 0.05 mm/sec at 30 sec, doppler tracking will be able to extract gravity data up to degree 50, and if a gravity gradiometer with an 0.01 E.U. sensitivity at 30 sec can be flown it will contribute significant information out to degree 75. The comparative signal-to-noise of the two techniques crosses over at degree 35. We thus see that the two techniques are complementary rather than competitive since below degree 35 doppler tracking has a better signal level while above degree 35 the gradiometer gives better data.

The average strength of the higher order gravity variations predicted in Fig. 5 and Fig. 5-7 of the Williamstown report use a statistical model based on the autocovariance analysis of a large variety of samples of gravimetry, Kaula (1963, p. 524) and are estimated to be correct within ± 30%. A statistical model assumes that the phases of the various harmonics are not correlated, whereas we might expect some correlation in phases to occur at the position of significant geophysical anomalies, such as mountain ranges. To obtain some feeling for this possibility, we have also looked at the gravity fields to be expected at altitude for reasonable mass anomalies on the surface.

D. Periodic Mass Models

In an attempt to study further the relative sensitivity of doppler velocity tracking measurements and gravity gradiometer

measurements for the higher order gravity fields, a massive disc mass model was used to generate gravity data and the signals expected for both a single disc and a periodic array of discs were calculated.

In the single disc model we chose a disc radius of 150 km or disc diameter of 300 km. The disc mass was chosen so that the gravity at the surface was 10 mgal. This particular choice of mass is not important to the question of the relative sensitivity since the gravity, gravity gradient and doppler velocity signals all vary directly as the mass, and if the real anomaly is down an order of magnitude all the curves should be changed by 10.

A plot of the results is shown in Fig. 6, which indicates that a disc with diameter 300 km, thickness 15 km, mass of 1.7×10^{16} kg and density difference of 0.015 gm/cc will create at an altitude of 250 km the following signals:

- Vertical gravity of 1.5 mgal peak
- Vertical gravity gradient variation of 0.11 E.U.
- Vertical doppler velocity shift of 1.0 mm/sec.

The analysis of a single disc is, however, not a close analogy to the periodic variation in the gravity field that is implied by the usual harmonic representation of the field. The disc model analysis was therefore expanded to a calculation of the signals expected over a periodic array of positive and negative disc anomalies. The mass (positive or negative) was assumed the same as in the single disc analysis. The curves

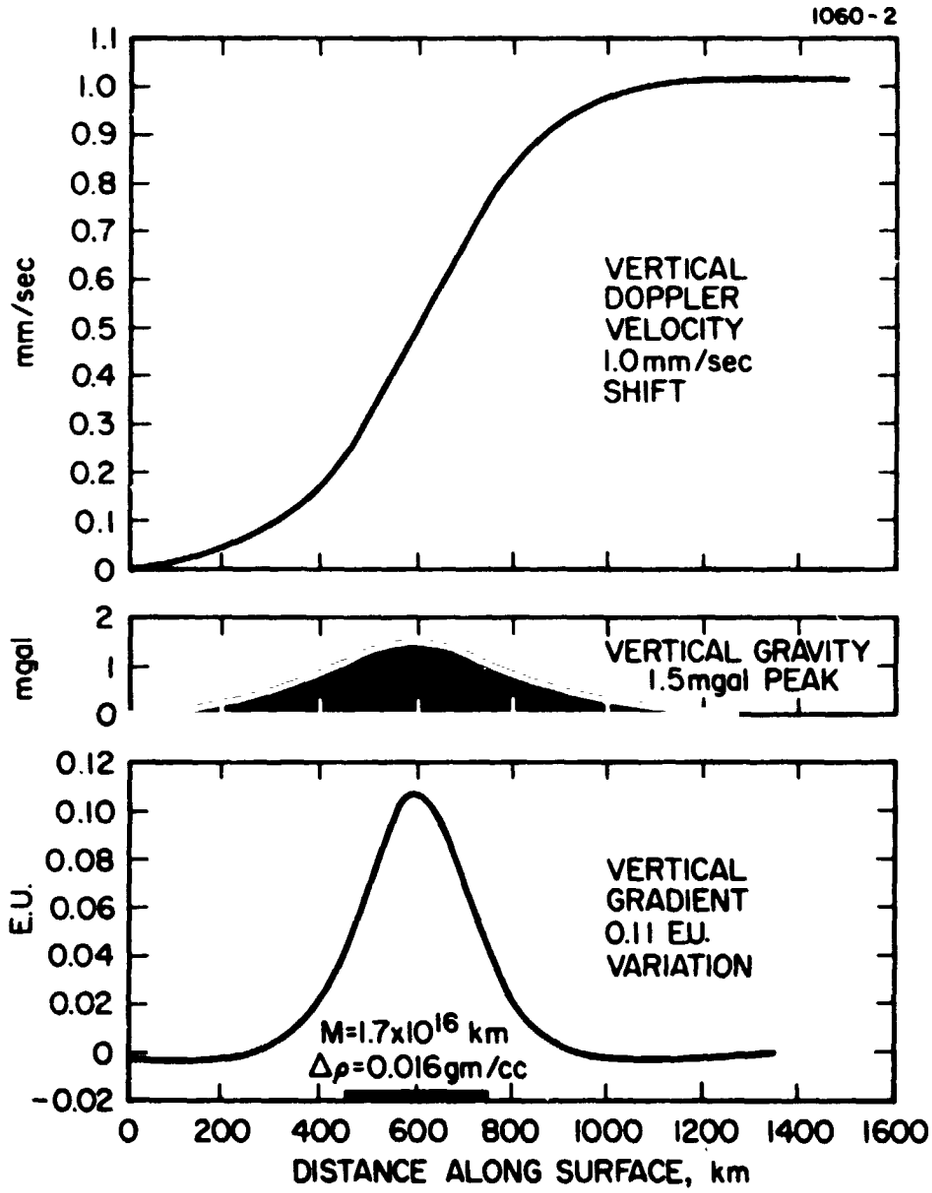

Fig. 6. Gravity Signals of Single 300 km Diameter Disc at 250 km Altitude.

in Fig. 7 are extrapolations of the data from the center portion of the disc array to eliminate end effects. The periodic signals were

- Vertical gravity ±0.65 mgal
- Vertical gravity gradient ±0.1 E.U.
- Vertical doppler velocity shift ±0.08 mm/sec.

We notice that the gravity gradient magnitude is almost the same as for the single disc. This is because the gravity gradient signal, being the spatial derivative of the acceleration, has a sharp cutoff, and the signal from an adjacent disc of opposite mass actually contributes slightly to the total signal. The magnitude of the periodic vertical gravity signal has decreased slightly from the single disc signal. The broad signature of the vertical gravity signal causes signals from adjacent discs of opposite sign to partially cancel.

Finally, notice the very large decrease, over an order of magnitude, in the vertical doppler velocity signal from the single disc case to the periodic disc case. This is because the doppler velocity signal is the integral of the acceleration signal and the integration tends to smooth out the periodic variation that we are looking for.

E. Gradiometer Noise Limit

The fundamental sensitivity of any sensor is determined by the thermal noise limitation. For the past ten years, we have been developing gravitational sensors working near their thermal noise limit, Forward [1965a], Forward [1968]. Because

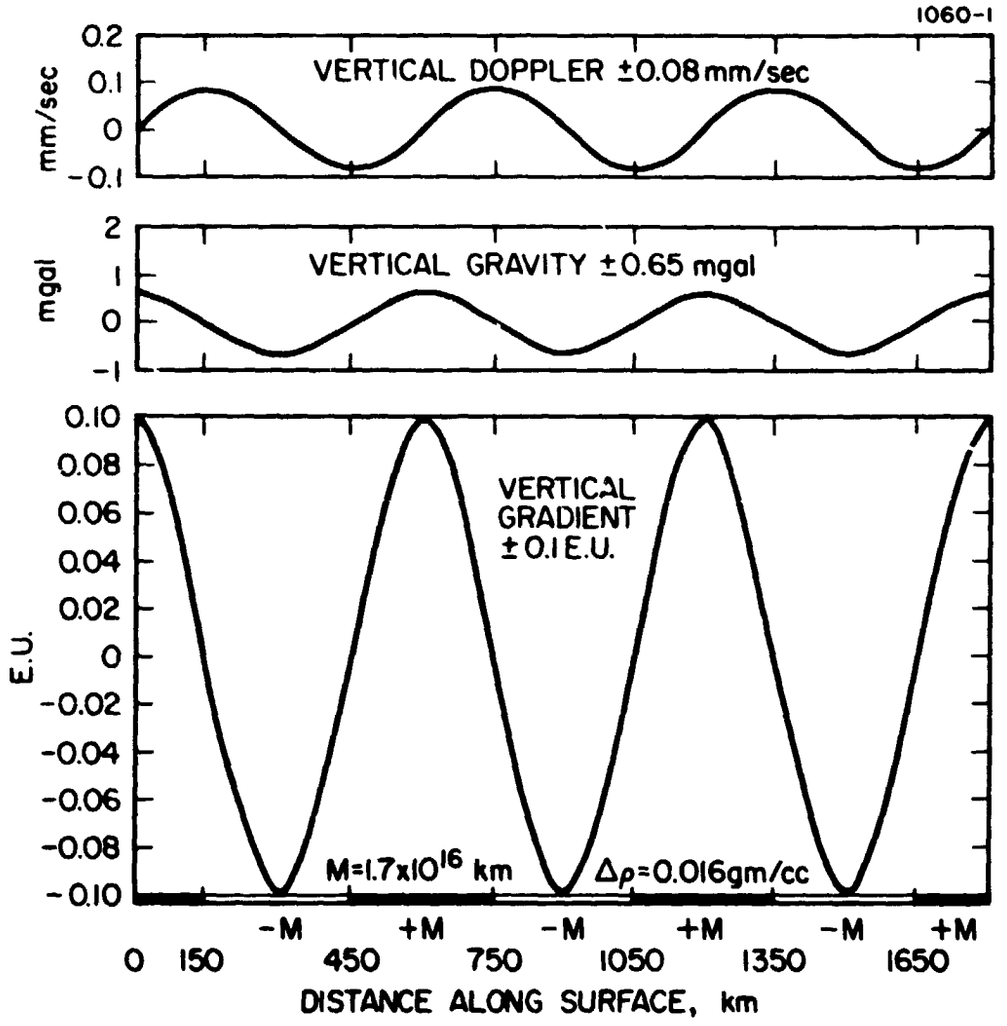

Fig. 7. Gravity Signals at 250 km Altitude from Periodic Disc Array.

this basic limit is dependent upon energy considerations, its calculation depends only upon very general parameters of the sensor, such as its temperature, mass, effective length, and time of integration. The results can then be applied to all gravity gradient sensors, regardless of their detailed design.

In our torsional sensor the thermal signal-to-noise energy ratio is obtained by comparing the gravitational gradient signal energy stored in the sensor to the kT of thermal noise in the resonant mode, Bell [1970].

The minimum gradient that can be measured for a thermally limited sensor, (S/N = 1) is

$$\Gamma = \frac{GM}{R^3} = \frac{1}{\tau r}\left(\frac{2kT}{m}\right)^{1/2} , \qquad (8)$$

where $\tau = Q/\omega$ is the 1/e time constant of the sensor.

For what might be the desired sensor for earth geodesy, one with a total arm mass of 4 kg, and an arm radius of 30 cm, the thermal noise equation gives us a kT limit of 0.005 E.U. for a 30 sec integration time. We should be able to reduce the measured noise below 2 kT with a properly designed structure and electronic matching circuit, Forward [1965a].

II. CONCLUSIONS

A new instrument for remote sensing of the earth's gravity field, the rotating gravity gradiometer, has been demonstrated in the laboratory. Analysis has shown that the sensor could provide significant improvement in the determination of the higher harmonics and local anomalies of the earth's gravity field.

Development of orbital and airborne versions are under way and should result in the near future in gravity measurement systems that will have a significant impact on geodesy and earth physics, navigation and orbit determination, and earth resources.

III. ACKNOWLEDGMENTS

I would like to acknowledge many valuable discussions with E. Sherry, P. Muller, and J. Whitcomb.

REFERENCES

Bell, C.C., R.L. Forward and H.P. Williams, "Simulated Terrain Mapping with the Rotating Gravity Gradiometer," Proc. Symposium on Dynamic Gravimetry, 115-128, Fort Worth, Texas, 1970.

Forward, R.L. "Detectors for Dynamic Gravitational Fields," Ph. D. Thesis, Dept. of Physics, University of Maryland, 1965a.

Forward, R.L., "Potating Gravitational and Inertial Sensors," Proc. AIAA Unmanned Spacecraft Meeting, 346-351, Los Angeles, California, 1965b.

Forward, R.L., D. Berman and L.R. Miller, "Thermal Noise Limited Operation of Dynamic Gravitational Detectors," Bull. Am. Phys. Soc., 13, 513, 1968.

Kaula, W.M. "Determination of the Earth's Gravitational Field," Rev. Geophysics, 1, 507-551, 1963.

Kaula, W.M., An Introduction to Planetary Physics, Wiley and Sons, New York, 1968.

Kaula, W.M., Ed., The Terrestrial Environment, Solid-Earth and Ocean Physics, Williams College Study Report, NASA-ERC and MIT-Measurement Systems Laboratory, Cambridge, Mass., 1969.

Rapp, R.H., "Gravitational Potential of the Earth Determined From a Combination of Satellite, Observed and Model Anomalies," J. Geophys. Res., 73, 6555-6562, 1968.

ATTACHMENT B*

DYNAMIC ANALYSIS OF THE SECOND ORDER GRADIOMETER

*This Attachment is included for information only and was not funded under the Contract.

HUGHES RESEARCH LABORATORIES
Malibu, California

a division of hughes aircraft company

Research Report 441

DYNAMIC ANALYSIS OF THE SECOND ORDER GRADIOMETER

R.W. Peterson

Advanced Projects Laboratory
Data Systems Division

TABLE OF CONTENTS

LIST OF ILLUSTRATIONS

LIST OF TABLES

I. INTRODUCTION

An ideal second order gravity gradiometer operating in an inertially fixed frame of reference will produce output signals proportional to the second order gradient of the gravity field only. The output of a nonideal sensor operating in a noninertial frame of reference will contain, among other noises, errors due to acceleration and rotation of the sensor frame of reference. The purpose of this report is to present a dynamic analysis of this latter class of errors using a simple model of the second order gradiometer, and then to apply the results of this analysis to the specific case of a satellite MASCON* experiment.

*One such experiment is described in HRL Proposal 70M-0691/C2395 Preliminary Proposal for the Apollo Gravity Gradimeter Sensor.

II. SENSOR ANALYSIS

A. Gradiometer Model

A simple mechanical model, consisting of three torsional springs and dampers and two inertia arms, will serve as the basis for this analysis. As shown in Fig. 1, the inertia arms are individually coupled to the case of the instrument through the supporting springs K_1, K_2 and are mutually coupled by the common torsional spring K_0. Each spring is assumed to contain viscous damping defined by the coefficients D_0, D_1, D_2 and is assumed to be infinitely rigid in all directions other than about the common torsional axis $\bar{k}$.

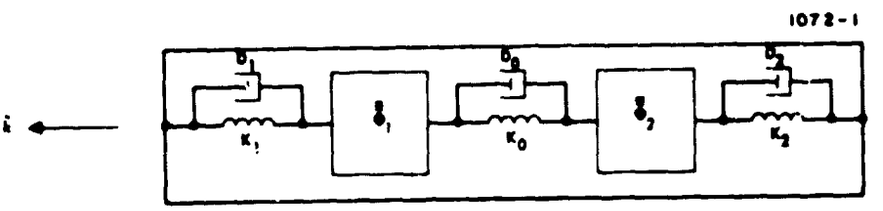

Fig. 1. Gradiometer Model.

The inertial tensors of the arms are defined in terms of the principal axes of the arms as in eqs. (1) and (2).

$$\bar{\bar{\Phi}}_1 \triangleq I_1 \left[\overline{i_1 i_1} + \overline{kk}\right] \tag{1}$$

$$\bar{\bar{\Phi}}_2 \triangleq I_2 \left[\overline{j_2 j_2} + \overline{kk}\right] . \tag{2}$$

The unit vectors $\bar{I}_1$, $\bar{J}_2$ are nominally orthogonal, but they become nonorthogonal because of the differential motion of the arms. In this analysis, the inertial tensors of (1) and (2) will be approximated by (3) and (4), wherein the tensors are described in a sensor case-fixed frame $\overline{ijk}$, and the products of inertia are neglected.

$$\bar{\bar{\Phi}}_1 \simeq I_1 \, [\bar{i}\bar{i} + \bar{k}\bar{k}] \tag{3}$$

$$\bar{\bar{\Phi}}_2 \simeq I_2 \, [\bar{j}\bar{j} + \bar{k}\bar{k}] \tag{4}$$

The common torsional spring K_0 also includes a strain transducer to sense the differential angular deflection of the inertia arms. The electrical output of this strain transducer is amplified, phase-sensitive demodulated, and filtered to produce the ultimate output of the gradiometer.

B. Equations of Motion

Because the ultimate output of the gradiometer is a function of the differential angular deflection of the inertia arms about the common torsional axis, it is of interest to derive the dynamic equations of motion which relate this parameter to the sensible inputs to the instrument. This derivation will be accomplished on the basis of the classical equivalence of torque to the time rate of change of the angular momentum of each arm.

The angular momenta of the arms are defined in terms of their inertial tensors and angular velocities as (5) and (6), where $\bar{\omega}$ is the inertial angular velocity of the sensor case, and the scalars $\dot{\theta}_1, \dot{\vartheta}_2$ are the velocities of the arms relative to the sensor case.

$$\bar{H}_1 \triangleq \bar{\bar{\Phi}}_1 \cdot [\bar{\omega} + \bar{k}\dot{\theta}_1] \tag{5}$$

$$\bar{H}_2 \triangleq \bar{\bar{\Phi}}_2 \cdot [\bar{\omega} + \bar{k}\dot{\theta}_2] \tag{6}$$

The time rates of change of these momenta are produced by external torques acting on the arms as the result of the gravity gradient, arm mass unbalance, and the elastic and

viscous coupling between the arms and between the arms and the case, as shown in (7) and (8).

$$\dot{\bar{H}}_1 = \bar{M}_{g1} + \bar{M}_{\mu 1} + \bar{M}_{2,1} + \bar{M}_{c1} \tag{7}$$

$$\dot{\bar{H}}_2 = \bar{M}_{g2} + \bar{M}_{\mu 2} + \bar{M}_{1,2} + \bar{M}_{c2} \tag{8}$$

For our present objectives, we require only the components of these momental rates about the sensor output axis $\bar{k}$, and from (5) and (6) these scalars may be expressed as (9) and (10).

$$\bar{k} \cdot \dot{\bar{H}}_1 = I_1\ddot{\theta}_1 + \bar{k} \cdot [\bar{\bar{\Phi}}_1 \cdot \bar{\omega} + \bar{\omega} \times (\bar{\bar{\Phi}}_1 \cdot \bar{\omega})] \tag{9}$$

$$\bar{k} \cdot \dot{\bar{H}}_2 = I_2\ddot{\theta}_2 + \bar{k} \cdot [\bar{\bar{\Phi}}_2 \cdot \dot{\bar{\omega}} + \bar{\omega} \times (\bar{\bar{\Phi}}_2 \cdot \bar{\omega})] \quad . \tag{10}$$

The elastic and viscous coupling torques acting on the arms may be expressed as (11) and (12).

$$\bar{k} \cdot [\bar{M}_{c1} + \bar{M}_{1,2}] = -[A_1 + A_0]\,\theta_1 + A_0\theta_2 \tag{11}$$

$$\bar{k} \cdot [\bar{M}_{c2} + \bar{M}_{2,1}] = -[A_2 + A_0]\,\theta_2 + A_0\theta_1 \tag{12}$$

where, by definition:

$$\left.\begin{aligned} A_0 &\triangleq D_0 S + K_0 \\ A_1 &\triangleq D_1 S + K_1 \\ A_2 &\triangleq D_2 S + K_2 \end{aligned}\right\} \quad . \tag{13}$$

The dynamic equations of arm motion may be stated in the matrix form (14) by combining equations (7) through (12).

$$\begin{bmatrix} (I_1 S^2 + A_1 + A_0) & (-A_0) \\ (-A_0) & (I_2 S^2 + A_2 + A_0) \end{bmatrix} \begin{bmatrix} \theta_1 \\ \theta_2 \end{bmatrix} = \begin{bmatrix} M_1 \\ M_2 \end{bmatrix} \tag{14}$$

where, by definition:

$$\left.\begin{aligned} M_1 &\triangleq \bar{k} \cdot [\bar{M}_{g1} + \bar{M}_{\mu 1} - (\bar{\bar{\phi}}_1 \cdot \dot{\bar{\omega}} + \bar{\omega} \times (\bar{\bar{\phi}}_1 \cdot \bar{\omega}))] \\ M_2 &\triangleq \bar{k} \cdot [\bar{M}_{g2} + \bar{M}_{\mu 2} - (\bar{\bar{\phi}}_2 \cdot \dot{\bar{\omega}} + \bar{\omega} \times (\bar{\bar{\phi}}_2 \cdot \bar{\omega}))] \end{aligned}\right\} . \tag{15}$$

The solution of (14) for the differential angular deflection of the arms is stated as (16).

$$(\theta_1 - \theta_2) = \frac{(I_2 S^2 + A_2) M_1 - (I_1 S^2 + A_1) M_2}{I_1 I_2 S^4 + [I_1 (A_2 + A_0) + I_2 (A_1 + A_0)] S^2 + A_1 A_2 + A_0 (A_1 + A_2)} \tag{16}$$

A normalized form of (16) is presented as (17), wherein the denominator is factored into two quadratics representing the *SUM MODE* and the *DIFFERENCE MODE* characteristic frequencies $\beta_{1,2}$ and ω_0.

$$(\theta_1 - \theta_2) = \frac{[S^2 + \alpha_2 S + \beta_2^2]\left[\frac{M_1}{I_1}\right] - [S^2 + \alpha_1 S + \beta_1^2]\left[\frac{M_2}{I_2}\right]}{[S^2 + \alpha_{1,2} S + \beta_{1,2}^2]\left[S^2 + \frac{\omega_0}{Q} S + \omega_0^2\right]} \tag{17}$$

where

$$\alpha_1 = D_1/I_1 \qquad \beta_1^2 = K_1/I_1$$
$$\alpha_2 = D_2/I_2 \qquad \beta_2^2 = K_2/I_2$$
$$\alpha_{12} \simeq \frac{D_1 + D_2}{I_1 + I_2} \qquad \beta_{12}^2 \simeq \frac{K_1 + K_2}{I_1 + I_2}$$
$$\frac{\omega_0}{Q} \simeq D_0 \left[\frac{I_1 + I_2}{I_1 I_2}\right] + \left[\frac{D_1 + D_2}{I_1 + I_2}\right]$$
$$\omega_0^2 \simeq \left[\frac{I_1 + I_2}{I_1 I_2}\right] K_0 + \left[\frac{K_1 + K_2}{I_1 + I_2}\right]$$

The sum mode parameters $\alpha_{1,2}$ $\beta_{1,2}$ are approximately equal to their counterparts in the numerator of (17) and become exactly equal to them when the spring rates K_1, K_2, damping D_1, D_2 and inertias I_1, I_2 are matched. Under these ideal conditions, the difference mode frequency ω_0 may be expressed as (18).

$$\omega_0^2 = (2K_0 + K)/I \tag{18}$$

where $K \triangleq K_1 = K_2$ and $I \triangleq I_1 = I_2$.

The differential angular deflection $\theta_1 - \theta_2$ may be scaled by ω_0^2/Q to yield an expression for an equivalent gradient signal, as shown in (19).

$$\Gamma_e \triangleq (\omega_0^2/Q)\ [\theta_1 - \theta_2] \tag{19}$$

Combining (17) and (19) yields (20).

$$\Gamma_e = \left[\frac{\omega_0^2}{Q}\right]\left[\frac{(S^2 + \alpha_2 S + \beta_2^2)\left(\frac{M_1}{I_1}\right) - (S^2 + \alpha_1 S + \beta_1^2)\left(\frac{M_2}{I_2}\right)}{(S^2 + \alpha_{1,2} S + \beta_{1,2}^2\left(S^2 + \frac{\omega_0}{Q} S + \omega_0^2\right)}\right]. \tag{20}$$

At this point it is instructive to expand and normalize (15) to obtain the forcing functions of (20). The result of this expansion is (21).

$$\left.\begin{aligned} \frac{M_1}{I_1} &= -\Gamma_{ij} - \dot{\omega}_k + \omega_i\omega_j + \Gamma_{\mu 1} \\ \frac{M_2}{I_2} &= \Gamma_{ij} - \dot{\omega}_k - \omega_i\omega_j + \Gamma_{\mu 2} \end{aligned}\right\} \tag{21}$$

where

$$\Gamma_{\mu 1} = (\bar{k} \cdot \bar{M}_{\mu 1})/I_1$$

$$\Gamma_{\mu 2} = (\bar{k} \cdot \bar{M}_{\mu 2})/I_2$$

The largest gradient error due to arm mass unbalance occurs when the individual unbalances are of opposite sign. Therefore, in this analysis, the largest mass unbalance error will be assumed to be as defined by (22).

$$\Gamma_{\mu 1} \triangleq -\Gamma_{\mu 2} \triangleq \Gamma_{\mu max} \tag{22}$$

The resulting equivalent gradient is obtained by combining (20), (21), and (22) and is presented as (23).

$$\Gamma_e = \left[\frac{\omega_0^2}{Q}\right] \left[\frac{\left[s^2 + \left(\frac{\alpha_1 + \alpha_2}{2}\right) s + \frac{\beta_1^2 + \beta_2^2}{2}\right] \left[-2\Gamma_{ij} + 2\omega_i\omega_j + 2\Gamma_{\mu max}\right]}{\left[s^2 + \alpha_{1,2}\, s + \beta_{1,2}^2\right] \left[s^2 + \frac{\omega_0}{Q}\, s + \omega_0^2\right]}\right]$$

$$+ \left[\frac{\omega_0^2}{Q}\right] \left[\frac{\left[(\alpha_1 - \alpha_2)\, s + (\beta_1^2 - \beta_2^2)\right]\dot{\omega}_k}{\left[s^2 + \alpha_{1,2}\, s + \beta_{1,2}^2\right] \left[s^2 + \frac{\omega_0}{Q}\, s + \omega_0^2\right]}\right] . \qquad (23)$$

Equation (23) illustrates the following three basic gradient error sources.

1. Rotational field ($2\omega_i\omega_j$)
2. Arm mass unbalance ($2\Gamma_{\mu max}$)
3. Sum Mode mismatch $(\beta_1^2 - \beta_2^2)\dot{\omega}_k$.

This equation also demonstrates a potentially large error due to excitation of the sum mode frequency $\beta_{1,2}$. To avoid this difficulty, care should be taken in the design of the instrument for a particular application such as to separate the sum mode frequency from the characteristic motion frequencies of the application.

Another property of (23) is that errors due to sum mode mismatch are attenuated as the square of frequency above the sum mode frequency up to the difference mode frequency ω_0. Above the difference mode frequency these errors are attenuated as the fourth power of frequency until the lead of the numerator becomes effective. For light damping of the sum mode, the lead becomes effective at $\omega \approx 2Q_{1,2}\beta_{1,2}$. This latter frequency is usually above the difference mode frequency by two orders of magnitude or better; beyond that frequency the error is attenuated further as the third power of frequency.

III. SATELLITE SENSOR INTERACTION

A. Satellite Application

In order to apply the general result of the gradiometer dynamic error analysis to the specific application of the satellite MASCON experiment, it is necessary to estimate the acceleration and rotation environment in which the sensor will be operating. This objective may be accomplished logically by estimating the satellite motions in its principal inertial axes and then transferring the effects of these motions to the sensor by considering the orientation of the sensor with respect to the satellite's principal inertial axes and center of mass.

B. Satellite Equations of Motion

The equations of motion of the satellite developed here will be based on the assumption of a lunar circular orbit. A set of local orbital coordinates $\overline{XYZ}$ are defined such that $\overline{Z}$ is normal to the orbital plane and such that $\overline{Y}$ coincides with the local lunar gravity vector. The remaining unit vector $\overline{X}$ is defined to be normal to $\overline{Y}$ and $\overline{Z}$ and tangent to the orbital path as shown in Fig. 2. The principal axes of the satellite $\overline{xyz}$ are defined to be rotated with respect to the local orbital frame $\overline{XYZ}$ by the classical Eulerian angles as defined by (24).

$$\overline{xyz} \triangleq [\Psi]_3 \, [\theta]_1 \, [\Phi]_3 \, \overline{XYZ} \tag{24}$$

The numerical subscripts of the rotation matrices indicate the axes about which the rotation is taken. The equations of motion will be based on the classical equivalence of torque to time rate of change of angular momentum as defined by (25).

$$\dot{\bar{H}}_S = \bar{M}_\Gamma + \bar{M}_d \quad . \tag{25}$$

The expansion of (25) in terms of the principal inertial tensor of the subsatellite $\bar{\bar{\Phi}}_s$ and the gravity gradient torque $\bar{M}_\Gamma$ is defined by (26), where other disturbance torques $\bar{M}_d$ are neglected.

$$\bar{\bar{\Phi}}_S \cdot \dot{\bar{\omega}} + \bar{\omega} \times [\bar{\bar{\Phi}}_s \cdot \bar{\omega}] = 3\Omega_0^2 \, [\bar{Y} \times (\bar{\bar{\Phi}}_s \cdot \bar{Y})] \tag{26}$$

where

$$\bar{\bar{\Phi}}_s \triangleq \overline{xx}\, A + \overline{yy}\, B + \overline{zz}\, C$$

$$\Omega_0^2 \triangleq GM / R_0^3$$

G = Universal gravitation constant

M = Lunar mass

R_0 = Mass center distance between moon and satellite

$\bar{\omega}$ = Inertial angular velocity of the satellite.

A simplified expansion of (26) is given as (27) where the nodal angle ϕ is assumed to be zero and the inclination angle θ is assumed to be small.

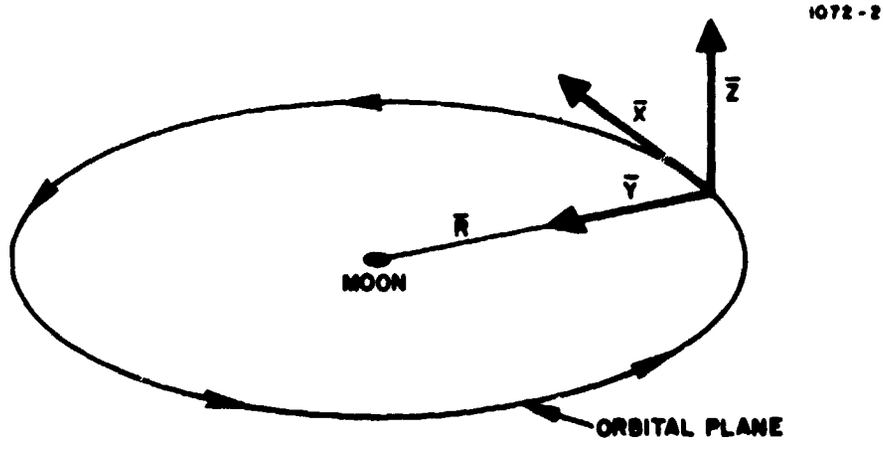

Fig. 2. Lunar Orbital Path Coordinates.

$$\dot{\omega}_x + k_1\omega_y\omega_z \simeq -3\Omega_0^2\theta k_1 \cos \omega_s t$$

$$\dot{\omega}_y - k_2\omega_x\omega_z \simeq 3\Omega_0^2\theta k_2 \sin \omega_s t$$

$$\dot{\omega}_z + k_3\omega_x\omega_y \simeq \frac{3}{2}\ \Omega_0^2 k_3 \sin 2\omega_s t \qquad (27)$$

where

$$k_1 \triangleq (C - B)/A \qquad \psi \triangleq \omega_s t \ .$$

$$k_2 \triangleq (C - A)/B$$

$$k_3 \triangleq (B - A)/C$$

A linear solution for the transverse rates ω_x, ω_y of (27) may be obtained through the assumptions that the subsatellite spin axis velocity is constant $\omega_z \simeq \omega_s$ and that the transverse inertia ratios k_1, k_2 are equal. The Laplace transformation of these linearized differential equations is stated in the matrix form of (28).

$$\begin{bmatrix} s & p \\ -p & s \end{bmatrix} \begin{bmatrix} \omega_x(S) \\ \omega_y(S) \end{bmatrix} \simeq \begin{bmatrix} \omega_x(0) - 3\Omega_0^2\theta k \left\{ \dfrac{S}{S^2 + \omega_s^2} \right\} \\ \omega_y(0) + 3\Omega_0^2\theta k \left\{ \dfrac{\omega_s}{S^2 + \omega_s^2} \right\} \end{bmatrix} \qquad (28)$$

where

$$k \triangleq k_1 \triangleq k_2$$

$$p \triangleq k\omega_s$$

The solution of (28) is stated as (29).

$$\omega_x(S) \simeq \frac{\omega_x(0)S - p\omega_y(0)}{[S^2 + p^2]} - \frac{[3\Omega_0^2\theta k]\ [S^2 + p\omega_s]}{[S^2 + p^2][S^2 + \omega_s^2]}$$

$$\omega_y(S) \simeq \frac{\omega_x(0)S + p\omega_x(0)}{[S^2 + p^2]} + \frac{[3\Omega_0^2\theta k]\ [\omega_s - p]S}{[S^2 + p^2]\ [S^2 + \omega_s^2]} . \qquad (29)$$

The time solution of (29) is stated as (30).

$$\omega_x \simeq \omega_x(0) \cos pt - \left[\omega_y(0) + \frac{3\Omega_0^2\theta k}{\omega_s + p}\right] \sin pt - \left[\frac{3\Omega_0^2\theta k}{\omega_s + p}\right] \sin \omega_s t$$

$$\omega_y \simeq \omega_x(0) \sin pt + \left[\omega_y(0) + \frac{3\Omega_0^2\theta k}{\omega_s + p}\right] \cos pt - \left[\frac{3\Omega_0^2\theta k}{\omega_s + p}\right] \cos \omega_s t \qquad (30)$$

In order to simplify expansion of the gradient error terms, (30) will be simplified as shown in (31).

$$\omega_x \simeq \Omega_p \cos pt - \Omega_s \sin \omega_s t$$

$$\omega_y \simeq \Omega_p \sin pt - \Omega_s \cos \omega_s t$$

$$\omega_z \simeq \omega_s \qquad (31)$$

where

$$\Omega_p \triangleq \omega_x(0)$$

$$\Omega_s \triangleq [3k\theta\Omega_0^2]/[\omega_s + p]$$

$$\omega_y(0) \triangleq -\Omega_s \quad .$$

Substitution of (31) into (27) yields the approximate angular accelerations of the satellite as (32), where $\omega_z \triangleq \omega_s$ and $\Omega_0^2 >> \Omega_s^2$.

$$\dot{\omega}_x \simeq -p\Omega_p \sin pt - \omega_s\Omega_s \cos \omega_s t$$

$$\dot{\omega}_y \simeq p\Omega_p \cos pt + \omega_s\Omega_s \sin \omega_s t$$

$$\dot{\omega}_z \simeq \frac{k_3}{2} [\, 3\Omega_0^2 \sin 2\omega_s t - \Omega_p^2 \sin 2pt + 2\Omega_p\Omega_s \cos (\omega_s - p)t \,] \,. \tag{32}$$

C. Gradiometer Reference Motion

The gradiometer case is assumed to be fixed in the satellite but that its reference axes are misaligned with respect to the principal axes of the satellite and that its center of mass is displaced from that of the satellite. The angular misalignment of the gradiometer is defined by the small, transverse angles α, β shown in matrix form as (33).

$$\overline{ijk} \triangleq \begin{bmatrix} 1 & 0 & -\alpha \\ 0 & 1 & \beta \\ \alpha & -\beta & 1 \end{bmatrix} \overline{xyz} \tag{33}$$

The gradiometer center of mass is located with respect to that of the satellite by the position vector $\bar{L}$. This location of the gradiometer results in the translational acceleration defined by (34).

$$\bar{a} = \dot{\bar{\omega}} \times \bar{\ell} + \bar{\omega} \times [\bar{\omega} \times \bar{\ell}] \quad . \tag{34}$$

The angular velocities and accelerations of the gradiometer may be described in terms of those of the satellite through the transformation of (33), as shown in (35) and (36).

$$\begin{aligned} \omega_i &\simeq \omega_x - \alpha\omega_z \\ \omega_j &\simeq \omega_y + \beta\omega_z \\ \omega_k &\simeq \omega_z + \alpha\omega_x - \beta\omega_y \quad . \end{aligned} \tag{35}$$

$$\begin{aligned} \dot{\omega}_i &\simeq \dot{\omega}_x - \alpha\dot{\omega}_z \\ \dot{\omega}_j &\simeq \dot{\omega}_y + \beta\dot{\omega}_z \\ \dot{\omega}_k &\simeq \dot{\omega}_z + \alpha\dot{\omega}_x - \beta\dot{\omega}_y \quad . \end{aligned} \tag{36}$$

D. Expansion of the Gradient Error Driving Functions

The gradient error driving functions are defined by (23) as $2\omega_i\omega_j$, $\dot{\omega}_k$, and $2\Gamma_{\mu max}$. Each of these driving functions will be expanded in the time domain, and the amplitudes and frequencies so derived will be tabulated.

The rotational field driving function $2\omega_i\omega_j$ from (35) may be expressed as (37)

$$2\omega_i\omega_j = 2\omega_x\omega_y + 2\omega_z\,(\beta\omega_x - \alpha\omega_y) - 2\alpha\beta\omega_z^2 \quad . \tag{37}$$

Expansion of (37) from (31) yields (38).

$$2\omega_i\omega_j \approx 2\omega_s\Omega_p\,[\beta\cos pt - \alpha\sin pt] - 2\alpha\beta\omega_s^2$$
$$+ \Omega_p^2 \sin 2pt - 2\Omega_p\Omega_s \cos(\omega_s - p)t$$
$$+ 2\omega_s\Omega_s\,[\alpha\cos\omega_s t - \beta\sin\omega_s t] + \Omega_s^2 \sin 2\omega_s t \quad (38)$$

The amplitudes and frequencies of the rotational field driving function are listed in Table I.

TABLE I

ROTATIONAL FIELD DRIVING FUNCTIONS

Frequency	Amplitude
dc	$2\alpha\beta\omega_s^2$
p	$2\omega_s\Omega_p\sqrt{\alpha^2+\beta^2}$
2p	Ω_p^2
$\omega_s - p$	$2\Omega_p\Omega_s$
ω_s	$2\omega_s\Omega_s\sqrt{\alpha^2+\beta^2}$
$2\omega_s$	Ω_s^2

T225

The sum mode mismatch driving function $\dot{\omega}_k$ from (32) and (36) may be expanded as (39).

$$\dot{\omega}_k = -\alpha[p\Omega_p \sin pt + \omega_s\Omega_s \cos\omega_s t]$$
$$- \beta[p\Omega_p \cos pt + \omega_s\Omega_s \sin\omega_s t]$$
$$+ \frac{k_3}{2}\,[3\Omega_0^2 \sin 2\omega_s t - \Omega_p^2 \sin 2pt + 2\Omega_p\Omega_s \cos(\omega_s - p)t] \quad (39)$$

The amplitudes and frequencies of the sum mode mismatch driving function are listed in Table II.

TABLE II

SUM MODE MISMATCH DRIVING FUNCTIONS

Frequency	Amplitude
p	$p\Omega_p \sqrt{\alpha^2 + \beta^2}$
2p	$\frac{1}{2} k_3 \Omega_p^2$
$\omega_s - p$	$k_3 \Omega_p \Omega_s$
ω_s	$\omega_s \Omega_s \sqrt{\alpha^2 + \beta^2}$
$2\omega_s$	$\frac{3}{2} k_3 \Omega_0^2$

T226

The arm mass unbalance driving function ($2\Gamma_{\mu max}$) is produced by the action of the gradiometer acceleration $\bar{a}$ acting on the individual mass unbalance of each arm. The torques developed about the gradiometer output axis are defined by (40) in terms of the individual arm mass unbalances $m\bar{\delta}_1$, $m\bar{\delta}_2$.

$$M_{\mu 1} = \bar{k} \cdot [m\bar{\delta}_1 \times \bar{a}]$$

$$M_{\mu 2} = \bar{k} \cdot [m\bar{\delta}_2 \times \bar{a}] \qquad (40)$$

An approximation to the arm mass unbalance driving function is stated as (41), where $\bar{\delta}_1 \triangleq -\bar{\delta}_2 \triangleq \bar{\delta}$.

$$2\Gamma_{\mu max} = \frac{2m}{I} [\bar{k} \cdot (\bar{\delta} \times \bar{a})] \quad . \qquad (41)$$

The expansion of (41) from (34) in the gradiometer reference frame is stated as (42).

$$2\Gamma_{\mu max} \simeq \frac{2m}{I}\left[\dot{\omega}_i(-\delta_i \ell_k) + \dot{\omega}_j(-\delta_j \ell_k) + \dot{\omega}_k(\delta_i \ell_i + \delta_j \ell_j)\right]$$
$$+ \frac{2m}{I}\left[\omega_i^2(-\delta_i \ell_j) + \omega_j^2(\delta_j \ell_i) + \omega_k^2(\delta_j \ell_i - \delta_i \ell_j)\right]$$
$$+ \frac{2m}{I}\left[\omega_i\omega_j(\delta_i \ell_i - \delta_j \ell_j) + \omega_i\omega_k(-\delta_j \ell_k) + \omega_j\omega_k(\delta_i \ell_k)\right]. \quad (42)$$

We are interested in estimating an upper bound for the mass unbalance driving function. In the interest of simplicity, an extreme upper bound may be defined from (42) by neglecting the algebraic signs of the coefficients. This inequality is stated as (43), where $(m\delta\ell_k/I) \triangleq \varepsilon$ and $(\ell_{ij}/\ell_k) \triangleq \rho$.

$$2\Gamma_{\mu max} \leq 2\varepsilon\left[\dot{\omega}_i + \dot{\omega}_j + (\omega_i + \omega_j)\,\omega_k\right]$$
$$+ \underline{2\varepsilon\rho}\left[2\dot{\omega}_k + \omega_i^2 + \omega_j^2 + 2\omega_k^2 + 2\omega_i\omega_j\right] \quad (43)$$

Because of its complexity, the time function of (43) will not be stated here. Rather, an estimate of the most significant terms is presented as Table III, where the misalignment angle γ is approximately $\sqrt{\alpha^2 + \beta^2}$. The dimensionless mass unbalance parameter $\varepsilon = [m\ell_k/I]$ is estimated to be $10^{-4} \leq \varepsilon \leq 10^{-5}$. The mass unbalance driving functions are much smaller than the most significant terms of the rotational field and sum mode mismatch functions.

TABLE III

MASS UNBALANCE DRIVING FUNCTION

Frequency	Amplitude
dc	$4\varepsilon(\gamma + \rho)\omega_s^2$
p	$4\varepsilon\omega_s\Omega_p$
2p	$2\varepsilon(\gamma + \rho)\Omega_p^2$
$\omega_s \pm p$	$4\varepsilon(\gamma + \rho)\Omega_p\Omega_s$
ω_s	$4\varepsilon\omega_s\Omega_s$
$2\omega_s$	$3\varepsilon k_3(\gamma + 2\rho)\Omega_0^2$

T227

The most significant gradient errors have been determined by substitution of the tabulated driving functions into (23). These gradient errors are listed in Table IV according to frequency. The magnitudes of these errors have been calculated for a set of representative parameters which are roughly the same as those used by DeBra in his preliminary analysis of this problem.* These parameters are defined by the following.

$\omega_s = 1$ Hz

$p = 0.1$ Hz

$\Omega_0 = 10^{-3}$ sec^{-1}

$\simeq 1.3 \times 10^{-8}$ sec^{-1}

$(\beta_{1,2}/2\omega_s) = 0.2$

$\theta = 0.3$ rad

$\gamma = 0.2$ rad

$\Omega p = 10^{-3}$ sec^{-1}

$k_3 = 0.1$

$\eta = 0.05$

$Q = 30$

*Private communication with Dr. Daniel DeBra, Stanford University.

TABLE IV

REPRESENTATIVE GRADIENT ERRORS

Frequency	Error Function	Error (E.U.)
dc	$\gamma^2\omega_s^2/Q$	5.3×10^7
p	$2\gamma\omega_s\Omega_p/Q$	8.4×10^4
2p	Ω_p^2/Q	33
$\omega_s \pm p$	$2\Omega_p\Omega_s/Q$	10^{-3}
ω_s	$2\gamma\omega_s\Omega_s/Q$	1.1
$2\omega_s$	$[1.5\eta k_3\Omega_0^2]\left[\frac{\beta_{1,2}}{2\omega_s}\right]^2$	0.3

T228

It is of interest to observe that the most significant error at the tuned resonant frequency $\omega_1 = 2\omega_s$ is produced by the sum mode mismatch, and that this error is only 0.3 E.U. for a 5% mismatch of the square of the sum mode frequencies β_1^2, β_2^2. The remaining errors in Table IV are all the result of the rotational field driving function $2\omega_i\omega_j$, and the largest of these occur at dc and at the satellite nutation frequency p.

To determine the effect of these error functions on the ultimate output of the gradiometer, we must model and examine the signal transmission properties of the gradiometer filter process. This process consists of the piezoelectric strain transducer and its amplifier matching circuitry, a phase-sensitive demodulator operating at the tuned resonant frequency $\omega_0 = 2\omega_s$, and a second order filter operating on the demodulator output. This process is illustrated in the block

diagram of Fig. 3 wherein a simple, untuned model of the strain transducer is shown with its gain normalized to unity at the tuned resonant frequency $\omega_0 = 2\omega_s$. The phase demodulation process acts as a frequency converter which produces the sums and differences of the input frequencies with the tuned resonant frequency $\omega_0 = 2\omega_s$. For example, input signals at the nutation frequency p will be converted to output signals at frequencies $2\omega_s \pm p$, and input signals at the tuned resonant frequency will be converted to dc and to the second harmonic of the tuned resonant frequency. This converted spectrum is then filtered by the second order post-demodulation filter to produce the output gradient signal Γ_0.

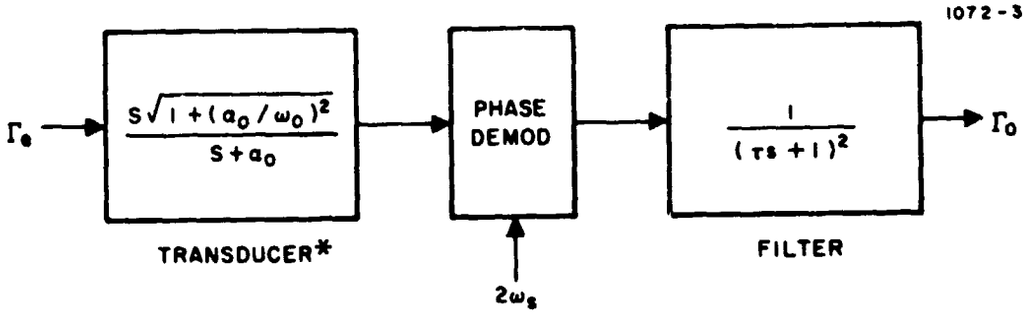

Fig. 3. Gradiometer Filter Process Block Diagram.

As previously stated, the large error magnitudes of Table IV occur at dc and at the subsatellite nutation frequency p. The dc term is blocked by the action of the strain transducer and does not appear in the gradient output. The term at nutation frequency is attenuated by the strain transducer an amount dependent on the parameter α_0. The

*$\alpha_0 = 1/R_0C_0$, where C_0 is the electrical capacity of the transducer and R_0 is its electrical load resistance.

normalized strain transducer gain at nutation frequency (for this model) is stated as (44).

$$\left|G_\tau(p)\right| = \frac{p\sqrt{1 + (\alpha_0/\omega_0)^2}}{\sqrt{p^2 + \alpha_0^2}} \quad . \tag{44}$$

The demodulator converts the nutation frequency to $2\omega_s \pm p$, and the second order output filter provides an additional attenuation dependent on the time constant τ. The gain of the output filter at $2\omega_s \pm p$ is approximately the same as at $2\omega_s$. This gain is stated as (45).

$$\left|G_f(2\omega_s)\right| = \frac{1}{1 + (2\omega_s\tau)^2} \quad . \tag{45}$$

The large nutation frequency error term of Table IV may be reduced to an acceptable output level by selection of the parameters α_0, τ. For example, this error term of 8.4×10^4 E.U. may be reduced to approximately 1.5 E.U. at the output by selecting $\alpha_0 = 2\omega_s$ and $\tau = 5$ sec. The combined gain of (44) and (45) using these parameters with $p = 0.1\ \omega_s$ and $\omega_s = 2\pi\ \text{sec}^{-1}$ is approximately 1.8×10^{-5}.

It should be emphasized that the filter estimates used here are conservative. An untuned model of the strain transducer was employed, and a moderate value of the output filter time constant was selected. It seems entirely feasible to provide an additional order of magnitude of attenuation on the nutation frequency error function without significant degradation of the proposed gradient signal measurement.

IV. SUMMARY AND CONCLUSIONS

A dynamic analysis of a simple model of the second order gravity gradiometer has been performed to determine the errors which result from acceleration and rotation of the gradiometer frame of reference. The results of this analysis were applied to the satellite MASCON experiment by estimation of the satellite motions when in lunar circular orbit.

Numerical evaluation of the motion-induced gradient errors indicates one potentially large error due to the rotational field produced by subsatellite nutation and gradiometer misalignment. It appears quite feasible to reduce this error to well below the 1 E.U. level by gradiometer filter design.